Prediction and Control of Rock Burst Phenomenon in Deep Underground Mining Based on Rock Behaviour

By:

Roohollah Shirani Faradonbeh

Thesis submitted in fulfilment of the requirements for the degree of

Doctor of Philosophy

The University of Adelaide

Faculty of Engineering, Computer and Mathematical Sciences

School of Civil, Environmental and Mining Engineering

Abstract

By depletion of minerals at shallow depths, there is a notable growing trend towards mining operations in deeper grounds whole the world. However, as the depth of mining and underground constructions increases, the occurrence of stress-induced failure processes, such as rockburst, both inside the rock masses, away from the mined-out areas, and near excavations is inevitable. Rockburst is defined as the sudden and violent failure of a large volume of overstressed rock, which can damage structures and workers, and considerably affect the economic viability of the projects. The propensity of rocks to bursting behaviour can be aggravated by the seismic disturbances induced by different sources in deep underground openings. Therefore, the in-depth understanding of the rockburst mechanism and its prediction and treatment is of paramount significance. Due to the high-complex and non-linear nature of this hazard and the vague relationship between its influential parameters, the common conventional criteria available in the literature, cannot predict rockburst occurrence and its risk level with sufficient accuracy. However, the machine learning (ML) algorithms, which benefit from an inherent intelligence procedure, can be utilised to overcome this problem.

During the last decade, significant progress has been made in implementing ML techniques to predict the propensity of rocks to bursting behaviour; however, the proposed models have complex internal structure and are difficult to use in practice. On the other hand, the experimental studies in this field are limited to measuring the bursting intensity of rocks under true-triaxial loading/unloading conditions. However, the complete stress-strain relation of rocks (i.e. the pre-peak and the post-peak regimes) subjected to different cyclic loading histories can open new insights into the rockburst/brittle failure mechanism and the long-term stability of the underground structures. The common load control techniques (i.e. the axial load-controlled and displacement-controlled techniques) cannot be employed directly to conduct the systematic cyclic loading tests and capture the failure behaviour of rocks, specifically for rocks showing class II/self-sustaining behaviour in the post-peak regime. Therefore, most current rock fatigue studies have focused on characterising the evolution of mechanical rock properties and damage parameters in the pre-peak regime.

Given the above, the main focus of this thesis was on developing practical and accurate models to predict rockburst-related parameters as well as better understanding the effect of seismic disturbances on the failure mechanism of rocks using data-driven and experimental approaches.

The robust ML algorithms, such as gene expression programming (GEP), GEP-based logistic regression (GEP-LR), classification and regression tree (CART) etc., were programmed and employed for the following tasks: (a) Providing a mathematical binary model to estimate the occurrence/non-occurrence of rockburst hazard; (b) developing a model to cluster the rockburst events based on their risk levels; (c) proposing a novel and practical multi-class classifier to distinguish three most common failure mechanisms of squeezing, slabbing and rockburst in underground mines based on intact rock properties; (d) quantifying the rockburst maximum stress (i.e. the stress level that bursting occurs) and bursting risk level based on the comprehensive database compiled from the true-triaxial unloading tests for different rock types and (e) predicting the peak strength variation of rocks subjected to cyclic loading histories. The obtained results from the above studies proved the high performance and capability of the used ML techniques in dealing with high-complex problems in mining projects, such as rockburst hazards. The newly proposed models in this research project outperformed the conventional rockburst criteria in terms of prediction accuracy and can be used efficiently in underground mining projects.

A new testing methodology namely “Double-Criteria Damage-Controlled Test Method” was developed in this research project to measure the complete stress-strain relation of rocks under different cyclic loading histories. This methodology, unlike the common testing methods, benefits from two controlling criteria, including the maximum stress level that can be achieved and the maximum lateral strain amplitude that the specimen is allowed to experience in a cycle during loading. The conducted uniaxial multi-level systematic cyclic loading tests on Tuffeau limestone proved the capability of this testing method in capturing the post-failure behaviour of rocks. The preliminary results also showed that rocks tend to behave more brittle by experiencing more cycles. Furthermore, a quasi-elastic behaviour dominated over the pre-peak regime during cyclic loading, which finally, resulted in strength hardening. In another comprehensive experimental study, 23 uniaxial single-level systematic cyclic loading tests were undertaken on Gosford sandstone specimens at different stress levels to unveil the failure mechanism of rocks subjected to seismic events. It was found that there exists a fatigue threshold (FTS) that lies between 86-87.5% so that below this threshold, no macroscopic damage is created in the specimen; rather, strength hardening induced by rock compaction occurs. Moreover, according to the evolution of damage parameters and brittleness index, the pre-peak and post-peak behaviour of rocks below the FTS was found to be independent of the cycle number. However, for the cyclic tests beyond the FTS, the instability of rocks increased

with the applied stress level, representing the propensity of rocks to brittle failures like rockburst.

To better replicate the rock stress conditions in deep underground mines and understand more about the evolution of some specific rock fatigue characteristics, such as strength hardening, FTS and post-peak instability with confining pressure, a comprehensive cyclic loading study was carried out on Gosford sandstone in triaxial loading conditions under seven confinement levels (σ_3/UCS_{avg}). It was found that by an increase in σ_3/UCS_{avg} from 10% to 100%, FTS decreases from 97% to 80%. An unconventional trend was observed for the stress-strain relations of rocks by varying σ_3/UCS_{avg}. A transition brittle to the ductile point was identified at σ_3/UCS_{avg}= 65%. Therefore, it can be inferred that with an increase in depth in rock engineering projects, the propensity of rock structures to brittle failures such as rock bursting at stress levels lower than the determined average peak strength can be aggravated. Also, it was observed that below the transition point, cyclic loading has a negligible effect on rock brittleness; while for σ_3/UCS_{avg}= 80% and 100%, the weakening effect of cyclic loading history was visible. According to the results of acoustic emission (AE), tangent Young's modulus (E_{tan}), cumulative irreversible axial strain (ω_a^{irr}) and axial strain at failure point (ε_{af}), it was found that for the hardening cyclic loading tests (with positive peak strength variation), the quasi-elastic behaviour was dominant during the pre-peak rock deformation. However, for the weakening cyclic loading tests (with negative peak strength variation), more plastic strains were accumulated within the rock specimens, which resulted in gradual damage evolution and stiffness degradation during cyclic loading before applying final monotonic loading. The peak deviator stress of Gosford sandstone under different confining pressures varied between -13.18% and 7.82%. An empirical model was developed using the CART algorithm as a function of confining pressure and the applied stress level. This model is helpful in predict peak strength variations of Gosford sandstone.

Keywords: Rockburst; Machine learning algorithm; Gene expression programming (GEP); Classification and regression tree (CART); Multi-class classification; True-triaxial unloading test; Failure mechanism; Systematic cyclic loading; Fatigue; Uniaxial cyclic loading test; Triaxial cyclic loading test; Acoustic emission; Brittleness; Strain energy; Pre-peak and post-peak behaviour; Brittleness; Damage; Irreversible Strain

Statement of Originality

I certify that this work contains no material which has been accepted for the award of any other degree or diploma in my name in any university or other tertiary institution and, to the best of my knowledge and belief, contains no material previously published or written by another person, except where due reference has been made in the text. In addition, I certify that no part of this work will, in the future, be used in a submission in my name for any other degree or diploma in any university or other tertiary institution without the prior approval of the University of Adelaide and where applicable, any partner institution responsible for the joint award of this degree.

The author acknowledges that copyright of published works contained within this thesis resides with the copyright holder(s) of those works.

I also give permission for the digital version of my thesis to be made available on the web, via the University's digital research repository, the Library Search and also through web search engines, unless permission has been granted by the University to restrict access for a period of time.

Roohollah Shirani Faradonbeh

Signature: **Date:** 26 August 2021

Acknowledgements

This research project would not have been possible without the support of many people. I am extremely indebted to my supervisors, Dr Abbas Taheri and Associate Professor Dr Murat Karakus of the School of Civil, Environmental and Mining Engineering, University of Adelaide, who continuously guided and supported me with full encouragement and enthusiasm during the PhD program. Their brilliant, skilful supervision enriched this study higher than my expectation.

The University of Adelaide is also gratefully acknowledged for the Beacon of Enlightenment PhD Scholarship, which enabled me to accomplish this research project.

I would also like to appreciate all the academic staff in the School of Civil, Environmental and Mining Engineering, particularly the mining laboratory staff, Mr Simon Golding and Mr Dale Hodson, for their aids in conducting the experimental works. Special thanks go to my office mates and friends for their time, advice and moral support.

I am grateful for my parents, whose constant love and support keep me motivated and confident. It was their love that raised me again when I got weary. Without you, I would not be the person I am today.

Finally, but by far most importantly, I owe my deepest gratitude to Marjan, who is my eternal love. I am forever thankful for the unconditional love and support throughout the entire thesis process and every day.

Table of Contents

List of Tables

List of Figures

Chapter 1

Thesis Overview

1.1. Introductory Background

With an increase in depth of mining and underground constructions, due to the complex stress state induced by different loading conditions (i.e. static, quasi-static and dynamic loadings), the occurrence of some destructive phenomena such as rockburst in the confined rock mass and/or near excavation is inevitable. Although there is no international consensus on the definition of a rockburst, it can be defined as a sudden and violent expulsion of overstressed rocks from the surrounding rock mass, resulting in the instantaneous release of accumulated strain energy. This phenomenon may cause injury to workers, damage to mine infrastructure and equipment, and possibly endanger the economic viability of the project (Cai and Kaiser 2018). From the viewpoint of the triggering mechanisms and physical modelling approaches, rockburst can be categorised into two main groups of strainburst and impact-induced rockburst (He et al. 2012). Strainburst, as a self-initiated rockburst, frequently occurs by local stress concentration at the edge of underground openings (brittle rocks) in the form of the sudden release of stored energy and is usually associated with the development of drifts, shafts, stope faces, and mining pillars. However, rockburst occurrence is not only associated with the strain energy accumulation in rocks during excavation but also with the human- (e.g. drilling and blasting operation, haulage system vibration, mechanical excavation, backfilling etc.) and/or environmental-induced (e.g. earthquake, volcanic activities, fault slip etc.) seismic disturbances (He et al. 2018). This type of rockburst is known as impact-induced rockburst. The deformation and failure characteristics of rocks subjected to seismic disturbances are completely different from those under conventional loading conditions (Taheri et al. 2016). Many factors affect the rockburst triggering, including the mechanical rock properties, excavation geometry, discontinuities, in-situ and mining-induced stresses and construction method, which have complicated rockburst mechanism (He et al. 2015). A considerable number of studies have been carried out by different researchers on rockburst hazard using theoretical and experimental approaches. However, due to the complex nature of rockburst and

many influential parameters, its mechanism is still unclear. Therefore, there exists a remarkable theoretical significance and engineering value to deeply understand the rockburst mechanism and find solutions for its prediction and treatment.

1.2. Literature Review and Research Gaps

1.2.1. Rockburst Occurrence and its Risk Level

The main focus of researchers during the last decade was on the prediction and control methods. From the viewpoint of prediction, rockburst can be assessed in the short term and long term. Short-term prediction of rockburst refers to the in-situ measurement techniques, including micro-seismic monitoring, microgravity, acoustic emission (AE), geological radar and so forth, which can be employed to determine the time and location of bursting. These techniques, however, are very costly and time-consuming. On the other hand, long-term prediction of rockburst is based on empirical criteria, numerical analyses, rockburst charts and data-driven techniques (soft-computing algorithms), which are usually used at the design stage of the projects to evaluate the propensity of different areas to bursting. These techniques are relatively quick, easy to use, and accurate, which can be implemented straightforwardly by engineers in practice. According to the state-of-the-art literature review conducted by (Zhou et al. 2018), approximately 100 rockburst empirical criteria have been proposed by different researchers from 1996 to the present, mostly based on strength/stress, strain and strain energy parameters. These criteria classify rockburst risk level (intensity) into four main classes of "None", "Light", "Moderate," and "Strong," based on the compiled information from the bursting location such as failure pattern, the scale of damage, and the sound of rockburst. The simplicity and operability are the most prominent advantages of empirical criteria.

However, the empirical criteria suffer from some critical drawbacks. Firstly, as mentioned above, rockburst is affected by many geological, rock mechanical and operational factors, whilst the empirical criteria only consider single or few parameters and cannot reflect the mutual effects of the influential factors for rockburst assessment. Secondly, the thresholds defined by the researchers for the empirical criteria are not unique, even for those having similar expressions. This is mainly due to the case study-based nature of these criteria and also the limited number of datasets used for their development by scholars. Thirdly, in several studies (Jian et al. 2012; Liu et al. 2013; Li et al. 2017), these criteria have shown low prediction accuracy, which raises doubts concerning their efficiency. Fourthly, some engineering assumptions have been applied to the empirical criteria which may affect their reliability. Given

such essential limitations and the complex non-linear nature of rockburst hazard, recently, the application of data-driven approaches such as machine learning (ML) algorithms have been increased in this field. The ML techniques (supervised and unsupervised algorithms) are capable of including more input parameters/predictors, dealing with noisy data, finding the latent non-linear relationships between inputs and the corresponding output and selecting the most influential parameters on rockburst occurrence using a smart feature selection procedure. As such, the ML algorithms do not need any prior knowledge concerning the mechanism of the problem and interrelationship of parameters, which is a significant benefit over the common criteria and statistical methods.

A considerable number of ML techniques, including artificial neural network (ANN), Bayesian network (BN), support vector machine (SVM), and logistic regression (LR), has been used extensively during the last decade by researchers to predict either rockburst occurrence/non-occurrence (a binary problem) or rockburst risk level (a multi-class problem) (Pu et al. 2019). In most of these studies, the uniaxial compressive strength (σ_c), uniaxial tensile strength (σ_t), maximum tangential stress (σ_θ), elastic strain energy index (W_{et}) and their combinations have been used as input parameters. The results prove the high performance of such algorithms in rockburst assessment. However, the ML techniques still have the following limitations: a) most of these algorithms are known as black-box techniques and have a complex internal computational procedure which is very difficult to understand by human, b) some of these techniques are prone to the over-fitting problem and may get stuck in local minima (solutions), and c) more importantly, most of the used techniques in the literature are not very practical since they cannot offer any mathematical or visual output to let the engineers and researchers apply them without using a code. Therefore, to overcome the above problems and provide practical and user-friendly models for the prediction of rockburst occurrence and its risk level (intensity), it is required to perform a comprehensive statistical analysis on the compiled database and utilise robust white-box techniques for modelling. Furthermore, by developing practical models that have an apparent internal structure, it will be possible to perform different statistical analyses, evaluate the rockburst vulnerability in associations with different input parameters, and finally propose an appropriate controlling technique.

From the viewpoint of rockburst control, several techniques have been proposed as potential solutions to mitigate this hazard (Saharan and Mitri 2011; Feng 2017; He et al. 2018): (1) Application of energy-absorbing bolts/cables which have a constant resistance under static and dynamic loadings and benefit from a large elongation capacity. These bolts/cables compared

with the ordinary ones, have higher resistance against dynamic loads and are capable of absorbing energy from multiple impacts, and finally, can maintain the large deformation of rock masses; (2) Application of ground preconditioning techniques such as destressing and water infusion (hydrofracturing). Destressing can be conducted using destress blasting and destress drilling (i.e. boreholes without explosives or pilot tunnels in civil tunnels excavated by TBMs) methods. The argument for destressing using blasting operation is that if destressing is carried out ahead of an advancing underground opening, the high-stress concentration zone would be transferred farther away from the working face into the solid rock mass. Therefore, a protective barrier (buffer zone) is created between the working face and the highly-stressed zone for the next mining operation. Hydrofracturing, as another rockburst control technique, changes the rock properties and decreases the ability of the rock masses in absorbing the strain energy (source of bursting). This method is mostly used for coal seams. (3) Application of alternative mining methods such as pillarless mining and mining with protective seams/veins or sacrifice galleries. This technique can be used in longwall mining of coal seams and can reduce the risk of spontaneous failures.

1.2.2. Rockburst and other Failure Mechanisms

In deep underground conditions, the rockburst is not the only failure mechanism. Different types of failure, such as high-stress slabbing and squeezing, may be observed based on the stress distribution around the excavation and the influential uncertain factors. However, to the author's knowledge, there has been no attempt to develop a practical model to distinguish different failure mechanisms for over-stressed rock masses in the deep underground. This is while the proper measurement of this issue at the initial stages of the projects can help engineers to optimise mining layout, apply the adequate supporting system and reduce high costs. According to the robustness and the approved capabilities of the ML techniques in dealing with high complex non-linear problems, this gap can be addressed properly by incorporating the most influential parameters on different failure modes and designing novel hybrid models (multi-class classifiers).

1.2.3. Experimental Studies and Rockburst Maximum Stress

As mentioned earlier, rockburst can also be investigated using experimental methods. In other words, the stress state around the excavations can be simulated using laboratory tests, and subsequently, study the failure mechanism/characteristics of rocks under different loading histories and loading conditions. Furthermore, the obtained results from these tests can be used

to calibrate the numerical models as well as to identify the critical stress conditions leading to dynamic failures. These experimental tests include uniaxial compression/tensile tests (Gong et al. 2019), conventional triaxial unloading tests (Huang et al. 2001), combined uniaxial and biaxial static-dynamic (cyclic) tests and true-triaxial loading/unloading tests (Bagde and Petroš 2005; He et al. 2010; Su et al. 2018). The conventional uniaxial compression and tensile tests usually have been used by the researchers to measure the mechanical rock properties (e.g. σ_c, σ_t, elastic modulus and so on), perform the energy analysis based on the obtained stress-strain curves and finally, to develop the strength- and strain/energy-based rockburst empirical criteria (e.g. rock brittleness index, $BI = \sigma_c/\sigma_t$). The combined static-dynamic (cyclic) tests in uniaxial, bi-axial and true-triaxial conditions are also significant to reproduce the stress state affecting on underground structures (e.g. mining pillars) which are exposed to in-situ stress and cyclic loading induced by different seismic sources (e.g. blasting waves). However, among the foregoing experimental methods, the true-triaxial unloading test can better simulate physically the rockburst process in deep underground conditions.

The true-triaxial unloading apparatus is capable of applying the in-situ stresses to the specimen simultaneously and independently, and by unloading the pressure on one or more surfaces of the specimen, can simulate the strain bursting at different locations of underground excavations. In studies undertaken using the true-triaxial testing system, the bursting propensity of rocks has been investigated based on the evolution of acoustic emission (AE) parameters (e.g. AE energy, hits, frequency, b-value), the kinetic energy of ejected rock fragments from the free face of the tested rock specimens, ejection velocity parameter, size of the rock fragments, the evolution of strain energy components and failure mode. Also, in some of these studies, the influence of different parameters such as temperature, moisture content, aspect ratio, loading and unloading rate, deviator stress, tunnel axial stress and radial stress gradient on rockbursting have been evaluated. Although considerable studies have been conducted using the true-triaxial test method for rockburst assessment by different researchers, most of them are limited to some specific rock types and loading histories, and there is no holistic and convenient approach to quantify the bursting potential of rocks. Rock specimens subjected to true-triaxial unloading conditions usually experience an explosion-like failure at a specific stress level, known as rockburst maximum stress (σ_{RB}). The proper estimation of this stress level for different rock types can help engineers to identify rockburst hazards in different in-situ stress conditions, to increase the long-term stability of the underground openings as well as for numerical studies. This task can be accomplished by compiling a comprehensive

database from rockburst tests and the application of robust ML techniques. By doing so, the developed model can be used conveniently in practice to predict bursting stress when the testing apparatus is not available.

1.2.4. Seismic Events and Rock Failure Behaviour

As stated earlier, rockburst can also be triggered by seismic disturbances induced by different sources in deep underground mines (i.e. impact-induced rockbursts). These seismic events can be replicated as time-dependent loads, i.e. cyclic and dynamic loadings, on a laboratory scale. Almost sixteen types of stress waves (waveforms) including ramp wave, sinusoidal wave, square wave, sawtooth wave and so forth can be generated in the laboratory to simulate rockburst with different magnitudes (He et al. 2018). The literature review (Bagde and Petroš 2005; Cerfontaine and Collin 2018) shows that different researchers have made tremendous efforts during the last decades to unveil the rock fatigue mechanism under different loading histories and loading conditions (i.e. uniaxial tests, triaxial tests, flexion tests, freeze-thaw tests and wetting and drying tests). Generally, prior studies can be classified into two main groups of systematic cyclic loading tests with a constant loading amplitude and damage-controlled cyclic loading tests with an incremental loading amplitude. However, systematic cyclic loadings having the ramp or sinusoidal waveforms can better represent the seismic events that are common during the mining operation. In rock fatigue studies, the results are usually analysed based on the information withdrawn from the measured stress-strain relations. Indeed, the complete stress-strain relation (i.e. the pre-peak and the post-peak regimes) is an efficient tool to manifest the evolution of strain energy (source of rockbursting) during the loading process as well as determining rock failure behaviour.

However, the majority of prior studies have focused on the effect of cyclic loading effect on the pre-peak characteristics of rocks (i.e. damage evolution, variation of peak strength and deformability parameters and determination of fatigue life and fatigue threshold stress), and, no significant progress has been made regarding the post-failure behaviour of rocks under cyclic loading. This is while in practical engineering, due to the release of in-situ rock stresses in the field, the surrounding rocks experience damage and instabilities in the post-peak state. In this regard, the rock brittleness showing the release mode of stored strain energy during loading is a very significant parameter in the process of rockburst assessment. However, the common method of brittleness measurement, i.e. $BI = \sigma_c/\sigma_t$, cannot represent the brittleness of rocks properly as the physical meaning of this index does not reflect the rock fracturing

process as well as σ_c and σ_t can be obtained from each other. Moreover, previous studies show that rocks with different σ_c and σ_t may have similar BI values representing the narrow range of variation of this index (Munoz et al. 2016; Meng et al. 2020). Hence, the rock brittleness can be measured in a more reliable manner based on the energy evolution in both the pre-peak and the post-peak regimes of rocks. On the other hand, rockburst usually occurs in rocks showing Class II behaviour during the failure stage accompanied by the release of excess energy and rock ejection (Li 2021).

Therefore, the proper measurement of post-peak behaviour of rocks under cyclic loading is of paramount significance to quantify the post-peak fracture energy, determine the rock brittleness, and consequently, understand more about the mechanism of severe geotechnical hazards like rockburst. However, as mentioned above, the current testing methods are not capable of capturing the post-peak stress-strain curve of rocks under cyclic loading adequately, specifically for brittle rocks which show a snap-back/self-sustaining failure behaviour in the post-peak regime. This is relevant to difficulties in controlling the axial load and damage extension in the post-peak regime for such rocks. The post-peak behaviour of rocks usually is characterised by either Class II (positive post-peak modulus representing an unstable fracture propagation) or a combination of Class I (negative post-peak modulus representing stable fracture propagation) and Class II behaviour. As it is discussed in detail in Chapters 6 and 7, the current axial load-controlled, axial displacement-controlled and lateral displacement-controlled loading techniques have significant limitations in controlling the axial load in the post-peak regime of rocks subjected to systematic cyclic loading. Thus, applying the current loading techniques results in a sudden failure without capturing the post-peak response properly. Therefore, a new testing methodology having the capability of performing different cyclic loading histories and measuring the complete stress-strain relations of rocks in both uniaxial and triaxial loading conditions is required.

1.2.5. Evolution of Rock Fatigue Characteristics

In prior rock fatigue studies, little attention has been made to some specific phenomena/parameters, including cyclic loading-induced strength hardening, fatigue threshold stress and post-peak instability of rocks and their variations at different confining pressures (σ_3) and stress levels. This is while in rock engineering projects, depending on the depth and geometry of excavations, surrounding rocks usually experience systematic cyclic loading at different confinement levels. Therefore, having an in-depth knowledge regarding the evolution

of the foregoing parameters with confinement level can open new insights into the failure mechanism of rocks, long-term stability of openings and reinforcement design. This task, however, requires applying a triaxial testing method, capable of recording the large lateral deformations created in the post-failure stage.

1.3. Research Objectives and Thesis Layout

Figure 1.1 represents the objectives, methodology and outcomes of this research schematically. According to the introductory background and the research gaps discussed in Sections 1.1 and 1.2, the present thesis addressed the following objectives:

1) To develop practical models to predict the occurrence or non-occurrence of rockburst hazard in deep underground mines through a binary expression and evaluate the effect of different parameters on rockbursting.

2) To assess rockburst risk levels (intensities) using robust ML techniques and evaluate the performance of the empirical criteria.

3) To measure the propensity of the over-stressed rock masses to different failure mechanisms in deep underground conditions.

4) To develop practical models for predicting both rockburst maximum stress (σ_{RB}) and rockburst risk index (I_{RB}) based on the results obtained from the true-triaxial unloading tests.

5) To develop a new experimental methodology to capture the post-failure behaviour of rocks subjected to systematic cyclic loading in uniaxial loading conditions.

6) To investigate the effect of pre-peak systematic cyclic loading at different stress levels on damage evolution and failure characteristics of rocks in uniaxial conditions.

7) To investigate the effect of confining pressure on some specific rock fatigue characteristics, including fatigue threshold stress, post-peak instability, and strength hardening induced by cyclic loading.

In this thesis, the data-driven approaches and rock mechanics laboratory tests were utilised as two main research tools to achieve the above objectives. According to the defined research objectives above, this thesis has been structured into eight chapters as follows:

The current chapter, Chapter 1, provides an introductory background regarding this research and contains topics including problem statement, literature review and research gaps, research objectives and thesis layout and conclusions and recommendations.

In Chapter 2, to address objective 1, a comprehensive study is carried out on the prediction of rockburst occurrence/non-occurrence based on a database containing 134 rockburst events, compiled from different underground mines. Several significant parameters, including uniaxial compressive strength (σ_c), uniaxial tensile strength (σ_t), maximum tangential stress (σ_θ) and elastic energy index (W_{et}) are chosen as input parameters, while a binary condition (i.e. "1" for occurrence and "0" for non-occurrence) is defined for rockburst as the output parameter. The homogeneity of the database is initially evaluated using different statistical tests. New models are then developed using three robust supervised ML techniques, including genetic algorithm-based emotional neural network (GA-ENN), decision tree-based C4.5 algorithm and gene expression programming (GEP) algorithm. Finally, the performance of the proposed new models, along with five empirical criteria, are evaluated, and the sensitivity analysis is performed on the best model to identify the most influential parameters on rockbursting. The results showed the high performance of the ML techniques in solving complex nonlinear geotechnical hazards like rockburst and their capability to improve practical models that can be used in the pre-design stages of an underground opening. The results of this study were published as a journal paper entitled "Long-term prediction of rockburst hazard in deep underground openings using three robust data mining techniques". The details of this paper are as follows:

Shirani Faradonbeh R, Taheri A (2019) Long-term prediction of rockburst hazard in deep underground openings using three robust data mining techniques. *Engineering with Computers* 35(2):659–675 (IF= 7.963, Q1)

In Chapter 3, two robust unsupervised algorithms, self-organizing map (SOP) and Fuzzy C-Mean (FCM) are used to cluster and identify rockburst risk level (intensity) as a multi-class problem based on the collected database (i.e. objective 2). The input parameters in this study are the same used in Chapter 2. The output, however, is a qualitative parameter showing different degrees of bursting, i.e. "None", "Light", "Moderate" and "Strong", which have been defined based on an empirical classification/visual inspection of rockburst location. These two applied unsupervised algorithms are capable of finding the latent relationships between the

input parameters and the corresponding output during a smart procedure, and finally, link each observation (rockburst event) to an appropriate cluster (risk level). In addition to SOM and FCM techniques, five empirical criteria are also employed to assess their capability in clustering rockburst events. Five common performance measures comprising accuracy (%), precision (%), Recall (%), F1 score (%) and Kappa (%) are calculated for all models and results are compared. This study revealed the superiority of the unsupervised ML techniques in terms of accuracy over the conventional criteria in assessing rockburst intensity. The results of this study were published as a journal paper entitled "Application of self-organizing map and fuzzy c-mean techniques for rockburst clustering in deep underground projects". The details of this paper are as follows:

Shirani Faradonbeh R, Shaffiee Haghshenas S, Taheri A, Mikaeil R (2020) Application of self-organizing map and fuzzy c-mean techniques for rockburst clustering in deep underground projects. *Neural Computing and Applications* 32(12):8545–8559 (IF= 5.606, Q1)

Chapter 4 aims to address objective 3, i.e. developing a practical and easy-to-use model for distinguishing different failure mechanisms of the over-stressed rock masses in deep underground conditions. For this aim, a database containing 35 failure events recorded from different underground projects is compiled. This database contains a wide range of rock types with compressive strength varying from 41 MPa to 335 MPa and includes three common types of failure, i.e. squeezing, strainbursting and slabbing. The intact rock properties, including uniaxial compressive strength (σ_c), Brazilian tensile strength (σ_t), elastic modulus (E) and Poisson's ratio (υ), which can be measured straightforwardly in the laboratory and have a significant effect on failure mechanisms are chosen as the predictors, while the failure mode is selected as the output parameter. In this chapter, a novel hybrid data-driven approach, namely gene expression programming based-logistic regression (GEP-LR), is proposed and implemented as a multi-class classifier to estimate the failure mechanism based on the given intact properties. Three separate binary mathematical models are initially developed using the GEP algorithm to reveal the relationship between failure mode and input parameters. Then, a probabilistic approach (i.e. LR) is linked to the GEP models to determine the probability of occurrence of each failure mechanism with high accuracy. Finally, the failure type having the highest probability index is selected as the output. The developed model in this study is provided as MatLab codes which researchers and engineers can use in practice to identify the

most probable failure type in different locations and consequently apply an appropriate controlling technique. The results of this study were prepared as a journal paper entitled "Rockburst assessment in deep geotechnical conditions using true-triaxial tests and data-driven approaches". The details of this paper are as follows:

Shirani Faradonbeh R, Taheri A, Karakus M (2020) The propensity of the over-stressed rock masses to different failure mechanisms based on a hybrid probabilistic approach. *Tunnelling and Underground Space Technology* x(x): x-x. The revised format submitted on 15/06/2021 (*Under review*) (IF= 5.915, Q1)

In Chapter 5, a comprehensive study is carried out by combining the results obtained from the true-triaxial unloading tests (rockburst tests) and two white-box machine learning (ML) algorithms to provide new models for estimating rockburst maximum stress (σ_{RB}) and its risk index (I_{RB}) (objective 4). The information of rockburst laboratory tests conducted from 2004 to 2012 are compiled in this study, and a series of statistical analyses are performed to provide a homogeneous database (i.e. removing missing values, identifying the outliers and natural groups in the original database). The prepared database contains different parameters including rock mass properties (i.e. UCS, E and ν), in-situ stresses, depth, rock density and horizontal pressure coefficient, which can be considered as input variables, and σ_{RB} and I_{RB}, which are defined as outputs. However, a systematic strategy, i.e. the stepwise selection and elimination (SSE) procedure, is followed to choose the most influential input parameters and subsequently decrease the complexity of the final models. The GEP algorithm that whose high performance in modelling complex problems was proved in previous chapters, is utilised along with the classification and regression tree (CART) algorithm to develop some explicit models (i.e. mathematical and graphical models) for estimating rockburst parameters. Validation of the developed models is completely verified using seven statistical indices and their corresponding thresholds. Parametric analysis is also performed in this study on the best models to evaluate the evolution of rockburst parameters by changing each input parameter within its range of values. The results point to the applicability of the proposed models for rockburst assessment with high reliability. These models can help researchers and engineers to estimate the stress level that rocks are prone to bursting and evaluate the rockburst risk level. The results of this study were published as a journal paper entitled "Rockburst assessment in deep geotechnical conditions using true-triaxial tests and data-driven approaches". The details of this paper are as follows:

Shirani Faradonbeh R, Taheri A, Ribeiro e Sousa L, Karakus M (2020) Rockburst assessment in deep geotechnical conditions using true-triaxial tests and data-driven approaches. *International Journal of Rock Mechanics and Mining Sciences* 128:104279 (IF= 7.135, Q1)

In Chapter 6, by reviewing the prior rock fatigue studies, a holistic classification is proposed for cyclic loading tests based on the loading history and load control technique. Also, a new experimental methodology, namely "Double-criteria damage-controlled cyclic loading test" is introduced in this chapter to capture the complete stress-strain relation of rocks (i.e. the pre-peak and the post-peak regimes) subjected to systematic cyclic loading (objective 5). In this new testing method, two criteria including the maximum axial stress level that cyclic loading is applied and the maximum lateral strain amplitude, $Amp.(\varepsilon_l)$, that a rock specimen is allowed to experience in a cycle during loading are adopted to control the axial load and damage extension before and after failure point. Tuffeau limestone is used in this study as a soft porous rock to evaluate the applicability of the proposed testing method in capturing the post-failure behaviour of rocks. A series of multi-level systematic cyclic loading tests are undertaken in this study by applying the axial load at approximately 81% of the determined average UCS, and the post-peak behaviour is captured in a controlled manner. Based on the obtained complete stress-strain relations, a preliminary evaluation is performed on post-peak behaviour as well as the evolution of fatigue damage parameters. Generally, the results represent the success of the proposed technique in measuring the full response of rocks under cyclic loading, which can open new insights regarding the rock failure mechanism. Also, a strength hardening induced by cyclic loading is observed for this rock type which needs to be further investigated. The results of this study were published as a journal paper entitled "Post-peak behaviour of rocks under cyclic loading using a double-criteria damage-controlled test method". The details of this paper are as follows:

Shirani Faradonbeh R, Taheri A, Karakus M (2021) Post-peak behaviour of rocks under cyclic loading using a double-criteria damage-controlled test method. *Bulletin of Engineering Geology and the Environment* 80(2):1713–1727 (IF= 4.298, Q1)

In Chapter 7, a more comprehensive experimental study is undertaken using the developed test method in Chapter 6 to investigate the effect of pre-peak systematic cyclic loading applied at different stress levels on both pre-peak and post-peak characteristics of Gosford sandstone in

uniaxial loading conditions (objective 6). This chapter also intends to examine some specific behaviours observed in the previous chapter (e.g. cyclic loading-induced strength hardening) in more depth. In this chapter, the uniformity of the testing material is initially evaluated based on the performed six UCS tests and the measured mechanical rock properties. Seventeen (17) single-level systematic cyclic loading tests are then designed at different stress levels ranging from 80% to 96% of the average monotonic strength (i.e. in the unstable crack propagation stage). This study defines two types of cyclic loading tests: hardening cyclic loading tests (the specimens that do not fail during 1500 cycles) and fatigue cyclic loading tests (the specimens that fail in the cycle). For both types of tests, the double-criteria damage-controlled cyclic loading test method is adjusted in such a way that the post-peak behaviour of rocks is captured in a controlled manner, and based on the measured complete stress-strain relations, the damage evolution, post-peak instability of rocks (rock brittleness) and strength hardening phenomenon is investigated comprehensively. The results of this study were published as a journal paper entitled "Failure behaviour of a sandstone subjected to the systematic cyclic loading: Insights from the double-criteria damage-controlled test method". The details of this paper are as follows:

Shirani Faradonbeh R, Taheri A, Karakus M (2021) Failure behaviour of a sandstone subjected to the systematic cyclic Loading: Insights from the double-criteria damage-controlled test method. *Rock Mechanics Rock Engineering* x(x): x-x (IF= 6.730, Q1)

In Chapter 8, for the first time, a comprehensive study is carried out in triaxial conditions to better replicate the stress state in deep underground openings and consequently understand more about the failure mechanism of rocks subjected to cyclic loading under different confining pressures. A modified triaxial testing system (by mounting four strain gauges on the Hoek cell membrane and connecting them to a half-bridge circuit) is utilised to provide a single lateral strain-based feedback signal. With this arrangement, failure behaviour was accurately investigated. Seven confinement levels (i.e. σ_3/UCS_{avg}= 10-100%) are defined to evaluate the effect of both confining pressure and systematic cyclic loading history on the evolution of some specific rock fatigue characteristics, including post-peak brittleness, fatigue threshold stress and strength hardening. At each confinement level, the specimens experience 1000 loading and unloading cycles at different stress levels. Should the specimen did not fail in cycles, a final monotonic loading is applied under lateral strain-controlled loading conditions to capture the failure behaviour. The non-destructive AE technique also is employed to analyse damage

evolution and support discussions. The results point to the significant effect of confining pressure on the failure mechanism (brittle/ductile) of rocks and the long-term stability of the underground structures. The obtained results from this study were prepared as a journal paper entitled "Fatigue failure characteristics of sandstone under different confining pressures" and submitted to the journal of "Rock Mechanics and Rock Engineering", which is currently under review. The details of this paper are as follows:

Shirani Faradonbeh R, Taheri A, Karakus M (2021) Fatigue failure characteristics of sandstone under different confining pressures. *Rock Mechanics and Rock Engineering* x(x): x-x. Submitted on 22/05/2021 (*Under Review*) (IF= 6.730, Q1)

Finally, in Chapter 9, conclusions drawn from this research project are summarised and some promising recommendations/directions are provided for future rockburst studies.

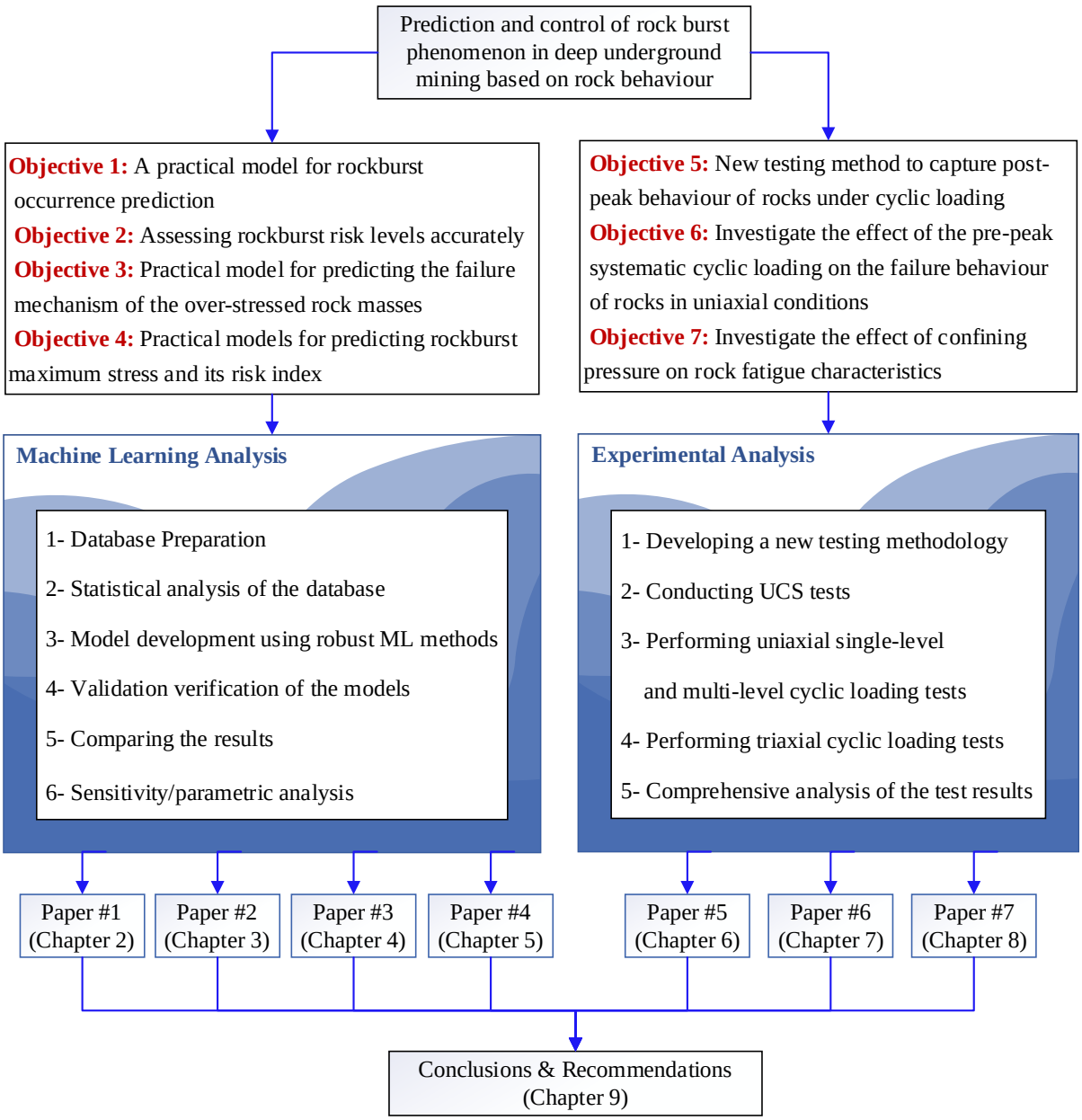

Figure 1.1 The objectives, methodologies and outcomes of the present thesis

References

Bagde MN, Petroš V (2005) Fatigue properties of intact sandstone samples subjected to dynamic uniaxial cyclical loading. *International Journal of Rock Mechanics and Mining Sciences* 42(2):237–250

Cai M, Kaiser P (2018) Rockburst support reference book—volume I: rockburst phenomenon and support characteristics. *Laurentian University*. 284

Cerfontaine B, Collin F (2018) Cyclic and fatigue behaviour of rock materials: review, interpretation and research perspectives. *Rock Mechanics and Rock Engineering* 51(2):391–414

Feng X (2017) Rockburst : mechanisms, monitoring, warning, and mitigation. *Butterworth-Heinemann*

Gong F, Yan J, Li X, Luo S (2019) A peak-strength strain energy storage index for rock burst proneness of rock materials. *International Journal of Rock Mechanics and Mining Sciences* 117:76–89

He M, e Sousa LR, Miranda T, Zhu G (2015) Rockburst laboratory tests database - Application of data mining techniques. *Engineering Geology* 185:116–130

He M, Ren F, Liu D (2018) Rockburst mechanism research and its control. *International Journal of Mining Science and Technology* 28(5):829–837

He M, Xia H, Jia X, et al (2012) Studies on classification, criteria and control of rockbursts. *Journal of Rock Mechanics and Geotechnical Engineering* 4(2):97–114

He MC, Miao JL, Feng JL (2010) Rock burst process of limestone and its acoustic emission characteristics under true-triaxial unloading conditions. *International Journal of Rock Mechanics and Mining Sciences* 47(2):286–298

Huang RQ, Wang XN, Chan LS (2001) Triaxial unloading test of rocks and its implication for rock burst. *Bulletin of Engineering Geology and the Environment* 60(1):37–41

Jian Z, Xibing L, Xiuzhi S (2012) Long-term prediction model of rockburst in underground openings using heuristic algorithms and support vector machines. *Safety Science* 50(4):629–644

Li CC (2021) Principles and methods of rock support for rockburst control. *Journal of Rock Mechanics and Geotechnical Engineering* 13(1):46–59

Li N, Feng X, Jimenez R (2017) Predicting rock burst hazard with incomplete data using Bayesian networks. *Tunnelling and Underground Space Technology* 61:61–70

Liu Z, Shao J, Xu W, Meng Y (2013) Prediction of rock burst classification using the technique

of cloud models with attribution weight. *Natural Hazards* 68:549–568

Meng F, Wong LNY, Zhou H (2020) Rock brittleness indices and their applications to different fields of rock engineering: A review. *Journal of Rock Mechanics and Geotechnical Engineering*, 68(2):549-568

Munoz H, Taheri A, Chanda EK (2016) Fracture Energy-Based Brittleness Index Development and Brittleness Quantification by Pre-peak Strength Parameters in Rock Uniaxial Compression. *Rock Mechanics and Rock Engineering* 49(12):4587–4606

Pu Y, Apel DB, Liu V, Mitri H (2019) Machine learning methods for rockburst prediction-state-of-the-art review. *International Journal of Mining Science and Technology* 29(4):565–570

Saharan MR, Mitri H (2011) Destress blasting as a mines safety tool: Some fundamental challenges for successful applications. In: *Procedia Engineering. Elsevier*, pp 37–47

Su G, Hu L, Feng X, et al (2018) True triaxial experimental study of rockbursts induced by ramp and cyclic dynamic disturbances. *Rock Mechanics and Rock Engineering* 51(4):1027–1045

Taheri A, Yfantidis N, L. Olivares C, et al (2016) Experimental Study on Degradation of Mechanical Properties of Sandstone Under Different Cyclic Loadings. *Geotechnical Testing Journal* 39(4):673-687

Zhou J, Li X, Mitri HS (2018) Evaluation method of rockburst: State-of-the-art literature review. *Tunnelling and Underground Space Technology* 81:632–659

Statement of Authorship

Title of Paper	Long-term prediction of rockburst hazard in deep underground openings using three robust data mining techniques
Publication Status	☑ Published ☐ Accepted for Publication ☐ Submitted for Publication ☐ Unpublished and Unsubmitted work written in manuscript style
Publication Details	**Shirani Faradonbeh R**, Taheri A (2019) Long-term prediction of rockburst hazard in deep underground openings using three robust data mining techniques. *Engineering with Computers* 35(2):659–675

Principal Author

Name of Principal Author (Candidate)	Roohollah Shirani Faradonbeh		
Contribution to the Paper	Literature review and database preparation, statistical analysis, development of models and preparation of the manuscript		
Overall percentage (%)	80%		
Certification:	This paper reports on original research I conducted during the period of my Higher Degree by Research candidature and is not subject to any obligations or contractual agreements with a third party that would constrain its inclusion in this thesis. I am the primary author of this paper.		
Signature		Date	17 June 2021

Co-Author Contributions

By signing the Statement of Authorship, each author certifies that:

i. the candidate's stated contribution to the publication is accurate (as detailed above);
ii. permission is granted for the candidate in include the publication in the thesis; and
iii. the sum of all co-author contributions is equal to 100% less the candidate's stated contribution.

Name of Co-Author	Abbas Taheri		
Contribution to the Paper	Research supervision, review and revision of the manuscript		
Signature		Date	21 June 2021

Chapter 2

Long-term Prediction of Rockburst Hazard in Deep Underground Openings using Three Robust Data Mining Techniques

Abstract

Rockburst phenomenon is the extreme release of strain energy stored in surrounding rock mass which could lead to casualties, damage to underground structures and equipment and finally endanger the economic viability of the project. Considering the complex mechanism of rockburst and a large number of factors affecting it, the conventional criteria cannot be used generally and with high reliability. Hence, there is a need to develop new models with high accuracy and easy to use in practice. This study focuses on the applicability of three novel data mining techniques including emotional neural network (ENN), gene expression programming (GEP), and decision tree-based C4.5 algorithm along with five conventional criteria to predict the occurrence of rockburst in a binary condition. To do so, a total of 134 rockburst events were compiled from various case studies and the models were established based on training datasets and input parameters of maximum tangential stress, uniaxial tensile strength, uniaxial compressive strength, and elastic energy index. The prediction strength of the constructed models was evaluated by feeding the testing datasets to the models and measuring the indices of root mean squared error (RMSE) and percentage of the successful prediction (PSP). The results showed the high accuracy and applicability of all three new models, however, the GA-ENN and the GEP methods outperformed the C4.5 method. Besides, it was found that the criterion of elastic energy index (EEI) is more accurate among other conventional criteria and with the results similar to the C4.5 model, can be used easily in practical applications. Finally, a sensitivity analysis was carried out and the maximum tangential stress was identified as the most influential parameter, which could be a guide for rockburst prediction.

Keywords: Rockburst occurrence, Data mining techniques, Emotional neural network, Gene expression programming, C4.5 algorithm, Conventional criteria

2.1. Introduction

One of the most important concerns in deep underground activities such as mining and civil projects is the occurrence of rockburst phenomenon. Rockburst is an unexpected and severe failure of a large volume of over-stressed rock caused by the instantaneous release of accumulated strain energy. This phenomenon usually is accompanied by other events such as spalling, slabbing, and throwing of rock fragments which could be led to injuries, deformation of supporting system, damage to equipment or even collapse of a large area of the underground excavation and finally cease the operation (Dong et al. 2013; Adoko et al. 2013; Li et al. 2017; Weng et al. 2018) . In deep underground activities, the induced seismicity has a great role in rockburst occurrence, therefore, the identification and localization of seismic events are essential in rockburst assessment (Dong et al. 2016a, b, 2017a, b). Great number of theoretical and experimental studies have been performed since 1930 by many researchers on the mechanism, prediction, and control of rockburst (Weng et al. 2017; Akdag et al. 2018). However, rockburst still remains an unsolved problem in deep mining (He et al. 2015). Rockbursts can be classified using various criteria comprising potential damage, failure pattern, scale, and severity. From the viewpoint of damage, it classifies into four classes of none, light, moderate, and strong. Based on the failure pattern, there are four types of failures including slabby spalling, dome failure, in-cave collapse, and bending failure. In terms of scale, rockbursts can be introduced as sparse with the rockburst length lower than 10 m, large-area with the rockburst length between 10-20 m and continuous rockburst with the length higher than 20 m. The severity of rockbursts can be assessed as a function of failure depth (He et al. 2012; Wang et al. 2012). According to the influence diagram developed by Sousa and Einstein (2007), many factors affect the occurrence of rockburst such as mechanical properties of rock, geological circumstances, construction method, and in-situ stress state. Considering the great number of effective parameters and the vague mechanism of rockburst, prediction, and control of this hazardous phenomenon is a very difficult task. Rockburst can be predicted in short-term and long-term. In-situ measurement techniques such as microseismic monitoring system and acoustic emission can be used to acquire the exact location and the specific time of rockburst occurrence at each stage of the project (i.e. in short-term). However, these techniques are time-consuming, costly, and require precise surveying strategies. On the other hand, rockburst prediction in long-term is mainly based on conventional criteria, numerical models, and data mining techniques. Compared to the short-term prediction technique, the long-term one can be served as a quick guide for engineers during the initial stages of the project and consequently,

enable them to decide about the excavating and controlling methods (Adoko et al. 2013; Li et al. 2017). During the last three decades, various rockburst proneness indices have been developed based on strength parameters and rock strain energy (see Table 2.1) [15].

Table 2.1 A summary of conventional criteria for rockburst prediction

Criterion	Equation	Input parameters	Rockburst discrimination
Russenes criterion (Russenes 1974)	$\frac{\sigma_\theta}{\sigma_c}$	σ_θ, σ_c	≥ 0.25
Hoek criterion (Hoek and Brown 1980)	$\frac{\sigma_c}{\sigma_\theta}$	σ_θ, σ_c	≤ 3.5
Stress coefficient (Wang et al. 1998)	$\frac{\sigma_\theta}{\sigma_c}$	σ_θ, σ_c	≥ 0.3
Rock brittleness coefficient (Wang et al. 1998)	$\frac{\sigma_c}{\sigma_t}$	σ_t, σ_c	≤ 40
Elastic energy index (Wang et al. 1998)	$\frac{E_R}{E_D}$	E_R, E_D	≥ 2.0

σ_θ is the maximum tangential stress, σ_c is the uniaxial compressive stress, σ_t is the uniaxial tensile stress, E_R is the retained energy, E_D is the dissipated energy

According to Table 2.1, the conventional criteria only consider very few input parameters, therefore, cannot take into account a wide range of parameters that may influence rock-bursting. Data mining is a relatively new computational method with the aim of discovering latent patterns and relationships between raw datasets which combines different areas such as statistics, machine learning, and so on. Data mining techniques have the capability to deal with the datasets containing multiple input and output variables (Berthold and Hand 2003; Jian et al. 2012). Hence, they have been used extensively in geosciences (Khandelwal et al. 2017a, b; Aryafar et al. 2018; Mikaeil et al. 2018a). As a first attempt, Feng and Wang (1994) developed two artificial neural networks (ANNs) to predict and control the probable rockbursts. Their successful experience encouraged other scholars to investigate the applicability of novel data mining techniques in rockburst assessment (Zhao 2005; Gong and Li 2007; Shi et al. 2010; Zhou et al. 2010). Although the methods used by the scholars could consider more input parameters, most of them are black-box, i.e. they cannot provide a clear and comprehensible relationship between the input and output parameters. Consequently, the developed models using such opaque techniques cannot easily be used in practice. On the other hand, the conventional criteria as reported in many studies, could not predict rockburst with high accuracy. Therefore, there is still a need to develop transparent and easy to use rockburst

models. In the current study, the applicability of three robust data mining techniques including genetic algorithm-based emotional neural network (GA-ENN), C4.5, and gene expression programming (GEP) in rockburst prediction was evaluated. Although the GA-ENN is a subset of black-box techniques, it is a new version of the ANN with enhanced capacities. In this study, for the first time, this method is used for a mining and geoscience problem. C4.5 and GEP techniques, in spite of the ones used in the previous studies, can provide simple models to predict rockburst occurrence. For this purpose, after preparing a database and assessing it statistically, three new predictive models were developed based on the training dataset. In continuing, a group of unused data (testing data) was fed to the trained models to testify their forecasting accuracy using two performance indices. Then, to have a comprehensive comparison, the results of the developed models were compared with the results of five conventional criteria. In the end, a sensitivity analysis was carried out to evaluate the influence of input parameters on the corresponding output.

2.2. Database Preparation

A database containing 134 rockburst events was prepared from literature (see the "Appendix A"). These rockburst events have been measured in diverse underground projects associated with coal and non-coal mines, powerhouse stations, hydropower stations, and so on (Jian et al. 2012; Dong et al. 2013; Adoko et al. 2013; He et al. 2015). Each record of the database contains four parameters which are the maximum tangential stress of surrounding rock (σ_θ), the uniaxial tensile strength of rock (σ_t), the uniaxial compressive strength of rock (σ_c), and the elastic energy index (W_{et}). Maximum tangential stress (σ_θ) around the excavation is a key factor that is affected by the rock stress, groundwater, shape, and diameter of excavation. Since it would not be possible to measure these four parameters in association with rockburst occurrence, maximum tangential stress can be regarded as a representative parameter of those parameters. Rock compressive strength σ_c and tensile strength σ_t are the parameters that represent the capability of rocks to store elastic strain energy as well as its tensile and shear failure characteristics. Many theories have been proposed to describe the rockburst mechanism, however, the most accepted one is "energy theory". Hence, several energy-based indices have been proposed by the researchers and most of them are correlated with each other and similarly related to rockburst occurrence. Among them, W_{et} (the ratio of stored strain energy to that dissipated energy during a cycle of loading-unloading under uniaxial compression) is the most common energy criterion which has a direct influence on rockburst in such a way that with the

increase of W_{et}, the probability of rockburst occurrence and its intensity will increase (Palmstrom 1995; Jian et al. 2012; Liu et al. 2013; Li et al. 2017). Therefore, in the current study, four parameters of σ_θ, σ_t, σ_c, and W_{et} were adopted as the input parameters. Table 2.2 shows the descriptive statistics of the relevant input parameters that are used to develop rockburst models. For convenience, the abbreviations of input parameters were considered for modelling instead of their symbols; they are characterized by MTS, UTS, UCS, and EEI for σ_θ, σ_t, σ_c, and W_{et}, respectively. To understand more about the relationship between the input parameters, Pearson correlation coefficients were computed which the results are listed in Table 2.3. According to this table, there are moderate correlations for the UTS-UCS and EEI-UCS if the categorizations proposed by Dancy and Reidy (2004) are followed.

Table 2.2 Descriptive statistics of the input parameters within the database

Parameter	Abbreviation	Unit	Minimum	Maximum	Mean	Std. deviation	Variance
σ_θ	MTS	MPa	2.6	108.4	51.354	28.567	816.055
σ_t	UTS	MPa	1.3	22.6	7.519	4.926	24.268
σ_c	UCS	MPa	20.0	306.6	127.957	59.417	3530.415
W_{et}	EEI	Dimensionless	0.85	10.6	4.726	2.196	4.824

Table 2.3 Correlation coefficients between the input parameters

Variables	T	UTS	UCS	EEI
T	1	0.569	0.589	0.508
UTS	0.569	1	0.650	0.443
UCS	0.589	0.650	1	0.636
EEI	0.508	0.443	0.636	1

Prior to any modelling, the statistical analysis of original database has high importance. The presence of outliers in the database negatively affects the ability of algorithms to find a precise relationship between input and output parameters and consequently, decreases the reliability of the developed model. Additionally, outliers may create some natural groups with different behaviours in a single dataset and if this is the case, it is necessary to identify them and develop separate models (Middleton 2000; Tiryaki 2008). The box-plot is a common and standardized method to display the distribution of data based on minimum, first quartile ($Q1$), median ($Q2$), third quartile ($Q3$), and maximum values. The measurements outside the range of ($Q1 -$

$3(Q3-Q1), Q3+3(Q3-Q1)$) are defined as extreme outliers and should to be omitted from the database, while those which are in the range of $(Q1-1.5(Q3-Q1), Q3+1.5(Q3-Q1))$ are known as suspected outliers which are common in a big database and could be considered in modelling (Middleton 2000). Fig. 2.1 shows the box-plots of input parameters. According to this figure, the median line is not in the centre of boxes which indicates that the input parameters do not have a symmetric distribution. Besides, with the exception of MTS, other input parameters have few suspected outliers.

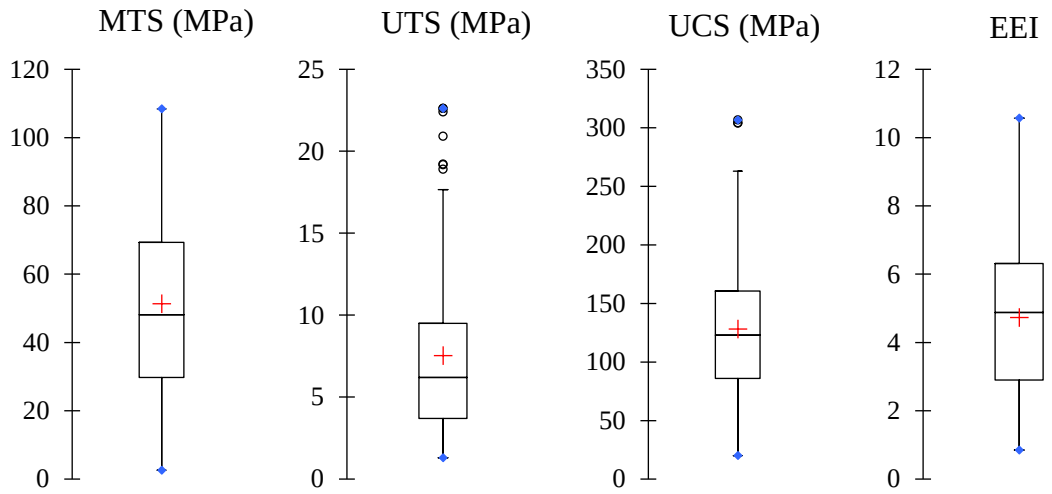

Figure 2.1 Box plots of input parameters

As a second effort, a principal component analysis (PCA) was conducted to check the existence or non-existence of natural groups in the database. PCA is a dimension reduction technique that enables the user to transform the initial correlated variables from an m-dimensional space to an n-dimensional one where $n < m$. The new uncorrelated variables are nominated as principal components (PCs) which are the linear combination of initial variables (Sayadi et al. 2012; Faradonbeh and Monjezi 2017). To perform this analysis, firstly, the datasets were normalized between 0 and 1 using the Min-Max method to eliminate the effect of range. In the second step, the correlation matrix was created for input parameters. Then, the eigenvalues and eigenvectors corresponding to the previous correlation matrix were calculated for each PC as follows:

$$XV = \lambda V \rightarrow (X-\lambda I)V = 0 \rightarrow determinant(X-\lambda I) = 0 \rightarrow \begin{cases} \lambda_1, \lambda_2, \dots, \lambda_n \\ V_1, V_2, \dots, V_n \end{cases} \quad (2.1)$$

where X, λ, and V are the matrix of datasets, eigenvalue, and eigenvectors, respectively.

Eventually, the PCs were obtained by multiplying the input parameters in related eigenvectors. Fig. 2.2 shows the scree plot of eigenvalues against the number of components. According to this figure, 92.872 % of the database variations can be explained just with three first PCs by projecting the observations on these axes (i.e. PC1, PC2, and PC3). The scatter plots of PC1-PC2 and PC1-PC3 are shown in Fig. 2.3. As can be seen, there is not any natural group, i.e. the concentration of observations in specific areas in the database. Besides, few suspected outliers mentioned in the previous analysis can be seen in this figure as well. As a result, it can be said that the prepared database is suitable for further analysis. The output parameter is the rockburst occurrence, if any, was nominated as “Yes” otherwise, was nominated as “No”. Since the output is a qualitative parameter, we transferred it to a binary parameter, i.e. 0 (No) and 1(Yes).

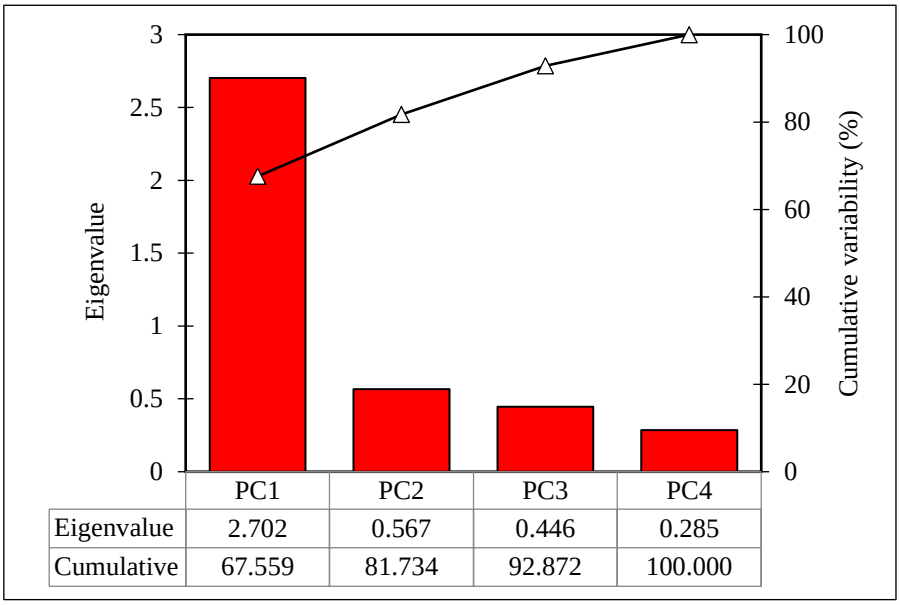

	PC1	PC2	PC3	PC4
Eigenvalue	2.702	0.567	0.446	0.285
Cumulative	67.559	81.734	92.872	100.000

Figure 2.2 Scree plot of PCA analysis

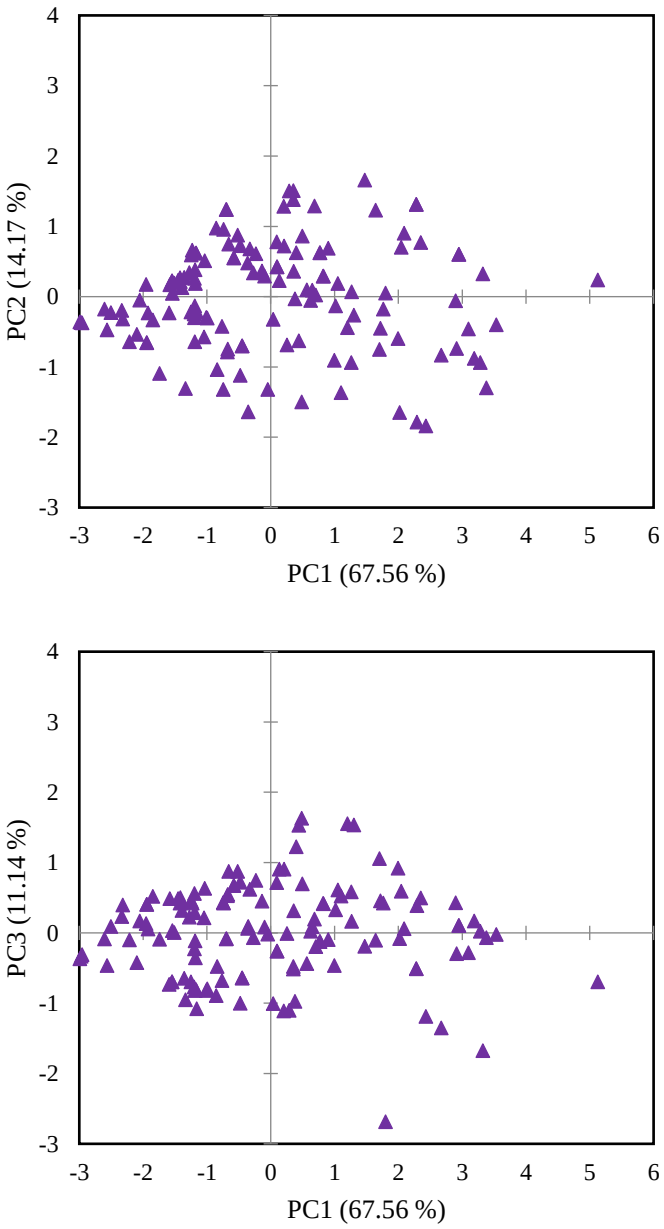

Figure 2.3 Scatter plots of PC1-PC2 and PC1-PC3

2.3. Data Mining Techniques

2.3.1. Genetic Algorithm-Based Emotional Neural Network (GA-ENN)

Artificial neural network (ANN), a brain-inspired approach, is a popular branch of soft computing techniques firstly invented by McCulloch and Pitts (1943) and has been used extensively in different areas (Jahed Armaghani et al. 2015; Mohamad et al. 2016; Saghatforoush et al. 2016; Mikaeil et al. 2018b). ANNs, however, suffer from a fundamental problem which is known generally as the curse of dimensionality, i.e. the number of learning parameters increases exponentially with increase in the number of neurons in input, hidden,

and output layers that finally lead to high computational complexity (CC). Recently, a limbic-based emotional neural network (ENN) is developed by Lotfi and Akbarzadeh-T (2014) based on the emotional process of the brain with a single layer structure. Unlike ANNs that is formed based on a biological neuron, ENNs are based on the interaction of four neural areas of the emotional brain comprising thalamus, sensory cortex, orbitofrontal cortex (OFC), and amygdala. These four areas using the features of expanding, comparing, inhibiting, and exciting, overcome the shortages related to the common ANNs and provide more precise solutions. Initial ENNs have a low CC during the learning process, but the number of patterns which can be stored is limited that makes a low information capacity (IC) for this method. Lotfi and Akbarzadeh-T (2016), thanks to a winner-take-all approach (WTA), introduced a new version of ENN with the name of WTAENN which is able to increase the IC of the algorithm. The structure of WTAENN with n input, one output, and $m = 1$ competitive part is shown in Fig. 2.4. According to this figure, original input data (i.e. $\vec{p} = [p_1, p_2, \dots, p_n]$) first enter to thalamus part. In the thalamus, input data will expand by the following equation:

$$[p_{n+1}, \dots, p_{n+k}] = FE_{j=1,\dots,n}(p_j) \tag{2.2}$$

where FE is an expander function which can be a Gaussian or Sinusoidal function or in general can be defined as:

$$FE_{j=1,\dots,n}(p_j) = \max_{j=1,\dots,n}(p_j) \tag{2.3}$$

Then, the expanded signals are sent to winner sensory cortex i^*which is selected if only and only if:

$$\forall i \ \left\|[p_1, p_2, \dots, p_n] - [c_{1,i^*}, c_{2,i^*}, \dots, c_{n,i^*}]\right\| \leq \left\|[p_1, p_2, \dots, p_n] - [c_{1,i}, c_{2,i}, \dots, c_{n,i}]\right\|, \ 1 \leq i \leq m \tag{2.4}$$

where $c_1, c_2, \dots, c_n$ are the learning weights.

Afterwards, the signals propagate to the related OFC and amygdala and the weights of $w_{1,i}, w_{2,i}, \dots, w_{n,i}$ from the ith OFC and the weights of $v_{1,i}, v_{2,i}, \dots, v_{n,i}$ from ith amygdala are used during the learning process to determine the final output. During the learning process, amygdala receives the imprecise input of p_{n+1} from the thalamus to determine the output signal of E_a. After that, amygdala receives an inhibiting signal from OFC (E_o) which with applying the activation function (e.g. $purelin$, $tansig$, $hardlim$ and $logsig$ functions), the final emotional signal (predicted value) will be achieved. The final output can be calculated by the following equation:

$$E_i(\vec{p}) = f(E_{ai} - E_{oi}) = f\left(\sum_{j=1}^{n+1}(v_{j,i}p_j) - \sum_{j=1}^{n}(w_{j,i}p_j) - b_i\right) \tag{2.5}$$

where $v_{j,i}$ is the weight of ith amygdala, p_j is the input pattern, $w_{j,i}$ is the weight belongs to ith OFC and b_i is the related bias.

Generally, in the process of WTAENN learning, the learning weights (i.e. competitive weights (c-weights), amygdala weights (v-weights) and OFC weights (w-weights)) should be adjusted (Lotfi and Akbarzadeh-T 2016).

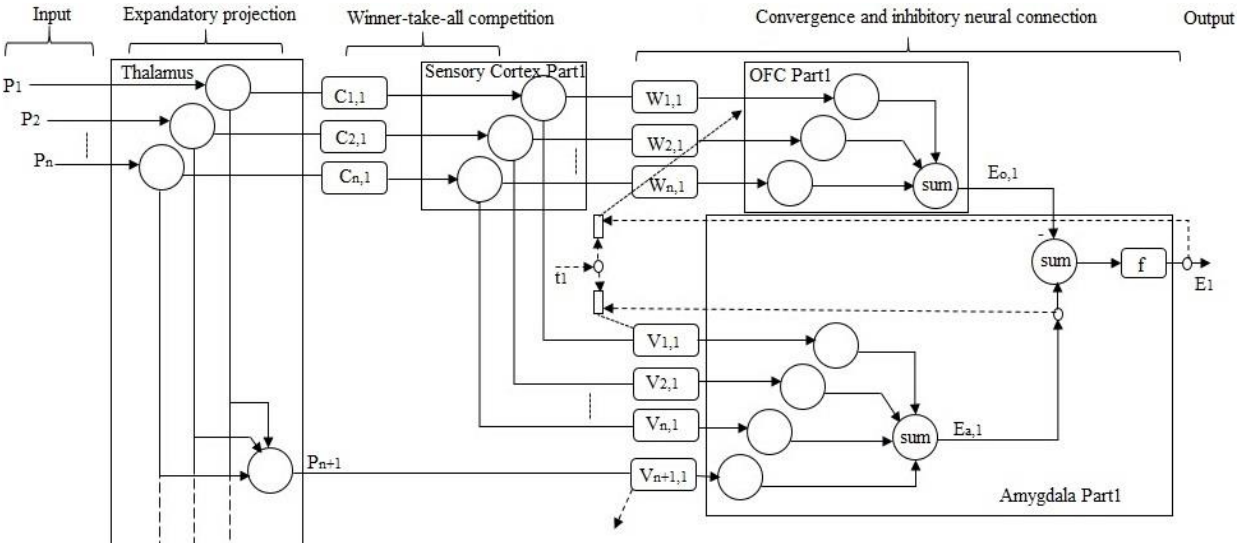

Figure 2.4 The structure of proposed WTAENN with the single competitive unit (Lotfi and Akbarzadeh-T 2016)

The genetic algorithm is the most popular optimization algorithm which can minimize a cost function to achieve the best solution. The solutions in GA are known as chromosomes and each chromosome consists of one or more genes. In relation to WTAENN, a chromosome can be expressed as follows:

$$Chromosome_k = [gene_1, gene_2, \dots, gene_m]_k \tag{2.6}$$

where,

$$gene_1 = \left[c_{1,1}, c_{2,1}, \dots, c_{n,1}, v_{1,1}, v_{2,1}, \dots, v_{n,1}, w_{1,1}, w_{2,1}, \dots, w_{n,1}, b_1\right] \tag{2.7}$$

$$gene_2 = \left[c_{1,2}, c_{2,2}, \dots, c_{n,2}, v_{1,2}, v_{2,2}, \dots, v_{n,2}, w_{1,2}, w_{2,2}, \dots, w_{n,2}, b_2\right] \tag{2.8}$$

$$gene_m = \left[c_{1,m}, c_{2,m}, \dots, c_{n,m}, v_{1,m}, v_{2,m}, \dots, v_{n,m}, w_{1,m}, w_{2,m}, \dots, w_{n,m}, b_m\right] \tag{2.9}$$

After generating the first population, the fitness of chromosomes will be evaluated by the following equation:

$$Fitness(Chrom_i) = \frac{1}{m}\left(\sum_{k=1}^{n}(Y^k - T^k)^2\right)^{0.5} \tag{2.10}$$

where Y^k is the output of the winner part for kth input pattern, T^k is the related target and m is the number of training pattern targets. By minimizing the cost function, the best learning weights for WTAENN can be obtained (Lotfi et al. 2014; Lotfi and Akbarzadeh-T 2014, 2016).

2.3.1.1. Rockburst Prediction Using GA-ENN

In this study, for the first time, the applicability of ENNs was examined to predict rockburst occurrence as a geotechnical engineering problem. In GA-based ENN algorithm, it is necessary to determine the optimum values of its parameters, i.e. the number of competitive parts (m), number of generations, and the population size. The MatLab code was used to develop this model. Since the input parameters have different units and range of values, in soft computing techniques, it is better to normalize datasets on account of speeding up the modelling process, reducing errors, and more importantly preventing the over-fitting phenomenon. So, the input parameters were normalized between 0 and 1 using the following equation:

$$X_{norm} = 1 - \frac{X_{max} - X_i}{X_{max} - X_{min}} \tag{2.11}$$

where X_i, X_{min}, X_{max}, and X_{norm} are ith actual value, minimum value, maximum value and the normalized value of an input parameter, respectively.

In the following, the initial database was divided into three parts of training (70% of the database), validation (10% of the database), and testing (20% of the database) to conduct a series of sensitivity analysis and subsequently to find the best combination of parameters. In the first analysis, the parameters of m and activation function were fixed on 1 and "$Hard-limit$", and the values of population size and the number of generations increased from 20 to 300. Fig. 2.5 shows the variation of mean square error (MSE) as the fitness function in each run. According to this figure, after generation no. 100, the MSE value remained constant and no change was observed up to generation no. 300. So, the value of 100 was selected as the optimum value for the parameters of population size and generation number. An increase in MSE can be seen between generations 60 to 100, which may refer to the stochastic mechanism of ENN algorithm for searching and finding the best combination of training coefficients (i.e. c, v, and w weights) among all the possible solutions. Similarly, the second analysis with the aim of finding the optimum value of m was executed by varying its value from 1 to 40 and recording the corresponding MSE values. The $m = 1$ provided the minimum value of MSE. Eventually, the algorithm was executed for several times based on the obtained optimum values for parameters and the best model was identified. Table 2.4 indicates the characteristics of the best GA-ENN model.

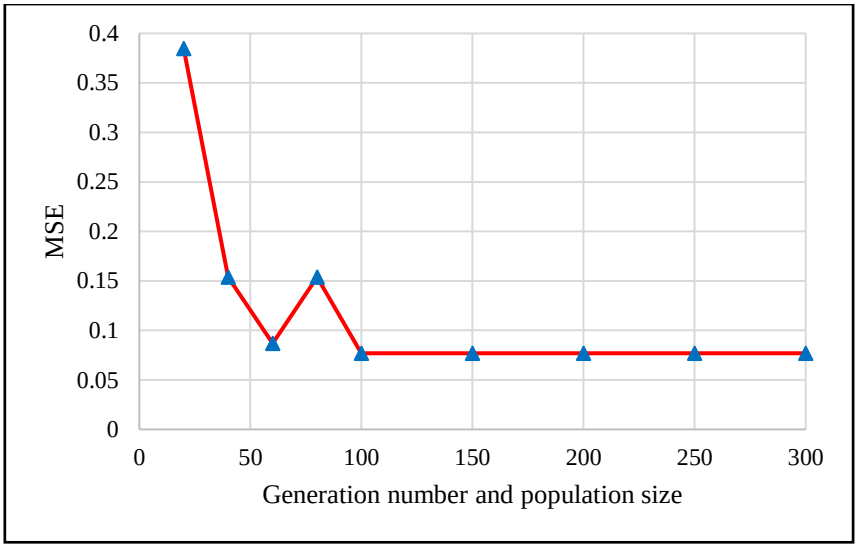

Figure 2.5 Variation of fitness function for different values of generation number and population size

Table 2.4 Characteristics of developed GA-ENN model

Parameter	Value
Input variables	MTS, UTS, UCS, EEI
Output variable	Rockburst occurrence
	Yes: 1
	No: 0
Generation number	100
Population size	100
Number of competitive units (m)	1
Activation function	Hard-limit

2.3.2. C4.5 Algorithm

One of the best-renowned data mining techniques is decision tree (DT). The decision tree is a nonparametric technique which benefits from simple and interpretable structure, low computational cost and the ability to represent graphically. DTs have proven their efficiency for various purposes such as classification, decision making and as a tool to make a relationship between independent variables and the dependent one (Breiman et al. 1984; Salimi et al. 2016; Hasanipanah et al. 2017b; Khandelwal et al. 2017a). The most important characteristic of a DT as a "white box" technique is its simple graphical structure which enables the user to clarify the relations between variables easier, while other machine learning techniques such as ANNs

have a vague internal computational procedure, which means the results are difficult to interpret. In the case of having a problem with many variables which act in reciprocally and non-linear ways, finding a comprehensive model may be very difficult. In these circumstances, DT can be a suitable alternative which is able to break down (sub-divide) the initial space into smaller parts so that the interactions are easier to manage. A decision tree is a collection of nodes (root node, internal nodes, and terminal or leaf nodes), arranged as a binary tree. The root node and internal nodes belong to decision stage and represent specific input variables which are connected together based on a smaller range of values. The terminal nodes, show the final classes (Coimbra et al. 2014; Jahed Armaghani et al. 2016; Liang et al. 2016; Hasanipanah et al. 2017a). There are various types of decision trees, including classification and regression tree (CART), Chi-squared automatic interaction detection (CHAID), C4.5, ID3, quick, unbiased, efficient statistical tree (QUEST). C4.5 proposed by Quinlan (1993), is a powerful classification algorithm which is derived from the development of ID3 algorithm and is able to handle numeric attributes, missing values, and noisy data (Ghasemi et al. 2017). C4.5 identifies decision tree classifiers and using a divide-and-conquer method grows the decision tree. The C4.5 algorithm acts in two main stages: tree constructing and pruning. Tree constructing starts by calling the training dataset. All of the datasets firstly are concentrated in the root node and then divided into homogeneous sub-nodes based on a modified splitting criterion, called gain ratio. The attribute with the highest normalized information gain is chosen to make the decision (Quinlan 1993). This splitting will continue till the stopping condition is met, i.e. all instances in a node belong to the same class and this node is identified as a leaf node. The generated DT by training dataset often is prone to the over-fitting problem because of having a great number of branches and such DTs fail to classify the new unused data. To overcome this problem, there is a need to prune the tree. Pruning is the process of reducing decision tree size by eliminating parts of the tree which have little power for classifying and this process finally led to increasing the accuracy of the classifier and its reliability (Quinlan 1993; Ture et al. 2009; Hssina et al. 2014).

2.3.2.1. Rockburst Prediction Using C4.5

In this study, the C4.5 algorithm was applied to the training dataset using WEKA (Waikato Environment for Knowledge Analysis) software. There are two main parameters which should be adjusted to develop a high-performance C4.5 classifier including confidence factor (CF) and the minimum number of instances (MNI) (data samples) per leaf. The CF is used to compute a

pessimistic upper bound on the error rate at a leaf/node. The smaller this value, the more pessimistic the estimated error is and generally the heavier the pruning. If a CF greater than 0.5 is chosen, then the pruning will be done on the basis of unchanged classification error on the training dataset and this is equivalent to turning off the pruning. The MNI affect the volume (i.e. the complexity) of the developed tree (Bui et al. 2012). Hence, according to Bui et al. (2012) and Ghasemi et al. (2017), the CF and MNI varied from 0.1 to 0.5 and 1 to 20 respectively, and the corresponding accuracy values were recorded. Finally, the optimum values of 0.25 and 2 were determined for CF and MNI, respectively. After adjusting the C4.5 parameters in WEKA software, the model was executed and the corresponding tree was obtained. Fig. 2.6 displays the results obtained by this algorithm which contains a root node, 5 internal nodes, and 7 leaves. There are two numbers in the parentheses of leaf nodes, which the first number belongs to the number of instances in that node and the second number shows the number of misclassified instances. The process of rockburst prediction using the developed tree model is very simple. For example, taking into account the values of 4.6, 3, 20, and 1.39 for MTS, UTS, UCS, and EEI respectively, and passing through the path of $MTS \leq 25.7$, $UTS \leq 4.55$, $EEI \leq 2.04$ and $UCS \leq 30$, the leaf node Yes (2,0) can be achieved which shows the occurrence of rockburst.

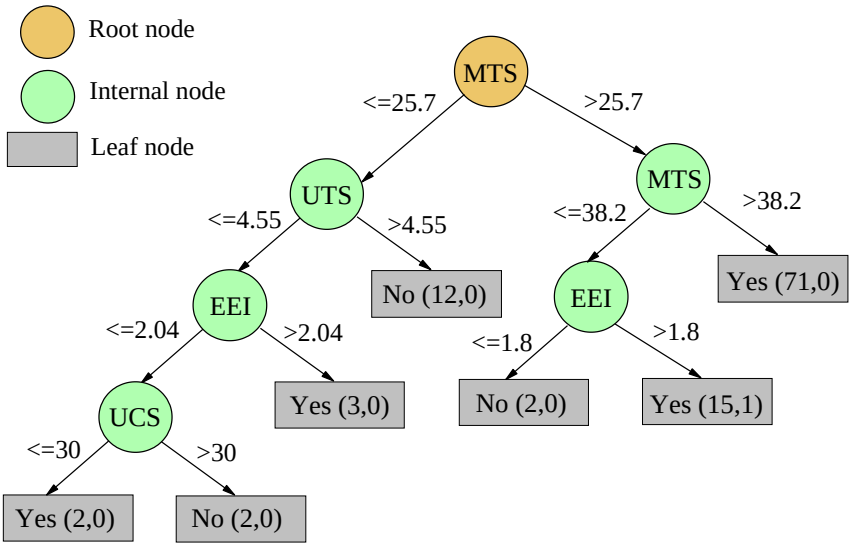

Figure 2.6 Developed C4.5 tree model based on training dataset

2.3.3. Gene Expression Programming (GEP)

During the progress of evolutionary algorithms (EAs) since 1975, Ferreira (2002) introduced a new powerful population-based algorithm called gene expression programming (GEP) that

takes advantage of basic GA and genetic programming (GP) methods. The main goal of the GEP is to find a rational mathematical relationship between the independent variables and the corresponding dependent in such a way that the defined fitness function reaches its minimal value. In GEP, possible solutions are in the form of fixed-length coded chromosomes consist of two groups of entities: terminals and functions. Terminals can be both of input variables and user-defined constant values. Functions are algebraic symbols e.g. $+$, $-$, $\times$, $/$, Ln, Log and so on. The chromosomes can consist of one or more genes, and each gene comprises two parts of the head and tail so that the genetic operators create effective changes in these areas to produce better solutions. In contrast to multiple non-linear regression techniques, there is no need to consider a pre-defined mathematical framework (e.g. exponential, power, logarithmic, etc.) for GEP to develop a model. As a matter of fact, the GEP algorithm during its intelligent search is capable to find the optimum combination of terminals and functions to provide a predictive equation with enough accuracy. As shown in Fig. 2.7, the process of GEP modelling starts with the random generation of chromosomes in Karva language (a symbolic expression of GEP chromosomes) which are then expressed and executed as the tree and mathematical structures, respectively. Then, the generated chromosomes are evaluated according to the pre-defined fitness function. Bests of the first population are copied into the next generation, and the others are influenced by genetic operators, including selection and reproduction (i.e. mutation, inversion, transposition, and recombination). Finally, the modified chromosomes are transferred to the next generation and this process will continue until the stopping criteria (maximum generation number or reach to pre-defined fitness) are met (Ferreira 2002; Güllü 2012; Armaghani et al. 2016; Faradonbeh et al. 2016, 2018). The detailed information concerning genetic operators and their mechanisms can be found in (Ferreira 2002).

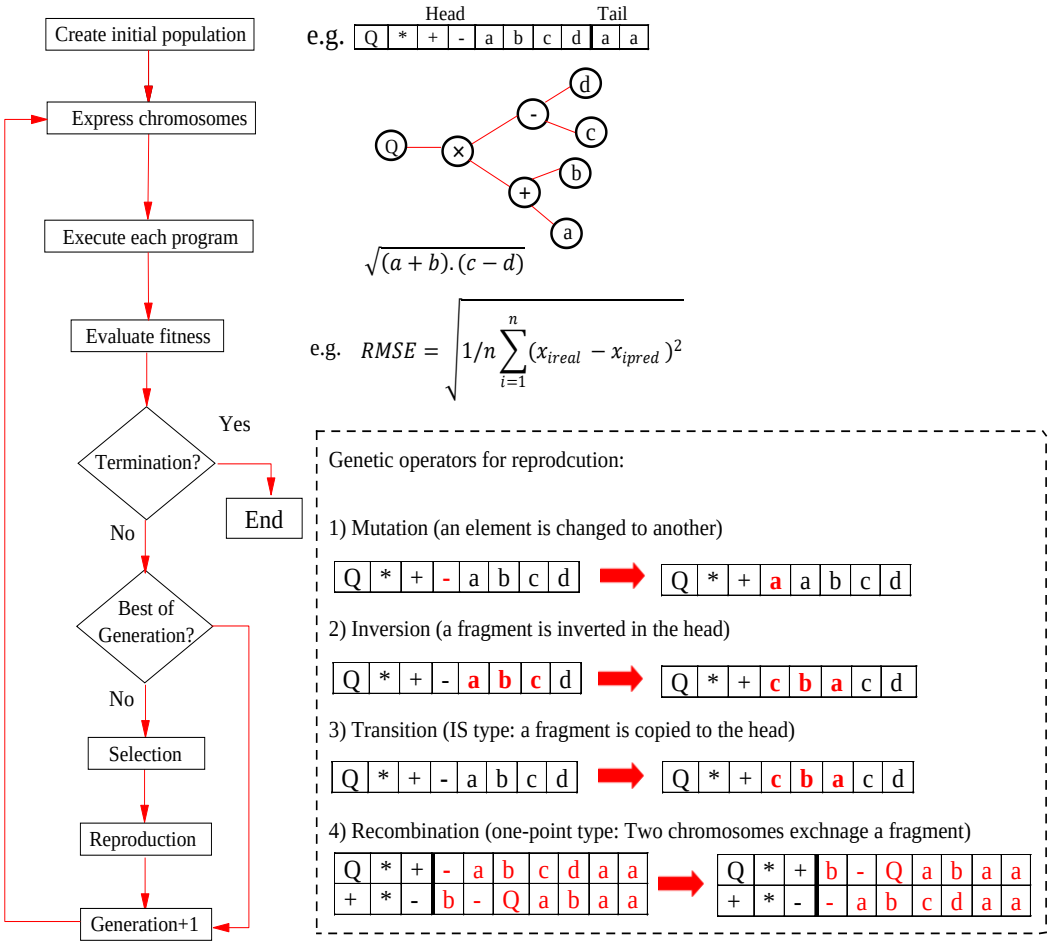

Figure 2.7 GEP flowchart

2.3.3.1. Rockburst Prediction using GEP

The GeneXproTools 5.0, an exceedingly flexible modelling tool designed for function finding, classification, time series prediction, and logic synthesis, was implemented to classify and predict rockburst events. This software classifies the value returned by the evolved model as “1” or “0” via the 0/1 rounding threshold. If the returned value by the evolved model is equal to or greater than the rounding threshold, then the record is classified as "1", "0" otherwise. Similar to the GA-ENN and C4.5 modelling, 80% of the database was applied to the software as the training dataset to develop the model. In the first step, a fitness function for the algorithm should be defined. The sensitivity/specificity with the rounding threshold of 0.5 was used for this aim. The sensitivity/specificity (SS_i) of a chromosome as a solution can be calculated by the following equation:

$$SS_i = SE_i . SP_i \tag{2.12}$$

where SE_i is the sensitivity and SP_i is the specificity of the chromosome i, and are given by the following formulas:

$$SE_i = \frac{TP_i}{TP_i + FN_i} \tag{2.13}$$

$$SP_i = \frac{TN_i}{TN_i + FP_i} \tag{2.14}$$

where TP_i, TN_i, FP_i, and FN_i represent, respectively, the number of true positives, true negatives, false positives, and false negatives. TP_i, TN_i, FP_i, and FN_i are the four different possible outcomes of a single prediction for a two-class case with classes "1" (Yes) and "0" (No). A false positive is when the outcome is incorrectly classified as "Yes" (or positive) when it is in fact "No" (or negative). A false negative is when the outcome is incorrectly classified as "No" when it is in fact "Yes". True positives and true negatives are obviously correct classifications. Keeping track of all these possible outcomes is such an error-prone activity, that they are usually shown in what is called a confusion matrix. Thus, the fitness value of chromosome i is evaluated by the following equation:

$$f_i = 1000.SS_i \tag{2.15}$$

which obviously ranges from 0 to 1000, with 1000 corresponding to the maximum prediction accuracy. In the second step, terminals and functions which are kernels of generated chromosomes should be assigned. Terminals are input parameters (i.e. MTS, UTS, UCS, and EEI). The most common arithmetic functions were selected as follows:

$$F = \{+, -, \times, /, Sqrt, Exp, Ln, \text{^}2, \text{^}3, 3Rt\} \tag{2.16}$$

The goal of GEP modelling is to develop a rockburst index in the form of $RBI = f(MTS, UTS, UCS, EEI)$. The third step is to determine the structural parameters, i.e. the number of genes and head size. These two parameters affect the length of the generated chromosomes and subsequently the complexity of the proposed formula. By trial and error, the best values of 4 and 9 were obtained for the number of genes and head size, respectively. In the fourth step, the ratios of genetic operators (i.e. mutation, inversion, transposition, and recombination) as chromosomes modifiers should be determined. A set of values has been recommended by the researchers for genetic operators that their validity has been confirmed in many engineering problems (Ferreira 2006; Kayadelen 2011; Güllü 2012; Khandelwal et al. 2016). So, these values were set for the operators in the current study as well (see Table 2.5). As the final step, since we face multi-genic chromosomes, we need to define a linking function

to link genes to each other. Addition (+) is a most common linking function which was used for this aim. After adjusting the GEP parameters (Table 2.5), the model was executed in training mode for 2000 generations and the results were recorded. Eq. 2.17 shows the developed rockburst index based on GEP algorithm. By feeding the input parameters to the Eq. 2.17 and comparing the calculated value with the Eq. 2.18, the rockburst occurrence can be determined.

$$RBI = \sqrt{Exp(MTS)} - \frac{UCS^3}{EEI} + 2T + \frac{Exp\left(\frac{MTS}{EEI}\right)}{(UTS - Exp(UTS)) \times \sqrt{\frac{EEI}{UTS}}} + EEI - EEI^9 \quad (2.17)$$

$$RBI^* = \begin{cases} 1\ (Yes) & RBI \geq 0.5 \\ 0\ (No) & RBI < 0.5 \end{cases} \quad (2.18)$$

Table 2.5 Characteristics of developed GEP models

Type of setting	Parameter	
General setting	Terminal set	MTS, UTS, UCS, EEI
	Function set	$+, -, \times, /, Sqrt, Exp, Ln, \text{^}2, \text{^}3, 3Rt$
	Fitness function	Sensitivity/Specificity
	Population size	90
	Number of generations	2000
	Head size	9
	Number of genes	4
	Linking function	Addition (+)
Genetic operators	Mutation rate	0.044
	Inversion rate	0.1
	Transposition rate	0.1
	One-point recombination rate	0.3
	Two-point recombination rate	0.3
	Gene recombination rate	0.1

2.4. Performance Evaluation of the Proposed Models

In this section, the remaining testing datasets (27 cases) were applied to the developed models of GA-ENN, C4.5, and GEP to evaluate their prediction performance. For further evaluation, five conventional criteria mentioned in Table 2.1 were considered as well. Table 2.6 shows the obtained results from eight different models in testing stage. A confusion matrix is a useful tool to describe the performance of a classifier on a set of test data. Each row of the matrix

represents the instances in an actual class while each column represents the instances in a predicted class (or vice versa). Table 2.7 shows the confusion matrices of the developed models. According to Tables 2.6 and 2.7, GA-ENN and GEP models have the equal number of misclassified cases (i.e. 4 cases), while this number is equal to 9 for stress coefficient and brittleness coefficient criteria. In the following, two indices of root mean squared error (RMSE) (an index to measure the deviation between the actual and predicted data) and the percentage of the successful prediction (PSP) (the percentile quotient of the number of correct predictions to the total number of testing data) were used to investigate the accuracy and capability of the models. Ideally, RMSE and PSP are equal to 0 and 100%, respectively. The results of performance indices are shown in Table 2.8. As can be seen in this table, all three new constructed models (i.e. GA-ENN, GEP, and C4.5) have higher accuracy and lower estimation error compared with five conventional criteria. Table 2.8 also shows that, two models of GA-ENN and GEP with the similar results outperformed the C4.5. On the other hand, EEI criterion acted just like the C4.5 model which shows that this criterion with its simple formula can be used effectively to predict rockburst occurrence in engineering projects. Fig. 2.8 compares the prediction performance of the developed models.

Table 2.6 Results of validation of developed models with testing dataset

No.	Input parameters				Actual Output	Developed models							
	MTS	UTS	UCS	EEI		GA-ENN	C4.5	GEP	Russenes criterion	Hoek criterion	SC	BC	EEI
1	45.7	3.2	69.1	4.1	1	1	1	1	1	1	1	1	1
2	62.4	9.5	235	9	1	1	1	1	1	0	0	1	1
3	55.6	18.9	256.5	9.1	1	1	1	1	0	0	0	1	1
4	41.6	2.7	67.6	3.7	1	1	1	1	1	1	1	1	1
5	30.3	3.1	88	3	1	1	1	1	1	1	1	1	1
6	28.6	12	122	2.5	1	1	1	1	0	0	0	1	1
7	4.6	3	20	1.39	0	0	1	0	0	0	0	1	0
8	2.6	3	20	1.39	0	0	1	0	0	0	0	1	0
9	33.6	10.8	156	5.2	1	1	1	1	0	0	0	1	1
10	23	3	80	0.85	1	1	0	0	1	1	0	1	0
11	80	6.7	180	5.5	0	1	1	1	1	1	1	1	1
12	19	4.48	153	2.11	1	0	1	0	0	0	0	1	1
13	38.2	3.9	53	1.6	0	1	0	0	1	1	1	1	0
14	73.2	5	120	5.1	1	1	1	1	1	1	1	1	1
15	3.8	3	20	1.39	0	0	1	0	0	0	0	1	0
16	89.56	17.13	190.3	3.97	1	1	1	1	1	1	1	1	1

17	18.8	6.3	171.5	7	0	0	0	0	0	0	0	1	1
18	105.5	12.1	170	5.76	1	1	1	1	1	1	1	1	1
19	39	2.4	70.1	4.8	1	1	1	1	1	1	1	1	1
20	27.8	2.1	90	1.8	0	1	0	0	1	1	1	0	0
21	30	3.7	88.7	6.6	1	1	1	0	1	1	1	1	1
22	40.6	2.6	66.6	3.7	1	1	1	1	1	1	1	1	1
23	11	5	115	5.7	0	0	0	0	0	0	0	1	1
24	59.82	7.31	85.8	2.78	1	1	1	1	1	1	1	1	1
25	7.5	3.7	52	1.3	0	0	0	0	0	0	0	1	0
26	11	4.9	105	4.7	0	0	0	0	0	0	0	1	1
27	57.6	5	120	5.1	1	1	1	1	1	1	1	1	1

BC brittleness coefficient criterion, *SC* stress coefficient criterion, *EEI* elastic energy index criterion

Table 2.7 Confusion matrices of developed models in testing stage

Model	Confusion matrix			Number of misclassified cases
GA-ENN		Predicted		4
		No	Yes	
Actual	No	7	3	
	Yes	1	16	
GEP		Predicted		4
		No	Yes	
Actual	No	9	1	
	Yes	3	14	
C4.5		Predicted		5
		No	Yes	
Actual	No	6	4	
	Yes	1	16	
Russenes criterion		Predicted		7
		No	Yes	
Actual	No	7	3	
	Yes	4	13	
Hoek criterion		Predicted		8
		No	Yes	
Actual	No	7	3	
	Yes	5	12	
Stress coefficient criterion		Predicted		9
		No	Yes	
Actual	No	7	3	
	Yes	6	11	
Brittleness coefficient criterion		Predicted		9
		No	Yes	
Actual	No	1	9	

	Yes	0	17	
Elastic energy index criterion		Predicted		5
		No	Yes	
Actual	No	6	4	
	Yes	1	16	

Table 2.8 Summary of the results based on test datasets

Model	Performance index	
	RMSE	PSP (%)
GA-ENN	0.385	85.185
GEP	0.385	85.185
C4.5	0.431	81.481
Elastic energy index criterion	0.430	81.481
Russenes criterion	0.509	74.074
Hoek criterion	0.544	70.370
Stress coefficient criterion	0.577	66.667
Brittleness coefficient criterion	0.577	66.667

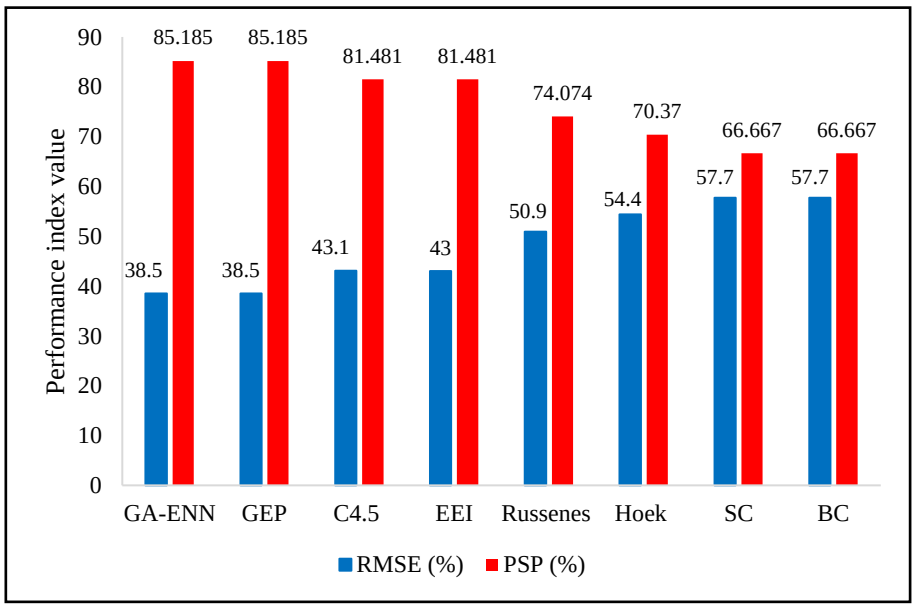

Figure 2.8 Comparison of performance indices for different models in testing stage (SC: stress coefficient criterion, BC: brittleness coefficient criterion)

2.5. Sensitivity Analysis

In this section a sensitivity analysis is performed to evaluate the effects of input parameters on rockburst prediction models. To this end, the relevancy factor (Kamari et al. 2015) was used which is calculated by Eq. 2.19.

$$r = \frac{\sum_{i=1}^{n}(I_{i,k}-\bar{I}_k)(P_i-\bar{P})}{\sqrt{\sum_{i=1}^{n}(I_{i,k}-\bar{I}_k)^2 \sum_{i=1}^{n}(P_i-\bar{P})^2}} \tag{2.19}$$

where $I_{i,k}$ and $\bar{I}_k$ are the ith and average values of the kth input parameter, respectively, P_i, and $\bar{P}$ are the ith and average values of the predicted rockburst., respectively, and n is the number of rockburst events. The higher r value the more influence the input has in predicting the output value. Fig. 2.9 shows the r values. As can be seen in this figure, the maximum tangential stress (MTS) is the most influential parameter in rockburst prediction, and uniaxial compressive strength (UCS) has the lowest impact. These results are in agreement with those obtained by others in a recent study (Li et al. 2017).

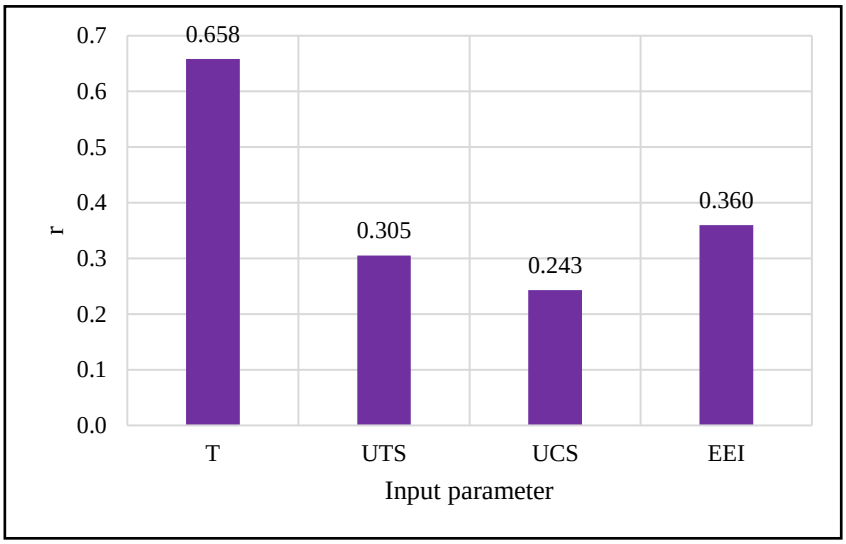

Figure 2.9 Relevancy factor of each input parameter

2.6. Discussion

A supplementary explanation regarding the proposed three models is contained in this section. As previously mentioned, this is the first attempt in the application of ENNs in earth sciences, and its results were promising. Accordingly, it is highly recommended to check the applicability of ENNs in combination with other meta-heuristic algorithms, as hybrid models, for different aims (e.g. classification, prediction, and minimization) for mining and

geotechnical engineering applications. However, as a black-box method like ANN, GA-ENN neither can provide any equation nor a visual pattern for users. This may be considered as a disadvantage for this algorithm, but it is possible to overcome this issue by using this technique to find some optimum coefficients of the multiple non-linear regressions in future studies. In contrast to GA-ENN, C4.5 has a very simple modelling mechanism. Its tree structure easily can be adopted as a guide by engineers in the projects to predict the rockburst occurrence just by tracking the values of inputs within the branches of the tree. In some cases, this algorithm may provide large and complex trees according to the defined controlling parameters, which finally decrease the applicability of the developed trees. Besides, C4.5 algorithm on account of its innate PCA characteristic may remove some input parameters during the training stage to increase the accuracy of the final output. Hence, the process of C4.5 modelling requires extensive modelling experiences. The common multiple non-linear regressions need a pre-defined mathematical structure, while the GEP algorithm is able to find the latent relationship between the input and output parameters without any presupposition. This can be introduced as the most important characteristic of GEP algorithm compared with the GA-ENN and C4.5 algorithms. In addition, GEP does not have the limitations of previous methods and is more practical. In the end, it is worth mentioning that the developed models are valid just in the defined ranges of values of inputs and for the new datasets out of these ranges, the models should be adjusted again.

2.7. Summary and Conclusions

This study was intended to assess rockburst hazard in deep underground openings using three renowned data mining techniques including GA-ENN, C4.5, and GEP. A database including the maximum tangential stress of the surrounding rock, the uniaxial tensile strength of rock, the uniaxial compressive strength of rock and the elastic energy index of 134 rockburst experiences in various underground projects was compiled. After a statistical analysis, the GA-ENN, C4.5, and GEP models were developed based on training datasets. In the following, the prediction performance of the models was evaluated by applying unused testing datasets. The results of the new models were compared with five conventional rockburst prediction criteria via performance indices of root mean squared error (RMSE) and percentage of the successful prediction (PSP). Finally, a sensitivity analysis was conducted to know about the influence of input parameters on rockburst using relevancy factor. The following conclusions has been drawn:

1) According to the results of statistical analysis, the original database neither has extreme outliers nor natural groups. So, it is suitable for further analysis.
2) According to the performance indices values, the models of GA-ENN, GEP, and C4.5 have high accuracy in predicting rockburst occurrence, respectively, while the criteria of stress coefficient and brittleness coefficient with the same performance indices values have the lowest capability for predicting.
3) Strain energy index (EEI) with the RMSE of 0.430 and PCP of 81.481% like C4.5 model, can be a beneficial tool to predict rockburst occurrence in practice.
4) The maximum tangential stress (MTS) is the most influential parameter to predict rockburst occurrence. This parameter should be controlled during the design of underground excavations by optimizing their geometry.

Appendix A

Table A.1 Database used in this article for rockburst analysis

No.	MTS (MPa)	UCS (MPa)	UTS (MPa)	EEI	Rockburst	Reference
1	89.56	190.3	17.13	3.97	Yes	(Dong et al. 2013)
2	89.56	170.28	12.07	5.76	Yes	
3	89.56	187.17	19.17	7.27	Yes	
4	56.1	131.99	9.44	7.44	Yes	
5	54.2	133.99	9.09	7.08	Yes	
6	70.3	128.52	8.73	6.43	Yes	
7	48.75	180	8.3	5	Yes	
8	62.5	175	7.25	5	Yes	
9	75	180	8.3	5	Yes	
10	57	180	8.3	5	Yes	
11	89	236	8.3	5	Yes	
12	50	130	6	5	Yes	
13	108	140	8	5.5	Yes	
14	18.8	178	5.7	7.4	No	
15	11	115	5	5.7	No	
16	55.4	176	7.3	9.3	Yes	
17	30.9	82.56	6.5	3.2	Yes	
18	89	128.6	13.2	4.9	Yes	
19	12.3	237.1	17.66	6.9	No	
20	55.6	256.5	18.9	9.1	Yes	
21	91.3	225.6	17.2	7.3	Yes	
22	61	171.5	22.6	7.5	Yes	
23	34.15	54.2	12.1	3.17	Yes	
24	108.4	138.4	7.7	1.9	Yes	
25	69.8	198	22.4	4.68	Yes	
26	105	171.3	22.6	7.27	Yes	
27	105	237.16	17.66	6.38	Yes	
28	105	304.21	20.9	10.57	Yes	
29	25.49	54.2	2.49	3.17	Yes	

30	72.07	147.09	10.98	6.53	Yes	
31	21.8	160	5.2	2.22	No	
32	20.9	160	5.2	2.22	No	
33	12.1	160	5.2	2.22	No	
34	75	170	11.3	9	Yes	
35	43.4	123	6	5	Yes	
36	62.6	165	9.4	9	Yes	
37	30	88.7	3.7	6.6	Yes	
38	105	128.61	13	5.76	Yes	
39	105	304	9.12	5.76	Yes	
40	105	306.58	13.9	6.38	Yes	
41	7.5	52	3.7	1.3	No	
42	24.93	99.7	4.8	3.8	No	
43	14.96	99.7	4.8	3.8	No	
44	34	150	5.4	7.8	No	(Adoko et al. 2013)
45	60.7	111.5	7.86	6.16	Yes	
46	54.2	134	9.09	7.08	Yes	
47	70.3	129	8.73	6.43	Yes	
48	35	133.4	9.3	2.9	Yes	
49	38.2	53	3.9	1.6	No	
50	11.3	90	4.8	3.6	No	
51	92	263	10.7	8	Yes	
52	62.4	235	9.5	9	Yes	
53	43.4	136.5	7.2	5.6	Yes	
54	11	105	4.9	4.7	No	
55	90	170	11.3	9	Yes	
56	90	220	7.4	7.3	Yes	
57	80	180	6.7	5.5	No	
58	98.6	120	6.5	3.8	Yes	
59	108.4	140	8	5	Yes	
60	56.8	112	2.2	5.2	Yes	(Zhang 2007)
61	58.2	83.6	2.6	5.9	Yes	
62	40.1	72.1	2.3	4.6	Yes	
63	41.6	67.6	2.7	3.7	Yes	
64	55.6	114	2.3	4.7	Yes	
65	30.3	88	3.1	3	Yes	
66	27.8	90	2.1	1.8	No	
67	29.1	94	2.6	3.2	Yes	
68	29.7	116	2.7	3.7	Yes	
69	62.1	132	2.4	5	Yes	
70	56.9	123	2.7	5.2	Yes	
71	55.6	114	2.3	4.7	Yes	
72	57.2	80.6	2.5	5.5	Yes	
73	39	70.1	2.4	4.8	Yes	
74	40.6	66.6	2.6	3.7	Yes	
75	39.4	69.2	2.7	3.8	Yes	
76	35.8	67.8	3.8	4.3	Yes	
77	45.7	69.1	3.2	4.1	Yes	
78	38.2	71.4	3.4	3.6	Yes	
79	39.4	65.2	2.3	3.4	Yes	
80	40.4	72.1	2.1	1.9	Yes	
81	26.9	62.8	2.1	2.4	Yes	

82	25.7	59.7	1.3	1.7	No	
83	43.62	78.1	3.2	6	Yes	(Jian et al. 2012)
84	47.56	58.5	3.5	5	Yes	
85	105.5	170	12.1	5.76	Yes	
86	105.5	190	17.1	3.97	Yes	
87	105.5	187	19.2	7.27	Yes	
88	68	107	6.1	7.2	Yes	
89	59.9	96.6	11.7	1.8	Yes	
90	55.9	128	6.29	8.1	Yes	
91	26.9	92.8	9.47	3.7	Yes	
92	33.6	156	10.8	5.2	Yes	
93	29.8	132	11.5	4.6	Yes	
94	28.6	122	12	2.5	Yes	
95	18.7	82	10.9	1.5	No	
96	19.7	142	4.55	2.26	Yes	
97	19	153	4.48	2.11	Yes	
98	17.4	161	3.98	2.19	Yes	
99	13.9	124	4.22	2.04	No	
100	46.2	105	5.3	2.3	Yes	
101	23	80	3	0.85	Yes	
102	46.4	100	4.9	2	Yes	
103	11	105	4.9	4.7	No	(Feng and Wang 1994)
104	18.8	171.5	6.3	7	No	
105	34	149	5.9	7.6	Yes	
106	38.2	53	3.9	1.6	No	
107	11.3	90	4.8	3.6	No	
108	92	263	10.7	8	Yes	
109	62.4	235	9.5	9	Yes	
110	43.4	136.5	7.2	5.6	Yes	
111	44.4	120	5	5.1	Yes	(Yang et al. 2010)
112	13.5	30	2.67	2.03	Yes	
113	70.4	110	4.5	6.31	Yes	
114	3.8	20	3	1.39	No	
115	57.6	120	5	5.1	Yes	
116	19.5	30	2.67	2.03	Yes	
117	81.4	110	4.5	6.31	Yes	
118	4.6	20	3	1.39	No	
119	73.2	120	5	5.1	Yes	
120	30	30	2.67	2.03	Yes	
121	15.2	53.8	5.56	1.92	No	(Zhang and Li 2009)
122	88.9	142	13.2	3.62	Yes	
123	59.82	85.8	7.31	2.78	Yes	
124	32.3	67.4	6.7	1.1	No	
125	30.1	88.7	3.7	6.6	Yes	
126	60	135	15.04	4.86	Yes	(Yi et al. 2010)
127	60	66.49	9.72	2.15	Yes	
128	60	106.38	11.2	6.11	Yes	
129	60	86.03	7.14	2.85	Yes	
130	60	149.19	9.3	3.5	Yes	
131	60	136.79	10.42	2.12	Yes	
132	63.8	110	4.5	6.31	Yes	
133	2.6	20	3	1.39	No	

134	35	133.4	9.3	2.9	Yes

References

Adoko AC, Gokceoglu C, Wu L, Zuo QJ (2013) Knowledge-based and data-driven fuzzy modeling for rockburst prediction. *International Journal of Rock Mechanics and Mining Sciences* 61:86–95

Akdag S, Karakus M, Taheri A, et al (2018) Effects of Thermal Damage on Strain Burst Mechanism for Brittle Rocks Under True-Triaxial Loading Conditions. *Rock Mechanics and Rock Engineering* 51(6):1–26

Armaghani DJ, Faradonbeh RS, Rezaei H, et al (2016) Settlement prediction of the rock-socketed piles through a new technique based on gene expression programming. *Neural Computing and Applications* 29(11):1115-1125

Aryafar A, Mikaeil R, Haghshenas SS, Haghshenas SS (2018) Application of metaheuristic algorithms to optimal clustering of sawing machine vibration. *Measurement: Journal of the International Measurement Confederation* 124:20–31

Berthold M, Hand D (eds) (2003) Intelligent data analysis: an introduction. Second edition. *Springer Science & Business Media*, 2

Breiman L, Friedman J, Stone CJ, Olshen RA (1984) Classification and Regression Trees. *CRC press*

Bui DT, Pradhan B, Lofman O, Revhaug I (2012) Landslide Susceptibility Assessment in Vietnam Using Support Vector Machines, Decision Tree, and Naıve Bayes Models. *Mathematical Problems in Engineering*

Coimbra R, Rodriguez-Galiano V, Olóriz F, Chica-Olmo M (2014) Regression trees for modeling geochemical data-An application to Late Jurassic carbonates (Ammonitico Rosso). *Computers and Geosciences* 73:198–207

Dancy C, Reidy J (2004) Statistics Without Maths for Psychology. *Pearson Education Limited, New York*

Dong L, Li X, Peng K (2013) Prediction of rockburst classification using Random Forest. *Transactions of Nonferrous Metals Society of China* 23(2):472–477

Dong L, Shu W, Li X, et al (2017a) Three Dimensional Comprehensive Analytical Solutions for Locating Sources of Sensor Networks in Unknown Velocity Mining System. *IEEE Access* 5:11337–11351

Dong L, Sun D, Li X, Du K (2017b) Theoretical and Experimental Studies of Localization Methodology for AE and Microseismic Sources Without Pre-Measured Wave Velocity in Mines. *IEEE Access* 5:16818–16828

Dong L, Wesseloo J, Potvin Y, Li X (2016a) Discrimination of Mine Seismic Events and Blasts Using the Fisher Classifier, Naive Bayesian Classifier and Logistic Regression. *Rock Mechanics and Rock Engineering* 49(1):183–211

Dong LJ, Wesseloo J, Potvin Y, Li XB (2016b) Discriminant models of blasts and seismic events in mine seismology. *International Journal of Rock Mechanics and Mining Sciences* 86:282–291

Faradonbeh RS, Armaghani DJ, Amnieh HB, Mohamad ET (2016) Prediction and minimization of blast-induced flyrock using gene expression programming and firefly algorithm. *Neural Computing and Applications* 29(6):269-281

Faradonbeh RS, Hasanipanah M, Amnieh HB, et al (2018) Development of GP and GEP models to estimate an environmental issue induced by blasting operation. *Environmental Monitoring and Assessment* 190(6):351

Faradonbeh RS, Monjezi M (2017) Prediction and minimization of blast-induced ground vibration using two robust meta-heuristic algorithms. *Engineering with Computers* 33(4):385-351

Feng X, Wang L (1994) Rockburst prediction based on neural networks. *Transactions of Nonferrous Metals Society of China* 4(1):7–14

Ferreira C (2006) Gene expression programming: mathematical modeling by an artificial intelligence. *Springer*

Ferreira C (2002) Gene Expression Programming in Problem Solving. In: Roy R, Köppen M, Ovaska S, et al. (eds) Soft Computing and Industry: Recent Applications. *Springer London*, London, pp 635–653

Ghasemi E, Kalhori H, Bagherpour R (2017) Stability assessment of hard rock pillars using two intelligent classification techniques: A comparative study. *Tunnelling and*

Underground Space Technology 68:32–37

Gong FQ, Li XB (2007) A distance discriminant analysis method for prediction of possibility and classification of rockburst and its application. *Chinese Journal of Rock Mechanics and Engineering* 26(5):1012-1018 (in Chinese)

Güllü H (2012) Prediction of peak ground acceleration by genetic expression programming and regression: A comparison using likelihood-based measure. *Engineering Geology* 141–142:92–113

Hasanipanah M, Faradonbeh RS, Amnieh HB, et al (2017a) Forecasting blast-induced ground vibration developing a CART model. *Engineering with Computers* 33(2):307-316

Hasanipanah M, Faradonbeh RS, Armaghani DJ, et al (2017b) Development of a precise model for prediction of blast-induced flyrock using regression tree technique. *Environmental Earth Sciences* 76(1)

He M, e Sousa LR, Miranda T, Zhu G (2015) Rockburst laboratory tests database - Application of data mining techniques. *Engineering Geology* 185:116–130

He M, Xia H, Jia X, et al (2012) Studies on classification, criteria and control of rockbursts. *Journal of Rock Mechanics and Geotechnical Engineering* 4(2):97–114

Hoek E, Brown ET (1980) Underground Excavations in Rock. *Institution of Mining and Metallurgy*, London

Hssina B, Merbouha A, Ezzikouri H, Erritali M (2014) A comparative study of decision tree ID3 and C4.5. *International Journal of Advanced Computer Science and Applications* 4(2):13–19

Jahed Armaghani D, Hajihassani M, Marto A, et al (2015) Prediction of blast-induced air overpressure: a hybrid AI-based predictive model. *Environmental Monitoring and Assessment* 187(11):1-13

Jahed Armaghani D, Mohd Amin MF, Yagiz S, et al (2016) Prediction of the uniaxial compressive strength of sandstone using various modeling techniques. *International Journal of Rock Mechanics and Mining Sciences* 85:174-186

Jian Z, Xibing L, Xiuzhi S (2012) Long-term prediction model of rockburst in underground openings using heuristic algorithms and support vector machines. *Safety Science*

50(4):629–644

Kamari A, Arabloo M, Shokrollahi A, et al (2015) Rapid method to estimate the minimum miscibility pressure (MMP) in live reservoir oil systems during CO2flooding. *Fuel 153*:310–319

Kayadelen C (2011) Soil liquefaction modeling by Genetic Expression Programming and Neuro-Fuzzy. *Expert Systems with Applications* 38(4):4080–4087

Khandelwal M, Armaghani DJ, Faradonbeh RS, et al (2016) A new model based on gene expression programming to estimate air flow in a single rock joint. *Environmental Earth Sciences* 75(9):739

Khandelwal M, Armaghani DJ, Faradonbeh RS, et al (2017a) Classification and regression tree technique in estimating peak particle velocity caused by blasting. *Engineering with Computers* 33(1):45–53

Khandelwal M, Shirani Faradonbeh R, Monjezi M, et al (2017b) Function development for appraising brittleness of intact rocks using genetic programming and non-linear multiple regression models. *Engineering with Computers* 33(1):13–21

Li N, Feng X, Jimenez R (2017) Predicting rock burst hazard with incomplete data using Bayesian networks. *Tunnelling and Underground Space Technology* 61:61–70

Liang M, Mohamad ET, Faradonbeh RS, et al (2016) Rock strength assessment based on regression tree technique. *Engineering with Computers* 32(2):343-354

Liu Z, Shao J, Xu W, Meng Y (2013) Prediction of rock burst classification using the technique of cloud models with attribution weight. *Natural Hazards* 68(2):549–568

Lotfi E, Akbarzadeh-T. MR (2016) A winner-take-all approach to emotional neural networks with universal approximation property. *Information Sciences* 346–347:369–388

Lotfi E, Akbarzadeh-T. MR (2014) Practical emotional neural networks. *Neural Networks* 59:61–72

Lotfi E, Khosravi A, Akbarzadeh-T MR, Nahavandi S (2014) Wind Power Forecasting using Emotional Neural Networks. In: *IEEE International Conference on Systems, Man, and Cybernetics. IEEE*, pp. 311-316

McCulloch WS, Pitts W (1943) A logical calculus of the ideas immanent in nervous activity.

The bulletin of mathematical biophysics 5(4):115–133

Middleton G V (2000) Data analysis in the earth sciences using MATLAB®. *Prentice Hall*, USA

Mikaeil R, Haghshenas SS, Hoseinie SH (2018a) Rock Penetrability Classification Using Artificial Bee Colony (ABC) Algorithm and Self-Organizing Map. *Geotechnical and Geological Engineering* 36(2):1309–1318

Mikaeil R, Haghshenas SS, Ozcelik Y, Gharehgheshlagh HH (2018b) Performance Evaluation of Adaptive Neuro-Fuzzy Inference System and Group Method of Data Handling-Type Neural Network for Estimating Wear Rate of Diamond Wire Saw. *Geotechnical and Geological Engineering* 36(6):3779-3791

Mohamad ET, Faradonbeh RS, Armaghani DJ, et al (2016) An optimized ANN model based on genetic algorithm for predicting ripping production. *Neural Computing and Applications* 28(1):393-406

Palmstrom A (1995) Characterizing the strength of rock masses for use in design of underground structures. In: I*nternational conference in design and construction of underground structures*

Quinlan JR (1993) C4.5: Programs for machine learning. *Elsevier*

Russenes B (1974) Analysis of Rock Spalling for Tunnels in Steep Valley Sides. *Master Thesis of Science, Norwegian Institute of Technology*

Saghatforoush A, Monjezi M, Shirani Faradonbeh R, Jahed Armaghani D (2016) Combination of neural network and ant colony optimization algorithms for prediction and optimization of flyrock and back-break induced by blasting. *Engineering with Computers* 32(2):255-266

Salimi A, Faradonbeh RS, Monjezi M, Moormann C (2016) TBM performance estimation using a classification and regression tree (CART) technique. *Bulletin of Engineering Geology and the Environment* 77(1):429-440

Sayadi AR, Lashgari A, Paraszczak JJ (2012) Hard-rock LHD cost estimation using single and multiple regressions based on principal component analysis. *Tunnelling and Underground Space Technology* 27(1):133–141

Shi XZ, Zhou J, Dong L, et al (2010) Application of unascertained measurement model to prediction of classification of rockburst intensity. *Chinese Journal of Rock Mechanics and Engineering* 29(1):2720–2726

Sousa R, Einstein HH (2007) Risk analysis for tunnelling projects using bayesian networks. In: *11th Congress of the International Society for Rock Mechanics*, 9-13 July 2007, Lisbon, Portugal. Massachusetts Institute of Technology, pp 1301–1304

Tiryaki B (2008) Predicting intact rock strength for mechanical excavation using multivariate statistics, artificial neural networks, and regression trees. *Engineering Geology* 99(1-2):51–60

Ture M, Tokatli F, Kurt I (2009) Using Kaplan-Meier analysis together with decision tree methods (C&RT, CHAID, QUEST, C4.5 and ID3) in determining recurrence-free survival of breast cancer patients. *Expert Systems with Applications* 36:2017–2026

Wang J, Zeng X, Zhou J (2012) Practices on rockburst prevention and control in headrace tunnels of Jinping II hydropower station. Journal of Rock Mechanics and Geotechnical Engineering 4(3):258–268

Wang YH, Li WD, Lee PKK, Tham LG (1998) Method of fuzzy comprehensive evaluations for rockburst prediction. *Chinese Journal of Rock Mechnanics and Engineering* 17(5):493-501 (in Chinese)

Weng L, Huang L, Taheri A, Li X (2017) Rockburst characteristics and numerical simulation based on a strain energy density index: A case study of a roadway in Linglong gold mine, China. *Tunnelling and Underground Space Technology* 69:223–232

Weng L, Li X, Taheri A, et al (2018) Fracture Evolution Around a Cavity in Brittle Rock Under Uniaxial Compression and Coupled Static–Dynamic Loads. *Rock Mechanics and Rock Engineering* 51(2):531–545

Yang JL, Li XB, Zhou ZL, Lin Y (2010) A Fuzzy assessment method of rock-burst prediction based on rough set theory. *Metal Mine* 39(6):26–29 (in Chinese)

Yi YL, Cao P, Pu CZ (2010) Multi-factorial comprehensive estimation for jinchuan's deep typical rockburst tendency. *Science & Technology Review* 28 (2) 76–80

Zhang JF (2007) Study on Prediction by Stages and Control Technology of Rockburst Hazard of Daxiangling Highway Tunnel. *M.Sc. Thesis, Southwest Jiaotong University, Chendu*

Zhang LX, Li CH (2009) Study on tendency analysis of rockburst and comprehensive prediction of different types of surrounding rock. In: Tang, CA (Ed), *Proceedings of the 13th International Symposium on Rockburst and Seismicity in Mines Rinton Press*, Dalian 1451–1456

Zhao HB (2005) Classification of rockburst using support vector machine. *Rock and Soil Mechanics* 26(4):642–644 (in Chinese)

Zhou J, Shi XZ, Dong L, et al (2010) Fisher discriminant analysis model and its application for prediction of classification of rockburst in deepburied long tunnel. *Journal of Coal Science and Engineering (China)* 16(2):144–149

Statement of Authorship

Title of Paper	Application of self-organising map and fuzzy c-mean techniques for rockburst clustering in deep undreground projects
Publication Status	☑ Published ☐ Accepted for Publication ☐ Submitted for Publication ☐ Unpublished and Unsubmitted work written in manuscript style
Publication Details	**Shirani Faradonbeh R**, Shaffiee Haghshenas S, Taheri A, Mikaeil R (2020) Application of self-organising map and fuzzy c-mean techniques for rockburst clustering in deep undreground projects. *Neural Computing and Applications* 32(12):8545–8559

Principal Author

Name of Principal Author (Candidate)	Roohollah Shirani Faradonbeh		
Contribution to the Paper	Literature review and database preparation, statistical analysis, development of models and preparation of the manuscript		
Overall percentage (%)	80%		
Certification:	This paper reports on original research I conducted during the period of my Higher Degree by Research candidature and is not subject to any obligations or contractual agreements with a third party that would constrain its inclusion in this thesis. I am the primary author of this paper.		
Signature		Date	17 June 2021

Co-Author Contributions

By signing the Statement of Authorship, each author certifies that:

i. the candidate's stated contribution to the publication is accurate (as detailed above);
ii. permission is granted for the candidate in include the publication in the thesis; and
iii. the sum of all co-author contributions is equal to 100% less the candidate's stated contribution.

Name of Co-Author	Sina Shaffiee Haghshenas		
Contribution to the Paper	Model Development, review of the manuscript		
Signature		Date	21 June 2021
Name of Co-Author	Abbas Taheri		
Contribution to the Paper	Research supervision, review and revision of the manuscript		
Signature		Date	21 June 2021
Name of Co-Author	Reza Mikaeil		
Contribution to the Paper	Review of the manuscript		
Signature		Date	21 June 2021

Chapter 3

Application of Self-Organizing Map and Fuzzy c-mean Techniques for Rockburst Clustering in Deep Underground Projects

Abstract

One of the main concerns associated with deep underground constructions is the violent expulsion of rock induced by unexpected release of strain energy from surrounding rock masses that is known as rockburst. Rockburst hazard causes substantial damages to the foundation of the structure, equipment and can be a menace to the safety of workers. This study was intended to find the latent relationship between the rockburst-related parameters based on the compiled data samples from deep underground projects using two robust clustering techniques of self-organizing map (SOM) and fuzzy c-mean (FCM). The parameters of maximum tangential stress, uniaxial compressive strength, uniaxial tensile strength, and elastic energy index were considered as input parameters. SOM model could classify data samples into four distinct classes (clusters) and the rockburst intensities were identified precisely. FCM also proved its performance in clustering task with high convergence speed and acceptable accuracy. Having a comparison, the results of SOM and FCM models were compared with ones calculated from five empirical criteria of Russenes, Hoek, tangential stress, elastic energy index, and rock brittleness coefficient. At best, the empirical criteria of Hoek and tangential stress coefficient could predict rockburst intensity with the accuracy of 56.90 %. By analyzing the SOM results as the best model, it was turned out that the maximum tangential stress around the openings has a crucial role in rockburst clustering and has the most influence on the occurrence of strong and moderate rockburst types. Hence, it was recommended as a possible solution to control these types of rockbursts by optimizing the diameter and shape of the underground openings.

Keywords: Rockburst, Self-organizing map, Fuzzy c-mean, Empirical criteria

3.1. Introduction

Nowadays, there are many important mining and civil projects such as hard rock mines, hydropower stations, nuclear power plants, and water conveyance and transportation tunnels under construction in the deep ground condition all over the world. It is proved that by increasing of the depth, in-situ stresses would show a linear or non-linear increment accompanied by the increase of groundwater, osmotic pressure, ground temperature, and the strength of rock (Sun and Wang 2000; Jian et al. 2012). For instance, by reaching the mining depth to about 1000 m, the in-situ stresses induced by overburden, geological condition, and mining operation may lead to stress concentration and subsequently bursting and failure (Weng et al. 2017; Akdag et al. 2018). Therefore, engineering activities in the deep underground environment is challenging and difficult due to rockburst and seismic events, the inrush of water, gas, and large-scale collapses (Feng et al. 2016). Among them, rockburst accidents are known as the most critical geotechnical disaster in many countries which leads to injuries and loss of life, damage to property, delays in project activities as well as enormous economic losses (Blake and Hedley 2003; Li et al. 2007; He et al. 2017). Hence, it is important to predict and control rockburst hazards underground. The instantaneous release of large amounts of strain energy stored in overstressed rock mass cause an unexpected and violent failure which is known as rockburst phenomenon (Blake and Hedley 2003). With respect to this definition, either the presence of high-levels of in-situ stresses exceeding the rock strength or the external triggering factors, e.g. mine extraction could provide the necessary circumstances for rockburst occurrence (Yan et al. 2015). From the perspective of mining, the rockbursts can be classified into three groups (see Fig. 3.1) (Blake and Hedley 2003; Castro et al. 2012; He et al. 2015):

- Strain bursts caused by the local concentration of high-stress at the edge of mining openings frequently occur during drilling for blasting or reinforcement. The consequences of strain bursts range from the ejection of small pieces of rock to the large-scale collapse of an opening as it tries to achieve a more stable shape. In civil engineering activities, the strain bursts are a common type of rockburst.
- Pillar bursts caused by exceeding the stress exerted on a support pillar from its strength are frequent in the sizeable mined-out area.
- Fault-slip bursts caused by the slippage along a geological plane have the mechanism like an earthquake and different magnitude and damage range.

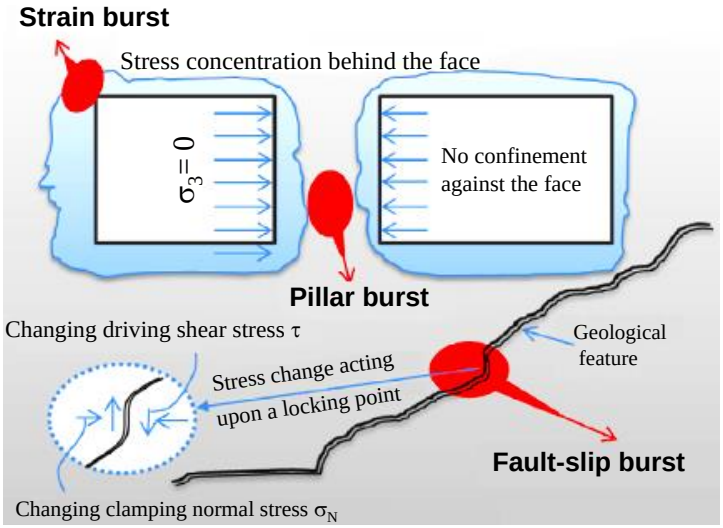

Figure 3.1 Schematic representation of rockburst types and the effect of confinement (Zhou et al. 2018)

Many researches have been carried out during the last decades by scholars not only on the understanding of the rockburst mechanism but also on developing reliable techniques to predict and mitigate its hazards. In terms of rockburst mechanism, many theories have been proposed to assess the stability and deformation localization of rock masses but most of them are assumptive and empirical (Shi et al. 2010; Tang et al. 2010; Jian et al. 2012; Cai 2016a). From the standpoint of prediction, the rockburst studies can be categorized into two following groups:

- Strength-based criteria: These criteria such as Turchaninov criterion (Turchaninov et al. 1972), Russenes criterion (Russenes 1974), Hoek criterion (Hoek and Brown 1980), Barton criterion (Barton et al. 1974), rock brittleness coefficient criterion (Wang et al. 1998), tangential stress criterion (Wang et al. 1998) and so on are rates composed of uniaxial compressive strength, uniaxial tensile strength, maximum tangential strength, axial stress around the opening, and in-situ stresses. The defined rates show specific types of rockbursts (see Table 3.1).
- Energy-based criteria: As the strain energy has a vital role in the occurrence of rockburst events, some scholars attempted to develop other criteria experimentally based on energy theory and consider both the strain energy accumulated in the rock specimen during the loading process and dissipated energy after deformation and failure. A summary of the most common energy-based criteria is listed in Table 3.1.

Table 3.1 Most common strength- and energy-based criteria for the prediction of rockburst intensity

Type	Criterion	Equation	None	Light	Moderate	Strong
Strength based	Russenes criterion (Russenes 1974)	$\frac{\sigma_\theta}{\sigma_c}$	< 0.25	$0.25 - 0.33$	$0.33 - 0.55$	> 0.55
	Barton et al. (Barton et al. 1974)	$\frac{\sigma_c}{\sigma_1}$	> 5	$(2.5 - 5]$	–	≤ 2.5
	Hoek criterion (Hoek and Brown 1980)	$\frac{\sigma_c}{\sigma_\theta}$	> 3.5	$2.0 - 3.5$	$1.7 - 2.0$	< 1.7
	Tangential stress coefficient (Wang et al. 1998)	$\frac{\sigma_\theta}{\sigma_c}$	≤ 0.3	$0.3 - 0.5$	$0.5 - 0.7$	> 0.7
	Rock brittleness coefficient (Wang et al. 1998)	$\frac{\sigma_c}{\sigma_t}$	> 40	$26.7 - 40$	$14.5 - 26.7$	< 14.5
Energy based	Brittleness index modified (BIM) (Aubertin et al. 1994)	$\frac{A_2}{A_1}$	–	> 1.5	$1.2 - 1.5$	$1.0 - 1.20$
	Burst energy coefficient (Li et al. 1996)	$\frac{W_e}{W_p}$	≤ 1	–	–	–
	Elastic energy index (Wang et al. 1998)	$\frac{E_R}{E_D}$	< 2.0	$2.0 - 3.5$	$3.5 - 5.0$	> 5.0
	Mo criterion (Mo et al. 2014)	$\frac{2(E_P - E_T)}{3E_X}$	≤ 1	–	–	–

σ_θ: maximum tangential stress, σ_c: uniaxial compressive strength, σ_1: major principal stress, σ_t: tensile strength, A_1: elastic energy stored in the rock, A_2: energy given by the total area below the stress-strain curve, W_e: the stored energy in the rock during loading before peak strength, W_p: the pre-peak dissipated energy during the failure process, E_P: the elastic energy accumulated, E_T: the dissipated energy, E_X: the post-peak dissipative strain energy

The next imperative issue concerning the rockburst study is providing solutions for its prevention and control. From this perspective, most of the studies focus on the use of microseismic monitoring systems, energy-absorbing bolts as well as some strategies to optimize the mining layout, blasting operation, and supporting system (Jha and Chouhan 1994; Frid 1997; Dou et al. 2009; Liu et al. 2013; He et al. 2014; Li et al. 2017; Zhao et al. 2017). According to the complex mechanism of rockburst and a large number of effective parameters on it, empirical criteria (especially the strength-based ones) could not show satisfactory results (Liu et al. 2013; Li et al. 2017; Zhao et al. 2017). On the other hand, developing energy-based criteria need to do an extreme experimental study which is a time-consuming and expensive process. Hereupon, the application of machine learning (ML) techniques thanks to their ability to deal with the complex non-linear problems and applying several input variables have been used widely to predict rockburst hazard in recent years. Feng and Wang (1994) for the first time used the artificial neural networks (ANNs) successfully to predict the intensity and location of rockburst. Following their success, further studies were carried out by other scholars

using novel ML techniques (Xie and Pan 2007; Gao 2010; Shi et al. 2010; Zhou et al. 2010; Zhang et al. 2011; Li and Liu 2015). It should be mentioned that most of the used ML techniques to assess rockburst phenomenon such as ANNs have a complicated internal structure and their results are not easy to use in practice. As such, they have just focused on the prediction task. Although these studies have been considered as potential solutions to the rockburst problem, they could not solve it completely. In fact, due to the high level of uncertainty and ambiguity in relation to the rockburst phenomenon, the supervised techniques such as ANNs are not able to properly assess such problems. Unsupervised learning algorithms are other branches of machine learning algorithms which can detect the hidden patterns in the database by checking the commonalities between the unlabelled datasets. The most common types of these algorithms are clustering techniques. Due to the complicated environment of rockburst hazard, unsupervised learning algorithms can be used to categorize the datasets into several distinct clusters for better analyzing. In this regard, Xie and Pan (2007) clustered the rockburst events successfully based on grey whitenization weight function according to the grey incidence matrix. In addition, an ant colony clustering optimization model was proposed by Gao (2010) to predict rockburst classes. In another study, Chen et al. (2013) proposed a new quantitative classification method for rockburst using hierarchical clustering analysis.

The results of the above studies were in good agreement (i.e. accuracy above 80%) with the practical records which show the capability of such techniques for rockburst assessment. However, there are few studies in the application of unsupervised learning algorithms for rockburst assessment, and models with the higher level of accuracy are needed. The current study focuses on the applicability of self-organizing map (SOM) and fuzzy c-mean (FCM) algorithms as two unsupervised clustering techniques in order to cluster and identify rockburst intensity simultaneously based on compiled datasets from deep underground openings. The SOM algorithm is a robust data mining tool with the ability to discover the non-linear relationships among high-dimensional data and picturing and clustering them on a low-dimensional space. Fuzzy c-mean (FCM) is also a renowned clustering technique that is similar to the k-means algorithm and using a generalized least-squares objective function creates fuzzy partitions for a set of the numerical dataset. Application of SOM and fuzzy c-mean algorithms in mining and geotechnics fields are limited to few studies (Das and Basudhar 2009; Rad et al. 2012; Mikaeil et al. 2018). In this study, the most influential parameters on the occurrence of rockburst, i.e. the maximum tangential stress, the uniaxial compressive strength, the uniaxial tensile strength, and the elastic energy index were considered as input parameters. The process

of clustering of rockburst datasets using SOM and FCM algorithms was conducted based on the 58 data samples. Afterwards, for the sake of checking the applicability of empirical criteria, five strength-based of them were selected and finally, their accuracy in clustering the rockburst data samples was evaluated.

3.2. Methodology

3.2.1. Self-Organizing Map Approach

In recent years, computational intelligence has been used as a powerful tool to deal with complex industrial and scientific problems (Armaghani et al. 2016; Faradonbeh et al. 2016; Khandelwal et al. 2016, 2017; Mikaeil et al. 2018). Undoubtedly, artificial neural networks (ANNs) are one of the most essential components of computational intelligence (Salemi et al. 2018; Aryafar et al. 2018). ANNs with a wide range of applications such as image processing, pattern recognition, time series prediction, control and robotic systems have a crucial role in scientific and practical areas. ANNs are efficient tools in dealing with complex systems, among which classic inferential and argumentative methods have not this ability. In recent years, ANNs have been used extensively in linear and non-linear problems in different sciences especially in earth sciences (Mohamad et al. 2016; Mahdevari et al. 2017). The self-organizing map (SOM), as an unsupervised algorithm, was proposed by Kohonen (1990) and is a specific type of ANNs which can be used efficiently in statistical and visual data analyses, especially for high-volume and non-uniform data. This method is based on some characteristics of the human brain that follows a specific classifying and mapping procedure (i.e. topographic mapping) to link the input signals to the corresponding processing area (Kohonen 1990; Yu et al. 2015). In the Kohonen model, the tasks of SOM are implemented by a number of neurons, which are placed together in a one-dimensional or two-dimensional (flat) topology and have a reciprocal behavior. Contrary to other artificial neural networks, SOM is composed of two layers, including an input layer and Kohonen layer (competitive layer) which are schematically shown in Fig. 3.2. The process of SOM training has three main phases of competition, cooperation, and adaptation. In the first phase, there is a competition among the neurons, and a neuron with the closest weight vector to the input signal vector will be selected as the winner, known as the best matching unit (BMU). Considering the input signal vector $X = [x_1, x_2, x_3, \dots, x_n]^T$ and the weight vector $W = [w_1, w_2, w_3, \dots, w_n]^T$, the distance between these two vectors is defined mathematically as Euclidean distance and can be computed by the following equation:

$$D = \|X - W\| = \sqrt{\sum_{i=1}^{n}(X_i - W_i)^2} \quad (3.1)$$

The so-called winner neuron (BMU) has the smallest D. In cooperation phase, the neurons which are located in the immediate vicinity of the BMU are recognized and then in the adaptation phase, these neurons are adjusted using Eq. 3.2 to shape a particular pattern on a plane (this pattern belongs to a particular feature of input signal vector).

$$W_{(t+1)} = W_t + \eta[X(t) - W(t)] \quad (3.2)$$

Where η is learning rate function that ranges between 0 and 1.

During the process of training, the data samples of input layer obtain a certain weight equal to W and the weight vectors of the BMU and relevant neighbours progressively will be more similar to the input data. Finally, the input data samples are attracted to the corresponding neurons on the competitive layer and the algorithm will be ceased by meeting the stopping condition (i.e. the maximum number of iteration) (Das and Basudhar 2009; Yu et al. 2015; Mikaeil et al. 2018a). More details concerning the SOM algorithm and its mathematical foundation can be found in the studies of Hagan et al. (1996) and Demuth et al. (2014).

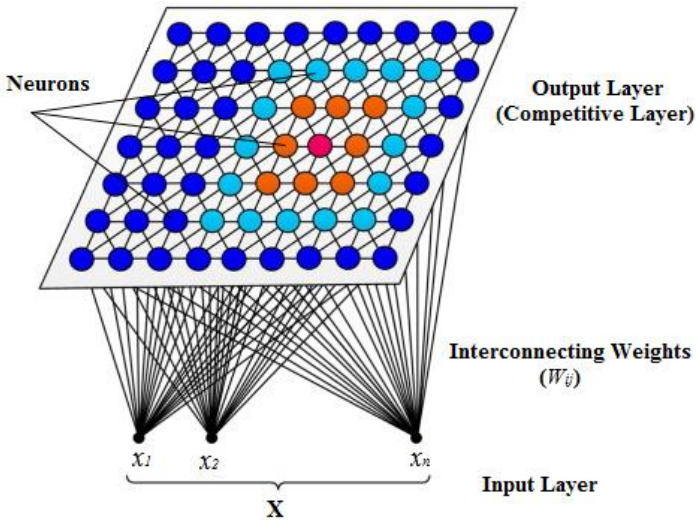

Figure 3.2 A schematic model of self-organizing map network (Malondkar et al. 2018)

3.2.2. Fuzzy C-Mean Approach

Zadeh first proposed the fuzzy science as a multi-valued logic versus the classic logic under the title “Fuzzy sets theory” (Zadeh 1996). The fuzzy logic can deal with problems in which due to the lack of knowledge and understanding of humans, it is complicated to identify and understand the system. Fuzzy clustering is one of the most important applications of the fuzzy

logic in various sciences. Fuzzy c-mean (FCM) is one of the clustering techniques which was first proposed by Bezdek (1981) based on the iterative optimization. In fact, FCM is the advanced version of hard c-means clustering in which unlike the classic clustering, the membership degree of data in a cluster can have a value in the range of $[0, 1]$. The process of FCM clustering can be summarized in four steps below:

Step 1: The number of classes (c) is determined. This is worth mentioning that the numerical value of c is larger than or equal to 2 and smaller than or equal to n (the number of data samples). Then, the value of the weight parameter (m') which defines the amount of fuzziness of the clustering process must be determined. This parameter has a significant role in the optimization process. The optimization process in the FCM algorithm can continue for r iterations, where $r = 0,1,2, \dots, n$.

Step 2: The centers of clusters in each iteration are calculated.

Step 3: After determining the centers of clusters, the partitioned matrix for the r^{th} iteration is updated in the form of $\tilde{U}^{(r)}$ using Eqs. 3.3-3.8.

$$\mu_{ik}^{(r+1)} = \left[\sum_{j=1}^{c} \left(\frac{d_{ik}^{(r)}}{d_{jk}^{(r)}}\right)^{\frac{2}{(m'-1)}}\right]^{-1} \qquad \text{for} \quad I_k = \varphi \tag{3.3}$$

$$\mu_{ik}^{(r+1)} = 0 \qquad \text{for all classes } \ i \ \text{ where } i \in \tilde{I}_k \tag{3.4}$$

$$I_k = \{i \,|\, 2 \le C < n \,;\; d_{ik}^{(r)} = 0\} \tag{3.5}$$

$$\tilde{I}_k = \{1,2, \dots, c\} - I_k \tag{3.6}$$

$$\sum_{i \in I_k} \mu_{ik}^{(r+1)} = 1 \tag{3.7}$$

where d_{ik} is the Euclidean distance between the centre of i^{th} cluster and k^{th} data and $\mu_{ik}^{(r+1)}$ is the membership degree of k^{th} data in the i^{th} cluster for $r + 1$ iteration.

Step 4: In the final step, the accuracy of clustering must be evaluated. In this regard, the minimum acceptance precision (ε_L) is defined and only after satisfying the Eq. 3.8, the algorithm will be ceased; otherwise, the algorithm is returned to the second step and the optimization process is iterated until an appropriate level of accuracy is achieved (Bezdek 1981; Caldas et al. 2017).

$$\left\| \tilde{U}^{(r+1)} - \tilde{U}^{(r)} = \varepsilon_L \right\| \tag{3.8}$$

3.3. Results and Discussion

3.3.1. Rockburst Data

In this study, a total of 58 rockburst events were compiled from the literature belong to various underground openings all around the world (Jian et al. 2012; Dong et al. 2013; Adoko et al. 2013). Due to difficulties in recording the rockburst-related parameters and the incompleteness of the data, it was tried to consider the most important parameters for further analyses. Recently, Zhou et al. (2018) have provided a state-of-the-art literature review about the application of different uncertainty theory, unsupervised learning and supervised learning algorithms in rockburst studies. In their study, maximum tangential stress (MTS) around the underground openings, uniaxial compressive strength (UCS) of rock, uniaxial tensile strength (UTS) of rock, and elastic energy index (EEI) were identified as the most common parameters for rockburst assessment. Maximum tangential stress around the excavation is a key factor that is affected by the rock stress, groundwater, shape, and diameter of excavation (Palmstrom 1995). Since it would not be possible to measure these four factors in association with rockburst occurrence, maximum tangential stress can be considered as a good representative of those factors. This parameter usually is calculated based on numerical analysis or the information obtained from in-situ stress tests (e.g. hollow inclusion strain gauge method) and the following equation (Zhao et al. 2017):

$$\sigma_\theta = \frac{1}{2}(\sigma_H + \sigma_V)\left(1 + \frac{a^2}{r^2}\right) - \frac{1}{2}(\sigma_H - \sigma_V)\left(1 + \frac{3a^4}{r^4}\right) cos2\theta \quad (3.9)$$

where σ_θ, σ_H, and σ_v denote the tangential stress, the major horizontal principal stress, and vertical stress, respectively. The parameters of r and a denote the tunnel's radius and the distance between the point of rockburst occurrence to the center of the tunnel, and θ represents the angle between the virtual line connecting the point of rockburst occurrence and the center of the tunnel and horizontal axis. The strength parameters i.e. the uniaxial compressive strength and the uniaxial tensile strength also are indicators which show the capability of rocks to store elastic strain energy before failure as well as their brittleness and indirectly, could describe the effect of joints and block size of rock mass (Liu et al. 2013). These two parameters can be easily measured using the related laboratory tests based on the collected rock samples from the case studies. As mentioned before, several energy-based indices have been proposed and most of them are correlated with each other and similarly related to rockburst occurrence. Among them, elastic energy index (EEI) is the most common energy criterion to assess rockburst. EEI is the ratio of stored energy to that dissipated during a single loading-unloading cycle under

uniaxial compression (Kidybiński 1981). This parameter also can be measured directly using the double-hole method or indirectly using the rebound method. Therefore, in the current study, four parameters of maximum tangential stress, uniaxial compressive strength, tensile strength, and the elastic energy index were adopted as input parameters for modelling. The goal parameter is the rockburst intensity. Rockburst is a qualitative parameter that in such studies rarely is introduced as a binary problem (i.e. "1" for rockburst occurrence, "0" otherwise) (Li et al. 2017; Shirani Faradonbeh and Taheri 2019) and mostly is measured and assessed based on four classes of intensities which their description are given in Table 3.2. Table 3.2 provides an empirical classification of characteristic behaviour of underground openings subjected to various rockburst intensities that can be used as a standard for rockburst measuring and further predictions. The statistical features of all collected rockburst datasets and abbreviation of parameters are listed in Table 3.3. Fig. 3.3 shows the rockburst classes in regard to each input parameter. In an ideal manner, each input parameter value should belong to only one class in order to have an easy clustering process. According to Fig. 3.3, it is apparent that some parameters values belong to more than one class which shows that these values do not have distinct boundaries between four classes of rockburst. So, it is not practicable to cluster the rockburst events precisely just by considering one input parameter. It may be possible to cluster the datasets by a combination of several parameters. In the following section, it is tried to cluster the datasets into several distinct groups using SOM and fuzzy c-mean techniques.

Table 3.2 Empirical classification of rockburst based on its intensity (Jian et al. 2012; Liu et al. 2013)

Rockburst intensity	Descriptive characteristic behaviours of the tunnels
None	No sound of rock burst and absence of rock burst activities
Light	May cause loosening of a few fragments. The surrounding rock will be deformed, cracked or rib-spalled. There would be a weak sound, but no ejection phenomenon
Moderate	Spalling and falls of thin rock fragments. The surrounding rock will be deformed and fractured; there may be a considerable number of rock chip ejections and loose and sudden destructions, accompanied by crisp crackling and often presented in the local cavern of surrounding rock
Strong	Loosening and falls, often as a violent detachment of fragments and platy blocks. The surrounding rock will be bursting severely and suddenly thrown out or ejected into the tunnel, accompanied by strong bursts and roaring sound, and will expand rapidly to the deep surrounding rock

Table 3.3 Descriptive statistics of collected rockburst dataset

Statistical feature	Input parameter			
	σ_θ	σ_c	σ_t	W_{et}
Abbreviation	T	UCS	UTS	EEI
Unit	MPa	MPa	MPa	Dimensionless
Minimum	2.6	20	1.3	1.1
Maximum	167.2	263	22.6	9
Mean	49.752	114.592	6.039	4.553
Variance (n)	1184.511	2673.039	18.545	4.332
Standard deviation (n)	34.417	51.701	4.306	2.081

	Output parameter (rockburst intensity)			
	None	Light	Moderate	Strong
Abbreviation	N	L	M	S
Number of samples	22	4	19	13

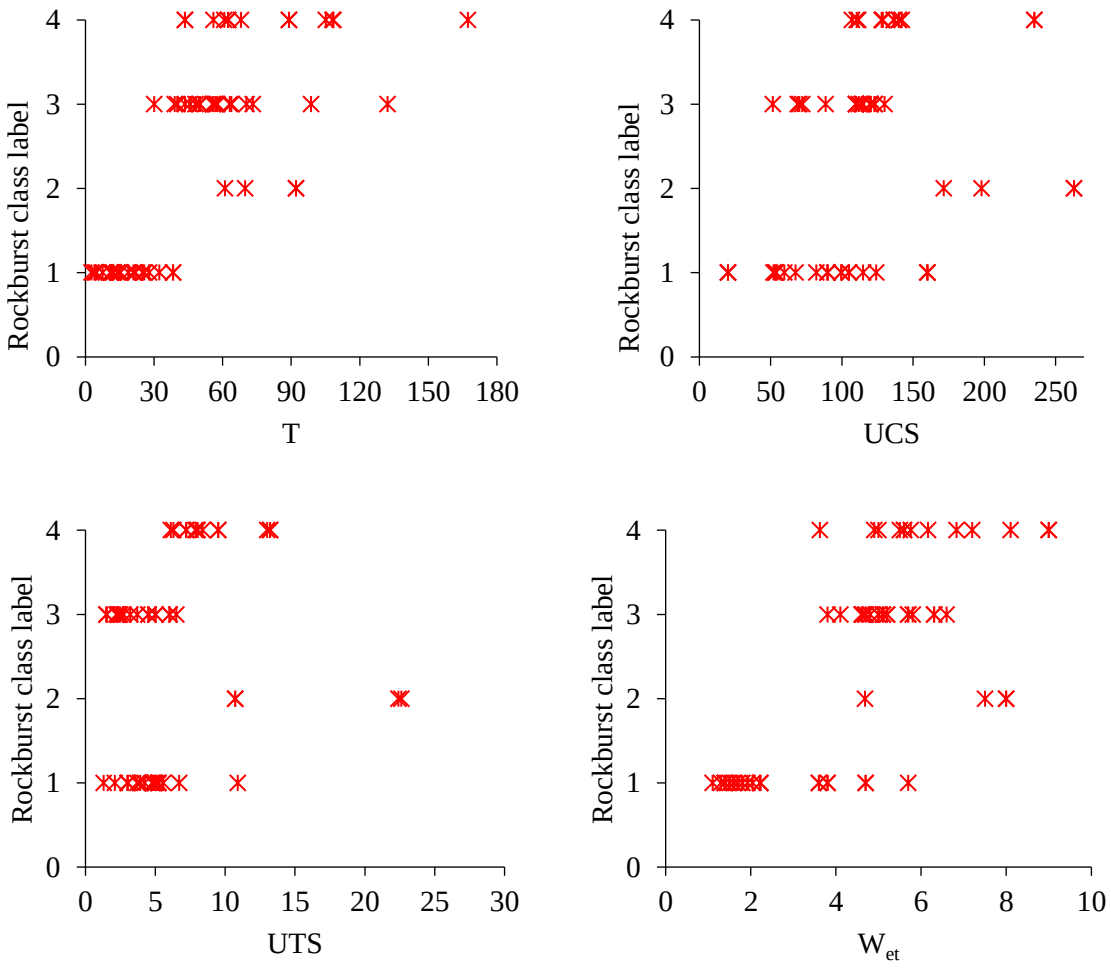

Figure 3.3 Rockburst class regarding each input parameter (1: None, 2: Light, 3: Moderate, 4: Strong)

3.3.2. Implementation of SOM Technique

For SOM modeling, 58 datasets with the main parameters of T, UCS, UTS, EEI, and the corresponding rockburst intensities were used, and the process of modeling was conducted in MATLAB software environment. First, all the 58 datasets related to the four mentioned parameters were normalized between 0 and 1 and considered as input data. Then, the controlling parameters were determined. These parameters have a significant role in the acceleration and improvement of convergence of algorithm in reaching the optimum response. In this study, in accordance with trial and error procedure and other scholars' suggestions (Chen and Kuo 2017; Mikaeil et al. 2018a, b), the optimum values of 100, 4, and 90 were obtained for controlling parameters of maximum iteration (epochs), Initneighbor (initial neighborhood size), and cover steps (the number of training steps for initial covering of the input space), respectively. Afterwards, the number of neurons (classes) in the competitive layer was defined as 4 (i.e. none, light, moderate, and strong). Eventually, by adjusting the required parameters, the algorithm was implemented for 100 iterations, and the results were obtained. By stopping the algorithm, 58 datasets were absorbed by 4 neurons (classes) on a two-dimensional lattice structure, and the classification process was completed. Fig. 3.4, as the hits plot, shows the number of data samples absorbed by each neuron. In Fig. 3.4, the axes show the Euclidean distance between classes. According to this figure, the four obtained classes have distinct boundaries. Besides, it can be seen obviously that the third neuron (class) is the most successful neuron in absorbing input data (by absorbing 22 data samples). In addition, the fourth, second and first neurons absorbed 19, 13, and 4 data samples, respectively. After assessing the contents of each class, it was found that all rockburst events in the first class (4 cases) belong to the light type and similarly, rockburst events in the second class (13 cases) belong to the strong type, rockburst events in the third class (22 cases) belong to the none type, and rockburst events in the fourth class (19 cases) belong to the moderate type. These four classes were labelled and shown in Fig. 3.4. This figure shows that SOM algorithm could classify the data samples into four classes in such a way that its results have the absolute consistency with the measured rockburst intensities by the operators in the field.

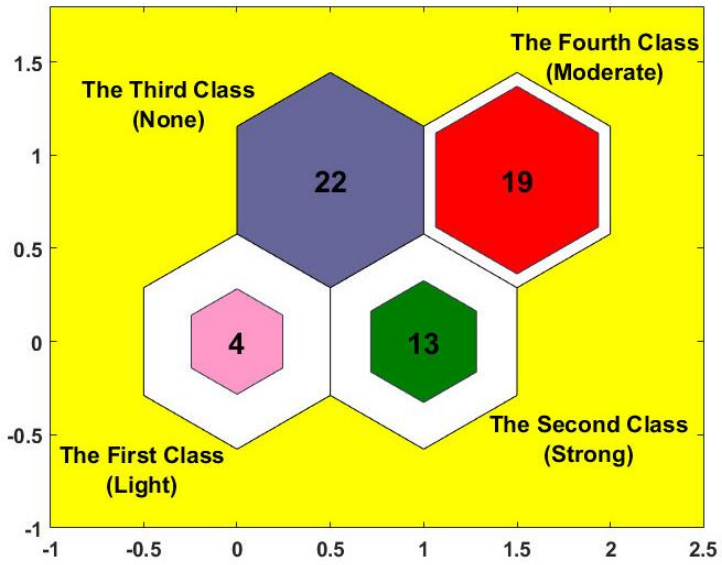

Figure 3.4 Hits plot for SOM model

In pursuance of more transparency, weighted distances between neighboring neurons were measured and displayed in Fig. 3.5. The axes in Fig. 3.5 show the weighted distances between neurons. The darker colors show that neurons (classes) are closer to each other and vice versa. For example, the distance between the first class (light) and the second one (strong) is less than the distance between the second class (strong) and the third one (none). As such, the distance between first class (light) and the third one (none) is less than the distance between the third class (none) and the fourth one (moderate). From another point of view, the distances between classes are in agreement with the definitions given in Table 3.2 for rockburst intensities. According to Fig. 3.5, the second and third classes have the maximum distance which can be referred to the rockburst characteristics explained in Table 3.2 for None and Strong types. To evaluate the relative importance of the input parameters for rockburst clustering using SOM, the weights of parameters corresponding to each class are shown graphically in Fig. 3.6. The darkness of the colors shows the high influence of the parameter on that class. By this figure, maximum tangential stress (T) has a high influence on the strong (the second class) and moderate (the fourth class) rockburst events, respectively. On the other hand, the parameters of UCS, UTS, and EEI similarly have a high influence on the moderate rockburst events (the fourth class).

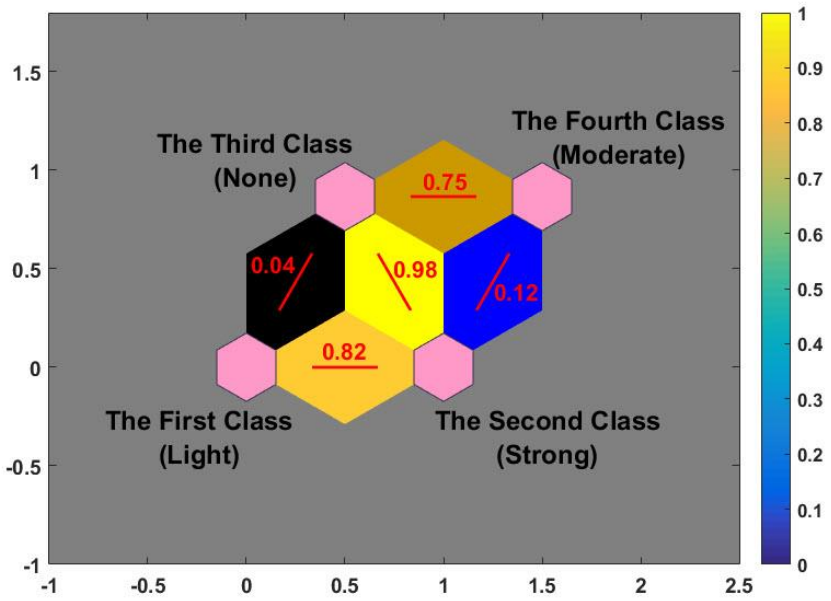

Figure 3.5 SOM neighbour weighted distances

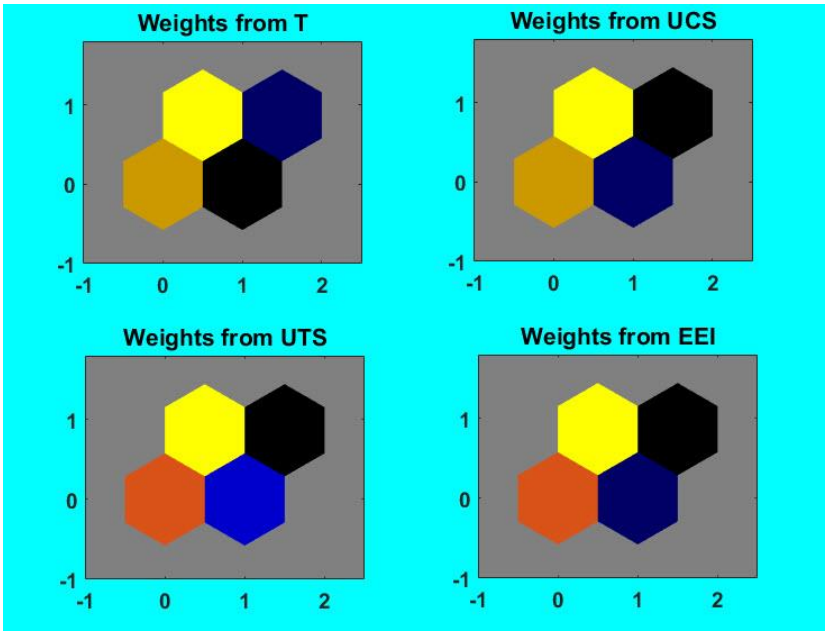

Figure 3.6 Weights of input parameters for each class

3.3.3. Implementation of Fuzzy C-mean Technique

Like SOM modeling, fuzzy c-mean (FCM) has some control parameters such as the maximum number of iterations, minimum acceptance precision (ε_L), and weighting parameter (m') which should be determined to achieve optimal results. Forasmuch as there is no definite way to precisely calculate these parameters, the common solution is to use a trial and error procedure and some differential equations that are suggested by other scholars (Rad et al. 2012, 2014; Mikaeil et al. 2018a). After calling the normalized data to the provided MATLAB code for

FCM and examining different combinations of control parameters, the values of 100, 0.00001, and 2 were obtained for the maximum iteration, ε_L, and m', respectively. Then, the algorithm was implemented based on the determined values and the variations of cost function was recorded that is shown in Fig. 3.7. According to this figure, up to iteration No. 30, the cost value gradually reduces and then becomes constant till iteration No. 33. In this iteration, the cost value and the precision level are equal to 1.8014 and 0.0001, respectively in which the precision level is larger than defined $\varepsilon_L = 0.00001$. So, because the Eq. 3.8 is not satisfied yet, FCM algorithm continues and in iteration No. 36 by reaching to the cost value of 1.8013 and $\varepsilon_L = 0$, the algorithm is stopped. It means that FCM was able to classify 58 data samples into four classes (clusters).

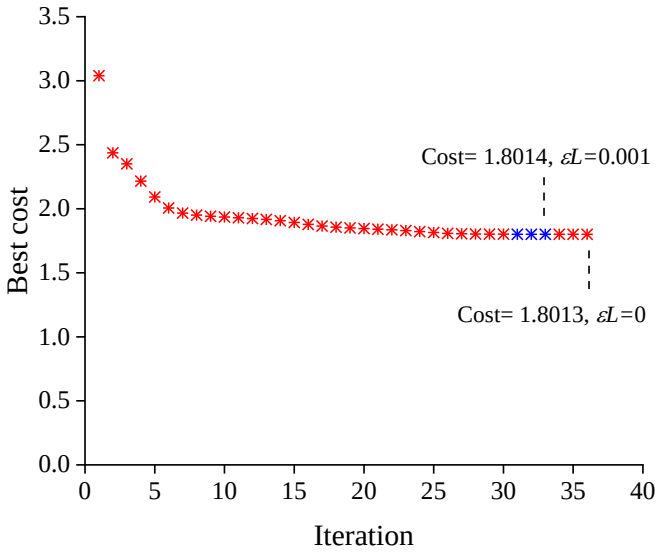

Figure 3.7 Variations of cost value during FCM modelling

Table 3.4 presents the membership degrees of each data sample for each class created by FCM. FCM is based on the minimization of the objective function and in its algorithm, the membership degree has an inverse relationship with the Euclidean distance. So, the sample with higher membership degree (or lower Euclidean distance) value in a class will belong to that class. By comparing the values listed in the rows in Table 3.4, it was turned out that the first class, the second class, the third class, and the fourth class have 5, 9, 26, and 18 data samples, respectively. For instance, membership degrees of sample No. 31 is 0.033, 0.087, 0.648, and 0.231 for the first, second, third and fourth classes, respectively, which based on the above explanation, this sample belongs to the third class. In other words, Table 3.4 gives information like the hits plot of SOM model. Then, by counting the majority of rockburst types in each class, the classes were nominated as Table 3.5, i.e. the first class is known as “light”,

the second class is known as “strong”, the third class is known as “moderate”, and the fourth class is known as “none”. To assess the importance of each input parameter on the developed clusters by FCM, the membership degree of the input parameters in each class were determined (see Table 3.5). The more the membership degree of the parameter, the high the influence of the parameter on that cluster. For instance, uniaxial compressive strength (UCS) has more influence on the creation of the first class (light rockburst types).

Table 3.4 Membership degrees of samples in four classes (clusters) created by FCM

Sample no.	Optimum partition			
	The first class	The second class	The third class	The fourth class
1	0.028	0.094	0.829	0.049
2	0.047	0.850	0.078	0.025
3	0.070	0.114	0.642	0.175
4	0.033	0.066	0.843	0.058
5	0.039	0.099	0.796	0.066
6	0.027	0.060	0.855	0.057
7	0.060	0.815	0.085	0.040
8	0.401	0.309	0.177	0.112
9	0.325	0.358	0.183	0.134
10	0.080	0.155	0.321	0.444
11	0.080	0.154	0.320	0.447
12	0.081	0.144	0.306	0.469
13	0.023	0.068	0.860	0.049
14	0.061	0.112	0.711	0.117
15	0.076	0.812	0.078	0.034
16	0.011	0.024	0.049	0.917
17	0.034	0.086	0.468	0.412
18	0.038	0.084	0.390	0.487
19	0.076	0.324	0.529	0.071
20	0.109	0.396	0.315	0.180
21	0.202	0.498	0.199	0.101
22	0.013	0.035	0.069	0.884
23	0.032	0.071	0.282	0.615
24	0.907	0.049	0.031	0.014
25	0.907	0.043	0.036	0.015
26	0.070	0.175	0.678	0.077
27	0.052	0.100	0.565	0.283
28	0.059	0.622	0.227	0.093
29	0.039	0.864	0.072	0.025
30	0.017	0.047	0.897	0.039
31	0.033	0.087	0.648	0.231
32	0.019	0.055	0.869	0.057
33	0.015	0.036	0.090	0.859

34	0.016	0.044	0.909	0.031
35	0.019	0.055	0.869	0.057
36	0.034	0.088	0.664	0.214
37	0.033	0.101	0.556	0.311
38	0.014	0.033	0.077	0.876
39	0.117	0.299	0.505	0.079
40	0.223	0.259	0.429	0.089
41	0.056	0.139	0.186	0.618
42	0.037	0.077	0.190	0.696
43	0.052	0.100	0.565	0.283
44	0.013	0.035	0.069	0.884
45	0.032	0.071	0.282	0.615
46	0.907	0.049	0.031	0.014
47	0.907	0.043	0.036	0.015
48	0.070	0.175	0.678	0.077
49	0.060	0.204	0.675	0.062
50	0.026	0.055	0.108	0.811
51	0.012	0.047	0.917	0.023
52	0.026	0.054	0.107	0.813
53	0.042	0.234	0.663	0.061
54	0.006	0.014	0.030	0.950
55	0.090	0.689	0.138	0.083
56	0.020	0.054	0.086	0.840
57	0.048	0.147	0.752	0.054
58	0.027	0.056	0.109	0.808

Table 3.5 Membership degrees of input parameters in each class

Input parameter	The first class (light)	The second class (strong)	The third class (moderate)	The fourth class (none)
T	0.4563	0.1207	0.2922	0.5750
UCS	0.8997	0.2586	0.4281	0.4950
UTS	0.4766	0.1876	0.1805	0.4387
EEI	0.9107	0.2226	0.5806	0.5689

3.4. Comparison of Results and Discussion

This section aims to evaluate the performance of the proposed models. For this, the 58 recorded/measured rockburst events by engineers from deep underground projects were compared with the classified data samples by SOM and FCM techniques. Considering the available input parameters, four most common strength-based criteria (i.e. Russenes criterion, Hoek criterion, tangential stress criterion, and the rock brittleness coefficient criterion) as well as an energy-based criterion (i.e. EEI criterion) were selected from Table 3.1 to assess their performance in identifying the rockburst class as well. The results of the comparison between

the SOM and FCM techniques along with the ones obtained from empirical criteria are given in Table 3.6. To have a quantitative insight regarding the performance of the developed models, five performance metrics i.e. accuracy rate (Grinand et al. 2008), Cohen's Kappa coefficient (Kappa) (Cohen 1960), precision, recall, and F1 score (Zhou et al. 2016) were calculated for different models based on the confusion matrices obtained from Table 3.6 (see Table 3.7) for each model. Accuracy rate is a primary criterion for evaluating the model, which is defined as the ratio of truly classified samples to the total number of samples. Ideally, this value equals 100%. The Kappa coefficient is a more robust index than accuracy rate that measures the proportion of precisely classified cases after removing the probability of chance agreement. Hence, Kappa is always somewhat lower than the accuracy rate, and according to the scale proposed by Landish and Koch (Landis and Koch 1977), a Kappa higher than 0.4 shows a good agreement. Precision is another metric that measures the accuracy of the model when it predicts a specific class. The ratio of correctly classified cases of a class by the model is defined as the recall. The F1 score is the harmonic mean of precision and recall metrics that its best value is 1. For all five metrics, a higher value shows the better performance.

Fig. 3.8 compares the models in terms of different performance indices. As can be seen from this figure, the SOM model could classify the rockburst events exactly with 100% value for all performance indices that show the high potential of this algorithm for dealing with such a complex geotechnical problem. In other words, SOM succeeded to find the latent relationship between the input parameters and the corresponding output and placed all data samples in their proper clusters. In this study, FCM classified the data samples during 36 iterations with a satisfactory precision level and proved its capability in dealing with geotechnical problems. However, in some cases, FCM was not able to place some data samples in proper clusters and finally showed a lower accuracy than the SOM model. For example, FCM placed the samples No. 3 and 4 in the third class (moderate), while in the field they have been measured as none (N) and moderate (M) rockburst types, respectively. In another case, both samples of 25 and 26 have been measured as the strong rockbursts in the field, while FCM put them in different classes of light and moderate, respectively. On the other hand, among the five conventional rockburst criteria, Hoek criterion showed slightly better performance than others, while rock brittleness coefficient identified as the worst model for clustering. Besides, the obtained Kappa values for EEI (33.3%) and rock brittleness coefficient (1.8%) are lower than 0.4 (40%), and according to Landish and Koch (Landis and Koch 1977), these models show a poor agreement and arbitrary classification, respectively. Hence, these models could not be used reliably to

classify and predict rockburst intensity. It should be noted that the empirical methods have been developed based on specific case studies and some engineering judgments and consider few input parameters, while the datasets compiled in this study have a broad range of rock properties and locations.

As mentioned in the introduction section, few studies have been done in relation to the application of unsupervised learning algorithms for assessing rockburst hazard. Among them, Xie and Pan (2007) and Gao (2010) could classify the rockburst events with grey whitenization weigh function cluster approach and ant colony clustering algorithm with the accuracy values of 80% and 83.3%, respectively. They used the maximum tangential stress, uniaxial compressive strength, uniaxial tensile strength, and elastic energy index as input parameters in their studies like the current study. Therefore, it can be concluded that the results obtained from SOM algorithm are more reliable and this method could be considered as a high-performance clustering system in geoscience, especially in assessing rockburst hazard. It is worth mentioning that the results of this study can provide feasible measures to prevent rockburst hazards. Since each of input parameters plays different roles, some indications can be extracted. As mentioned in section 3.3.2, the maximum tangential stress (T) has a significant impact on the occurrence of strong and moderate rockbursts, respectively, whereas other input parameters mostly affect moderate rockbursts. Large values of T could led to more intense rockbursts in underground openings. As discussed by Palmstrom (1995) and Shirani Faradonbeh and Taheri (2019), the tangential stress around the openings is the representative of four components of rock stress, groundwater, the shape of the structure, and diameter. Therefore, it is very important to control these four parameters. With respect to difficulties in controlling the rock stress and groundwater pressure, it is easier to control maximum tangential stress indirectly by optimizing the shape and diameter of underground openings in practical projects. It can be a primary measure to control rockburst.

Table 3.6 Results of clustered data samples using different models

No.	Measured	Russenes	Hoek	Tangential	Brittleness	EEI	FCM	SOM
1	M	M	L	L	M	M	M	M
2	S	S	S	S	M	S	S	S
3	N	N	N	N	M	S	M	N
4	M	M	L	L	N	S	M	M
5	M	M	M	M	N	S	M	M
6	M	M	L	L	N	S	M	M
7	S	S	S	M	S	M	S	S
8	L	M	L	L	S	S	L	L
9	L	M	L	L	S	M	S	L
10	N	N	N	N	L	L	N	N

11	N	N	N	N	L	L	N	N
12	N	N	N	N	L	L	N	N
13	M	M	L	L	M	M	M	M
14	M	M	L	L	M	S	M	M
15	S	S	S	S	S	S	S	S
16	N	N	N	N	S	N	N	N
17	N	L	N	N	M	M	M	N
18	N	N	N	N	M	M	N	N
19	S	M	M	M	S	S	M	S
20	M	S	S	S	M	M	S	M
21	S	S	S	S	S	S	S	S
22	N	S	S	S	S	N	N	N
23	N	N	N	N	M	M	N	N
24	L	M	L	L	M	S	L	L
25	S	L	N	N	M	S	L	S
26	S	L	L	L	M	S	M	S
27	N	N	N	N	M	M	M	N
28	M	S	S	S	M	M	S	M
29	S	S	S	S	M	M	S	S
30	M	M	M	M	N	S	M	M
31	M	S	M	M	L	M	M	M
32	M	M	L	L	N	M	M	M
33	N	L	L	L	N	N	N	N
34	M	M	L	L	N	S	M	M
35	M	M	L	L	N	M	M	M
36	M	S	M	M	L	M	M	M
37	M	S	S	M	M	M	M	M
38	N	M	L	L	N	N	N	N
39	S	S	S	M	M	S	M	S
40	S	M	L	L	M	S	M	S
41	N	N	N	N	S	N	N	N
42	N	N	N	N	L	L	N	N
43	N	N	N	N	M	M	M	N
44	N	S	S	S	S	N	N	N
45	N	N	N	N	M	M	N	N
46	L	M	L	L	M	S	L	L
47	S	L	N	N	M	S	L	S
48	S	L	L	L	M	S	M	S
49	M	S	S	M	M	S	M	M
50	N	N	N	N	S	N	N	N
51	M	M	L	L	M	S	M	M
52	N	N	N	N	S	N	N	N
53	M	S	S	M	M	S	M	M
54	N	L	N	N	S	N	N	N
55	S	S	S	M	S	M	S	S
56	N	M	L	L	S	N	N	N
57	M	S	M	M	M	S	M	M
58	N	N	N	N	S	N	N	N

N none, *L* light, *M* moderate, *S* strong

Table 3.7 Confusion matrix for different models

No.	Model		Confusion matrix				No.	Model		Confusion matrix			
1	Russenes		Predicted				5	EEI		Predicted			
			N	L	M	S				N	L	M	S
	Actual	N	15	3	2	2		Actual	N	11	4	6	1
		L	0	0	4	0			L	0	0	1	3
		M	0	0	11	8			M	0	0	9	10
		S	0	4	2	7			S	0	0	3	10
2	Hoek		Predicted				6	FCM		Predicted			
			N	L	M	S				N	L	M	S
	Actual	N	17	3	0	2		Actual	N	18	0	4	0
		L	0	4	0	0			L	0	3	0	1
		M	0	9	5	5			M	0	0	17	2
		S	2	3	1	7			S	0	2	5	6
3	Tangential		Predicted				7	SOM		Predicted			
			N	L	M	S				N	L	M	S
	Actual	N	17	3	0	2		Actual	N	22	0	0	0
		L	0	4	0	0			L	0	4	0	0
		M	0	9	8	2			M	0	0	19	0
		S	2	3	4	4			S	0	0	0	13
4	Brittleness		Predicted										
			N	L	M	S							
	Actual	N	2	4	7	9							
		L	0	0	2	2							
		M	7	2	10	0							
		S	0	0	8	5							

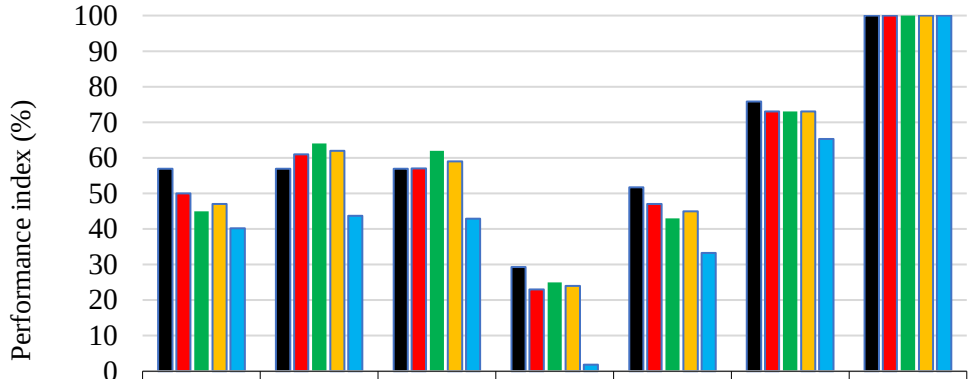

	Russenes	Hoek	Tangential stress	Brittleness	EEI	FCM	SOM
Accuracy (%)	56.9	56.9	56.9	29.3	51.7	75.8	100
Precision (%)	50	61	57	23	47	73	100
Recall (%)	45	64	62	25	43	73	100
F1 score (%)	47	62	59	24	45	73	100
Kappa (%)	40.2	43.7	42.9	1.8	33.3	65.3	100

Figure 3.8 Comparison of the proposed models' performance for rockburst clustering based on five indices

3.5. Summary and Conclusions

Many empirical equations have been proposed by researchers to predict rockburst intensities in recent years. However, according to the literature, they are not sufficient and reliable. The maximum tangential stress, uniaxial compressive strength, uniaxial tensile strength, and elastic energy index are the most common input parameters which are used to predict rockburst intensity. In this study by considering these four parameters, it was attempted to apply two novel clustering techniques namely self-organizing map (SOM) and fuzzy c-mean (FCM) to 58 rockburst data samples that are collected from several underground projects to classify and determine rockburst intensity. In addition, the capability of five common empirical criteria was assessed. Five performance metrics including accuracy rate, precision, recall, F1 score, and Kappa were used to assess the performance of the proposed models. The SOM algorithm with its especial mechanism classified all data into 4 distinct clusters and predicted rockburst intensity with the accuracy rate, precision, recall, f1 score, and Kappa values equal to 100 %. In addition, SOM indicated that the distances between classes are consistent with the intensities that are described by engineers. The evaluation of the weights of input parameters in each created class by SOM showed the high influence of maximum tangential stress (T) of surrounding rock mass on the clustering process, especially on the occurrence of strong and moderate rockburst events. Therefore, to tackle the rockburst problem, it is recommendable to optimize the shape and diameter of the underground openings. Despite the high and acceptable accuracy rate of FCM model (75.86 %), this method was not able to classify some data samples in appropriate clusters. Nevertheless, FCM outperformed the five empirical criteria that were studied in this research. Among the empirical criteria, Hoek criterion and tangential stress coefficient showed better performance in clustering the rockburst datasets, while rock brittleness coefficient criterion showed the lowest performance. Finally, it can be concluded that the SOM and FCM algorithms are strong enough to discover the latent relationships between the independent parameters and the corresponding dependent one. Specifically, in geoscience, we deal with high-complex and non-linear problems which there is no definite solution for them, and these kinds of algorithms can help engineers to have an insight into the hazards.

References

Adoko AC, Gokceoglu C, Wu L, Zuo QJ (2013) Knowledge-based and data-driven fuzzy modeling for rockburst prediction. *International Journal of Rock Mechanics and Mining Sciences* 61:86–95

Akdag S, Karakus M, Taheri A, et al (2018) Effects of Thermal Damage on Strain Burst Mechanism for Brittle Rocks Under True-Triaxial Loading Conditions. *Rock Mechanics and Rock Engineering* 51(6):1–26

Armaghani DJ, Faradonbeh RS, Rezaei H, et al (2016) Settlement prediction of the rock-socketed piles through a new technique based on gene expression programming. *Neural Computing and Applications* 29(11):1115-1125

Aryafar A, Mikaeil R, Haghshenas SS, Haghshenas SS (2018) Application of metaheuristic algorithms to optimal clustering of sawing machine vibration. *Measurement: Journal of the International Measurement Confederation* 124:20–31

Aubertin M, Gill DE, Simon R, others (1994) On the use of the brittleness index modified (BIM) to estimate the post-peak behavior of rocks. In: *1st North American Rock Mechanics Symposium*

Barton N, Lien R, Lunde J (1974) Engineering classification of rock masses for the design of tunnel support. *Rock Mechanics Felsmechanik Mécanique des Roches* 6(4):189–236

Bezdek JC (1981) Models for Pattern Recognition. In: Pattern Recognition with Fuzzy Objective Function Algorithms. *Springer US*, Boston, MA, pp 1–13

Blake W, Hedley DGF (2003) Rockbursts: Case Studies from North American Hard-Rock Mines. *Society for Mining, Metallurgy & Exploration, Incorporated*

Cai M (2016) Prediction and prevention of rockburst in metal mines- A case study of Sanshandao gold mine. *Journal of Rock Mechanics and Geotechnical Engineering* 8(2):204–211

Caldas R, Hu Y, de Lima Neto FB, Markert B (2017) Self-Organizing Maps and Fuzzy C-Means Algorithms on Gait Analysis Based on Inertial Sensors Data. *Springer*, Cham, pp 197–205

Castro LAM, Bewick RP, Carter TG (2012) An overview of numerical modelling applied to

deep mining. *Innovative numerical modelling in geomechanics* 393–414

Chen BR, Feng XT, Li QP, et al (2013) Rock Burst Intensity Classification Based on the Radiated Energy with Damage Intensity at Jinping II Hydropower Station, China. *Rock Mechanics and Rock Engineering* 48(1):289–303

Chen ZY, Kuo RJ (2017) Combining SOM and evolutionary computation algorithms for RBF neural network training. *Journal of Intelligent Manufacturing* 1–18

Cohen J (1960) A Coefficient of Agreement for Nominal Scales. *Educational and Psychological Measurement* 20(1):37–46

Das SK, Basudhar PK (2009) Utilization of self-organizing map and fuzzy clustering for site characterization using piezocone data. *Computers and Geotechnics* 36(1-2):241–248

Demuth HB, Beale MH, De Jess O, Hagan MT (2014) Neural network design. *Martin Hagan*

Dong L, Li X, Peng K (2013) Prediction of rockburst classification using Random Forest. *Transactions of Nonferrous Metals Society of China* 23(2):472–477

DOU L ming, LU C ping, MU Z long, GAO M shi (2009) Prevention and forecasting of rock burst hazards in coal mines. *Mining Science and Technology* 19(5):585–591

Faradonbeh RS, Armaghani DJ, Monjezi M, Mohamad ET (2016) Genetic programming and gene expression programming for flyrock assessment due to mine blasting. International *Journal of Rock Mechanics and Mining Sciences* 88:254-264

Feng X, Wang L (1994) Rockburst prediction based on neural networks. *Transactions of Nonferrous Metals Society of China* 4(1):7–14

Feng XT, Yu Y, Feng GL, et al (2016) Fractal behaviour of the microseismic energy associated with immediate rockbursts in deep, hard rock tunnels. *Tunnelling and Underground Space Technology* 51:98–107

Frid V (1997) Rockburst hazard forecast by electromagnetic radiation excited by rock fracture. *Rock Mechanics and Rock Engineering* 30(4):229–236

Gao W (2010) Prediction of rock burst based on ant colony clustering algorithm. *Chinese Journal of Geotechnical Engineering* 32(6):874–880

Grinand C, Arrouays D, Laroche B, Martin MP (2008) Extrapolating regional soil landscapes from an existing soil map: Sampling intensity, validation procedures, and integration of

spatial context. *Geoderma* 143(1-2):180–190

Hagan MT, Demuth HB, Beale MH, others (1996) Neural network design. *Pws Pub*. Boston

He J, Dou L, Gong S, et al (2017) Rock burst assessment and prediction by dynamic and static stress analysis based on micro-seismic monitoring. *International Journal of Rock Mechanics and Mining Sciences* 100(93):46–53

He M, e Sousa LR, Miranda T, Zhu G (2015) Rockburst laboratory tests database - Application of data mining techniques. *Engineering Geology* 185:116–130

He M, Gong W, Wang J, et al (2014) Development of a novel energy-absorbing bolt with extraordinarily large elongation and constant resistance. *International Journal of Rock Mechanics and Mining Sciences* 67:29–42

Hoek E, Brown ET (1980) Underground Excavations in Rock. *Institution of Mining and Metallurgy*, London

Jha PC, Chouhan RKS (1994) Long range rockburst prediction: A seismological approach. *International Journal of Rock Mechanics and Mining Sciences* 31(1):71–77

Jian Z, Xibing L, Xiuzhi S (2012) Long-term prediction model of rockburst in underground openings using heuristic algorithms and support vector machines. *Safety Science* 50(4):629–644

Khandelwal M, Armaghani DJ, Faradonbeh RS, et al (2016) A new model based on gene expression programming to estimate air flow in a single rock joint. *Environmental Earth Sciences* 75(9):739

Khandelwal M, Armaghani DJ, Faradonbeh RS, et al (2017) Classification and regression tree technique in estimating peak particle velocity caused by blasting. *Engineering with Computers* 33(1):45–53

Kidybiński A (1981) Bursting liability indices of coal. *International Journal of Rock Mechanics and Mining Sciences* 18(4):295–304

Kohonen T (1990) The self-organizing map. *Proceedings of the IEEE* 78(9):1464–1480

Landis JR, Koch GG (1977) The Measurement of Observer Agreement for Categorical Data. *Biometrics* 33(1):159–174

Li B, Liu Y (2015) Determination of classification of rock burst risk based on random forest

approach and its application. *Sci Technol Rev* 33(1):57–62

Li C, Cai M, Qiao L, Wang S (1996) Rock complete stress-strain curve and its relationship to rockburst. *Journal of University of Science and Technology Beijing* 21(6):513-5 (in Chinese)

Li N, Feng X, Jimenez R (2017) Predicting rock burst hazard with incomplete data using Bayesian networks. *Tunnelling and Underground Space Technology* 61:61–70

Li T, Cai MF, Cai M (2007) A review of mining-induced seismicity in China. *International Journal of Rock Mechanics and Mining Sciences* 44:1149–1171

Liu Z, Shao J, Xu W, Meng Y (2013) Prediction of rock burst classification using the technique of cloud models with attribution weight. *Natural Hazards* 68:549–568

Mahdevari S, Shahriar K, Sharifzadeh M, Tannant DD (2017) Stability prediction of gate roadways in longwall mining using artificial neural networks. *Neural Computing and Applications* 28(11):3537–3555

Malondkar A, Corizzo R, Kiringa I, et al (2018) Spark-GHSOM: Growing hierarchical self-organizing map for large scale mixed attribute datasets. *Information Sciences* 496:572-591

Mikaeil R, Haghshenas SS, Haghshenas SS, Ataei M (2018a) Performance prediction of circular saw machine using imperialist competitive algorithm and fuzzy clustering technique. *Neural Computing and Applications* 29(6):283–292

Mikaeil R, Haghshenas SS, Hoseinie SH (2018b) Rock Penetrability Classification Using Artificial Bee Colony (ABC) Algorithm and Self-Organizing Map. *Geotechnical and Geological Engineering* 36(2):1309–1318

Mikaeil R, Haghshenas SS, Ozcelik Y, Gharehgheshlagh HH (2018c) Performance Evaluation of Adaptive Neuro-Fuzzy Inference System and Group Method of Data Handling-Type Neural Network for Estimating Wear Rate of Diamond Wire Saw. *Geotechnical and Geological Engineering* 36(6):3779-3791

Mo C, Tan H, Su G, Jiang J (2014) A New Rockburst Proneness Index Based on Energy Principle. International Conference on Civil Engineering, *Energy and Environment*

Mohamad ET, Faradonbeh RS, Armaghani DJ, et al (2016) An optimized ANN model based

on genetic algorithm for predicting ripping production. *Neural Computing and Applications* 28(1):393-406

Palmstrom A (1995) Characterizing the strength of rock masses for use in design of underground structures. In: *International conference in design and construction of underground structures*, p 10

Rad MY, Haghshenas SS, Haghshenas SS (2014) Mechanostratigraphy of cretaceous rocks by fuzzy logic in East Arak, Iran. In: *The 4th International Workshop on Computer Science and Engineering-Summer*, WCSE

Rad MY, Haghshenas SS, Kanafi PR, Haghshenas SS (2012) Analysis of Protection of Body Slope in the Rockfill Reservoir Dams on the Basis of Fuzzy Logic. In: *IJCCI*. pp 367–373

Russenes B (1974) Analysis of Rock Spalling for Tunnels in Steep Valley Sides. *Master Thesis of Science, Norwegian Institute of Technology*

Salemi A, Mikaeil R, Haghshenas SS (2018) Integration of Finite Difference Method and Genetic Algorithm to Seismic analysis of Circular Shallow Tunnels (Case Study: Tabriz Urban Railway Tunnels). *KSCE Journal of Civil Engineering* 22(5):1978–1990

Shi XZ, Zhou J, Dong L, et al (2010) Application of unascertained measurement model to prediction of classification of rockburst intensity. *Chinese Journal of Rock Mechanics and Engineering* 29(1):2720–2727 (in Chinese)

Shirani Faradonbeh R, Taheri A (2019) Long-term prediction of rockburst hazard in deep underground openings using three robust data mining techniques. *Engineering with Computers* 35(2):659–675

Sun J, Wang S (2000) Rock mechanics and rock engineering in China: developments and current state-of-the-art. *International Journal of Rock Mechanics and Mining Sciences* 37(3):447–465

Tang C, Wang J, Zhang J (2010) Preliminary engineering application of microseismic monitoring technique to rockburst prediction in tunneling of Jinping II project. *Journal of Rock Mechanics and Geotechnical Engineering* 2(3):193–208

Turchaninov IA, Markov GA, Gzovsky M V., et al (1972) State of stress in the upper part of the Earth's crust based on direct measurements in mines and on tectonophysical and seismological studies. *Physics of the Earth and Planetary Interiors* 6(4):229–234

Wang YH, Li WD, Lee PKK, Tham LG (1998) Method of duzzy comprehensive evaluations for rockburst prediction. *Chinese Joirnal of Rock Mechanics and Engineering* 17(5):493-501 (in Chinese)

Weng L, Huang L, Taheri A, Li X (2017) Rockburst characteristics and numerical simulation based on a strain energy density index: A case study of a roadway in Linglong gold mine, China. *Tunnelling and Underground Space Technology* 69:223–232

Xie X-B, Pan C-L (2007) Rockburst prediction method based on grey whitenization weight function cluster theory. *Journal of Hunan University Natural Sciences* 34(8):16–20

Yan P, Zhao Z, Lu W, et al (2015) Mitigation of rock burst events by blasting techniques during deep-tunnel excavation. *Engineering Geology* 188:126–136

Yu H, Khan F, Garaniya V (2015) Risk-based fault detection using Self-Organizing Map. R*eliability Engineering & System Safety* 139:82–96

Zadeh LA (1996) Fuzzy sets. In: Fuzzy Sets, Fuzzy Logic, And Fuzzy Systems: Selected Papers by Lotfi A Zadeh. *World Scientific*, pp 394–432

Zhang Q, Wang W, Liu T (2011) Prediction of rock bursts based on particle swarm optimization-BP neural network. *J China Three Gorges Univ* 33(6):41–45

Zhao G, Wang D, Gao B, Wang S (2017) Modifying rock burst criteria based on observations in a division tunnel. *Engineering Geology* 216:153–160

Zhou J, Li X, Mitri HS (2018) Evaluation method of rockburst: State-of-the-art literature review. *Tunnelling and Underground Space Technology* 81:632–659

Zhou J, Li X, Mitri HS (2016) Classification of rockburst in underground projects: comparison of ten supervised learning methods. *Journal of Computing in Civil Engineering* 30(5):4016003

Zhou J, Shi XZ, Dong L, et al (2010) Fisher discriminant analysis model and its application for prediction of classification of rockburst in deepburied long tunnel. *Journal of Coal Science and Engineering (China)* 16(2):144–149

Statement of Authorship

Title of Paper	The propensity of the over-stressed rock masses to different failure mechanisms based on a hybrid probabilistic approach
Publication Status	☐ Published ☐ Accepted for Publication ☑ Submitted for Publication ☐ Unpublished and Unsubmitted work written in manuscript style
Publication Details	**Shirani Faradonbeh R**, Taheri A, Karakus M (2021) The propensity of the over-stressed rock masses to different failure mechanisms based on a hybrid probabilistic approach. *Tunnelling and Underground Space Technology* x(x):x–x. Note: Under review [the revised format submitted on 15 June 2021]

Principal Author

Name of Principal Author (Candidate)	Roohollah Shirani Faradonbeh		
Contribution to the Paper	Literature review and database preparation, statistical analysis, development of models and preparation of the manuscript		
Overall percentage (%)	80%		
Certification:	This paper reports on original research I conducted during the period of my Higher Degree by Research candidature and is not subject to any obligations or contractual agreements with a third party that would constrain its inclusion in this thesis. I am the primary author of this paper.		
Signature		Date	17 June 2021

Co-Author Contributions

By signing the Statement of Authorship, each author certifies that:

i. the candidate's stated contribution to the publication is accurate (as detailed above);

ii. permission is granted for the candidate in include the publication in the thesis; and

iii. the sum of all co-author contributions is equal to 100% less the candidate's stated contribution.

Name of Co-Author	Abbas Taheri		
Contribution to the Paper	Research supervision, review and revision of the manuscript		
Signature		Date	21 June 2021

Name of Co-Author	Murat Karakus		
Contribution to the Paper	Review and revision of the manuscript		
Signature		Date	21 June 2021

Chapter 4

The Propensity of the Over-Stressed Rock Masses to Different Failure Mechanisms Based on a Hybrid Probabilistic Approach

Abstract

The simultaneous impact of excavation-induced stress concentration and mining disturbances on deep underground mines/tunnels can result in severe and catastrophic failure like strain bursting. In this regard, the proper measurement of proneness to different rock failure mechanisms has great importance in terms of safety and economics. This study proposes a practical hybrid gene expression programming-based logistic regression (GEP-LR) model, as a multi-class classifier, to detect the failure mechanism (i.e. squeezing, slabbing and strain burst) in hard rock based on four intact rock properties. Three non-linear binary models are developed to predict the occurrence/non-occurrence of each failure mechanism. The logistic regression technique is linked to the developed GEP models to measure the occurrence probability of each failure mechanism. Finally, the failure mechanism that has the maximum probability of occurrence is selected as the predicted output. The performance analysis of the developed model shows that it is efficiently capable of detecting failure mechanisms with high accuracy. The failure mechanism detection models are presented in MATLAB codes to be easily used in practice by engineers/researchers as an initial guide for failure/stability analysis of underground openings. Finally, the validity of the proposed model is further evaluated by new datasets compiled from different studies.

Keywords: Failure mechanism; Strain burst; Slabbing; Squeezing; Gene expression programming; Logistic regression

4.1. Introduction

The mechanical rock properties and their corresponding deformation failure mechanisms are dramatically different in deep underground than those in shallow conditions. This is due to the high geo-stress, ground-water pressure and high-temperature environment, which affect the rock mass for a long time. In this regard, many studies have been undertaken to investigate the parameters that influence the stability of underground structures using theoretical analyses, experimental and numerical simulations (Hoek and Brown 1980; Barla et al. 2011; Saadat and Taheri 2020; Li et al. 2020; Shirani Faradonbeh et al. 2021). Rock fracturing around deep excavations is mostly governed by the rock type, rock mass jointing degree and its orientation relative to the excavation free faces, the geometry of the excavation, in-situ stress magnitude and its orientation relative to the excavation direction (Wagner 2019). In deep mining and geotechnical projects, the highly uncertain governing factors are coupled to the stress distribution around the excavations, making the failure mechanism prediction one of the most challenging issues in terms of safety, the economic viability of the projects etc. The dominant failure mechanism in deep mining/tunnelling projects is strain burst or slabbing rather than shearing or squeezing (Fairhurst and Cook 1966). Palmstrom and Stille (2007) give a summary of different failure mechanisms and their characteristics in the underground. Also, a brief description of the common failure mechanisms in underground projects is presented below.

One of the common failure mechanisms is squeezing, a non-violent rock behaviour/failure mechanism, which is characterised as a large time-dependent deformation associated with creep induced by over-stressing of massive rocks (Kabwe and Karakus 2020; Kabwe et al. 2020). These massive rocks usually have a high percentage of micaceous or clay minerals. Squeezing creates a plastic zone around the underground openings, which will result in cross-sectional area reduction during an aseismic process. The potential of rocks to squeezing is influenced by different parameters such as the geological conditions, rock mass mechanical properties, in-situ stresses, groundwater pressure, the geometry of the opening and the supporting system (Aydan et al. 1993; Barla 1995). Fig. 4.1a shows an example of a highly deformed cross-section of the Saint Martin access adit (Lyon–Turin base tunnel) induced by squeezing. According to Ortlepp (1997), slabbing refers to the formation of the densely spaced stress-induced slabs (onion-skin-like fractures) on the boundary of an underground opening (i.e. roof and sidewalls). The spacing of these slabs depends on the rock heterogeneity, rock strength, as well as in-situ stresses (Li et al. 2011). This failure mechanism is more common in moderate to hard over-stressed massive rocks and initiates in excavated regions having high

maximum tangential stresses by creating a local V-shaped notch on the opening boundary (Ortlepp 2001). Fig. 4.1b displays the slabbing failure in the roof of a mine drift excavated in quartzite at 1000 m depth.

Strain burst is a term for the much more violent fracturing of rocks than slabbing accompanied by the high seismicity, rock chips ejection and sudden release of strain energy that can pose a serious threat to workers, equipment and project life (Fig. 4.1c). The coupled static-dynamic loading conditions induced by stress redistribution after excavations and the dynamic disturbances generated by drilling and blasting, roof collapse, fault-slip, etc. provide a high-stress zone around the openings, which in turn triggers the strain bursting proneness effectively (Akdag et al. 2018; Shirani Faradonbeh et al. 2019; Shirani Faradonbeh et al. 2020; Wang et al. 2020). Many factors affect the bursting proneness of rocks, and owing to its vague mechanism, strain burst is known as a high-complex non-linear problem and difficult to predict (He et al. 2015; Shirani Faradonbeh and Taheri 2019). Among these influential factors, the intact rock properties have a critical role in the occurrence of this phenomenon in the deep underground. The uniaxial compressive strength (σ_c) and tensile strength (σ_t) are among the most prominent intact rock properties which can be used for assessing the rock capacity to store elastic strain energy (Munoz et al. 2016; Munoz and Taheri 2017; Shirani Faradonbeh et al. 2020). These parameters also represent the tensile and shear failure characteristics of rocks (Liu et al. 2013; Shirani Faradonbeh and Taheri 2019). The σ_c and σ_t have been used frequently in many strain burst studies as the rock brittleness index (i.e. $B = \sigma_c/\sigma_t$) (Cai 2016) or potential energy of elastic strain (i.e. $PES = \sigma_c^2/2E_u$, where E_u is the unloading modulus) (Wsang and Park 2001) to evaluate the probability of strain burst occurrence and its intensity. Lee et al. (2004) investigated the interrelationship of rock strength parameters (i.e. σ_c and σ_t) and strain burst index (PES) mathematically by conducting the experimental tests on the obtained specimens from a waterway tunnel in Korea, and they proposed a strain burst chart as shown in Fig. 4.2a. In this chart, the bursting intensity is predicted based on the defined four classes of very low (VL), low (L), medium (M), and very high (VH). These classes follow the standard classification assigned for strain burst intensity which is based on visual inspection of the failure, rock ejection, sound and seismicity (Liu et al. 2013; Shirani Faradonbeh et al. 2019). In another study, by plotting the σ_c values against the brittleness index ($B = \sigma_c/\sigma_t$) values, Diederichs (2007) proposed a chart (see Fig. 4.2b) to predict the strain burst risk level. In that study, the low value of B shows the dominance of extension cracking (spalling potential) in the damage process, while the rocks with high σ_c can accumulate more strain energy and

consequently have a higher potential to bursting. In addition, the strength parameters have been used extensively to assess this hazard by different researchers using supervised and unsupervised data-mining algorithms (Pu et al. 2019). On the other hand, the modulus of rigidity is an important parameter to study the stress distribution in the rock mass. Under mining-induced disturbances, some rocks tend to react elastically, while others may show plastic deformation. However, in hard rocks, the elastic characteristics are more dominant. Therefore, they can store a great amount of elastic strain energy. This energy can be released as an excess energy with seismicity in a violent manner (Singh 1987; Shirani Faradonbeh and Taheri 2019; Shirani Faradonbeh et al. 2019; Akdag et al. 2019). Singh (1987) evaluated the relationship between the burst proneness index ($\eta = E_R/E_D$, where E_R and E_D are the retained energy and the dissipated energy during a loading-unloading cycle) and elastic modulus experimentally, and reported that the η increases with the increase of elastic modulus. Hence, the elastic deformation parameters such as elastic modulus and Poisson's ratio can be considered as prominent indicators for strain burst proneness measurement.

As mentioned earlier, the failure mechanisms are highly dependent on intrinsic rock properties, because in deep underground conditions, the rock masses have less discontinuities, and the existing ones cannot freely slide on each other to create structurally controlled failures (i.e. the failure is stress-driven). This is while in the shallow ground (low in-situ stress conditions), the failure process is controlled by the persistence and distribution of natural fractures (discontinuities), i.e. the failure is structure-driven (Kaiser et al. 2000). Therefore, discontinuities do not have a dominant role in the stability of structures. Besides, it is quite easy and convenient to determine intact rock properties such as uniaxial compressive strength (σ_c), tensile strength (σ_t), elastic modulus (E) and Poisson's ratio (ν) compared with other parameters such as in-situ stresses, maximum tangential stress around the openings, etc. The proper measurement of failure mechanisms at the initial stages of the project can aid engineers to optimise the project layout and provide an adequate supporting system to prevent the occurrence of irreparable damages like fatalities, destruction of supporting systems and equipment, as well as the negative impact of such failure types on the economic viability of the project. However, to the best of our knowledge, there is no practical and easy-to-use model to distinguish the failure mechanisms, especially the strain burst and slabbing, and measure the propensity of competent over-stressed rock masses to different failure mechanisms. Due to the non-linearity nature of the failure mechanisms and the complex relationship between the failure mechanisms and their corresponding influential factors, the common linear and non-linear

mathematical models cannot be implemented to unveil the latent relationships between parameters. Hence, soft computing techniques can be assumed as alternative approaches to tackle this difficulty. These techniques learn from the experiences and recognise the patterns in the database automatically (Mitchell 1997). From this perspective, soft computing techniques have been used extensively in mining and geotechnical engineering (Shirani Faradonbeh et al. 2017; Zhou et al. 2018; Haghshenas et al. 2019). In this study, the gene expression programming-based logistic regression (GEP-LR) technique is proposed as a new and practical probabilistic model to measure the propensity of the competent over-stressed rock masses to different failure mechanisms including squeezing, slabbing and strain burst. The intact rock properties (i.e. σ_c, σ_t, E and ν) which can be measured easily by the common laboratory tests are used as indicators for modelling. The methodology and the obtained results are discussed in detail.

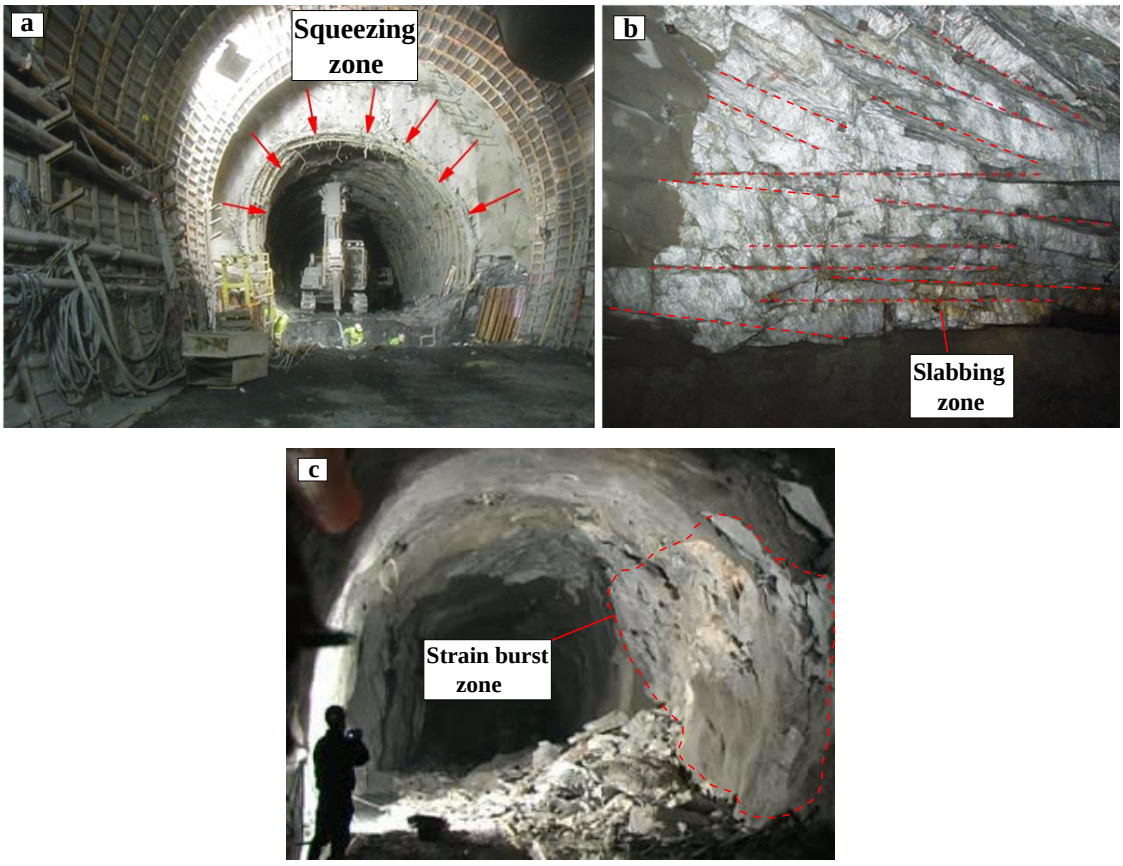

Figure 4.1 Different failure mechanisms in underground excavations: (a) squeezing (modified from Barla et al. 2010), (b) high-stress slabbing (modified from Li et al. 2011) and (c) strain burst (modified from Yan et al. 2012)

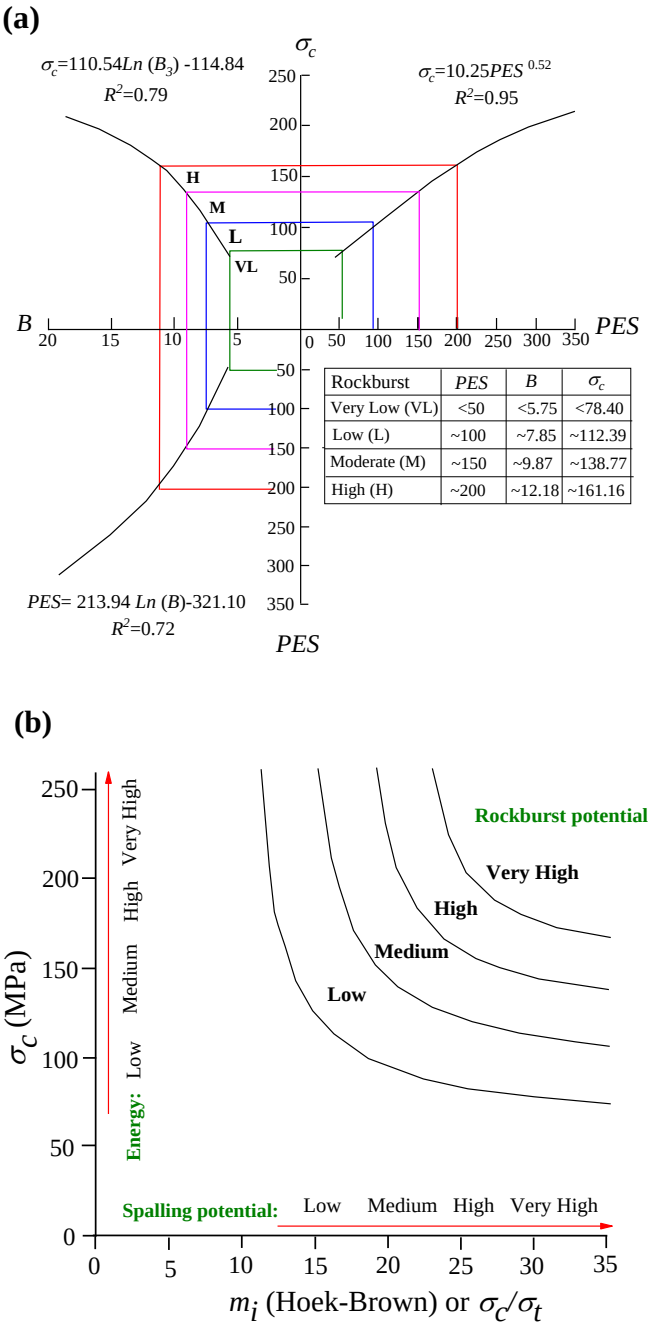

Figure 4.2 Strain burst assessment using intact rock properties: (a) potential of spalling and bursting based on σ_c and σ_t (modified from Lee et al. 2004), and (b) strain burst intensity prediction based on σ_c, B and PES (modified from Diederichs 2007)

4.2. Database

The database (see Table 4.1) used in this study comprises the intact rock properties, i.e. uniaxial compressive strength (σ_c), Brazilian tensile strength (σ_t), elastic modulus (E) and Poisson's ratio (ν) measured experimentally for the rock specimens that are collected from different

underground hard rock mines (mostly in Australia) with the known failure mechanism (Lee et al. 2018). Each dataset corresponds to a specific failure mechanism (i.e. strain burst, slabbing and squeezing) defined based on the in-situ observations of the fracturing process. The definition of these failure mechanisms is as those explained in the previous section. It should be mentioned that this database only covers the intact rock properties for the competent and over-stressed rock masses and does not consider the blocky over-stressed rock masses or the competent rock masses which have not yet been over-stressed (Lee et al. 2018). According to the rock mass classification system developed by Barton et al. (1974) (i.e. the Q-system), the competent rock masses are characterised by $Q > 60$. The results of a minimum of five reliable tests are used for each case study to measure the intact rock properties (Sainsbury and Kurucuk 2019). The σ_c values in Table 4.1 have been normalised using Eq. 4.1 owing to the size-scale dependency of rocks (Lee et al. 2018).

$$\sigma_c = \frac{\sigma_d}{(50/d)^{0.18}} \tag{4.1}$$

where σ_c is the normalised uniaxial compressive strength and σ_d and d are the measured uniaxial compressive strength and the diameter of the tested specimen, respectively.

The σ_t, on the other hand, has been measured using the common Brazilian test method on the specimens having 50 mm diameter. The elastic deformation parameters of E and ν also have been standardised in this database to the mid-third values by considering a minimum of five reliable test results. The box-plot is a common technique to evaluate the distribution of datasets in their range of values using some statistical indices such as minimum value, first quartile (Q_1), second quartile/median (Q_2), third quartile (Q_3) and the maximum value. Fig. 4.3 demonstrates the box-plots for the intact rock properties. As can be seen in this figure, the parameters have a wide range of values, and the datasets for all parameters follow an almost normal distribution. This makes mathematical modelling more feasible and easier.

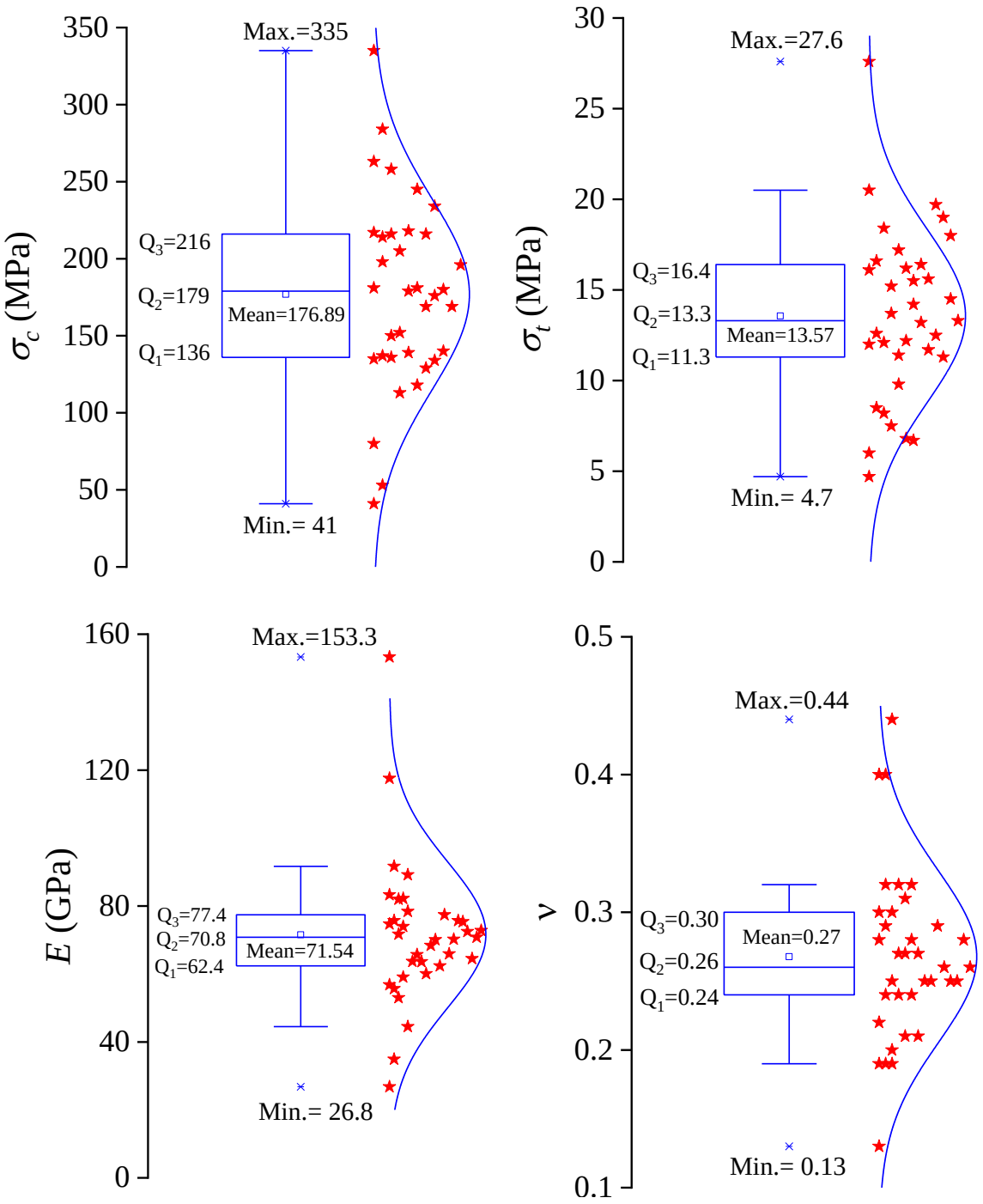

Figure 4.2 Box plots of the intact rock properties and the scatter of datasets around normal distribution curve, *Min*.= minimum value, *Max*.= maximum value, Q1= 1st quartile, Q2= 2nd quartile (median), Q3= 3rd quartile and Mean= average value

Table 4.1 Database used in this study for failure mechanism detection and results of modelling (after Lee et al. 2018)

No.	Rock type	σ_c (MPa)	σ_t (MPa)	E (GPa)	ν	Failure mechanism	Probability value (p)			Predicted class
							Class1	Class2	Class3	
1	Massive sulphide	263	16.1	117.6	0.2	Strain burst (3)	0.000	0.054	1.000	3
2	Massive sulphide	181	12	83.3	0.3	Strain burst (3)	0.000	0.475	0.923	3
3	Massive sulphide	198	16.6	153.3	0.3	Strain burst (3)	0.000	0.006	0.968	3
4	Massive sulphide	150	6	74.7	0.3	Strain burst (3)	0.001	0.001	0.999	3
5	Gabbro	152	12.6	75.7	0.3	Strain burst (3)	0.001	0.007	0.922	3
6	Dolerite	335	18.4	91.7	0.3	Strain burst (3)	0.000	0.067	1.000	3
7	Dolerite	217	12.1	71.7	0.3	Strain burst (3)	0.000	0.407	0.984	3
8	Buck quartz	135	8.5	74	0.1	Strain burst (3)	0.001	0.024	1.000	3
9	Dolerite	214	13.7	82	0.2	Strain burst (3)	0.000	0.006	0.938	3
10	Dolerite	179	11.4	78.4	0.2	Strain burst (3)	0.000	0.002	0.972	3
11	Porphyry	216	15.2	56.8	0.2	Strain burst (3)	0.001	0.293	1.000	3
12	Porphyry	284	27.6	63.7	0.2	Strain burst (3)	0.000	0.000	0.506	3
13	Porphyry	258	12.2	65.7	0.3	Strain burst (3)	0.000	0.202	0.969	3
14	Monzodiorite	137	8.2	55.7	0.3	Strain burst (3)	0.357	0.325	0.992	3
15	Pegmatite	205	7.5	63.6	0.2	Strain burst (3)	0.000	0.215	0.904	3
16	Volcanoclastics	136	17.2	60.1	0.3	Strain burst (3)	0.089	0.493	0.658	3
17	Grit	181	16.2	68.4	0.3	Strain burst (3)	0.001	0.487	0.999	3
18	Basalt	113	9.8	70.1	0.3	Slabbing (2)	0.078	1.000	0.007	2
19	Basalt	169	20.5	62.4	0.4	Slabbing (2)	0.005	1.000	0.029	2
20	Gabbro	139	15.5	77.4	0.3	Slabbing (2)	0.001	0.736	0.020	2
21	Dolerite	176	14.2	65.9	0.3	Slabbing (2)	0.001	0.692	0.048	2
22	Basalt	180	16.4	70.2	0.2	Slabbing (2)	0.000	0.982	0.359	2
23	Basalt	169	15.6	82.2	0.2	Slabbing (2)	0.000	0.570	0.016	2
24	Basalt	196	19.7	75.7	0.2	Slabbing (2)	0.000	1.000	0.013	2
25	Basalt	218	19	89.2	0.3	Slabbing (2)	0.000	0.999	0.014	2
26	Dolerite	245	13.2	75.4	0.3	Slabbing (2)	0.000	0.904	0.211	2
27	Gabbro	216	11.7	72.5	0.3	Slabbing (2)	0.000	0.777	0.486	2
28	Volcanoclastics	118	12.5	64.5	0.2	Slabbing (2)	0.086	1.000	0.000	2
29	Andesite	129	11.3	70.8	0.3	Slabbing (2)	0.010	0.519	0.263	2
30	Meta-sediments	234	18	53	0.3	Slabbing (2)	0.001	0.864	0.173	2
31	Conglomerate	134	14.5	72.8	0.3	Slabbing (2)	0.003	1.000	0.994	2
32	Granite breccia	140	13.3	59.1	0.3	Slabbing (2)	0.081	0.529	0.001	2
33	Ultramafics	80	6.8	26.8	0.4	Squeezing (1)	1.000	0.335	0.001	1
34	Ultramafics	53	6.7	34.9	0.3	Squeezing (1)	1.000	0.290	0.042	1
35	Ultramafics	41	4.7	44.5	0.4	Squeezing (1)	1.000	0.300	0.009	1
Total accuracy of GEP-LR multi-class classifier:										100%

4.3. Methodology and Results

As mentioned earlier, soft computing algorithms, e.g. artificial neural network (ANN) and support vector machine (SVM), have shown promising results in dealing with non-linear problems in different mining and geotechnical projects. However, these techniques suffer from several limitations, such as the necessity for defining the structure of models in advance, getting trapped in the local minimum and the inability to generate the practical prediction equations (Alavi et al. 2016). Therefore, the common soft computing techniques cannot provide practical models for assessing different failure mechanisms in deep underground openings. In this regard, a new hybrid gene expression programming-based logistic regression (GEP-LR) model is proposed in this section to measure the probability of occurrence of the different failure mechanisms in underground hard rock mines as a function of intact rock properties. According to Table 4.1, the parameters of σ_c, σ_t, E and ν are defined as quantitative input/independent parameters, while the failure mechanism as the output/dependent parameter is qualitative, having three types of failure. The dependent parameter does not need to have a normal distribution regarding the independent parameters. For simplicity, the dependent parameter is labelled as "1" in the case of squeezing failure, "2" in the case of slabbing failure, and "3" in the case of strain burst failure (see Table 4.1). The failure mechanisms concerning each independent parameter can be seen in Fig. 4.4. Ideally, to have a simple classification process, every datapoint should belong to a specific failure mechanism. As can be observed in Fig. 4.4, the parameters have some values belonging to more than one class, which means that it is impossible to predict the failure mechanism merely using one of the independent parameters. However, a combination of independent parameters along with a robust multi-class classification technique can be useful for the correct classification of failure mechanisms. The following sections present a description of the GEP algorithm as a robust classifier and the hybridisation process of GEP with logistic regression (LR) to predict the occurrence probability of each failure mechanism.

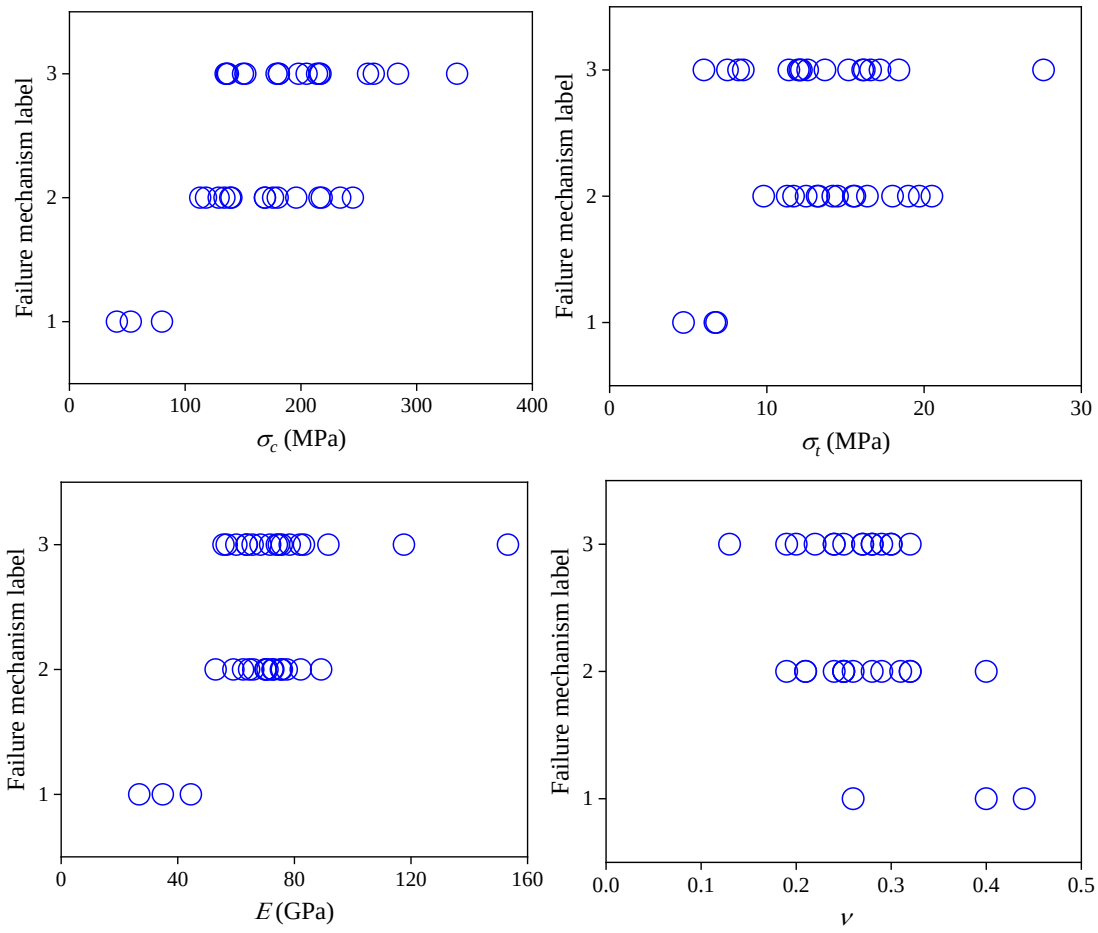

Figure 4.4 Failure mechanism with respect to each independent parameter

4.3.1. GEP-Based Binary Models

As a population-based algorithm, the gene expression programming (GEP) proposed by Ferreira (2002) is a modified and improved version of the basic genetic algorithm (GA) and genetic programming (GP). GEP algorithm opens the black-box nature of the prior soft computing algorithms (e.g. ANN) by providing mathematical equations representing the latent non-linear relationship between the parameters. Due to this significant capability of the GEP algorithm, it has been used recently by different researchers to appraise various mining and geotechnical problems (Armaghani et al. 2016; Jahed Armaghani et al. 2017; Khandelwal et al. 2017; Salimi et al. 2016). In the GEP algorithm, as shown in Fig. 4.5a, the solutions are in the form of linear fixed-length coded strings/chromosomes (single-gene or multiple-gene chromosomes) consisting of two main parts of head and tail in which the genetic operators are applied on these areas to improve the quality of solutions. The head of a chromosome contains symbols representing both terminals (input parameters and constant values) and mathematical functions (e.g. +, -, × and /) and always starts with a function, whereas the tail is composed of only terminals. The head length/size (h) that affects the complexity of the solutions usually is

determined by the user through a trial-and-error procedure. However, the length of the tail (t) is a function of head size and the maximum argument number (n_{max}) and can be determined using the following equation:

$$t = h(n_{max} - 1) + 1 \quad (4.2)$$

Fig. 4.5 schematically displays the foundation of the GEP algorithm. However, the detailed mechanism of GEP can be found in Ferreira (2002). According to Fig. 4.5, the main steps of the GEP modelling procedure can be summarised as follows:

- A population of potential solutions/models initially are generated in the form of linear chromosomes using a random combination of terminals and mathematical functions following the Karva language (a language invented for reading and expressing the information encoded in the chromosomes) (Fig. 4.5a).
- These coded solutions then are automatically parsed into visual tree structures known as expression trees (ETs) (Fig. 4.5b). To do so, for each gene, the first function of the head is selected as the root node, and according to its argument number, some empty sub-nodes are generated. The terminals and functions in the chromosome are then placed in the sub-nodes from top to down and left to right in each line. This process continues until a line containing terminals is formed. As the terminals have no argument, no further sub-nodes are generated. Then, the created sub-ETs for different genes are linked together using a linking function (e.g. "/" in Fig. 4.5b) to form a single large ET. The ETs ease and speed up the process of function finding and mathematical interpretation of coded chromosomes. Thereafter, the mathematical formulation of solutions is extracted for further assessment (Fig. 4.5c).
- The fitness of solutions is evaluated using a fitness function defined by the user (Fig 4.5d), and if the termination criterion (i.e. the maximum number of iteration or a prescribed fitness value) did not meet, the best solutions are selected using the fitness proportionate selection technique (Ferreira 2002) to reproduce with modification (Fig. 4.5e) based on the defined ratios for genetic operators (i.e. mutation, inversion, transposition, and reproduction). As seen in Fig. 4.5f, these operators try to improve the fitness of solutions by changing an element through a gene length (i.e. mutation), inverting a fragment in the head of a gene (i.e. inversion), copying a fragment to the head of a gene (transposition), and exchanging a fragment between two chromosomes

(i.e. recombination). Afterwards, improved solutions are transferred to the next generation (Fig. 4.5g).

- The above process continues until the termination criterion is met.

In this study, firstly, three separate GEP-based binary models are developed to predict the occurrence (i.e. "1") or non-occurrence (i.e. "0") of each class of failure mechanism based on the procedure explained above. GeneXproTools 5.0 computer program is used to develop the GEP models. The intact rock properties of σ_c, σ_t, E and ν are defined as the terminals/input parameters. Furthermore, the computer program is allowed to select up to ten constant values randomly in the range of [-10,10], should the performance of the solutions is improved. Finally, the following comprehensive range of mathematical functions is selected to provide a broader search space for the algorithm, and consequently, generate solutions with higher fitness values:

$$\text{Function set} = \{+, -, \times, /, Exp, Ln, \text{^}2, \text{^}3, Sqrt, 3Rt, Sin, Cos, Tan, Atan\} \quad (4.3)$$

where $Sqrt, 3Rt$ and $Atan$ respectively represent square root, cube root and arctangent.

As shown in Fig. 4.5d, the correlation coefficient (r) is defined as the fitness function to evaluate the performance of the generated solutions. For the classification task, the learning algorithm of the GEP converts the returned value by the evolved model into "1" or "0" using a rounding threshold. If the evolved model's returned value is equal to or greater than the rounding threshold, then the record is classified as "1", "0" otherwise. The correlation coefficient r_i of the solution/model i is calculated as follows:

$$r_i = \frac{Cov(T,P)}{\sigma_t . \sigma_p} \quad (4.4)$$

where $Cov(T,P)$ is the covariance of the target and model outputs; and σ_t and σ_p are the corresponding standard deviations.

As it stands, r_i cannot be used directly as a fitness function since, for the fitness proportionate selection technique, the value of fitness must increase with efficiency. Therefore, the following equation is employed to determine the fitness f_i of a solution i:

$$f_i = 1000 \times r_i \times r_i \quad (4.5)$$

where f_i ranges from 0 to 1000, with 1000 corresponding to the ideal.

Taking into account the previously suggested values (Alavi et al. 2016; Ferreira 2002; Hoseinian et al. 2017) for other GEP parameters, including the population size, the number of

genes for each chromosome, head size, linking function and the genetic operators, several preliminary runs are also performed to find the optimum solution with highest fitness value for each failure mechanism class. The obtained optimum values for the GEP parameters are listed in Table 4.2. By applying these settings to the software, and running the algorithm for 3000 generations/iterations (i.e. the termination criterion), the following optimum GEP-based binary models are achieved:

$$\text{Squeezing} = Y_1 = Ln(E) \times \left(\frac{1}{\sigma_c^2}\right) \times \left(\frac{e^{\sqrt{v}}}{E^3+\sigma_t}\right);$$

$$\text{Failure status} = \begin{cases} 1 & Y_1 \geq 2.2029 \times 10^{-9} \\ 0 & Y_1 < 2.2029 \times 10^{-9} \end{cases} \tag{4.6}$$

$$\text{Slabbing} = Y_2 = \left[tan(E) + \sigma_t - \left(\left(\frac{\sigma_t - 4.1812}{2}\right) \times (v - 3.1256)\right)\right] \times$$

$$\sqrt[3]{\tan\left(\sigma_c^{\frac{1}{6}} - \sqrt[3]{v - \sigma_c - E}\right)} \times [\tan(\sigma_t - 0.6500E + v^3) - v];$$

$$\text{Failure status} = \begin{cases} 1 & Y_1 \geq 8.1788 \\ 0 & Y_1 < 8.1788 \end{cases} \tag{4.7}$$

$$\text{Strain burst} = Y_3 = \sqrt[3]{E + \tan\left(-7.4736v(\sigma_c + \sigma_t)\right)} + \frac{\frac{9.572}{\sigma_t} + \sin(v - E) + \sin(0.2490\sigma_c)}{2} + \sigma_c^{1/9};$$

$$\text{Failure status} = \begin{cases} 1 & Y_1 \geq 6.2353 \\ 0 & Y_1 < 6.2353 \end{cases} \tag{4.8}$$

By calculating the Y-values using input parameters and feeding them to the developed binary classifiers, i.e. Eqs. 4.6 to 4.8, the occurrence/non-occurrence of each failure mechanism can be predicted. However, a multi-class classifier is still needed to determine the most probable failure mechanism based on the given intact rock properties. Indeed, the GEP algorithm has been basically designed for binary classification and cannot be implemented directly for the multi-class classification tasks like failure mechanism detection, which has three classes of squeezing, slabbing and strain burst. This can be defined as a limitation of this algorithm. However, in the next section, an efficient strategy is employed to adapt the GEP algorithm for the multi-class classification task.

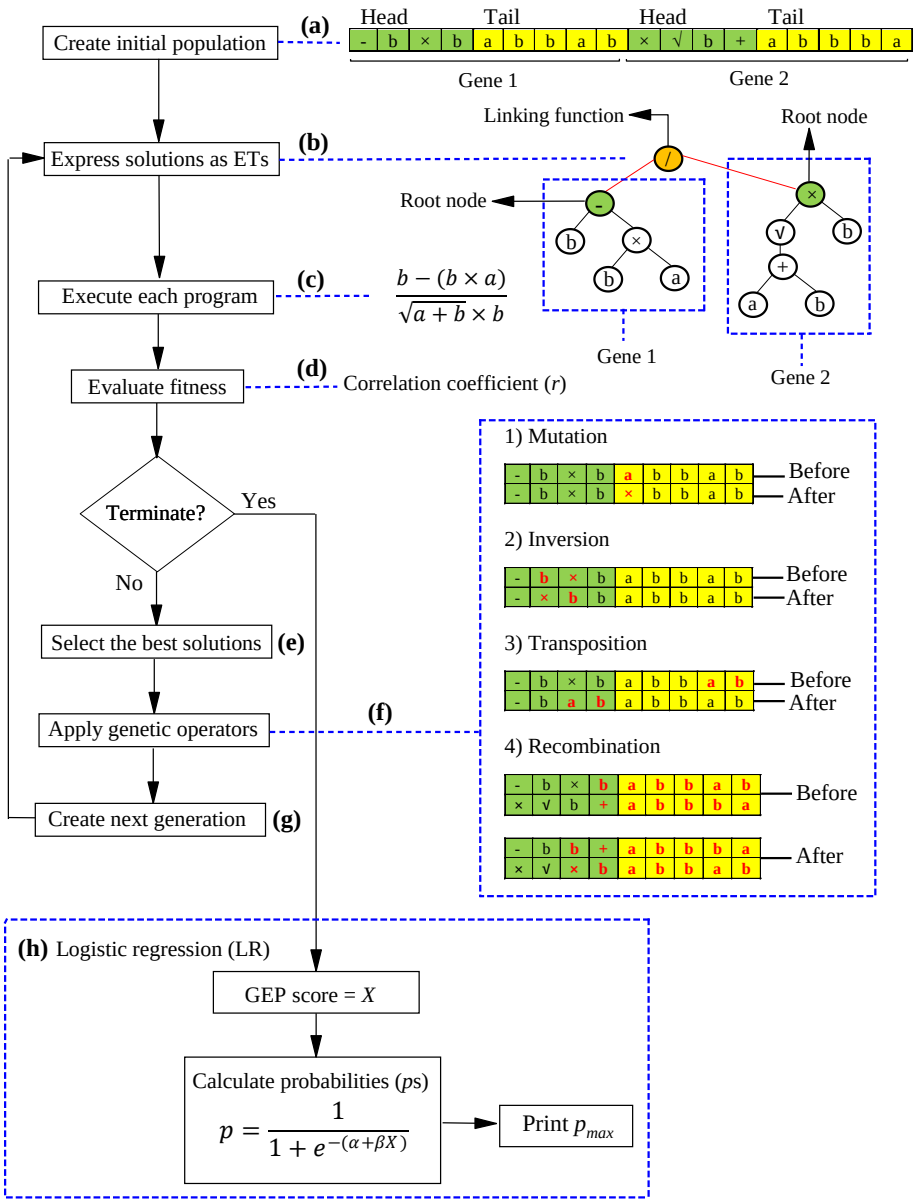

Figure 4.5 The multi-class classification procedure used in this study

Table 4.1 The settings for GEP-based models

Parameter		Setting		
		Squeezing failure	Slabbing failure	Strain burst failure
General	Population size	100	100	85
	Number of genes	3	3	3
	Head size	8	9	9
	Linking function	Multiplication (×)	Multiplication (×)	Addition (+)
	Fitness function	Correlation coefficient	Correlation coefficient	Correlation coefficient
Genetic operators	Mutation rate	0.00138	0.00138	0.00138
	Inversion rate	0.00546	0.00546	0.00546
	Transposition rate	0.00546	0.00546	0.00546
	Recombination rate	0.00277	0.00277	0.00277

4.3.2. Hybrid GEP-LR Models

In this section, for combining the developed binary models and achieve the final output for three different classes, a probabilistic approach based on logistic regression (LR) is linked to the GEP models. The logistic regression is used to assign probabilities to model scores and generate a reliable multi-class classification system (Fig. 4.5h). By calculation of probabilities, the categorical predictions of different failure mechanisms become possible. Logistic regression predicts a $logit$ transformation for the probability of the presence of the dichotomous output parameter based on a linear relationship with a set of input parameters (Youn and Gu 2010). Consider the following failure state for a dataset collected from an underground mine:

$$Y = \begin{cases} 0, & \text{Non} - \text{occurrence} \\ 1, & \text{Occurrence} \end{cases} \tag{4.9}$$

where Y is the binary output of a specific failure mechanism.

If a set of n independent parameters is denoted by the vector $X = (x_1, x_2, \dots, x_n)$, the $p(Y = 1|X)$ is defined as the probability of Y to be 1. The logistic regression of Y on X is defined as follows:

$$\text{logit}(p(Y = 1|X)) = \log\left(\frac{p(Y=1|X)}{1-p(Y=1|X)}\right) = \ln\left(\frac{p(Y=1|X)}{P(Y=0|X)}\right) = \alpha + \beta X \tag{4.10}$$

where $\frac{p(Y=1|X)}{1-p(Y=1|X)}$ is the ratio of the probability of a failure mechanism occurrence over the probability of its non-occurrence. The coefficients of α and β are the intercept and slope of the regression line, respectively.

A rounding threshold (cut-off probability) of 0.5 is usually used to identify the classes of "0" and "1" for each binary model in such a way that if the p values are less than 0.5, they are categorised into "0", while for the p values equal or greater than 0.5, they are categorised into "1". By solving the logistic regression for p, Eq. 4.11 can be obtained for the calculation of the probabilities.

$$p = \frac{1}{1+e^{-(\alpha+\beta X)}} \tag{4.11}$$

As the general logistic regression method explained above is used for the binary classification, and a linear relationship is usually considered for $\alpha + \beta X$ (i.e. $\alpha + \beta_1 X_1 + \beta_2 X_2 + \cdots + \beta_n X_n$), the Eq. 4.11 cannot be solely used in this study for the existing problem. Hence, the developed

GEP model for each failure class is substituted for X in Eq. 4.11. By doing so, the X will be a non-linear combination of the input parameters. In Eq. 4.10, log odds ($\ln\left(\frac{p}{1-p}\right)$) is the main component of the logistic regression which can be used to derive the coefficients of α and β. For this purpose, by defining several quartiles or bins for the model outputs, the distribution of "1s" and "0s" classes is calculated for each bin. The probability of "1s" (p) and "0s" ($1-p$) for each bin is defined, respectively, as the ratio of the number of "1s" to the total number of cases and the ratio of the number of "0s" to the total number of cases. This process is repeated for all bins. Based on the calculated probabilities, the odds ratio and log odds values for all the bins are obtained. Finally, by plotting the log odds values on the y-axis against the model output in the x-axis and performing a weighted linear regression, the intercept (α) and slope (β) of the regression line for each of the models can be easily derived.

In this study, the computer program is adjusted so that the developed GEP-based models in the previous section (i.e. Y_1, Y_2 and Y_3) are linked to the logistic regression algorithm automatically to provide hybrid models. Indeed, each GEP-based model is fed as the independent parameter (i.e. "X") to Eq. 4.11, and finally, the probabilities (ps) are determined for different failure mechanisms. The failure class having a higher probability value is selected as the dominant state (Fig. 4.5h). To make the developed hybrid models easy to use by other researchers, in this study, they are presented as MatLab codes in Table 4.3. In this table, d1, d2, d3 and d4 represent σ_c, σ_t, ν and E, respectively. The component G_iC_j in this table represents the jth randomly generated constant value by the algorithm in the range of [-10, 10] for the ith gene. The logistic regression parameters of intercept (α) and slope (β) are also determined by the algorithm based on the procedure explained above. Fig. 6 shows the binary classifications carried out by each GEP-based model and the variation of measured probability (p) concerning the real class of each observation (dataset). According to Fig. 4.6, it can be seen that during the binary classification of all three failure mechanisms, the observations having similar classes are ordered in separate clusters of "0" and "1" based on the threshold defined for the probability parameter (p) (here is $p = 0.5$). Also, no misclassification of datasets can be seen for squeezing and slabbing failure mechanisms, but only one dataset misclassified as strain burst while it is not strain burst in reality. To have more insights regarding the implementation of the proposed strategy for failure mechanism detection in underground mines, a design example is presented in the following. Considering the values of 135 MPa, 8.5 MPa, 74 GPa, and 0.13, respectively, for σ_c, σ_t, E, and ν (i.e. the dataset No. 8 in Table 4.1), the occurrence probability of each

failure mechanism can be measured using the MatLab codes provided in Table 4.3. The probability of each failure mechanism for this dataset is obtained as follows:

- Probability of class 1 (squeezing failure) $= p_1 = 0.117\%$
- Probability of class 2 (slabbing failure) $= p_2 = 2.395\%$
- Probability of class 3 (strain burst failure) $= p_3 = 99.99\%$

Based on the above p values, in this case, the failure mechanism of strain burst has the highest probability (99.99%), and therefore, class 3 is the predicted class for the given intact rock properties.

Table 4.2 The MatLab codes developed by GEP-LR technique for the failure mechanism detection of competent over-stressed rock masses

Failure mechanism	MATLAB code

Class 1 (Squeezing)	function result = gepModel(d)
	y = 0.0;
	y = reallog(d4);
	y = y * (d1/(d1^3));
	y = y * (exp(realsqrt(d3))/((d4^3)+d2));
	SLOPE = 4934947336.96859;
	INTERCEPT = -10.8714129911233;
	p = 1.0 / (1.0 + exp(-(SLOPE * y + INTERCEPT)));
	result = p;

Class 2 (Slabbing)	function result = gepModel(d)
	G1C5 = 8.05608417004914;
	G1C7 = -4.18124546037172;
	G1C4 = -4.93040132044435;
	G3C1 = -1.53843806268502;
	y = 0.0;
	y = ((tan(d4)+d2)-(((d3-G1C4)-G1C5)*((G1C7+d2)/2.0)));
	y = y * gep3Rt(tan((gep3Rt(realsqrt(d1))-gep3Rt(((d3-d1)-d4)))));
	y = y * (tan((d2+((d4/G3C1)+(d3^3))))-d3);
	SLOPE = 8.31234734032252E-02;
	INTERCEPT = -0.679851333349592;
	p = 1.0 / (1.0 + exp(-(SLOPE * y + INTERCEPT)));
	result = p;
	function result = gep3Rt(x)
	if (x < 0.0),
	  result = -((-x)^(1.0/3.0));
	else
	  result = x^(1.0/3.0);

	end
Class 3 (Strain burst)	function result = gepModel(d)
	G1C2 = -7.47367778557695;
	G2C3 = 9.57225880465376;
	G2C9 = 4.01837214270455;
	y = 0.0;
	y = (gep3Rt(realsqrt((d4+tan((((d2+d1)*(d3*G1C2)))))))^2);
	y = y + ((((G2C3/d2)+sin((d3-d4)))+sin((d1/G2C9)))/2.0);
	y = y + gep3Rt(gep3Rt(d1));
	SLOPE = 8.76302130910031;
	INTERCEPT = -54.6402851913329;
	p = 1.0 / (1.0 + exp(-(SLOPE * y + INTERCEPT)));
	result = p;
	function result = gep3Rt(x)
	if (x < 0.0),
	result = -((-x)^(1.0/3.0));
	else
	result = x^(1.0/3.0);
	end

(a)

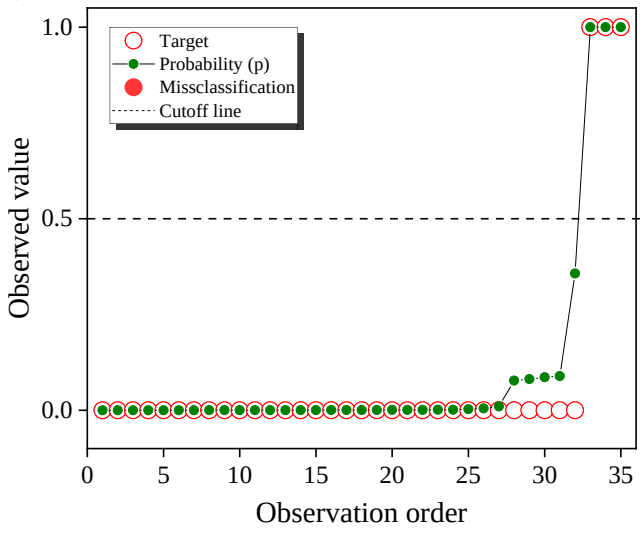

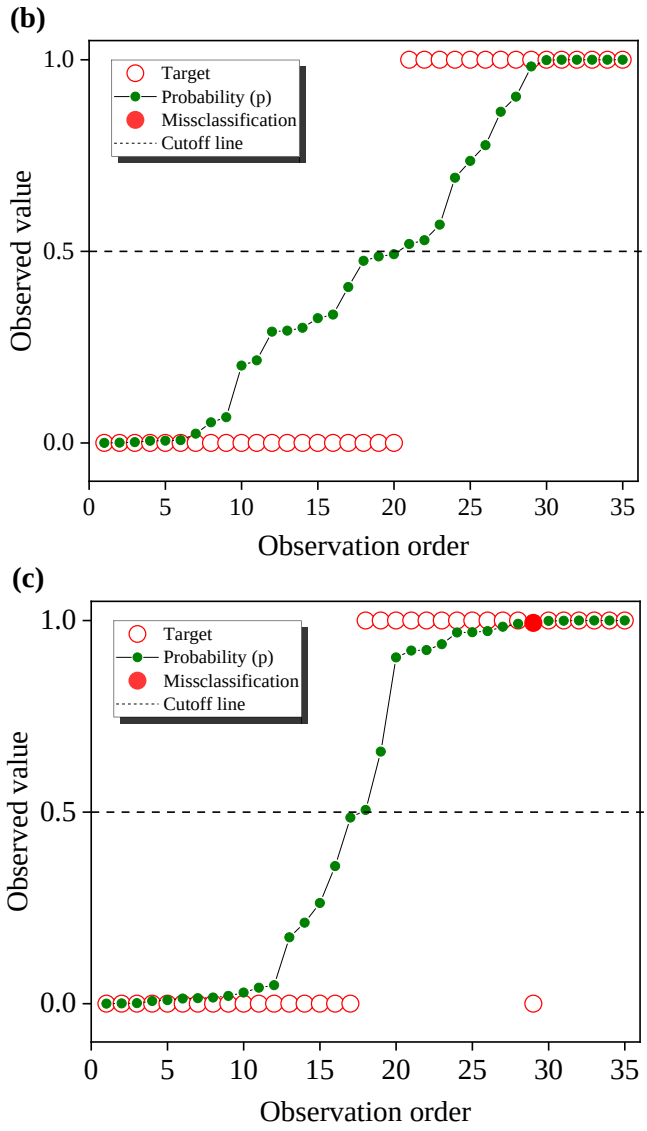

Figure 4.6 Binary classification of (a) squeezing, (b) slabbing and (c) strain burst by GEP-LR technique

4.3.3. Performance of the Developed GEP-LR Model

It is required to evaluate the performance of the developed multi-class classifier. For this, the confusion matrices initially are calculated for binary GEP-based models of each failure mechanism. The confusion matrix is a useful tool that contains information concerning the real and predicted classifications (Fawcett 2006). In a confusion matrix, if the actual output is positive (e.g. strain burst) and it is classified as positive by the classifier, it is named as true positive (TP). In contrast, if it is classified as negative (i.e. non-strain burst), it is named as false negative (FN). On the other hand, if the real output is negative and the classifier detects it as a negative, it is named true negative (TN), while if it is classified as positive, it is named false positive (FP). Another measure for assessing a classifier is the receiver operating

characteristic (ROC) curve. The ROC curve is an illustrative method that shows the diagnostic ability of a binary classifier model as its threshold (cut-off) value is changed (Metz 1978). This curve can be obtained by plotting the true positive rate (i.e. $TPR = \frac{TP}{TP+FN}$) against the false positive rate (i.e. $FPR = \frac{FP}{FP+TN}$). The classifier having no discrimination ability or with the area under the curve (AUC) equal to 0.5 produces a ROC curve that follows the diagonal line of 45° (random classification), whereas for a perfect classification, the ROC curve follows the left hand and top axes of the unit square with $TPR = 1$, $FPR = 0$, and $AUC = 1$ (Fawcett 2006). The results of confusion matrices and ROC curves for all three GEP-LR models are shown in Table 4.4 and Fig. 4.7, respectively. Clearly can be seen from Table 4.4 that the whole datasets relating to the squeezing failure (i.e. TP $= 3$) and slabbing failure (i.e. TP $= 15$) are correctly classified/predicted (i.e. 100% accuracy) by the GEP-LR models without having any misclassified dataset (i.e. FP $=$ FN $= 0$). On the other hand, out of a total of 35 datasets, 17 cases of strain burst failure mechanism are correctly classified (i.e. 97.14% accuracy), and only one case is incorrectly classified as strain burst while it is not, as shown in Fig. 4.6c. In Figure 4.7, all ROC curves are in the upper triangle area showing no random classification. Figure 4.7 also proves the perfect classification of the GEP-LR technique for categorising the class 1 (i.e. squeezing) and class 2 (i.e. slabbing) failure mechanisms datasets as their ROC curves pass through $(0,1)$ coordinate with $AUC = 1$. However, the $AUC = 0.964$ is obtained for the third GEP-LR model which represents an outstanding discrimination ability according to Hosmer Jr et al. (2013). To check the total performance of the proposed GEP-LR multi-class classifier, the probabilities (ps) are calculated for all 35 datasets based on the MatLab codes given in Table 4.3 for each failure mechanism. The results can be seen in Table 4.1. By applying the $argmax$ function to the obtained probabilities, the class having a higher probability is chosen as the predicted output (class). The comparison of the real failure mechanisms and the predicted ones shows that although a single misclassification happened in the binary classification of the strain burst failure mechanism, the proposed multi-class classifier can predict the final output with 100% accuracy, as shown schematically in Fig. 4.8.

Table 4.4 Confusion matrices of the GEP-LR models for each failure mechanism

Squeezing mode (class1)		Predicted class	
		Yes	No
Actual class	Yes	3 (TP)	0 (FN)
	No	0 (FP)	32 (TN)
Slabbing mode (class 2)		**Predicted class**	
		Yes	No
Actual class	Yes	15 (TP)	0 (FN)
	No	0 (FP)	20 (TN)
Strain burst mode (class 3)		**Predicted class**	
		Yes	No
Actual class	Yes	17 (TP)	0 (FN)
	No	1 (FP)	17 (TN)

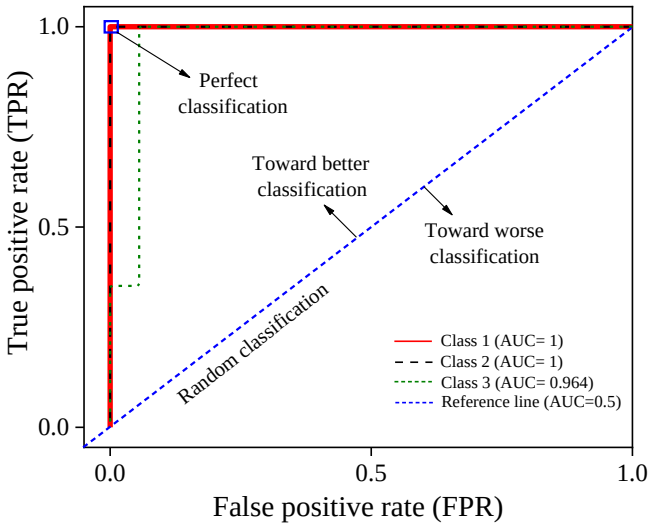

Figure 4.7 The ROC curves for three GEP-LR models

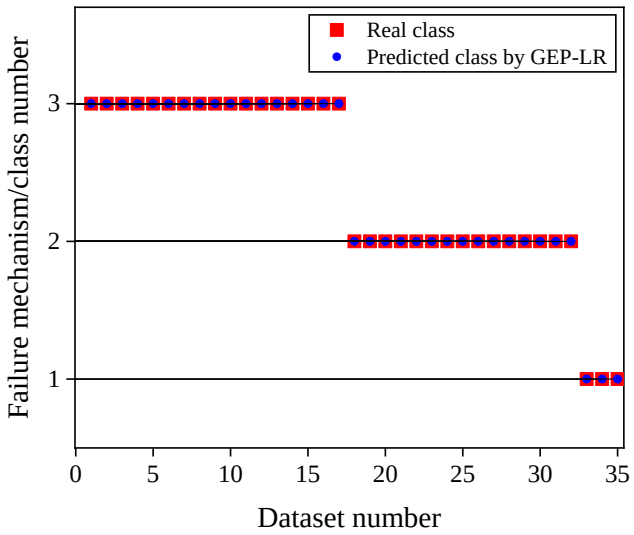

Figure 4.8 The comparison of the real and predicted failure mechanisms

4.3.4. Model Validation

To further assess the validity of the proposed hybrid model in distinguishing different failure mechanisms, nine unseen/new sets of intact rock properties are extracted from different studies with known failure states (see Table 4.5). Table 4.5 illustrates the rock types, the intact rock properties and the corresponding failure mechanisms for these datasets. The GEP scores are initially calculated using Eqs. 4.6 to 4.8, and then, the occurrence probability (p) of each failure mechanism/class is determined based on the hybrid models/ probabilistic approaches presented in Table 4.3. The obtained p values are listed in Table 4.5. As discussed earlier, the class having the highest probability is selected as the predicted class by this multi-class classifier. As seen in Table 4.5, the failure mechanism of all nine new datasets is correctly predicted by the developed hybrid model (i.e. the prediction accuracy is 100%), which is consistent with the results obtained in the previous section. These results along with those obtained in section 4.3.3, prove the high performance and robustness of the proposed technique in this study for assessing such a complex non-linear geotechnical problem (i.e. failure mechanism detection).

Table 4.5 The results of the hybrid model validation

Reference	Rock type	σ_c (MPa)	σ_t (MPa)	E (GPa)	ν	Failure mechanism	Probability value (p)			Predicted class
							Class1	Class2	Class3	
Wang et al. (2020)	Granite	126.2	7.6	69.6	0.2	Strain burst (3)	0.009	0.404	0.750	3
Wang et al. (2020)	Marble	129.2	6.2	72.8	0.2	Strain burst (3)	0.003	0.494	0.999	3
Li et al. (2011)	Granite	203.3	8.3	51.7	0.2	Slabbing (2)	0.004	0.478	0.035	2
Li et al. (2011)	Granite	184.2	8.3	57.6	0.2	Slabbing (2)	0.002	0.759	0.455	2
Kang et al. (2021)	Sandstone	91	6.9	21.2	0.2	Squeezing (1)	1	0.212	0.000	1
Kang et al. (2021)	Mudstone	37.7	3.7	14.7	0.2	Squeezing (1)	1	0.331	0.000	1
Yassaghi and Salari-Rad (2005)	Tuff	95	11.1	11.4	0.3	Squeezing (1)	1	0.447	0.000	1
Yassaghi and Salari-Rad (2005)	Andesitic-Basaltic	110	13.5	19.7	0.2	Squeezing (1)	1	0.721	0.018	1
Bilgin and Algan (2012)	Metadetritic rocks	48.5	3.2	20.5	0.3	Squeezing (1)	1	0.239	0.000	1

4.4. Discussion

The strategy of hybridising the gene expression programming (GEP) and the logistic regression (LR) is used for the first time in mining and geotechnical engineering as a multi-class classifier for the prediction of failure mechanism in underground mines. As discussed in the previous sections, the proposed GEP-LR model shows high performance in distinguishing the three types of failure; however, several issues should be addressed in future studies. Firstly, in this study, the GEP-LR multi-class classifier developed based on a database limited to 35 case studies related to the over-stressed competent rock masses. At the same time, the functionality of the machine learning algorithms relies on the data size. Therefore, due to the flexibility and applicability of the proposed model in this study, it is highly recommended to update the model with a bigger database that can be obtained in the future. Secondly, the database provided in this study is not balanced in terms of the number of classes for each failure mechanism. As shown in Table 4.1, the current database, respectively, has 17, 15, and 3 datasets for strain burst, slabbing, and squeezing failure mechanisms. The reliability and generality of the model can be improved by providing an equal number of datasets for all failure mechanisms/classes, especially for squeezing, which has only 3 cases in this study. Considering the foregoing issues into account, the proposed model in this study should be used as a tool for preliminary assessment of failure mechanism in underground projects. Consequently, the required arrangements can be considered for the long-term stability of the underground projects based on the predicted output.

4.5. Conclusions

In this study, a novel hybrid system combining the gene expression programming (GEP) and the logistic regression (LR) techniques is presented for measuring the occurrence probability of three failure mechanisms (i.e. squeezing, slabbing and strain burst) based on intact rock properties for competent over-stressed rock masses. This database includes the parameters of σ_c, σ_t, E, and ν as the independent (input) parameters for modelling, while the dependent (output) parameter is the failure mechanism. The GEP algorithm is a robust technique for function finding, especially for high-complex non-linear tasks like failure mechanism detection in underground mining and geotechnical projects. The initial assessment of the original database (Fig. 4.4) shows that the failure mechanisms cannot be predicted solely by a single indicator because some of their values belong to more than one class, which shows the necessity of the application of robust non-linear techniques to deal with such complex multi-class

classification problems. To do so, three separate models are developed using the GEP algorithm to predict the occurrence or non-occurrence of each failure mechanism. Since the original GEP algorithm can implement the classification aim just in binary condition, it is not possible to predict the final failure mechanism. A probabilistic approach is linked to the developed GEP models for measuring the probability (p) of occurrence of each failure mechanism, which can solve this problem. Therefore, the obtained GEP scores are fed to the general logistic regression equation (Eq. 4.11) to calculate the probabilities. The class which has the highest p-value is selected as the final prediction. The failure mechanism prediction models are presented as MatLab codes for future applications as well as for optimization purposes. The performance analysis of the GEP-based binary models for each failure mechanism using the confusion matrices (Table 4.4) and ROC curves (Fig. 4.7) shows that the GEP models can predict the occurrence or non-occurrence of each failure mechanism, respectively, with 100% (AUC=1), 100% (AUC=1), and 97.14% (AUC=0.964) accuracy for squeezing, slabbing and strain bursting failure. Also, total accuracy of 100% is obtained for the multi-class classifier (GEP-LR model) by comparing the predicted failure mechanisms with those measured by the engineers in underground mines (Table 4.1). The obtained values for the performance indices show the high capability and robustness of the proposed model as a practical tool for preliminary assessment of the failure mechanism for over-stressed rock masses. The results obtained from the model validation using the nine unseen/new datasets compiled from different studies also proved the robustness of the proposed model. However, the model's reliability and generality can be improved by updating the GEP-LR model using a more comprehensive database in futures studies.

Acknowledgements

The first author would like to acknowledge the University of Adelaide for providing the research fund (Beacon of Enlightenment PhD Scholarship) and modelling facilities to conduct this research.

References

Akdag S, Karakus M, Taheri A, Nguyen G, Manchao H (2018) Effects of Thermal Damage on Strain Burst Mechanism for Brittle Rocks Under True-Triaxial Loading Conditions. *Rock Mechanics and Rock Engineering* 51(6):1657–1682

Akdag S, Karakus M, Nguyen GD, Taheri A, Bruning T (2019) Evaluation of the propensity of strain burst in brittle granite based on post-peak energy analysis. *Underground Space*

Alavi AH, Gandomi AH (2011) A robust data mining approach for formulation of geotechnical engineering systems. *Engineering Computations* (Swansea, Wales) 28:242–274

Armaghani DJ, Faradonbeh RS, Rezaei H, et al (2016) Settlement prediction of the rock-socketed piles through a new technique based on gene expression programming. *Neural Computing and Applications* 29(11), 1115-1125

Aydan Ö, Akagi T, Kawamoto T (1993) The squeezing potential of rocks around tunnels; theory and prediction. *Rock mechanics and rock engineering* 26(2), 137–163

Barla G (1995) Squeezing rocks in tunnels. *ISRM News Journal* 2(3), 44–49

Barla G, Bonini M, Debernardi D (2010) Time dependent deformations in squeezing tunnels. *ISSMGE International Journal of Geoengineering Case Histories* 2(1), 40–65

Barla G, Bonini M, Semeraro M (2011) Analysis of the behaviour of a yield-control support system in squeezing rock. *Tunnelling and Underground Space Technology* 26(1), 146–154

Barton N, Lien R, Lunde J (1974) Engineering classification of rock masses for the design of tunnel support. *Rock Mechanics Felsmechanik Mécanique des Roches* 6(4), 189–236

Bilgin N, Algan M (2012) The performance of a TBM in a squeezing ground at Uluabat, Turkey. *Tunnelling and Underground Space Technology* 32, 58-65

Cai M (2008) Influence of intermediate principal stress on rock fracturing and strength near excavation boundaries—Insight from numerical modeling. *International Journal of Rock Mechanics and Mining Sciences* 8(2), 204–211

Diederichs M (2007) The 2003 Canadian Geotechnical Colloquium: Mechanistic interpretation and practical application of damage and spalling prediction criteria for deep tunneling. *Canadian Geotechnical Journal* 44(9), 1082–1116

Fairhurst C, Cook NGW (1966) The phenomenon of rock splitting parallel to the direction of maximum compression in the neighborhood of a surface. In: Proceedings of the first congress on the international society of rock mechanics. *International Society of Rock Mechanics Lisbon*, pp 687–692

Fawcett T (2006) An introduction to ROC analysis. *Pattern recognition letters* 27(8), 861–874

Ferreira C (2002) Gene Expression Programming in Problem Solving. In: Roy R, Köppen M, Ovaska S, et al. (eds) Soft Computing and Industry: Recent Applications. *Springer London*, London, pp 635–653

Haghshenas SS, Shirani Faradonbeh R, Mikaeil R, Haghshenas SS, Taheri A, Saghatforoush A, Dormishi A (2019) A new conventional criterion for the performance evaluation of gang saw machines. *Measurement*. 146, 159-170

Hoek E, Brown ET (1980) Underground Excavations in Rock. *Institution of Mining and Metallurgy*, London

Hoseinian FS, Faradonbeh RS, Abdollahzadeh A, et al (2017) Semi-autogenous mill power model development using gene expression programming. *Powder Technology* 308, 61-69

Jahed Armaghani D, Faradonbeh RS, Momeni E, et al (2017) Performance prediction of tunnel boring machine through developing a gene expression programming equation. *Engineering with Computers* 34(1), 129-141

Kabwe E, Karakus M, Chanda EK (2020) Isotropic damage constitutive model for time-dependent behaviour of tunnels in squeezing ground. *Computers and Geotechnics* 127, 103738

Kabwe E, Karakus M, Chanda EK (2020) Time-dependent solution for non-circular tunnels considering the elasto-viscoplastic rockmass. *International Journal of Rock Mechanics and Mining Sciences* 133, 104395

Kaiser PK, Diederichs MS, Martin CD, Sharp J, Steiner W (2000) Underground works in hard rock tunnelling and mining. In ISRM international symposium. *International Society for Rock Mechanics and Rock Engineering*

Kang H, Jiang P, Wu Y, Gao F (2021) A combined “ground support-rock modification-destressing” strategy for 1000-m deep roadways in extreme squeezing ground condition. *International Journal of Rock Mechanics and Mining Sciences* 142, p.104746

Khandelwal M, Mahdiyar A, Armaghani DJ, et al (2017) An expert system based on hybrid ICA-ANN technique to estimate macerals contents of Indian coals. *Environmental Earth Sciences* 76(11), 1-14

Lee M, Penney A, Sainsbury BL (2018) Proneness of competent over-stressed intact rock to violent fracturing. In: AusRock 2018: Fourth Australasian Ground Control In Mining Conference. *Australian Institute of Mining and Metallurgy* pp. 170–184

Lee SM, Park BS, Lee SW (2004) Analysis of rockbursts that have occurred in a waterway tunnel in Korea. *International Journal of Rock Mechanics and Mining Sciences* 41, 911–916

Li D, Li CC, Li X (2011) Influence of sample height-to-width ratios on failure mode for rectangular prism samples of hard rock loaded in uniaxial compression. *Rock Mechanics and Rock Engineering* 44(3), 253–267

Li G, Ma F, Guo J, et al (2020) Study on deformation failure mechanism and support technology of deep soft rock roadway. *Engineering Geology* 264, 105262

Liu Z, Shao J, Xu W, Meng Y (2013) Prediction of rock burst classification using the technique of cloud models with attribution weight. *Natural Hazards* 68(2), 549–568

Metz CE (1978) Basic principles of ROC analysis. In: Seminars in nuclear medicine. *WB Saunders*, pp. 283–298

Mitchell, T.M., 1997. Does machine learning really work? *AI Magazine* 18(3), 11–20

Munoz H, Taheri A, Chanda EK (2016) Fracture Energy-Based Brittleness Index Development and Brittleness Quantification by Pre-peak Strength Parameters in Rock Uniaxial Compression. *Rock Mechanics and Rock Engineering* 49(12):4587–4606

Munoz H, Taheri A (2017) Specimen aspect ratio and progressive field-strain pattern development of sandstone under uniaxial compression by 3D Digital Image Correlation. J. *Rock Mechanics and Geotechnical Engineering* 9(4): 599-610

Ortlepp WD (2001) The behaviour of tunnels at great depth under large static and dynamic pressures. *Tunnelling and Underground Space Technology* 16(1), 41–48

Ortlepp WD (1997) Rock fracture and rockbursts: an illustrative study. *South African Institute of Mining and Metallurgy*

Palmstrom A, Stille H (2007) Ground behaviour and rock engineering tools for underground excavations. *Tunnelling and Underground Space Technology* 22(4), 363–376

Pu Y, Apel DB, Liu V, Mitri H (2019) Machine learning methods for rockburst prediction-state-of-the-art review. *International Journal of Mining Science and Technology* 29(4), 565–570

Saadat M, Taheri A (2020) Effect of contributing parameters on the behaviour of a bolted rock joint subjected to combined pull-and-shear loading: A DEM approach, *Rock Mechanics and Rock Engineering* 53(1), 383-409

Sainsbury BA, Kurucuk N (2019) Impact of intact rock properties on proneness to rockbursting. *Bulletin of Engineering Geology and the Environment* 79, 1939-1946

Salimi A, Faradonbeh RS, Monjezi M, Moormann C (2016) TBM performance estimation using a classification and regression tree (CART) technique. *Bulletin of Engineering Geology and the Environment* 77(1), 429-440

Shirani Faradonbeh R, Salimi A, Monjezi M, Ebrahimabadi A, Moormann C (2017) Roadheader performance prediction using genetic programming (GP) and gene expression programming (GEP) techniques. *Environmental Earth Sciences* 76(16), 1-12

Shirani Faradonbeh R, Shaffiee Haghshenas S, Taheri A, Mikaeil R (2020) Application of self-organizing map and fuzzy c-mean techniques for rockburst clustering in deep underground projects. *Neural Computing and Applications* 32(12), 8545-8559

Shirani Faradonbeh, R., Taheri, A., 2019. Long-term prediction of rockburst hazard in deep underground openings using three robust data mining techniques. *Engineering with Computers* 35(2), 659–675

Shirani Faradonbeh R, Taheri A, Sousa LR, Karakus M (2020) Rockburst assessment in deep geotechnical conditions using true-triaxial tests and data-driven approaches. *International Journal of Rock Mechanics and Mining Sciences* 128, 104279

Shirani Faradonbeh, R., Taheri, A., Karakus, M., 2021. Post-peak behaviour of rocks under cyclic loading using a double-criteria damage-controlled test method. *Bulletin of Engineering Geology and the Environment* 80(2), 1713-27

Singh SP (1987) The influence of rock properties on the occurrence and control of rockbursts. *Mining Science and Technology* 5(1), 11–18

Wagner, H., 2019. Deep Mining: A Rock Engineering Challenge. *Rock Mechanics and Rock Engineering* 52(5), 1417-1446

Wang, J.-A., Park, H.D., 2001. Comprehensive prediction of rockburst based on analysis of strain energy in rocks. *Tunnelling and Underground Space Technology* 16(1), 49–57

Wang S, Huang L, Li X (2020) Analysis of rockburst triggered by hard rock fragmentation using a conical pick under high uniaxial stress. *Tunnelling and Underground Space Technology* 96, 103195

Yan, P., Lu, W., Chen, M., Shan, Z., Chen, X., Zhou, Y., 2012. Damage-free coring technique for rock mass under high in-situ stresses. *Journal of Rock Mechanics and Geotechnical Engineering* 4(1), 44–53

Yassaghi A, Salari-Rad H (2005) Squeezing rock conditions at an igneous contact zone in the Taloun tunnels, Tehran-Shomal freeway, Iran: a case study. *International Journal of Rock Mechanics and Mining Sciences* 42(1), 95-108

Youn, H., Gu, Z., 2010. Predicting Korean lodging firm failures: An artificial neural network model along with a logistic regression model. *International Journal of Hospitality Management* 29, 120–127

Zhou, J., Li, X., Mitri, H.S., 2018. Evaluation method of rockburst: State-of-the-art literature review. *Tunnelling and Underground Space Technology* 81, 632–659

Statement of Authorship

Title of Paper	Rockburst assessment in deep geotechnical conditions using true-triaxial tests and data-driven approaches
Publication Status	☑ Published ☐ Accepted for Publication ☐ Submitted for Publication ☐ Unpublished and Unsubmitted work written in manuscript style
Publication Details	**Shirani Faradonbeh R**, Taheri A, Ribeiro Sousa L, Karakus M (2020) Rockburst assessment in deep geotechnical conditions using true-triaxial tests and data-driven approaches. *International Journal of Rock Mechanics and Mining Sciences* 128:104279

Principal Author

Name of Principal Author (Candidate)	Roohollah Shirani Faradonbeh		
Contribution to the Paper	Literature review and database preparation, statistical analysis, development of models and preparation of the manuscript		
Overall percentage (%)	80%		
Certification:	This paper reports on original research I conducted during the period of my Higher Degree by Research candidature and is not subject to any obligations or contractual agreements with a third party that would constrain its inclusion in this thesis. I am the primary author of this paper.		
Signature		Date	17 June 2021

Co-Author Contributions

By signing the Statement of Authorship, each author certifies that:

i. the candidate's stated contribution to the publication is accurate (as detailed above);
ii. permission is granted for the candidate in include the publication in the thesis; and
iii. the sum of all co-author contributions is equal to 100% less the candidate's stated contribution.

Name of Co-Author	Abbas Taheri		
Contribution to the Paper	Research supervision, review and revision of the manuscript		
Signature		Date	21 June 2021

Name of Co-Author	Luis Ribeiro e Sousa		
Contribution to the Paper	Database preparation and review of the manuscript		
Signature		Date	21 June 2021

Name of Co-Author	Murat Karakus		
Contribution to the Paper	Review and revision of the manuscript		
Signature		Date	21 June 2021

Chapter 5

Rockburst Assessment in Deep Geotechnical Conditions using True-Triaxial Tests and Data-Driven Approaches

Abstract

Deep underground excavations in mining and civil engineering are subjected to high in-situ stresses which can cause rockburst. Rockburst is an instantaneous release of a large amount of strain energy stored in rockmass that can lead to injuries, deaths, and damage to infrastructures. Many studies have been done regarding rockburst, however, there is no practical model to predict the stress level that rockburst occurs (i.e. maximum rockburst stress) and its related risk (i.e. rockburst risk index) based on real rockburst tests, and the main rock mechanical properties. In this study, a comprehensive database of true-triaxial unloading tests on rocks having a wide range of properties was compiled. The agglomerative hierarchical clustering (AHC) analysis was carried out on the original database to evaluate the presence of natural groups and outliers. Then, the stepwise selection and elimination (SSE) procedure were employed for dimension reduction of the problem and identifying the most influential attributes on rockburst parameters. Afterward, two robust non-linear algorithms, including gene expression programming (GEP) and classification and regression tree (CART) were used to develop the predictive models for rockburst maximum stress and its risk index. The validation verification of the proposed models using several indices proved the high prediction performance of the developed non-linear models. Finally, a parametric analysis was carried out to evaluate the influence of each input parameter on the corresponding output. The proposed models in this study are practical and do not require any presupposition about rockburst mechanism, which makes them be used easily in practice by engineers at the design and progress stages of the underground projects.

Keywords: Rockburst maximum stress, Rockburst risk index, True-triaxial test, Gene expression programming, Classification and regression tree

5.1. Introduction

Deep underground conditions can be characterised by the high level of in-situ stresses, high groundwater pressure, high temperature, and high brittleness of rocks (Jian et al. 2012; Ranjith et al. 2017). Consequently, the deep underground activities such as mining and tunnelling are usually subjected to different nature-induced hazards during and after their closure. One of them is related to seismic events (Feng 2017). When the deviatoric stress either in the confined rock mass or near an excavation reaches to the confined or unconfined rock mass strength, the seismic events are occurred and may lead to unstable failure by a shear slip or shear rupture. The radiated energy may then damage the excavation and cause rockburst damage (Cai and Kaiser 2018). Rockburst is the most severe disaster that threatens the safety of mining operation and the stability of the excavation surface. Rockburst can be defined as a dynamic instability phenomenon of the surrounding rock mass of an underground opening in the highly-stressed zone that is accompanied by a violent release of strain energy stored in the rock mass (Zhou et al. 2018). Rockbursts can occur either during the excavation (are known as strainbursts) or after excavation (are known as impact-induced or delayed rockbursts) based on the triggering factors in the form of a strip of rock slices, rock fall, ejection of rock fragments, with roaring sound (Feng 2017; He et al. 2018). Due to the violent and unexpected nature of this phenomenon, it may lead to worker injury, damage to mine infrastructure and equipment, and possibly economic loss of underground excavation (see Fig. 5.1) (Li et al. 2007; He et al. 2017; Weng et al. 2017). Many factors including the rock mechanical properties, excavation geometry, discontinuities, in-situ and mining-induced stresses, and construction method, may affect the rockburst triggering (Sousa 2010). Hence, rockburst prediction and mitigation are one of the most challenging problems in rock engineering. In last decades, a considerable investigation has been carried out on rockburst to understand more about its mechanism, prediction, and controlling methods theoretically and experimentally (Jian et al. 2012; He et al. 2018). In terms of rockburst mechanism, many theories such as the energy theory, the strength theory, the burst liability theory, the bifurcation theory, and the chaos theory have been proposed by researchers to study the strain localisation and the stability of the rock mass (Shi et al. 2010; Tang et al. 2010; Jian et al. 2012).

From the viewpoint of rockburst prediction, more than 100 empirical criteria have been proposed by scholars mostly based on strength, strain, and strain energy parameters. Moreover, novel and robust data-mining techniques including the supervised and unsupervised algorithms have been used recently by researchers to predict both the rockburst occurrence (as a binary

problem) and its intensity (as a four-class problem) (Zhou et al. 2018; Shirani Faradonbeh and Taheri 2019). In terms of rockburst control, several techniques such as the application of energy-absorbing bolts (He et al. 2014), ground preconditioning (e.g. destress drilling, destress blasting, water injection), and alternative mining methods (e.g. pillarless mining and mining with sacrifice galleries) have been suggested as the potential solutions for rockburst mitigation (Saharan and Mitri 2011). Rockburst also has been investigated by laboratory tests since these tests can provide useful information about rockburst mechanism, the influence of different parameters on bursting behaviour, calibrating the numerical models, and identifying the stress state prone to severe failure (He et al. 2015, 2018). Many attempts have been made by different researchers to simplify the process of failure using conventional testing methods including uniaxial and biaxial compression tests (Cook 1963; Singh 1987; Barquins and Petit 1992; Linkov 1996; Wang and Park 2001), dynamic uniaxial compression tests (Wang and Park 2001; Bagde and Petroš 2005), triaxial compression unloading tests (Wang and Huang 1998; Xu 2003; Chen and Su 2010) as well as the true-compression triaxial tests (Cheon et al. 2006; Chen and Su 2010; Su et al. 2017a; Wang et al. 2019).

Despite the many excellent efforts made so far, the common testing methods cannot properly simulate the stress state of the rock mass where rockburst occurs. As a matter of fact, rockburst usually occurs near the excavated boundary while the stress state after the excavation is transformed from a triaxial equilibrium state ($\sigma_1 > \sigma_2 > \sigma_3$) to a newly redistributed state ($\sigma_3 \approx 0, \sigma_1 \neq 0, \sigma_2 \neq 0$). In this new state, the tangential stress (σ_θ) increases progressively and may reach the ultimate strength of the rock element and rockburst may occur (see Fig. 5.2). More recently, a modified true-triaxial testing system was introduced by He et al. (2010) which can unload the pressure on one surface of the rock sample and replicate the stress concentration in the surrounding rock mass of the free face and measure the released kinetic energy during bursting. This apparatus consists of several main components including the main hydraulic loading and unloading system, a data acquisition system that continuously records the changes in forces and displacements, the high-speed cameras for measuring the kinetic energy of the ejected rock fragments during bursting, an acoustic emission (AE) system to track the process of damage accumulation during the test, and an infrared monitoring system to measure surface temperature of the sample and inspect the internal damage (He et al. 2012, 2015). In true-triaxial testing apparatus as can be seen from Fig. 5.3, the loads are applied simultaneously to the prismatic specimen in all three principal stress directions to reach a pre-defined in-situ stress state, and the loads are kept constant on the specimen for a while to achieve a uniform

stress distribution in the specimen. Finally, the platen is removed abruptly from one surface of the sample that is subjected to radial stress (σ_3) while the axial stress (σ_2) is held constant and σ_1 is increased gradually until the specimen fails. Due to the superiority of the modified true-triaxial testing system over the conventional testing methods, many researchers recently have used this machine to study the influence of different parameters such as moisture content (Sun et al. 2016; Liu et al. 2018; Chen et al. 2019), temperature (Su et al. 2017a; Akdag et al. 2018), tunnel axis stress (Su et al. 2017b), aspect ratio of the rock sample (Zhao and Cai 2015) and unloading rate (Zhao et al. 2014; Li et al. 2014) on rockburst hazard. During the rockburst tests, the rocks experience a severe failure at a specific stress level which is known as rockburst maximum stress (σ_{RB}) (see Fig. 5.3). The correct prediction of this stress level for different rock types by considering the most important rock mechanical characteristics can help engineers to recognise rockburst hazards in different in-situ stress conditions, to increase the stability of the underground structures as well as for numerical studies. Furthermore, the predictor model can be used to estimate bursting stress when rockburst testing facilities are not available. In this regard, He et al. (2015) proposed three models using multiple linear regression (MLR), artificial neural network (ANN), and support vector machine (SVM) techniques to predict σ_{RB} and rockburst risk index (I_{RB}) based on the database compiled from true-triaxial tests.

In their study, ANN and SVM as two subsets of soft computing algorithms outperformed the common multiple regression model and were identified as possible solutions for studying such a complex problem. Although these techniques can provide models with suitable accuracy, they are known as “black-box” methods i.e. their internal structure and calculations are not clear and easy to understand by a human. In addition, such algorithms may stick in local minimum during the training process, and their outputs may not be very reliable. Above all, these techniques are not very practical since they cannot offer any mathematical or visual output to let the users apply them without using a code (Cortez and Embrechts 2011). It is also worth mentioning that many factors affect rockburst hazard and its related parameters, and selecting the most influential ones during the modelling, can affect the complexity, accuracy, and more importantly the reliability of the developed models. To triumph over such complexities and open the black-box methods, the extraction of rules from the model, and the use of visualization techniques are recommended (Cortez and Embrechts 2011). Contrary to ANN and SVM techniques, there are other powerful algorithms such as genetic programming (GP), gene expression programming (GEP), and classification and regression tree (CART) that

can provide more practical outputs. The successful application of these algorithms has been reported by other researchers in mining and geotechnical engineering fields (Armaghani et al. 2016; Salimi et al. 2016; Hasanipanah et al. 2017b; Khandelwal et al. 2017). Hence, it is necessary to use state-of-the-art modelling techniques to address the mentioned difficulties and develop new models for predicting rockburst maximum stress and its risk index based on field conditions. As it has been summarized in Fig. 5.4, this study focuses on the following steps: 1) compiling a database based on the true-triaxial unloading tests on different rock types and performing a broad statistical analysis on it to create a homogeneous database and to select the most influential parameters based on an appropriate strategy; 2) Developing genetic-based and decision tree-based models for the prediction of maximum rockburst stress (σ_{RB}) and rockburst risk index (I_{RB}) based on the selected input parameters; 3) validation verification of the developed models; and 4) conducting a parametric analysis to assess the effect of input parameters on the corresponding outputs.

Figure 5.1 Rock ejection and deformation of the supporting system due to strainbursting (Feng et al. 2017)

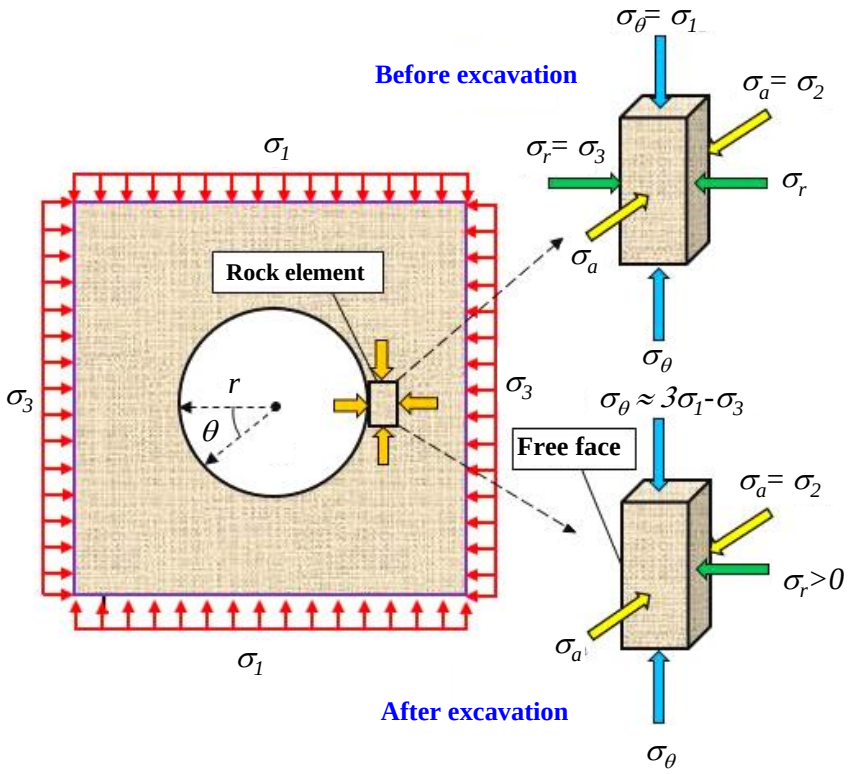

Figure 5.2 The schematic representation of the rock element stress state before and after tunnelling, modified from Su et al.(2017a)

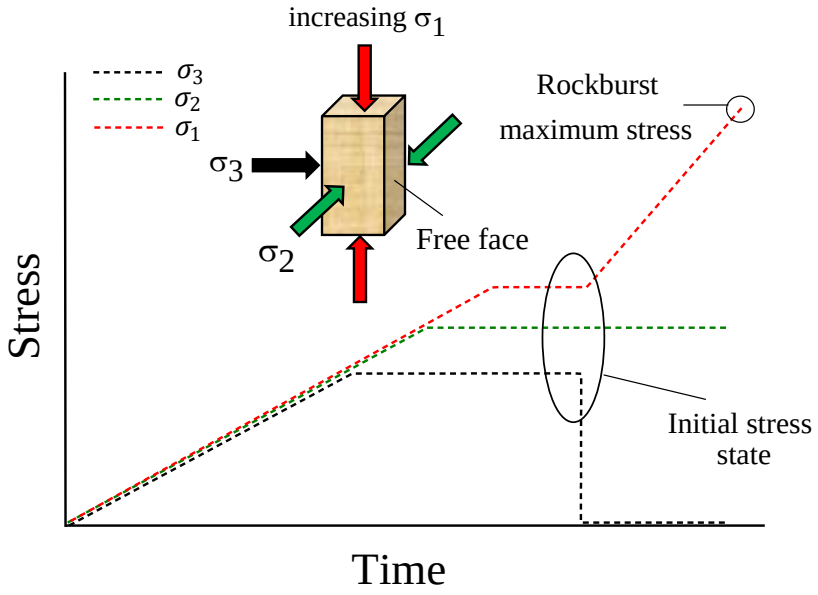

Figure 5.3 Loading path for rockburst true-triaxial tests

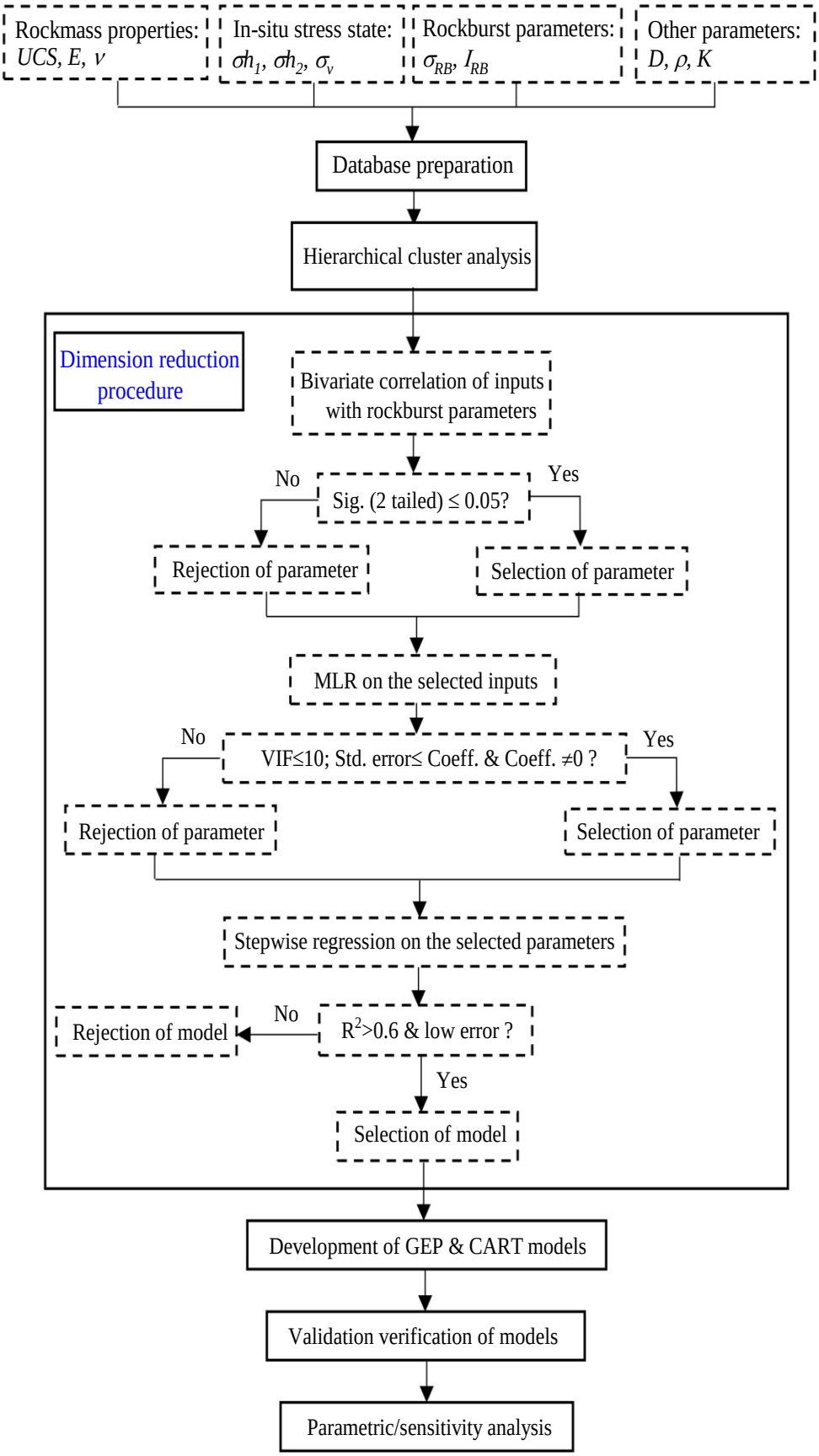

Figure 5.4 Process of rockburst assessment in this study (UCS: uniaxial compressive strength; E: Young's modulus; ν: Poisson's ratio; σ_{h1}: horizontal in-situ stress; σ_{h2}:

horizontal in-situ stress in the face to be unloaded; σ_v: vertical in-situ stress; σ_{RB}: rockburst maximum stress; I_{RB}: rockburst risk index; D: depth, ρ: density, K: horizontal pressure coefficient (ratio of average horizontal stresses to the vertical stress due to overburden), MLR: multiple linear regression; VIF: variance inflation factor; R^2: coefficient of determination)

5.2. Data Collection and Statistical Analysis

In this study, a database containing information about the 139 rockburst laboratory tests conducted on different rock types from 2004 to 2012 at the State Key Laboratory for Geomechanics and Deep Underground Engineering (SKLGDUE), China was compiled. The tested rock samples were gathered from the depth of 200 m to 3375 m. This database consists of many parameters such as rock mechanical properties, in-situ stresses, rock sample depth, rockburst critical depth, rock density, rock specific weight, mineral contents of rocks, loading and unloading rates of the true-triaxial tests, rockburst maximum stress, rockburst risk index, test duration and bursting mechanism. Considering a circular shape for the tunnel crown, the stress concentration factor equal to 2, and the specific weight of 27 kN/m^3 for the overburden rock mass, the rockburst critical depth (H_e) was calculated by the following equation:

$$\mathrm{H_e} = 18.52\sigma_{RB} \tag{5.1}$$

The rockburst risk index ($\mathrm{I_{RB}}$) also was calculated for all the samples through the following equation (He 2009):

$$\mathrm{I_{RB}} = \frac{\mathrm{H}}{\mathrm{H_e}} = 0.054\frac{\mathrm{H}}{\sigma_{\mathrm{RB}}} \tag{5.2}$$

He (2009) defined a new classification for I_{RB} as shown in Table 5.1. Based on this classification, a 56% of the tested samples have low I_{RB}, 13% of the samples have very high I_{RB}, and the remained 31% of samples have moderate to high I_{RB}. Since all the foregoing parameters have not been collected during the rockburst tests, there are some missing values in the database. To have a homogeneous database, the missing values (30 records) were eliminated from the primary database, and finally, the results of 109 tests were considered for further analyses. Before developing any model, the presence of natural groups and outliers in the raw database was evaluated using agglomerative hierarchical clustering (AHC) analysis. In fact, the presence of outliers and natural groups can decrease the generality and liability of the developed models (Hudaverdi 2012; Faradonbeh and Monjezi 2017; Shirani Faradonbeh and

Taheri 2019) The AHC is the most common type of clustering techniques which is used in earth sciences (Hudaverdi 2012). The AHC follows a bottom-up procedure that iteratively creates the single object clusters and then these clusters are merged into the larger clusters based on the similarity or dissimilarity criteria. The common criterion for clustering is "distance", and this means that objects in the same cluster have the least distance from each other, while objects in different clusters are at a great distance from one another. The process of cluster generating and merging is continued until all the objects (datasets) are placed in a single cluster or the pre-defined termination condition is satisfied. For measuring the distance between the objects, the average-linkage function that measures the average distance of any object of one cluster from an object of the other cluster was used to form the clusters (Kaufman and Rousseeuw 2009; Saxena et al. 2017):

$$\frac{1}{|A||B|}\sum_{a\in A}\sum_{b\in B} d(a,b) \tag{5.3}$$

where A and B are two clusters with the sizes of $|A|$ and $|B|$, respectively. a and b are objects from the mentioned clusters and d is the squared Euclidean distance between two objects.

Table 5.1 Rockburst risk index classification, He et al. (2015)

Rockburst risk index (I_{RB})	Class
$I_{RB} < 0.6$	Low
$0.6 < I_{RB} \leq 1.2$	Moderate
$1.2 < I_{RB} \leq 2.0$	High
$I_{RB} \geq 2.0$	Very high

Fig. 5.5 shows the dendrogram derived from the conducted clustering analysis by AHC. A dendrogram is a tool that represents the relative size of the calculated distances at which the objects and clusters are combined. The objects with the low squared Euclidean distance (high similarity) are close together and vice versa. The *X*-axis shows the dataset number and the *Y*-axis shows the rescaled value of the distance. To prevent Fig. 5.5 to be crowded and large, the numbers of the datasets have been summarised on the *X*-axis. Clearly can be seen from Fig. 5.5 that the whole 109 collected datasets were clustered into one distinct group between the rescaled distances of 0 and 5 except for two cases of 75 and 76 which were placed in the second group. By checking the database, it was found out that the main parameter that caused to grouping is depth, and the members of group 2 belong to the depth of 3375 m which are known as outliers for the current database. Therefore, these two cases were removed from the database to avoid the influence of their distinctive behaviour on the modelling process, and the

subsequent analysis was carried out on the 107 data samples. Fig. 5.6 shows the histogram and the descriptive statistics of all the 11 measured parameters. This figure illustrates that there are specific ranges of values for the parameters in which the predictions are meaningful. Accordingly, future predictions with a new database should be conducted only in these ranges. Although the current database covers a great range of values for the parameters and includes different rock types, it is possible to extend these ranges in the future by new information obtained from true-triaxial tests to increase the generality of the developed models.

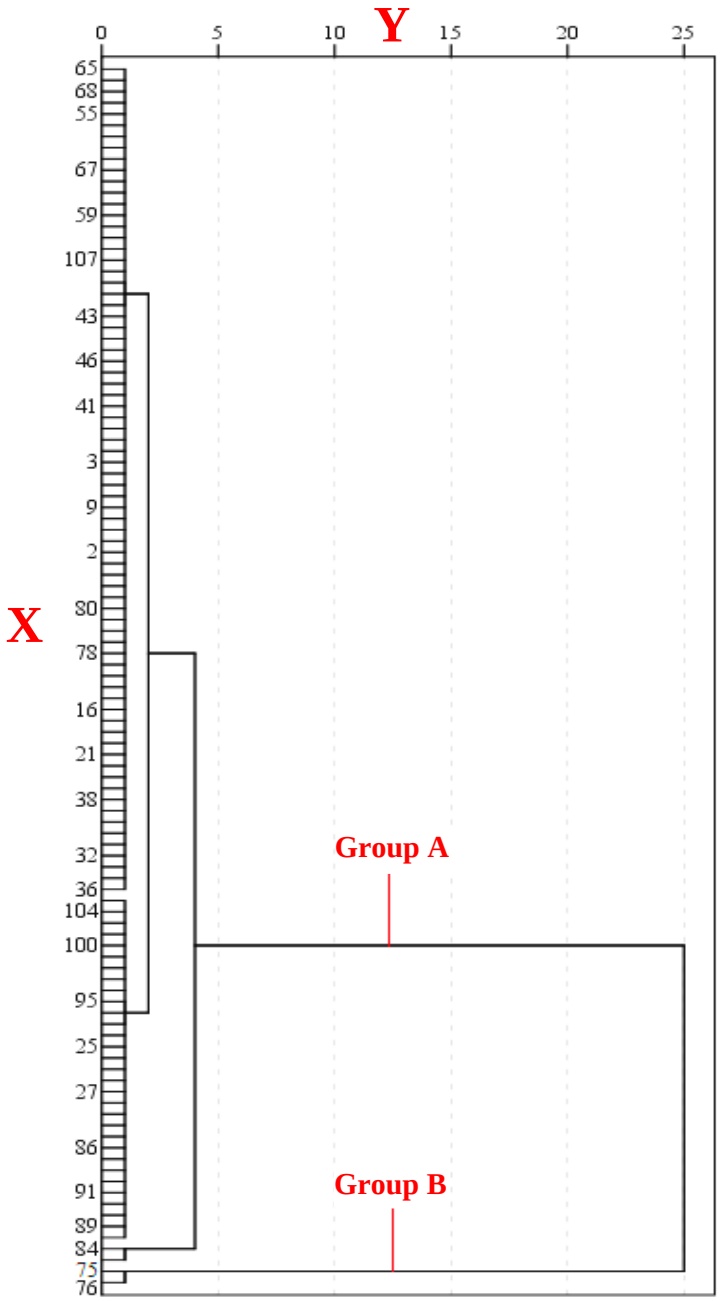

Figure 5.5 Dendrogram resulting from agglomerative hierarchical clustering (AHC) analysis

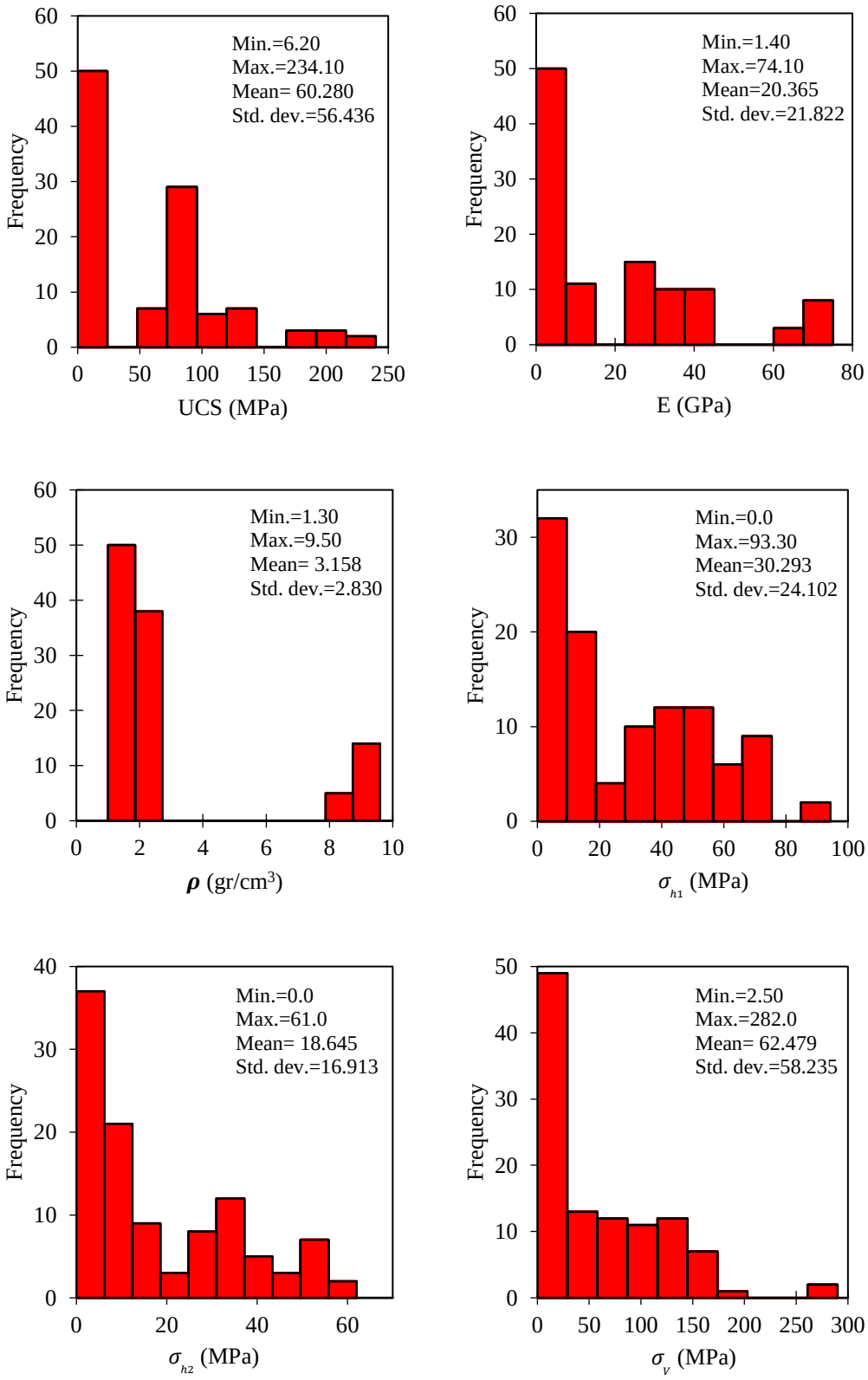

Figure 5.6 Histogram of the collected parameters along with the descriptive statistics

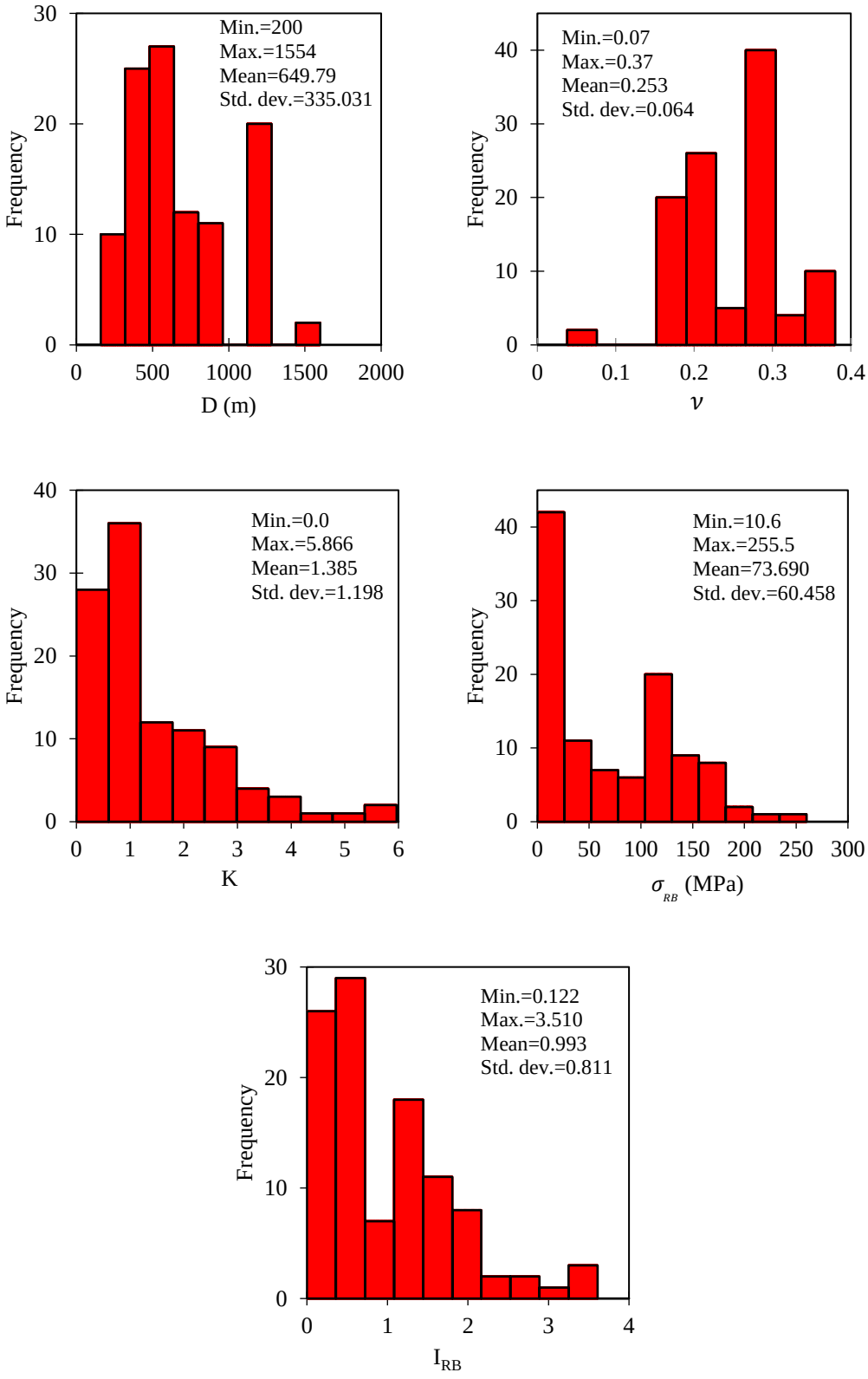

Figure 5.6 (Continued)

5.3. Methods and Results

5.3.1. Stepwise Selection and Elimination Process

This section aims to do a systematic stepwise selection and elimination (SSE) analysis to identify the most important parameters on the outputs and reduce the complexity of the developed models. The process of parameter reduction also is carried out using the variable pressure tools of the robust data-mining techniques i.e. GEP and CART. There are several critical statistical terms which have been used in this study for the primary assessment of the database and are defined in the following. Multicollinearity, a high correlation between the independent (predictor) variables, can be considered as one of the most prominent challenges for multiple regressions. The existence of this phenomenon may lead to developing an unstable regression model having high values for variance and covariance coefficients (Sayadi et al. 2012). Variance inflation factor (VIF) is a statistical index to quantify the extent of the multicollinearity between the independent (input) parameters. This index is the ratio of model variance considering several inputs to the variance of the model with a single input parameter. The VIF lower than 10 shows the non-existence of multicollinearity (James et al. 2013). Another important index is Sig. (2-tailed) or p-value of the correlations. The Sig (2-tailed) represents the significance of the correlation at a prescribed alpha level (5%). The Sig. (2-tailed) should be less than or equal to 0.05 to reject the influence of chance factor. The coefficient of determination (denoted by R^2) is another statistical measure for evaluation of the model performance. This index interprets the proportion of the output (dependent) variable's variance that is predictable from the input (independent) variables. An R^2 of 1 indicates that the regression predictions perfectly fit the data (Montgomery et al. 2012; James et al. 2013; Kumar Sharma and Rai 2017).

In the current study, uniaxial compressive strength (UCS), Young's modulus (E), Poisson's ratio (ν), horizontal in-situ stress (σ_{h1}), horizontal in-situ stress in the face to be unloaded (σ_{h2}), vertical in-situ stress (σ_v), depth (D), density (ρ), and horizontal pressure coefficient (K) are known as the input parameters for the maximum rockburst stress (σ_{RB}), while all the mentioned parameters are considered as inputs for the rockburst risk index (I_{RB}). The SPSS software package 25.0 was used for performing the statistical evaluations. Initially, the database was fed to the software, and the Person's correlation coefficient (r) between the input parameters as well as between the inputs and the corresponding outputs was calculated. Table 5.2 lists the calculated correlation values. As can be seen from this table, all the inputs significantly

correlating with σ_{RB} (i.e. $Sig.(2-tailed) \leq 0.05$), while D (depth) with the $Sig. > 0.05$ and low correlation coefficient ($r = -0.128$) was removed from the input parameters for further modelling of I_{RB}. The elimination of parameters does not show that they have not any influence on the output, but simply it means that the effect of those parameters will be minimum in predicting the output. As an initial multicollinearity assessment between input parameters, no one of the correlations exceeds from the condition of $r > 0.90$ (Hemmateenejad and Yazdani 2009). However, these input parameters may show multicollinearity when a combination of them are used as regressors in MLR. Based on the above analysis, all the inputs (except parameter D for I_{RB}) were retained for multiple linear regression (MLR). The MLR models with the possible multicollinearity were developed separately using the selected parameters for both σ_{RB} and I_{RB}.

Table 5.3 shows the model summary, calculated coefficients, and the statistical indices for evaluating the developed MLR models. In this stage, according to Fig. 5.4, several conditions including $VIF < 10$, $Std.error \leq Coeff.(B)$, and $Coeff.(B) \neq 0$ were checked for different inputs to retain them for further evaluations. Considering Table 5.3, for rockburst maximum stress (σ_{RB}), the parameters of K and ρ have $VIF > 10$ and t-significance higher than 0.05, respectively, which shows that the effect of these parameters on the σ_{RB} is insignificant. Therefore, these parameters were removed for further modelling of σ_{RB}. About the rockburst risk index (I_{RB}), all the VIF values for inputs are less than 10, but the t-significance values of the UCS, σ_v, σ_{h1}, and σ_{h2} are higher than 0.05. Thus, these parameters also were removed from the input set of I_{RB}. In the next step, two stepwise selection and elimination procedures were performed using the selected inputs for each dependent parameter. In this procedure, a parameter which is entered in the model at the initial stage of selection may be removed at the later stages. In fact, the calculations in this process are like the forward selection and backward procedure (Sarkhosh et al. 2012).

Table 5.4 summarises the results of the stepwise selection and elimination procedure carried out using the algorithm provided in the SPSS 25. In this algorithm, the parameters enter the model if the probability (significance level) of its F value is less than the Entry value (i.e. 0.05) and are eliminated if the probability is greater than the Removal value (i.e. 0.100). Entry must be less than Removal, and both values must be positive. As given in Table 5.4, during the process of selection and elimination, the correlation coefficient (R) between the measured output and the predicted one was increased from 0.884 (model 1) to 0.910 (model 3) for σ_{RB}

and from 0.754 (model 1) to 0.821 (model 5) for I_{RB}, respectively. In other words, the parameters of UCS, E, and σ_v can explain 82.8% ($R^2 = 0.828$) variations in σ_{RB}. As such, the parameters of σ_{RB}, K, E, ν, and ρ can explain 67.4% ($R^2 = 0.674$) variations in I_{RB}. Thus, these parameters were known as the most influential ones among the initial inputs to describe the rockburst parameters. The regression coefficients and the collinearity statistics of the best SSE-based models are shown in Table 5.5. In both models, the VIF factor that shows the multicollinearity is lower than 10, the t-significance is lower than 0.05, and the Std. error values are lower than the regression coefficients which show the reliability of the SSE process in identifying the most influential parameters.

Considering the above analyses, the agglomerative hierarchical clustering (AHC) accompanied by the stepwise selection and elimination (SSE) method could provide a homogeneous rockburst database by removing the outliers and decreasing the dimensionality of the problem. This process also can be useful for the complexity reduction of the next predictive models by applying a few input parameters. Due to the high non-linear and complex nature of rockburst hazard (He et al. 2015; Pu et al. 2019; Shirani Faradonbeh and Taheri 2019) there is a need to use the non-linear data-mining algorithms to provide more accurate predictive models for rockburst parameters. To do so, two robust data-driven approaches including the gene expression programming (GEP) as a meta-heuristic algorithm and the classification and regression tree (CART) as a subset of decision tree algorithms were selected for discovering the non-linear latent relationships with more accuracy and lower estimation error. These algorithms despite the various datamining and soft computing techniques such as ANNs, SVM, etc. can provide practical and easy to use outputs for the engineers and the researchers when the true-triaxial testing machine is not available. A summary of the modelling procedure by these techniques is presented in the following sections.

Table 5.2 Pearson's correlation (r) coefficient between different parameters

		UCS	ρ	E	ν	σ_v	σ_{h1}	σ_{h2}	D	K	σ_{RB}	I_{RB}
UCS	r	1										
	Sig.											
ρ	r	0.827	1									
	Sig.	0.000										
E	r	0.796	0.829	1								
	Sig.	0.000	0.000									
ν	r	-0.555	-0.438	-0.594	1							
	Sig.	0.000	0.000	0.000								
σ_v	r	0.660	0.491	0.458	-0.367	1						
	Sig.	0.000	0.000	0.000	0.000							
σ_{h1}	r	0.737	0.523	0.515	-0.420	0.846	1					
	Sig.	0.000	0.000	0.000	0.000	0.000						
σ_{h2}	r	0.713	0.549	0.648	-0.460	0.685	0.803	1				
	Sig.	0.000	0.000	0.000	0.000	0.000	0.000					
D	r	0.450	0.065	0.247	-0.563	0.450	0.554	0.430	1			
	Sig.	0.000	0.509	0.010	0.000	0.000	0.000	0.000				
K	r	0.667	0.717	0.655	-0.362	0.629	0.712	0.791	-0.005	1		
	Sig.	0.000	0.000	0.000	0.000	0.000	0.000	0.000	0.961			
σ_{RB}	r	0.820	0.664	0.668	-0.484	0.884	0.838	0.762	0.413	0.707	1	
	Sig.	0.000	0.000	0.000	0.000	0.000	0.000	0.000	0.000	0.000		
I_{RB}	r	-0.617	-0.539	-0.624	0.255	-0.619	-0.645	-0.618	-0.128	-0.656	-0.754	1
	Sig.	0.000	0.000	0.000	0.008	0.000	0.000	0.000	0.188	0.000	0.000	

* Correlation is significant at the 0.05 level (2-tailed)

Table 5.3 Summary of the MLR models for σ_{RB} and I_{RB} with the selected parameters (with multicollinearity)

Model summary				
Dependent parameter	r	r-square	Adjusted r-square	Std. error of the estimate
σ_{RB}	0.952	0.906	0.897	19.385
I_{RB}	0.832	0.692	0.664	0.470

Rockburst maximum stress (σ_{RB})

Parameters	Unstandardized coefficients		standardized coefficients	t	Sig.	Collinearity statistics	
	B	Std. Error	Beta			Tolerance	VIF
(Constant)	71.247	20.947		3.401	0.001		
UCS	0.380	.093	0.354	4.097	0.000	0.130	7.719
ρ	-1.844	1.794	-0.086	-1.028	0.307	0.138	7.271
E	.400	0.193	0.144	2.072	0.041	0.200	5.005
ν	-125.188	50.304	-0.132	-2.489	0.015	0.344	2.908
σ_v	0.594	0.061	0.572	9.688	0.000	0.278	3.592
σ_{h1}	0.650	0.246	0.259	2.639	0.010	0.101	9.926
σ_{h2}	0.664	0.284	0.186	2.342	0.021	0.154	6.490
D	-0.060	0.016	-0.333	-3.750	0.000	0.123	8.146
K	-15.291	5.571	-0.303	-2.745	0.007	0.080	12.556

Rockburst risk index (I_{RB})

Parameters	Unstandardized coefficients		standardized coefficients	t	Sig.	Collinearity statistics	
	B	Std. Error	Beta			Tolerance	VIF
(Constant)	2.766	0.282		9.816	0.000		
UCS	0.001	0.002	0.065	0.415	0.679	0.129	7.733
ρ	0.107	0.042	0.375	2.528	0.013	0.144	6.926
E	-0.020	0.005	-0.550	-4.286	0.000	0.193	5.194
ν	-3.406	0.932	-0.268	-3.653	0.000	0.589	1.698
σ_v	0.003	0.002	0.223	1.535	0.128	0.151	6.629
σ_{h1}	-0.006	0.005	-0.185	-1.305	0.195	0.158	6.335
σ_{h2}	0.011	0.006	0.231	1.807	0.074	0.194	5.167
K	-0.221	0.083	-0.327	-2.662	0.009	0.210	4.751
σ_{RB}	-0.011	0.002	-0.805	-4.689	0.000	0.108	9.284

Table 5.4 MLR models developed based on SSE method (without multicollinearity) for σ_{RB} and I_{RB}

Rockburst maximum stress (σ_{RB})					
Stepwise selection and elimination			Model summary		
Model	Variables entered	Variables removed	r	r-square	Std. error
1	σ_v	$UCS, E, \nu, \sigma_{h1}, \sigma_{h2}, D$	0.884	0.781	28.412
2	UCS	E, ν, σ_{h1}, σ_{h2}, D	0.938	0.880	21.102
3	E	ν, σ_{h1}, σ_{h2}, D	0.910	0.828	20.399
Rockburst risk index (I_{RB})					
Stepwise selection and elimination			Model summary		
Model	Variables entered	Variables removed	r	r-square	Std. error
1	σ_{RB}	ρ, E, ν, K	0.754	0.568	0.564
2	K	ρ, E, ν	0.773	0.598	0.591
3	ν	ρ, E	0.784	0.615	0.604
4	E	ρ	0.805	0.649	0.635
5	ρ		0.821	0.674	0.658

Table 5.5 The statistical parameters of the best SSE-based MLR models

Rockburst maximum stress (σ_{RB})							
Model	Unstandardized coefficients		Standardized coefficients	t	Sig.	Collinearity statistics	
	B	Std. error	Beta			Tolerance	VIF
(Constant)	6.019	3.080		1.954	0.053		
σ_v	0.650	0.046	0.626	14.196	0.000	0.552	1.811
UCS	0.301	0.069	0.281	4.336	0.000	0.256	3.912
E	0.437	0.152	0.158	2.881	0.005	0.358	2.794
Rockburst risk index (I_{RB})							
Model	Unstandardized coefficients		Standardized coefficients	t	Sig.	Collinearity statistics	
	B	Std. error	Beta			Tolerance	VIF
(Constant)	2.780	0.278		10.006	0.000		
σ_{RB}	-0.008	0.001	-0.601	-6.749	0.012	0.406	2.463
K	-0.158	0.062	-0.233	-2.556	0.000	0.388	2.578
ν	-3.501	0.922	-0.276	-3.797	0.000	0.612	1.634
E	-0.018	0.004	-0.497	-4.280	0.000	0.239	4.189
ρ	0.091	0.032	0.319	2.830	0.006	0.254	3.933

5.3.2. Non-linear Regression Analysis

Non-linear regression (NLR) attempts to find a function which is a non-linear combination of the input parameters using a method of successive approximation (Archontoulis and Miguez 2015; Bethea 2018). In geoscience, most of the dependent parameters show a non-linear relationship with the related influential parameters. So, the non-linear regression analysis has been widely used by researchers in the last decades (Armaghani et al. 2016; Jahed Armaghani et al. 2017; Ghasemi 2017). The NLR technique is capable of accommodating a broad range of functions including exponential, power, logarithmic, sigmoid, logistic, trigonometric, Gaussian, etc. that boosts the process of function finding. Another advantage of the NLR is the efficient use of data, i.e. it can provide reasonable estimates of the unknown parameters for a comparatively small data. However, the common NLR technique suffers from several significant drawbacks. In NLR, there is no a closed-form and holistic mathematical structure between the dependent and the independent parameters as there is in multiple linear regression (MLR), while the choice of the model structure is a crucial task to obtain the best solution. In addition, the selection and utilizing the suitable mathematical functions from the large library of functions need an iterative optimization procedure that is not possible in common NLR modellings. Accordingly, the researchers may have to use numerical optimization algorithms to find the best-fitting parameters but still, there is a need to define the starting values for the unknown parameters in these methods. Inappropriate assigning the starting values may cause to getting caught in the local minima rather than finding the global minimum that introduces the least squares estimates (Motulsky and Ransnas 1987; Archontoulis and Miguez 2015; Bethea 2018). For these difficulties, the researchers prefer to use a non-linear regression form that has been used successfully in similar applications. Hereupon, the application of intelligent algorithms is needed to cope with these issues. In the following sections, the process of rockburst assessment using two robust non-linear techniques comprising the gene expression programming (GEP) and classification and regression tree (CART) are explained.

5.3.2.1. Rockburst Assessment Using GEP-based Models

Soft computing is the relatively new branch of data-mining methods and can be considered as an alternative to the prevalent hard computing methods for solving the real-world problems (Mitchell 1997; Alavi et al. 2016). Soft computing techniques have been successfully employed in mining, rock mechanics, and geotechnical problems but despite their good performance, they cannot generate practical equations, and their structure needs to be assigned in advance by the

user (Alavi and Gandomi 2011). By inspiring from the Darwinian principle of "Survival of the Fittest" (Nazari and Pacheco Torgal 2013) and the natural evolution, a new subset of soft computing was introduced as the evolutionary algorithm (EA). Generally speaking, EAs work with a randomly generated population of individuals which are then improved using a group of genetic operators (e.g. mutation, crossover and reproduction) and finally, the solutions are encoded into the specific forms such as binary strings in genetic algorithm. The main differences between EAs are related to the method of presenting the solutions, genetic operators, selection mechanism, and the performance measurement method (Ferreira 2002a; Alavi et al. 2016). Gene expression programming (GEP) (Ferreira 2002b) is a well-known evolutionary algorithm that inherits two essential features from its siblings i.e. the use of simple, fixed-length, and linear chromosomes with different shapes and sizes from genetic algorithm (GA) and the expression tree (ET) structure from genetic programming (GP) that improves the robustness of GEP for solving the non-linear problems (Power et al. 2019). The main entities of GEP algorithm are terminal set (input parameters and constant values), function set (e.g. $+, -, \times, \div$), fitness function (for evaluating the generated solutions), and genetic operators (mutation, inversion, transposition, and recombination).

A flowchart detailing the GEP modelling procedure is shown in Fig. 5.7. In summary, GEP generates a population of chromosomes (solution/individual) by combining the user-defined terminals and functions. These chromosomes follow a bilingual and unequivocal expression system that is called Karva language (Ferreira 2006). The chromosomes have a specified number of genes (sub -ETs) which are linked together using a linking function (e.g. "/" in Fig. 5.7 that links two genes of a chromosome). Each gene contains two parts of head and tail that the terminals (inputs) and functions (mathematical functions) are placed in them and the genetic operators are applied to these areas to modify the solutions. To have a quick understanding regarding the built-in mathematical equations of chromosomes, the Karva coded programs are then parsed into ETs. Then, the mathematical form of the programs is extracted from ETs and their fitness is evaluated by a fitness function. If the stopping condition(s) such as reaching to a specific number of iterations or the desired fitness value is not met, the selected chromosomes are replicated into a new generation, and the remained ones undergo a modification process using the genetic operators. The above process is repeated and finally, the best solution (predictive model) describing the relationship between the input and output parameters is found. More details about the mechanism of genetic operators and GEP algorithm can be found

in Ferreira.(Ferreira 2006) In the current study, the selected inputs from the SSE analysis were considered as terminal sets to formulate the rockburst parameters nonlinearly as follows:

$$\sigma_{RB} = f(UCS, E, \sigma_v) \tag{5.4}$$

$$I_{RB} = f(\sigma_{RB}, K, \upsilon, E, \rho) \tag{5.5}$$

The rockburst database was divided randomly into training and testing subsets. The training set (80 % of the database) was used to train the model and discover the relationship between inputs and outputs, and the remaining datasets were used to validate the performance of the proposed models. It should be noted that the influence of using different groups of training and testing datasets were also evaluated on the accuracy of the models. However, no noticeable change in the results was observed. For evaluating the generated solutions during the GEP modelling, it is necessary to use a fitness function. As mentioned in section 5.3.1, to propose models with lower complexity, it is possible to apply variable pressure tools to compress the developed models as much as possible by eliminating the parameters which have lower importance in a non-linear structure. To this end, the root mean squared error (RMSE) with parsimony pressure was applied to the GEP models of σ_{RB} and I_{RB} (Roy et al. 2002). The $RMSE_i$ of a chromosome (solution) i is calculated by the following equation:

$$RMSE_i = \sqrt{\frac{1}{n}\sum_{j=1}^{n}(P_{ij} - T_j)^2} \tag{5.6}$$

where P_{ij} is the predicted value by the chromosome i for the dataset j, and T_j is the measured value for dataset j.

The $RMSE_i$ varies between 0 and infinity, with 0 corresponding to the ideal. Since the process of selection in GEP algorithm is based on the increase of fitness, Equation (6) cannot be used directly. Thus, the following expression was used for fitness function which obviously ranges between 0 to 1000, with 1000 corresponding to the ideal:

$$RMSE_i' = 1000 \times \frac{1}{1+RMSE_i} \tag{5.7}$$

On the other hand, to apply the parsimony pressure on future models, overall fitness was defined as:

$$RMSE_i'' = RMSE_i' \times (1 + \frac{1}{5000} \times \frac{S_{max} - S_i}{S_{max} - S_{min}}) \quad (5.8)$$

where S_i is the size of the GEP program, S_{max} and S_{min} are the maximum and minimum program sizes which are calculated by the following equations:

$$S_{max} = G(h + t) \quad (5.9)$$

$$S_{min} = G \quad (5.10)$$

where G is the number of genes, and h and t are the head size and tail size, respectively.

A group of trigonometric and straightforward mathematical functions i.e. $\{+, -, *, /, \sqrt{}, Ln, \text{^}2, \text{^}3, \text{^}1/3, sin, cos, tan\}$ were selected as the function set based on the previous non-linear studies using GEP algorithm (Kayadelen 2011; Faradonbeh and Monjezi 2017; Hoseinian et al. 2017). The other GEP parameters including the number of chromosomes, head size, the number of genes, and the values of genetic operators were changed for different runs to obtain the best solution in such a way that provides not only high accuracy but also less complexity. Table 5.6 presents the architecture of the obtained GEP models for both rockburst maximum stress (σ_{RB}) and rockburst risk index (I_{RB}). By applying the parsimony pressure to the models, the density parameter (ρ) was identified intelligently as the low-impact parameter in the non-linear form of I_{RB}. Therefore, this parameter was removed by GEP automatically during modelling and the number of inputs for I_{RB} decreased from 5 to 4. About σ_{RB}, the GEP algorithm identified the three inputs of UCS, E, and σ_v as the influential parameters for modelling as formerly proved by SSE analysis. The ability of GEP in identifying the low-influence parameters and excluding them during modelling can be considered as an internal sensitivity analysis that distinguishes GEP from other soft computing techniques. Fig. 5.8 displays the variations of the coefficient of determination (R^2) during 5000 generations (iterations) in both training and testing stages of GEP modelling for rockburst parameters. According to this figure, after a few numbers of generations (less than 1000), a rapid increase of R^2 for the generated solutions can be seen which shows the high speed and high capability of GEP algorithm in function finding. From the generation 1000 to 3500, a gentle enhancement in the quality of solutions are visible, and finally, the algorithm converges into an optimum value and its value almost remains constant to reach the stopping condition (i.e. the pre-defined number of generations: 5000). The obtained R^2 values for training and testing stages of σ_{RB} are 0.9266 and 0.9398, respectively, while the foregoing values are 0.8824 and 0.9459, respectively for I_{RB}. Figs. 5.9 shows the correlation of the experimentally measured values of

σ_{RB} and I_{RB} versus the predicted ones by the constructed GEP models for training and testing data groups. As seen, the data points have almost a uniform distribution around the fitted lines in both GEP-based models which show the goodness-of-fit of the models. The developed models and their performance are discussed in more details in sections 5.4 and 5.5. Eventually, the mathematical forms of the proposed GEP models for σ_{RB} and I_{RB} were extracted from their K-expression and ETs as Eqs. 5.11 and 5.12. To avoid the prolongation of the paper, the ETs and their K-expressions have not presented here.

$$\sigma_{RB} = (\sqrt[3]{\sigma_v + Esin(E-\sigma_v) + E})(\sqrt[3]{E + \sigma_v + Esin(E)})\, Ln(Ln(\sigma_v) + UCS) \tag{5.11}$$

$$I_{RB} = \frac{e^{\sqrt[6]{K}(E+\sqrt[4]{v})}}{(v+K)(E-v)\, Ln(\sigma_{RB})} \tag{5.12}$$

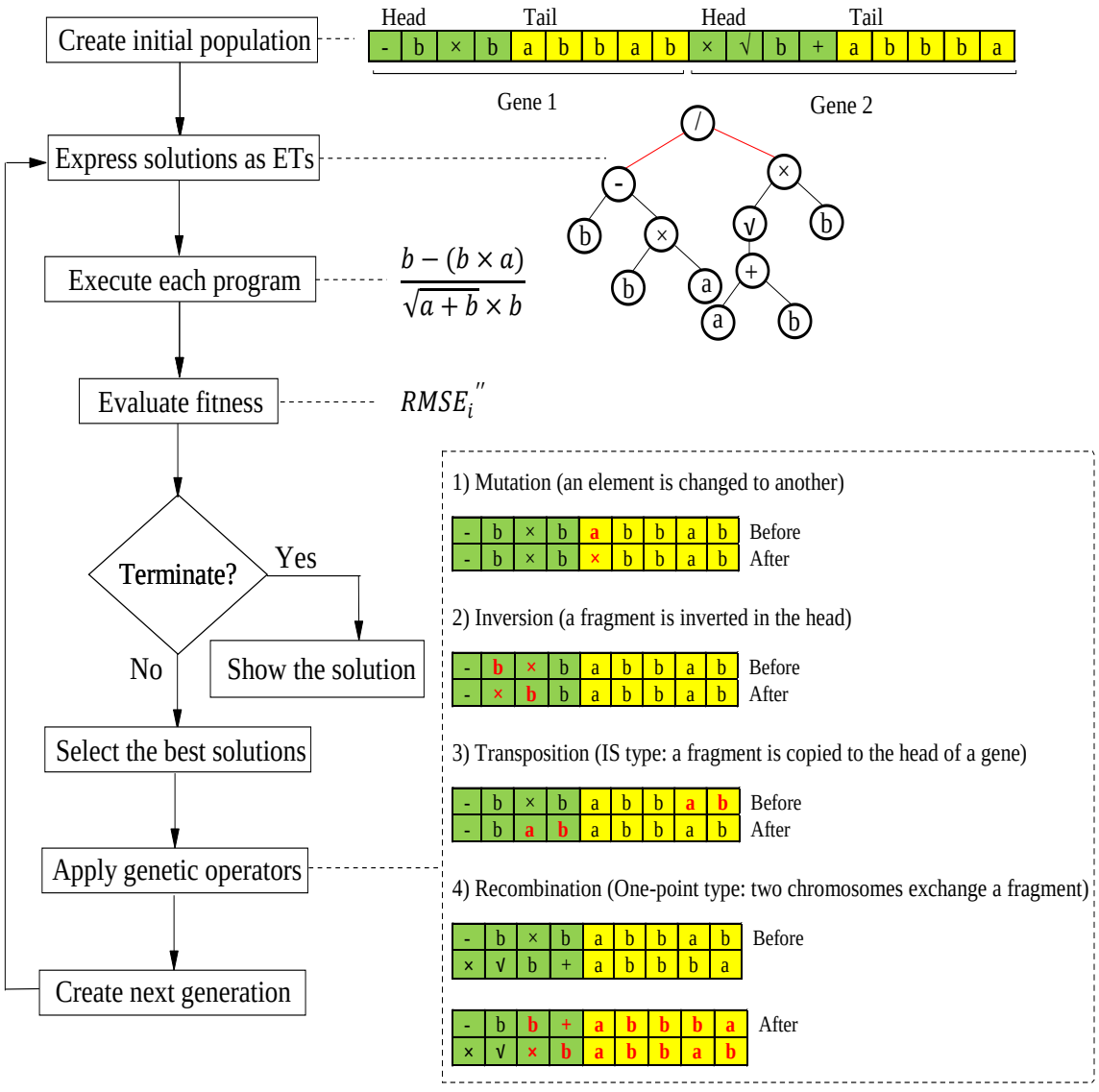

Figure 5.7 Process of function finding using GEP algorithm

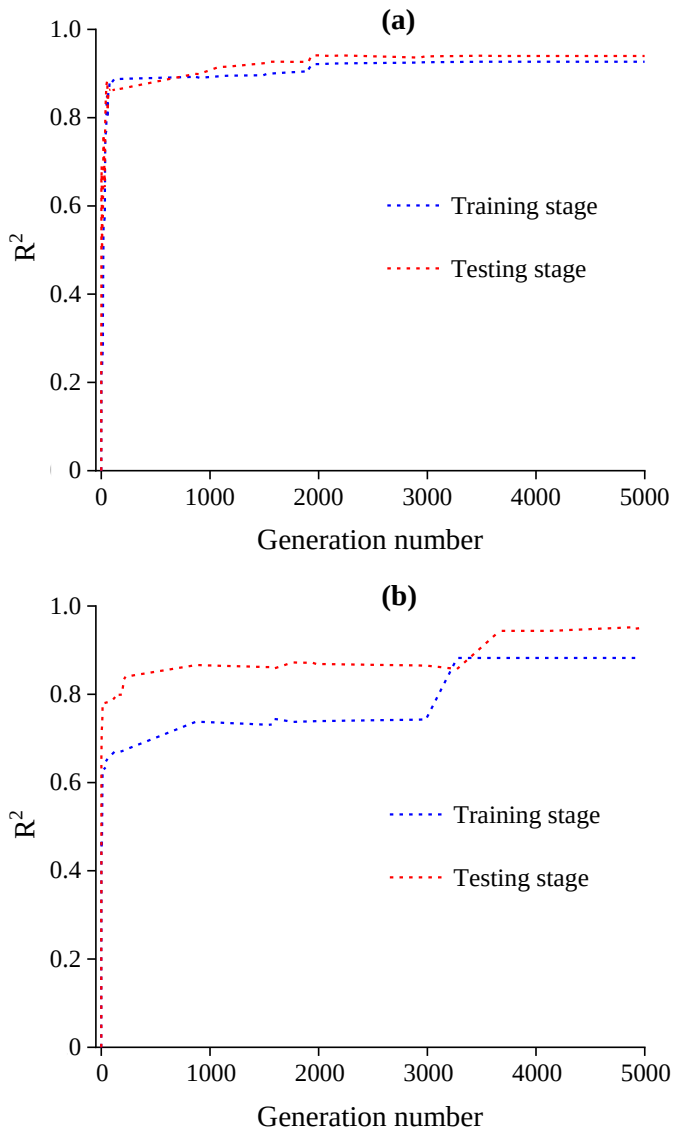

Figure 5.8 Improvement of R2 during GEP modelling for (a) σ_{RB} and (b) I_{RB}

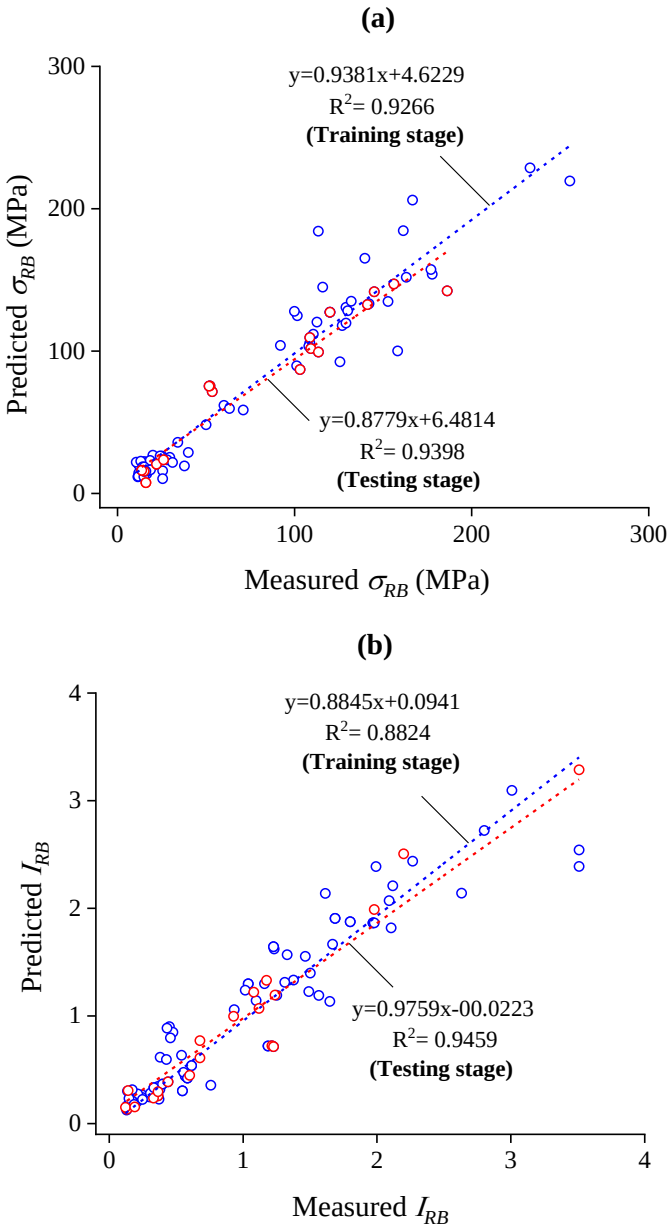

Figure 5.9 Measured vs. predicted values using the GEP models in training and testing stages for: (a) σ_{RB} and (b) I_{RB}

Table 5.6 The architecture of the GEP and CART models

GEP parameter	Setting	
	σ_{RB}	I_{RB}
Terminal set	UCS, E, σ_v	σ_{RB}, K, υ, E, ρ
Excluded parameter	-	ρ
Function set	+, −, ∗, /, √, Ln, ^2, ^3, $\sqrt[3]{}$, sin, cos, tan	
Population size	90	100
Generation number	5000	5000
Head size	9	9
Number of genes	3	2
Linking function	Multiplication (×)	Multiplication (×)

Fitness function	$RMSE_i''$	$RMSE_i''$
Parsimony pressure	Yes	Yes
Mutation rate	0.01	0.04
Inversion rate	0.1	0.1
Transposition	0.1	0.1
One-point recombination	0.3	0.3
Two-point recombination	0.3	0.3
Gene recombination	0.1	0.1

CART parameter	Setting	
	σ_{RB}	I_{RB}
Initial inputs	UCS, E, σ_v	σ_{RB}, K, υ, E, ρ
Excluded parameter	-	ρ
Minimum number of cases for parent node	3	3
Minimum number of cases for child node	1	1
Minimum change of impurity level	0.0005	0.0003
Maximum tree depth	6	5
Number of intervals	10	10
Impurity measure	LSD	LSD
Total number of nodes	27	33

5.3.2.2. Rockburst Assessment Using Classification and Regression Tree (CART)

Decision tree as a powerful subset of data-mining techniques has been used in different real-world applications for different aims such as decision making, classification, prediction, pattern recognition, etc. (Kantardzic 2003; Hasanipanah et al. 2017a) A decision tree is a tree comprising a root node (i.e. a parameter that can provide maximum degree of discrimination), some internal nodes representing input parameters, branches which link the nodes together and contain the binary questions regarding the internal nodes, and some leaf nodes representing the solutions (predicted value or a specific class of the dependent parameter). Each path from the root node to a leaf node can be summarised as a rule that this feature makes the decision tree to be known as a rule-based algorithm (Mahjoobi and Etemad-Shahidi 2008). Based on the type of dependent parameter, i.e. being continuous or categorical, the established tree structure is nominated as regression tree (RT) or classification tree (CT), respectively. The decision tree has several subgroups such as ID3 (Quinlan 1986), C4.5, C5.0, CART, CHAID, Exhaustive CHAID, and QUEST (Mahjoobi and Etemad-Shahidi 2008) which have been used for different aims by scholars (Khandelwal et al. 2017; Ghasemi et al. 2017). Among these techniques, the CART algorithm introduced by Breiman et al. (1984) has several advantages that distinguish it among other decision tree algorithms. This algorithm, despite the parametric statistical techniques (e.g. regression analyses), is inherently non-parametric (rule-based), i.e. no

assumption is made with the distribution of values of the independent parameters. On the other hand, CART can handle the highly skewed (multimodal) quantitative data as well as the qualitative parameters with ordinal or non-ordinal structures (Breiman et al. 1984; Salimi et al. 2016).

In this algorithm, it is not necessary to eliminate the multicollinearity between the independent parameters. Moreover, CART algorithm can be applied on a database with no homogeneity. CART also can handle the existence of outliers in the raw database by isolating them into a separate node. Because of the mentioned advantages, flexibility, and practical output (tree structure) of this algorithm, it was used in this study for the prediction of rockburst parameters obtained from true-triaxial tests. As a matter of fact, since the output parameters in this study (i.e. σ_{RB} and I_{RB}) are continuous, the aim is to develop two regression trees (RTs) for each parameter. The process of RT building in CART algorithm focuses mainly on the three following components: (1) a group of questions in the form of $X \leq a$? where X is an input parameter and a is a constant value in a range that the parameter X varies. In CART, the response to this type of question is "yes" or "no"; (2) the best split on a parameter is determined using a split criterion; (3) calculation of summary statistics for internal nodes. The goal in CART modelling is to create sub-nodes (children) which are more homogeneous and purer than parent nodes based upon the reduction in impurity or improvement score. The term "pure" is related to the values of given parameter i.e. in the complete pure node, all cases have a similar value of the splitting parameter and consequently, the node's variance equal to zero. This issue is compared for all the input parameters and the best improvement is chosen for splitting. This procedure continues until one of the stopping conditions is triggered (Breiman et al. 1984). In CART, the least squared deviation (LSD) is used as an impurity measure. The LSD function for splitting a parent node t into two newly generated sub-nodes $t_{L(eft)}$ and $t_{R(ight)}$ can be calculated using the following equation (Breiman et al. 1984; Bevilacqua et al. 2003):

$$\Phi_{(t)} = R^2(t) - p_L R^2(t_L) - p_R R^2(t_R) = \frac{1}{N(t)} \sum_{i \epsilon t} [y_i - \bar{y}(t)]^2 - p_L \frac{1}{N(t_L)} \sum_{i \epsilon t_L} [y_i - \bar{y}(t_L)]^2 - p_R \frac{1}{N(t_R)} \sum_{i \epsilon t_R} [y_i - \bar{y}(t_R)]^2 \quad (5.13)$$

where $R^2(t_x)$ is the weighted variance related to the sub-node (child) t_x, p_L is the proportion of cases in parent node t which are classified in the left node (t_L), p_R is the proportion of cases in parent node t which are classified in the right node (t_R), $N(t_x)$ is the number of cases

classified in sub-node t_x ($x\epsilon\{R, L\}$), y_i is the value of the objective parameter for the case i, $\bar{y}(t)$ is the mean value of parent node, and $\bar{y}(t_x)$ is the mean value of the sub-node t_x.

The best split is obtained by maximizing the $\Phi_{(t)}$ showing the reduction of impurity of an RT model. This splitting process leads to creating a tree structure based on several "if-then" rules that make it easy to represent. The splitting process proceeds until each leaf node meets at least one of the stopping criteria. The stopping criteria include: (1) reaching the maximum tree depth; (2) the number of cases (datasets) in the terminal node is less than the predefined minimum parent size; (3) the number of cases in the sub-nodes resulting from the best splits is less than pre-defined minimum child size. The stopping criteria used in this study for CART models are tabulated in Table 6. These criteria and their corresponding values were obtained in such a way that the results provide a good trade-off between the prediction accuracy of regression trees and their complexity (dimension). All these settings also prevent the models from getting stuck in over-fitting problems. The use of a high number of maximum tree depth can lead to producing a large tree structure with high complexity that makes it complicated to use in practice. Additionally, a maximum number of intervals equal to 10 was considered for both models to let the model break down the initial min-max range of each input parameter to different ranges during the splitting process. In this study, the CART models for rockburst parameters (σ_{RB} and I_{RB}) were developed using a code written in MatLab R2019a software environment. To have the same modelling conditions for further assessments, the training and testing datasets used for GEP were fed again to the CART algorithm.

According to Table 5.6, for rockburst risk index (I_{RB}) model, like the GEP-based one, the density (ρ) parameter has been excluded from the model since the CART benefits from an internal principal component analysis (PCA) that enables it to consider most influential parameters. Figs. 5.10 and 5.11 demonstrate the constructed RTs for σ_{RB} and I_{RB} using CART algorithm, respectively. The tree model of σ_{RB} contains 27 nodes and starts with UCS as a root node, while the I_{RB} model has 33 nodes that starts with σ_{RB} as the root node. The extraction of final predicted values of σ_{RB} and I_{RB} from these regression trees is an easy task. For instance, in Fig. 5.10, consider the experimentally measured values of 82.7 MPa, 24.3 GPa, 114.6 MPa, and 108.6 MPa for UCS, E, σ_v, and σ_{RB}, respectively; by tracking the associated tree structure from the root node (i.e. node1: UCS) and the path $UCS \geq 40.45$, $\sigma_v < 169.455$, $\sigma_v \geq 63.3$, $UCS < 151.3$, $\sigma_v < 143.5$, and $\sigma_v < 118.4$, the tree reaches to the leaf node 22 that predicts the value of 116.1 for σ_{RB}. The same process can be done for I_{RB} as well. As stated at the

beginning of the current section, CART is a rule-based technique i.e. its internal calculations can be expressed clearly for user/reader by means of "if-then" rules, and this prominent feature makes the CART as a white-box technique unlike the soft computing techniques such as ANNs, SVMs that suffer from the lack of this characteristic. Tables A.1 and A.2 in Appendix A show the generated rules for each node in the developed CART models for σ_{RB} and I_{RB}. To have a primary insight regarding the prediction power of the CART models, the scatter plots of measured values of rockburst parameters versus the predicted ones using this technique were depicted in Fig. 5.12. As it is clear from this figure, the CART algorithm could predict σ_{RB} and I_{RB} with high accuracy like GEP models both in training and testing stages, and the data samples have an appropriate scatter around the fitted line. The developed models and their performance are discussed in more details in sections 5.4 and 5.5.

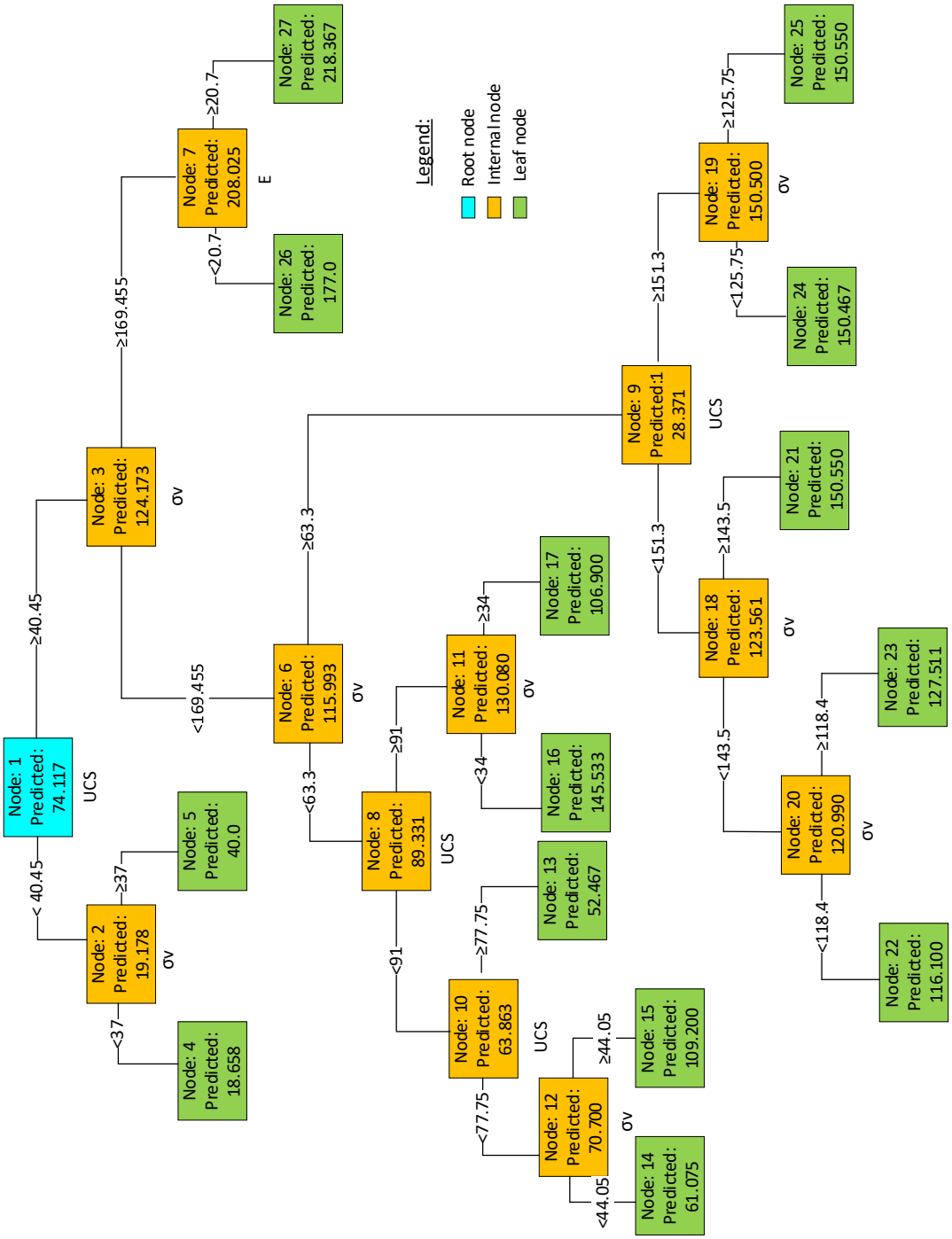

Figure 5.10 Regression tree model generated by the CART algorithm for σ_{RB}

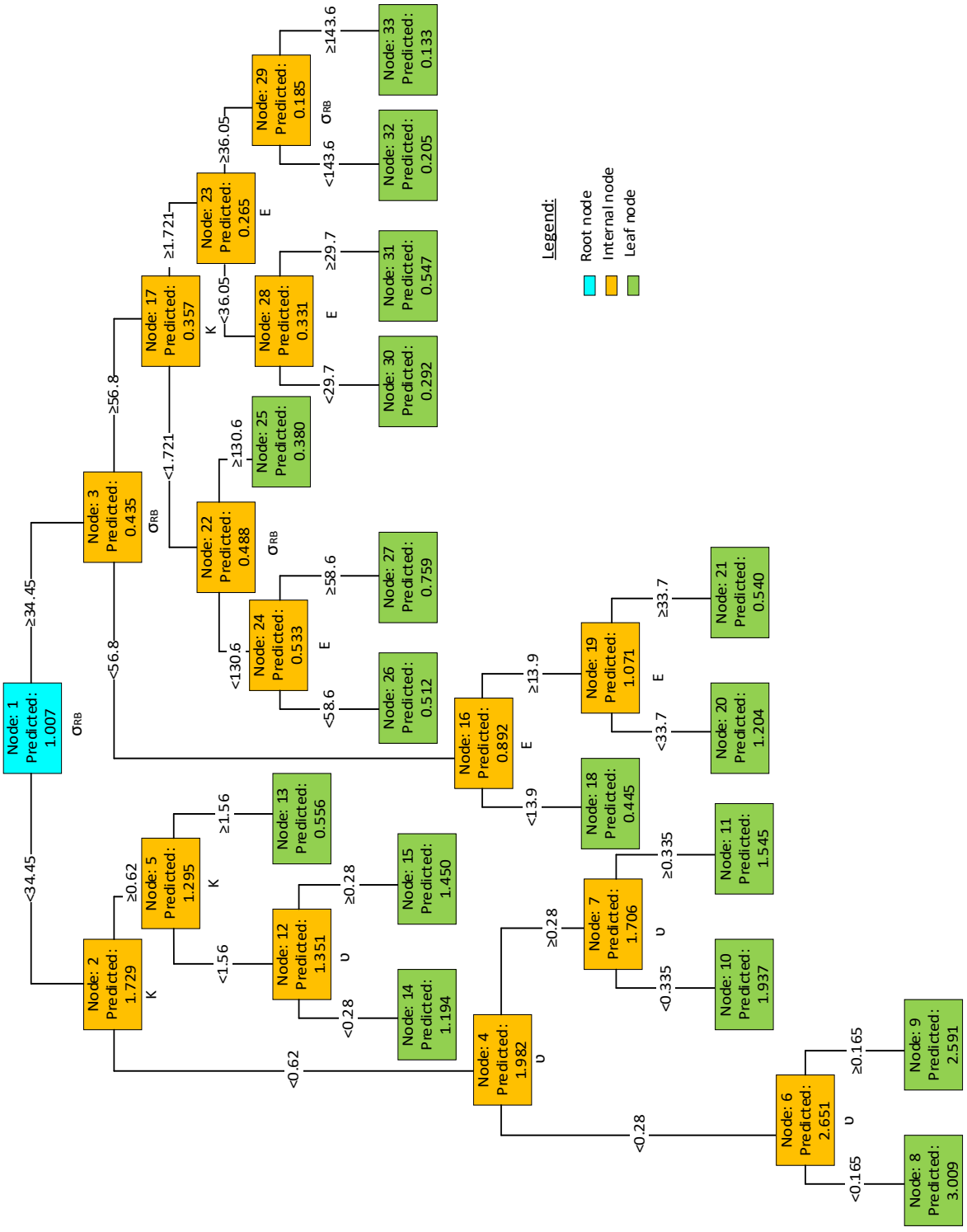

Figure 5.11 Regression tree model generated by the CART algorithm for I_{RB}

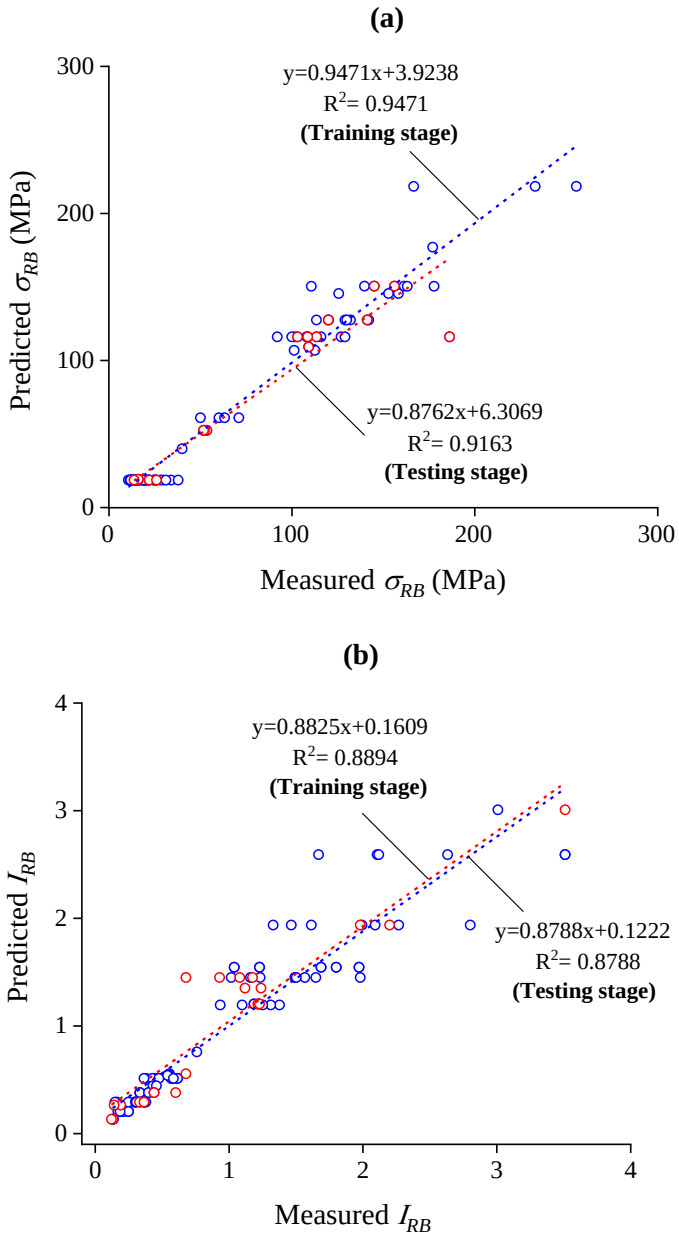

Figure 5.12 Measured vs. predicted values using the CART models in training and testing stages for: (a) σ_{RB} and (b) I_{RB}

5.4. Validation Verification

Based on a logical hypothesis (Smith 1986; Alavi and Gandomi 2011) there is a good correlation between the measured and predicted values of a dependent parameter when the absolute correlation coefficient ($|R|$) is greater than 0.8, and the error indices such as root mean squared error ($RMSE$) and mean absolute error (MAE) are at low values. There are no definite values for R^2, $RMSE$, and MAE indices for all applications, and their appropriate values usually in different sciences depend on the range of variations of the response parameter as well as the

sensitivity of the problem. Furthermore, to assess the performance of the developed models in depth, new validation indices have been proposed by other researchers. Golbraikh and Tropsha (2002) defined two indices of k and k' to validate the models on testing datasets. In addition, Roy and Roy (2008) proposed an indicator called R_m along with another related parameter of R_O^2 to check the predictability of the proposed models. The corresponding values of the k, k', R_m, and R_O^2 can be calculated based on the measured (h_i) and predicted (t_i) values of the output parameters (here are σ_{RB} and I_{RB}). The mathematical expressions of the above indices and their threshold values are listed in Table 5.7. Taking into account the recommendations, at least a slope of the regression lines (i.e. k or k') through the origin should be close to 1, while k is the slope of the regression line when h_i is plotted versus t_i, and k' is the regression line when t_i is plotted versus h_i (Golbraikh and Tropsha 2002). The squared correlation coefficient between the predicted and measured values (R_O^2) should be close to 1. The R_m, then, can be calculated by R and R_O^2 values, and a threshold of > 0.5 is recommended for this index to introduce a model as valid. The foregoing indices were calculated for the developed GEP-based and CART-based models, and their values are listed in Table 5.7. Indeed, the indices of R, k, k', R_m, and R_O^2 were used to verify the validity of the models in testing stage as recommended by other researchers (Mohammadzadeh et al. 2016; Soleimani et al. 2018). Then, the statistical indices of R^2, $RMSE$, and MAE were calculated to compare the prediction performance of the GEP and CART models for σ_{RB} and I_{RB} based on testing datasets to select the best models. It can be observed from Table 5.7 that the both proposed models in this study satisfy all the required conditions, and this guarantees that the derived models are strongly credible i.e. the results are not based on chance factor. In addition, comparing the R^2, $RMSE$, and MAE values of GEP and CART models show that both proposed models have a high degree of accuracy and low estimation error, and subsequently have this capability to be used in practical applications. However, the GEP models of σ_{RB} and I_{RB} outperformed the CART models and have slightly better performance. The next section aims to do a parametric analysis on the selected models (i.e. GEP models) to appraise the effect of the variation of input parameters on the predicted values.

Table 5.7 Statistical indices for the external validation of the developed models

Item	Formula	Threshold	σ_{RB}		I_{RB}	
			GEP	CART	GEP	CART
1	$R = \frac{\sum_{i=1}^{n}(h_i - \bar{h_i})(t_i - \bar{t_i})}{\sqrt{\sum_{i=1}^{n}(h_i - \bar{h_i})^2 \sum_{i=1}^{n}(t_i - \bar{t_i})^2}}$	$R > 0.8$	0.969	0.957	0.972	0.943
2	$k = \frac{\sum_{i=1}^{n}(h_i t_i)}{\sum_{i=1}^{n} {h_i}^2}$	$0.85 < k < 1.15$	0.934	0.931	0.962	0.981
3	$k' = \frac{\sum_{i=1}^{n}(h_i t_i)}{\sum_{i=1}^{n} {t_i}^2}$	$0.85 < k' < 1.15$	1.046	1.040	1.014	0.971
4	$R_m = R^2(1 - \sqrt{\lvert R^2 - R_O^2 \rvert})$	$R_m > 0.5$	0.763	0.698	0.739	0.596
	$R_O^2 = 1 - \frac{\sum_{i=1}^{n}(t_i - h_i^O)^2}{\sum_{i=1}^{n}(t_i - \bar{t_i})^2}$, $h_i^O = k\, t_i$	Should be close to 1	0.987	0.986	0.997	0.999
5	R^2	Should be close to 1	0.939	0.916	0.946	0.889
6	$RMSE = \sqrt{\frac{1}{n}\sum_{i=1}^{n}(h_i - t_i)^2}$	Should be minimum (based on output range)	14.249	16.426	0.195	0.273
7	$MAE = \frac{1}{n}\sum_{i=1}^{n}\lvert h_i - t_i \rvert$	Should be minimum (based on output range)	9.803	8.041	0.136	0.187

h_i: measured output; t_i: predicted output

5.5. Parametric Analysis

To investigate the influence of each input parameter on the predicted values of the corresponding output, a parametric analysis was carried out based on the selected GEP models for σ_{RB} and I_{RB}. This analysis also can be another validation for the GEP models by evaluating how well the results (predicted values) agree with the physical behaviour of the rockburst parameters. To do so, the desired independent parameter should be varied within its range of values, while other independent parameters are constant in their averages. Figs. 5.13 and 5.14 plot the variation of input parameters against the predicted values for rockburst parameters. As it is seen in Fig. 5.13, the σ_{RB} increases monotonically in a non-linear fashion with UCS and σ_v. This result is expected since with the increase of UCS, the capacity of the rock to accumulate the strain energy increases, and finally, bursting occurs at a higher stress level violently (Singh 1987). On the other hand, the in-situ stresses, especially the vertical in-situ stress (σ_v) are increased in a linear or non-linear relationship with depth (Wagner 2019) and subsequently, due to a high geo-stress state in deep conditions, the σ_{RB} is enhanced. However, there are many fluctuations in σ_{RB} values with the increase of Young's modulus (E) of rocks, but in general, an increment trend can be seen. It should be mentioned that a parameter may do not show a meaningful relationship solely with the output parameter, while it can be an influential

component in a combination of other parameters in a non-linear form. As mentioned in the GEP modelling section, during the modelling procedure, by applying the variable pressure coefficient, excluding any of the selected three parameters (i.e. UCS, E, and σ_v) from the modelling procedure did not improve the accuracy and complexity of the model.

Regarding I_{RB}, a non-linear decreasing trend can be observed for its values with all input parameters of Young's modulus (E), Poisson's ratio (ν), horizontal pressure coefficient (K), and rockburst maximum stress (σ_{RB}). As can be seen from Fig. 5.14, with the increase of E until 20 MPa, the rockburst risk index is decreased suddenly but it remains almost constant with a further increment of E. Moreover, with the increase of Poisson's ratio (ν) in its range of values, the risk value decreases from 0.473 to 0.40 that according to Table 1, the risk of rockburst occurrence is low. Hence, it seems that the variation of ν has no significant influence on rockburst risk. However, it is still necessary to do more tests on rocks with a greater range of ν to check its influence on risk parameter. Generally, the risk of rockburst occurrence for rocks with low strength (or lower σ_{RB}) which are in low depth (or higher K) is higher than high-strength rocks in deep conditions. From the results displayed in Figs. 5.13 and 5.14, several non-linear equations between rockburst parameters (σ_{RB}, and I_{RB}) and their related input parameters (except for $\sigma_{RB} - E$ and $I_{RB} - E$) are extracted as follows:

$$\sigma_{RB} = 19.911Ln(UCS) + 10.636, \quad R^2 = 0.9974 \tag{5.14}$$

$$\sigma_{RB} = -0.0007{\sigma_v}^2 + 0.7162\sigma_v + 41.092, \quad R^2 = 0.9877 \tag{5.15}$$

$$I_{RB} = 0.49e^{-0.535\upsilon}, \quad R^2 = 0.9997 \tag{5.16}$$

$$I_{RB} = -0.0186K^3 + 0.2124K^2 - 0.7981K + 1.1997, \quad R^2 = 0.9521 \tag{5.17}$$

$$I_{RB} = 1.2524{\sigma_{RB}}^{-0.244}, \quad R^2 = 0.9859 \tag{5.18}$$

According to the above results, clearly can be seen that there is a good correlation between the rockburst parameters and the inputs. These equations provide a series of simple equations for calculating σ_{RB} and I_{RB} based on the single rock mechanical parameter as a primary assessment. These equations may be relevant to investigate rockburst potential. In the end, it is necessary to mention that the developed models in this study are based on the collected datasets and a specific range of values for different parameters. So, for future applications, if the input parameters are out of these ranges, the proposed models should be adjusted again.

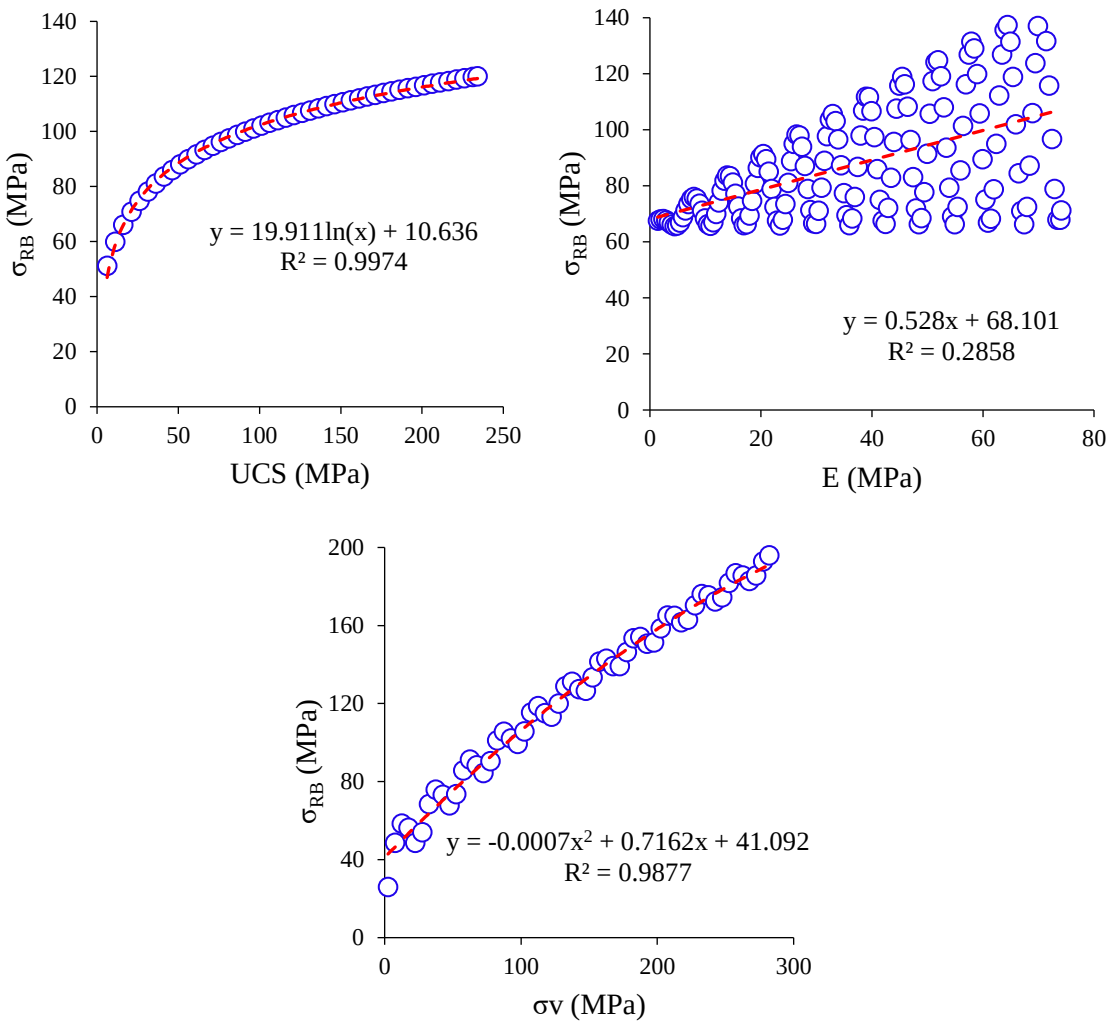

Figure 5.13 Parametric analysis of σ_{RB} on GEP model

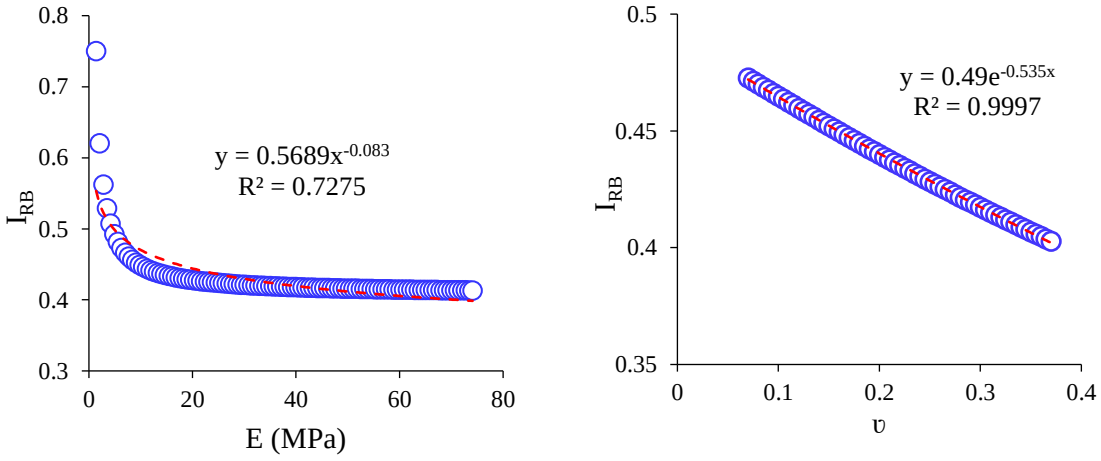

Figure 5.14 Parametric analysis of I_{RB} on GEP model

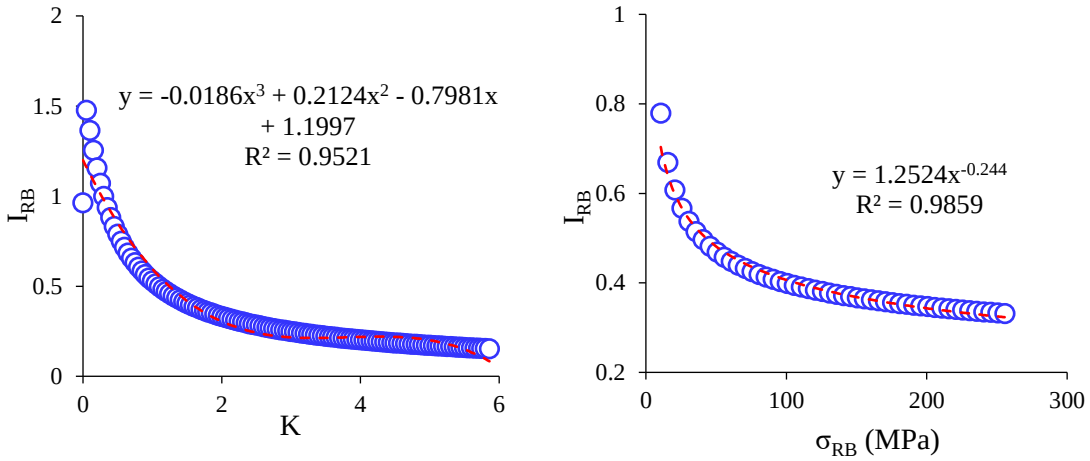

Figure 5.14 (Continued)

5.6. Summary and Conclusions

As a catastrophic geohazard, rockburst threatens the safety of workers and infrastructures in deep geotechnical conditions. In this study, considering the importance of the stress level that rockburst occurs for different rock types in real stress circumstances, two important rockburst parameters including the maximum rockburst stress (σ_{RB}) and rockburst risk index (I_{RB}) were formulated using the information obtained from true-triaxial unloading tests and two robust data-driven approaches. A comprehensive strategy was applied to the compiled database using the correlation analysis, the agglomerative hierarchical clustering (AHC) technique, and the stepwise selection and elimination (SSE) procedure to provide a homogeneous database free from any outliers, natural groups, and especially, to identify the most influential parameters on σ_{RB} and I_{RB}. Then, new non-linear models were developed using robust algorithms of gene expression programming (GEP) and classification and regression tree (CART). Finally, a parametric analysis was conducted to study the variation of σ_{RB} and I_{RB} with the change of input parameters. The conclusions obtained from this study are presented in the following.

The correlation analysis, AHC, SSE, and multiple regression analysis techniques, as recommended and implemented in the current study, have presented promising results by dimension reduction (i.e. eliminating the redundant input parameters) and choosing the statistically significant parameters that affect the rockburst parameters (i.e. σ_{RB} and I_{RB}). This procedure simplifies the rockburst assessment at the field scale. The obtained dendrogram by AHC analysis (Fig. 5.5) showed that there is no natural group in the compiled database except for two data samples that were identified as outliers and subsequently were eliminated from the original database. Therefore, the database was identified as a homogeneous database for

further analysis. The statistically ascertained and selected dominant parameters affecting σ_{RB} and I_{RB} in deep geotechnical conditions have been found as UCS, E, and σ_v for the maximum rockburst stress (σ_{RB}), and ρ, K, E, υ and σ_{RB} for the rockburst risk index (I_{RB}) by SSE and multicollinearity analyses.

The proposed non-linear GEP-based and CART-based models by providing the mathematical functions and visual patterns could unravel the latent relationships between the rockburst parameters (i.e. σ_{RB} and I_{RB}) and their corresponding influential parameters, and the validity of these models was proved based on several statistical indices (Table 5.7). However, the GEP-based models with the values of 0.9398, 14.2493, and 9.8025 for the performance indices of R^2, $RMSE$, and MAE for σ_{RB} and the values of 0.9459, 0.1947, and 0.1365 for the foregoing performance indices for I_{RB} outperformed the CART models. The results show that the used robust techniques can be useful tools for solving the high-complex non-linear problems which are common in mining and geotechnical projects. The results obtained from the parametric analysis on the proposed GEP models for σ_{RB} and I_{RB} showed that the stress level that rockburst occurs increases monotonically with the increase of UCS and σ_v. As such, the risk of rockburst occurrence showed a downward non-linear trend with K, E, υ and σ_{RB} parameters. On the other hand, the parametric analysis revealed that there are strong correlations between the rockburst parameters and their input parameters which show that the selected inputs are potential indicators for assessing and predicting rockburst phenomenon in deep underground openings.

Appendix A

Table A.1 If-then rules of the constructed regression tree for σ_{RB}

Node	Rule
1	-
2	If UCS in [6.2, 40.45) then σ_{RB}= 19.178 in 47.7% of cases
3	If UCS in [40.45, 234.1) then σ_{RB}= 124.173 in 52.3% of cases
4	If σ_v in [7.2, 37) and UCS in [6.2, 40.45) then σ_{RB}= 18.658 in 46.5% of cases
5	If σ_v in [37, 40) and UCS in [6.2, 40.45) then σ_{RB}= 40 in 1.2% of cases
6	If σ_v in [22.3, 169.455) and UCS in [40.45, 234.1) then σ_{RB}= 115.993 in 47.7% of cases
7	If σ_v in [169.455, 282) and UCS in [40.45, 234.1) then σ_{RB}= 208.025 in 4.7% of cases
8	If σ_v in [22.3, 63.3) and UCS in [40.45, 234.1) then σ_{RB}= 89.331 in 15.1% of cases
9	If σ_v in [63.3, 169.455) and UCS in [40.45, 234.1) then σ_{RB}= 128.371 in 32.6% of cases
10	If UCS in [40.45, 91) and σ_v in [22.3, 63.3) then σ_{RB}= 63.863 in 9.3% of cases
11	If UCS in [91, 234.1) and σ_v in [22.3, 63.3) then σ_{RB}= 130.080 in 5.8% of cases
12	If UCS in [40.45, 77.75) and σ_v in [22.3, 63.3) then σ_{RB}= 70.700 in 5.8% of cases
13	If UCS in [77.75, 91) and σ_v in [22.3, 63.3) then σ_{RB}= 52.467 in 3.5% of cases

14	If σ_v in [22.3, 44.05) and UCS in [40.45, 77.75) then σ_{RB}= 61.075 in 4.7% of cases
15	If σ_v in [44.05, 63.3) and UCS in [40.45, 77.75) then σ_{RB}= 109.200 in 1.2% of cases
16	If σ_v in [22.3, 34) and UCS in [91, 234.1) then σ_{RB}= 145.533 in 3.5% of cases
17	If σ_v in [34, 63.3) and UCS in [91, 234.1) then σ_{RB}= 106.900 in 2.3% of cases
18	If UCS in [40.45, 151.3) and σ_v in [63.3, 169.455) then σ_{RB}= 123.561 in 26.7% of cases
19	If UCS in [151.3, 234.1) and σ_v in [63.3, 169.455) then σ_{RB}= 150.500 in 5.8% of cases
20	If σ_v in [63.3, 143.5) and UCS in [40.45, 151.3) then σ_{RB}= 120.990 in 24.4% of cases
21	If σ_v in [143.5, 169.455) and UCS in [40.45, 151.3) then σ_{RB}= 150.550 in 2.3% of cases
22	If σ_v in [63.3, 118.4) and UCS in [40.45, 151.3) then σ_{RB}= 116.100 in 14.0% of cases
23	If σ_v in [118.4, 143.5) and UCS in [40.45, 151.3) then σ_{RB}= 127.511 in 10.5% of cases
24	If σ_v in [63.3, 125.75) and UCS in [151.3, 234.1) then σ_{RB}= 150.467 in 3.5% of cases
25	If σ_v in [125.75, 169.455) and UCS in [151.3, 234.1) then σ_{RB}= 150.550 in 2.3% of cases
26	If E in [14.1, 20.7) and σ_v in [169.455, 282) and UCS in [40.45, 234.1) then σ_{RB}= 177 in 1.2% of cases
27	If E in [20.7, 66.7) and σ_v in [169.455, 282) and UCS in [40.45, 234.1) then σ_{RB}= 218.367 in 3.5% of cases

Table A.2 If-then rules of the constructed regression tree for I_{RB}

Node	Rule
1	-
2	If σ_{RB} in [10.6, 34.45) then I_{RB}= 1.729 in 44.2% of cases
3	If σ_{RB} in [34.45, 255.5) then I_{RB}= 0.435 in 55.8% of cases
4	If K in [0.222, 0.62) and σ_{RB} in [10.6, 34.45) then I_{RB}= 1.982 in 27.9% of cases
5	If K in [0.62, 2.245) and σ_{RB} in [10.6, 34.45) then I_{RB}= 1.295 in 16.3% of cases
6	If ν in [0.07, 0.28) and K in [0.222, 0.62) and σ_{RB} in [10.6, 34.45) then I_{RB}= 2.651 in 8.1% of cases
7	If ν in [0.28, 0.37) and K in [0.222, 0.62) and σ_{RB} in [10.6, 34.45) then I_{RB}= 1.706 in 19.8% of cases
8	If ν in [0.07, 0.165) and K in [0.222, 0.62) and σ_{RB} in [10.6, 34.45) then I_{RB}= 3.009 in 1.2% of cases
9	If ν in [0.165, 0.28) and K in [0.222, 0.62) and σ_{RB} in [10.6, 34.45) then I_{RB}= 2.591 in 7.0% of cases
10	If ν in [0.28, 0.335) and K in [0.222, 0.62) and σ_{RB} in [10.6, 34.45) then I_{RB}= 1.937 in 8.1% of cases
11	If ν in [0.335, 0.37) and K in [0.222, 0.62) and σ_{RB} in [10.6, 34.45) then I_{RB}= 1.545 in 11.6% of cases
12	If K in [0.62, 1.56) and σ_{RB} in [10.6, 34.45) then I_{RB}= 1.351 in 15.1% of cases
13	If K in [1.56, 2.245) and σ_{RB} in [10.6, 34.45) then I_{RB}= 0.556 in 1.2% of cases
14	If ν in [0.27, 0.28) and K in [0.62, 1.56) and σ_{RB} in [10.6, 34.45) then I_{RB}= 1.194 in 5.8% of cases
15	If ν in [0.28, 0.33) and K in [0.62, 1.56) and σ_{RB} in [10.6, 34.45) then I_{RB}= 1.450 in 9.3% of cases
16	If σ_{RB} in [34.45, 56.8) then I_{RB}= 0.892 in 8.1% of cases
17	If σ_{RB} in [56.8, 255.5) then I_{RB}= 0.357 in 47.7% of cases
18	If E in [3.5, 13.9) and σ_{RB} in [34.45, 56.8) then I_{RB}= 0.445 in 2.3% of cases
19	If E in [13.9, 43.1) and σ_{RB} in [34.45, 56.8) then I_{RB}= 1.071 in 5.8% of cases
20	If E in [13.9, 33.7) and σ_{RB} in [34.45, 56.8) then I_{RB}= 1.204 in 4.7% of cases
21	If E in [33.7, 43.1) and σ_{RB} in [34.45, 56.8) then I_{RB}= 0.540 in 1.2% of cases
22	If K in [0, 1.721) and σ_{RB} in [56.8, 255.5) then I_{RB}= 0.488 in 19.8% of cases
23	If K in [1.721, 5.866) and σ_{RB} in [56.8, 255.5) then I_{RB}= 0.265 in 27.9% of cases
24	If σ_{RB} in [56.8, 130.6) and K in [0, 1.721) then I_{RB}= 0.533 in 14.0% of cases
25	If σ_{RB} in [130.6, 255.5) and K in [0, 1.721) then I_{RB}= 0.380 in 5.8% of cases
26	If E in [14.1, 58.6) and σ_{RB} in [56.8, 130.6) and K in [0, 1.721) then I_{RB}= 0.512 in 12.8% of cases
27	If E in [58.6, 74.1) and σ_{RB} in [56.8, 130.6) and K in [0, 1.721) then I_{RB}= 0.759 in 1.2% of cases
28	If E in [14.1, 36.05) and K in [1.721, 5.866) and σ_{RB} in [56.8, 255.5) then I_{RB}= 0.331 in 15.1% of cases

29	If E in [36.05, 71) and K in [1.721, 5.866) and σ_{RB} in [56.8, 255.5) then I_{RB}= 0.185 in 12.8% of cases
30	If E in [14.1, 29.7) and K in [1.721, 5.866) and σ_{RB} in [56.8, 255.5) then I_{RB}= 0.292 in 12.8% of cases
31	If E in [29.7, 36.05) and K in [1.721, 5.866) and σ_{RB} in [56.8, 255.5) then I_{RB}= 0.547 in 2.3% of cases
32	If σ_{RB} in [56.8, 143.6) and E in [36.05, 71) and K in [1.721, 5.866) then I_{RB}= 0.205 in 9.3% of cases
33	If σ_{RB} in [143.6, 255.5) and E in [36.05, 71) and K in [1.721, 5.866) then I_{RB}= 0.133 in 3.5% of cases

References

Akdag S, Karakus M, Taheri A, et al (2018) Effects of Thermal Damage on Strain Burst Mechanism for Brittle Rocks Under True-Triaxial Loading Conditions. *Rock Mechanics and Rock Engineering* 51(6):1–26

Alavi AH, Gandomi AH (2011) A robust data mining approach for formulation of geotechnical engineering systems. *Engineering Computations* 28(3):242–274

Alavi AH, Hasni H, Lajnef N, et al (2016) Damage detection using self-powered wireless sensor data: An evolutionary approach. *Measurement: Journal of the International Measurement Confederation* 82:254–283

Archontoulis S V, Miguez FE (2015) Nonlinear regression models and applications in agricultural research. *Agronomy Journal* 107(2):786–798

Armaghani DJ, Faradonbeh RS, Rezaei H, et al (2016) Settlement prediction of the rock-socketed piles through a new technique based on gene expression programming. *Neural Computing and Applications* 29(11):1115-1125

Bagde MN, Petroš V (2005) Fatigue properties of intact sandstone samples subjected to dynamic uniaxial cyclical loading. *International Journal of Rock Mechanics and Mining Sciences* 42(2):237–250

Barquins M, Petit J-P (1992) Kinetic instabilities during the propagation of a branch crack: effects of loading conditions and internal pressure. *Journal of Structural Geology* 14(8-9):893–903

Bethea RM (2018) Statistical methods for engineers and scientists. *Routledge*

Bevilacqua M, Braglia M, Montanari R (2003) The classification and regression tree approach to pump failure rate analysis. *Reliability Engineering & System Safety* 79(1):59–67

Breiman L, Friedman J, Stone CJ, Olshen RA (1984) Classification and Regression Trees. *CRC press*

Cai M, Kaiser P (2018) Rockburst support reference book—volume I: rockburst phenomenon and support characteristics. *Laurentian University*

Chen G, Li T, Wang W, et al (2019) Weakening effects of the presence of water on the brittleness of hard sandstone. *Bulletin of Engineering Geology and the Environment* 78(3):1471–1483

Chen J, Su G (2010) True triaxial experimental study on hard rock under high geo-stress condition based on excavation and support. In: 2010 *International Conference on Mechanic Automation and Control Engineering*. pp 1465–1467

Cheon DS, Keon S, Park C, Ryu C (2006) An experimental study on the brittle failure under true triaxial conditions. *Tunnelling and underground space technology* 21(3-4)

Cook NGW (1963) The basic mechanics of rockbursts. *Journal of the Southern African Institute of Mining and Metallurgy* 64(3):71–81

Cortez P, Embrechts MJ (2011) Opening black box Data Mining models using Sensitivity Analysis. In: *IEEE Symposium on Computational Intelligence and Data Mining*

Faradonbeh RS, Monjezi M (2017) Prediction and minimization of blast-induced ground vibration using two robust meta-heuristic algorithms. *Engineering with Computers* 1–17

Feng XT, Chen B, Feng G, Zhao Z, Zheng H (2017) Description and engineering phenomenon of rockbursts. In: Rockburst: Mechanisms, Monitoring, Warning, and Mitigation. first ed. *Elsevier-Health Sciences Division* 3-17

Ferreira C (2006) Gene expression programming: mathematical modeling by an artificial intelligence. *Springer*

Ferreira C (2002) Gene Expression Programming in Problem Solving. In: Roy R, Köppen M, Ovaska S, et al. (eds) Soft Computing and Industry: Recent Applications. *Springer London*, London, pp 635–653

Ghasemi E (2017) Particle swarm optimization approach for forecasting backbreak induced by bench blasting. *Neural Computing and Applications* 28(7):1855–1862

Ghasemi E, Kalhori H, Bagherpour R (2017) Stability assessment of hard rock pillars using two intelligent classification techniques: A comparative study. *Tunnelling and Underground Space Technology* 68:32–37

Golbraikh A, Tropsha A (2002) Beware of q2! *Journal of Molecular Graphics and Modelling* 20(4):269–276

Hasanipanah M, Faradonbeh RS, Amnieh HB, et al (2017a) Forecasting blast-induced ground vibration developing a CART model. *Engineering with Computers* 33(2):307-316

Hasanipanah M, Faradonbeh RS, Armaghani DJ, et al (2017b) Development of a precise model for prediction of blast-induced flyrock using regression tree technique. *Environmental Earth Sciences* 76(1)

He J, Dou L, Gong S, et al (2017) Rock burst assessment and prediction by dynamic and static stress analysis based on micro-seismic monitoring. *International Journal of Rock Mechanics and Mining Sciences* 100(93):46–53

He M (2009) The mechanism of rockburst and its countermeasure of support. *Consultation Report for the Key Technology of Safe and Rapid Construction for Jinping LI Hydropower Station High Overburden and Long Tunnels* 23–28

He M, e Sousa LR, Miranda T, Zhu G (2015) Rockburst laboratory tests database - Application of data mining techniques. *Engineering Geology* 185:116–130

He M, Gong W, Wang J, et al (2014) Development of a novel energy-absorbing bolt with extraordinarily large elongation and constant resistance. *International Journal of Rock Mechanics and Mining Sciences* 67:29–42

He M, Ren F, Liu D (2018) Rockburst mechanism research and its control. *International Journal of Mining Science and Technology* 28(5):829–837

He M, Xia H, Jia X, et al (2012) Studies on classification, criteria and control of rockbursts. J*ournal of Rock Mechanics and Geotechnical Engineering* 4(2):97–114

He MC, Miao JL, Feng JL (2010) Rock burst process of limestone and its acoustic emission characteristics under true-triaxial unloading conditions. *International Journal of Rock Mechanics and Mining Sciences* 47(2):286–298

Hemmateenejad B, Yazdani M (2009) QSPR models for half-wave reduction potential of steroids: A comparative study between feature selection and feature extraction from subsets of or entire set of descriptors. *Analytica Chimica Acta* 634(1):27–35

Hoseinian FS, Faradonbeh RS, Abdollahzadeh A, et al (2017) Semi-autogenous mill power

model development using gene expression programming. *Powder Technology* 308:61-69

Hudaverdi T (2012) Application of multivariate analysis for prediction of blast-induced ground vibrations. *Soil Dynamics and Earthquake Engineering* 43:300–308

Jahed Armaghani D, Faradonbeh RS, Momeni E, et al (2017) Performance prediction of tunnel boring machine through developing a gene expression programming equation. *Engineering with Computers* 34(1):129-141

James G, Witten D, Hastie T, Tibshirani R (2013) An introduction to statistical learning. *Springer*

Jian Z, Xibing L, Xiuzhi S (2012) Long-term prediction model of rockburst in underground openings using heuristic algorithms and support vector machines. *Safety Science* 50(4):629–644

Kantardzic M (2003) Data Mining: Concepts, models, methods, and algorithms. *John Wiley & Sons*

Kaufman L, Rousseeuw PJ (2009) Finding groups in data: an introduction to cluster analysis. *John Wiley & Sons*

Kayadelen C (2011) Soil liquefaction modeling by Genetic Expression Programming and Neuro-Fuzzy. *Expert Systems with Applications* 38(4):4080–4087

Khandelwal M, Armaghani DJ, Faradonbeh RS, et al (2017) Classification and regression tree technique in estimating peak particle velocity caused by blasting. *Engineering with Computers* 33(1):45–53

Kumar Sharma S, Rai P (2017) Establishment of blasting design parameters influencing mean fragment size using state-of-art statistical tools and techniques. *Measurement* 96:34–51

Li D, Zhao F, Zheng M (2014) Fractal characteristics of cracks and fragments generated in unloading rockburst tests. *International Journal of Mining Science and Technology* 24(6):819–823

Li T, Cai MF, Cai M (2007) A review of mining-induced seismicity in China. *International Journal of Rock Mechanics and Mining Sciences* 44:1149–1171

Linkov AM (1996) Rockbursts and the instability of rock masses. *International Journal of Rock Mechanics and Mining Sciences & Geomechanics Abstracts* 33(7):727–732

Liu X, Liang Z, Zhang Y, et al (2018) Experimental study on the monitoring of rockburst in tunnels under dry and saturated conditions using AE and infrared monitoring. *Tunnelling and Underground Space Technology* 82:517–528

Mahjoobi J, Etemad-Shahidi A (2008) An alternative approach for the prediction of significant wave heights based on classification and regression trees. *Applied Ocean Research* 30(3):172–177

Mitchell TM (1997) Does machine learning really work? *AI Magazine* 18:11–20

Mohammadzadeh S D, Bolouri Bazaz J, Vafaee Jani Yazd SH, Alavi AH (2016) Deriving an intelligent model for soil compression index utilizing multi-gene genetic programming. *Environmental Earth Sciences* 75(3):262

Montgomery DC, Peck EA, Vining GG (2012) Introduction to Linear Regression Analysis. *Wiley*

Motulsky HJ, Ransnas LA (1987) Fitting curves to data using nonlinear regression: a practical and nonmathematical review. *The FASEB journal* 1(5):365–374

Nazari A, Pacheco Torgal F (2013) Modeling the compressive strength of geopolymeric binders by gene expression programming-GEP. *Expert Systems with Applications* 40(14):5427–5438

Power HE, Gharabaghi B, Bonakdari H, et al (2019) Prediction of wave runup on beaches using Gene-Expression Programming and empirical relationships. *Coastal Engineering* 144:47–61

Pu Y, Apel DB, Xu H (2019) Rockburst prediction in kimberlite with unsupervised learning method and support vector classifier. *Tunnelling and Underground Space Technology* 90:12–18

Quinlan JR (1986) Induction of decision trees. *Machine Learning* 1:81–106

Ranjith PG, Zhao J, Ju M, et al (2017) Opportunities and Challenges in Deep Mining: A Brief Review. *Engineering* 3(4):546–551

Roy PP, Roy K (2008) On Some Aspects of Variable Selection for Partial Least Squares Regression Models. *QSAR & Combinatorial Science* 27(3):302–313

Roy R, Köppen M, Ovaska S, et al (2002) Soft Computing and Industry: Recent Applications

Saharan MR, Mitri H (2011) Destress blasting as a mines safety tool: Some fundamental challenges for successful applications. In: *Procedia Engineering. Elsevier* 26(37-47) pp 37–47

Salimi A, Faradonbeh RS, Monjezi M, Moormann C (2016) TBM performance estimation using a classification and regression tree (CART) technique. *Bulletin of Engineering Geology and the Environment*, 77(1):429-440

Sarkhosh M, Ghasemi JB, Ayati M (2012) A quantitative structure- property relationship of gas chromatographic/mass spectrometric retention data of 85 volatile organic compounds as air pollutant materials by multivariate methods. *Chemistry Central journal* 6 Suppl 2:S4–S4

Saxena A, Prasad M, Gupta A, et al (2017) A review of clustering techniques and developments. *Neurocomputing* 267:664–681

Sayadi AR, Lashgari A, Paraszczak JJ (2012) Hard-rock LHD cost estimation using single and multiple regressions based on principal component analysis. *Tunnelling and Underground Space Technology* 27(1):133–141

Shi XZ, Zhou J, Dong L, et al (2010) Application of unascertained measurement model to prediction of classification of rockburst intensity. *Chinese Journal of Rock Mechanics and Engineering* 29(1):2720–2726

Shirani Faradonbeh R, Taheri A (2019) Long-term prediction of rockburst hazard in deep underground openings using three robust data mining techniques. *Engineering with Computers* 35(2):659–675

Singh SP (1987) The influence of rock properties on the occurrence and control of rockbursts. *Mining Science and Technology* 5(1):11–18

SMITH GN (1986) Probability and statistics in civil engineering. *Collins Professional and Technical Books* 244

Soleimani S, Rajaei S, Jiao P, et al (2018) New prediction models for unconfined compressive strength of geopolymer stabilized soil using multi-gen genetic programming. *Measurement* 113:99–107

Sousa LR (2010) Risk Analysis for Tunneling Projects. *Massachusetts Institute of Technology, Cambridge*

Su G, Chen Z, Ju JW, Jiang J (2017a) Influence of temperature on the strainburst characteristics of granite under true triaxial loading conditions. *Engineering Geology* 222:38–52

Su G, Jiang J, Zhai S, Zhang G (2017b) Influence of Tunnel Axis Stress on Strainburst: An Experimental Study. R*ock Mechanics and Rock Engineering* 50(6):1551–1567

Sun X, Xu H, Zheng L, et al (2016) An experimental investigation on acoustic emission characteristics of sandstone rockburst with different moisture contents. *Science China Technological Sciences* 59(10):1549–1558

Tang C, Wang J, Zhang J (2010) Preliminary engineering application of microseismic monitoring technique to rockburst prediction in tunneling of Jinping II project. *Journal of Rock Mechanics and Geotechnical Engineering* 2(3):193–208

Wagner H (2019) Deep Mining: A Rock Engineering Challenge. *Rock Mechanics and Rock Engineering*, 1417-1446

Wang J-A, Park HD (2001) Comprehensive prediction of rockburst based on analysis of strain energy in rocks. *Tunnelling and Underground Space Technology* 16(1):49–57

Wang X, Huang R (1998) Analysis of deformation and failure features characteristics of rock under unloading conditions and their effects on rock burst. Mountain Research 16(4):281–285

Wang Y, He M, Liu D, Gao Y (2019) Rockburst in Sandstone Containing Elliptic Holes with Varying Axial Ratios. *Advances in Materials Science and Engineering*

Weng L, Huang L, Taheri A, Li X (2017) Rockburst characteristics and numerical simulation based on a strain energy density index: A case study of a roadway in Linglong gold mine, China. *Tunnelling and Underground Space Technology* 69:223–232

Xu LS (2003) Research on the experimental rock mechanics of rockburst under unloading condition. *Journal of Chongqing Jiaotong University* 22(1):1–4

Zhao XG, Cai M (2015) Influence of specimen height-to-width ratio on the strainburst characteristics of Tianhu granite under true-triaxial unloading conditions. *Canadian Geotechnical Journal* 52(7):890–902

Zhao XG, Wang J, Cai M, et al (2014) Influence of Unloading Rate on the Strainburst Characteristics of Beishan Granite Under True-Triaxial Unloading Conditions. *Rock*

Mechanics and Rock Engineering 47(2):467–483

Zhou J, Li X, Mitri HS (2018) Evaluation method of rockburst: State-of-the-art literature review. *Tunnelling and Underground Space Technology* 81:632–659

Statement of Authorship

Title of Paper	Post-peak behaviour of rocks under cyclic loading using a double-criteria damage-controlled test method
Publication Status	☑ Published ☐ Accepted for Publication ☐ Submitted for Publication ☐ Unpublished and Unsubmitted work written in manuscript style
Publication Details	**Shirani Faradonbeh R**, Taheri A, Karakus M (2021) Post-peak behaviour of rocks under cyclic loading using a double-criteria damage-controlled tests method. *Bulletin of Engineering Geology and the Environment* 80(2):1713–1727

Principal Author

Name of Principal Author (Candidate)	Roohollah Shirani Faradonbeh		
Contribution to the Paper	Literature review, conducting the laboratory tests, analysis of the results and preparation of the manuscript		
Overall percentage (%)	80%		
Certification:	This paper reports on original research I conducted during the period of my Higher Degree by Research candidature and is not subject to any obligations or contractual agreements with a third party that would constrain its inclusion in this thesis. I am the primary author of this paper.		
Signature		Date	17 June 2021

Co-Author Contributions

By signing the Statement of Authorship, each author certifies that:

i. the candidate's stated contribution to the publication is accurate (as detailed above);
ii. permission is granted for the candidate in include the publication in the thesis; and
iii. the sum of all co-author contributions is equal to 100% less the candidate's stated contribution.

Name of Co-Author	Abbas Taheri		
Contribution to the Paper	Research supervision, review and revision of the manuscript		
Signature		Date	21 June 2021

Name of Co-Author	Murat Karakus		
Contribution to the Paper	Review and revision of the manuscript		
Signature		Date	21 June 2021

Chapter 6

Post-Peak Behaviour of Rocks Under Cyclic Loading Using a Double-Criteria Damage-Controlled Test Method

Abstract

Cyclic loading-induced hazards are severe instability problems concerning surface and underground geotechnical projects. Therefore, it is crucial to understand the rock failure mechanism under cyclic loading. An innovative double-criteria damage-controlled testing method was proposed in this study to capture the complete stress-strain response of porous limestone, especially the post-peak behaviour, under systematic cyclic loading. The proposed test method was successful in applying the pre-peak cyclic loading and then in controlling the self-sustaining failure of rock during the post-peak cyclic loading. The results showed that the strength of the rock specimens slightly increased with an increase in the fatigue life in the pre-peak region due to cyclic loading-induced hardening. Additionally, a combination of class I and class II behaviours was observed in the post-peak region during the cyclic loading tests; the class II behaviour was more dominant by the increase in fatigue life in the pre-peak region. Damage evolution was assessed based on several parameters, such as the elastic modulus, energy dissipation ratio, damage variable and crack damage threshold stress, both in the pre-peak and post-peak regions. It was found that when the cyclic loading stress is not close to the peak strength, due to a coupled mechanism of dilatant microcracking and grain crushing and pore filling, quasi-elastic behaviour dominates the cyclic loading history, causing more elastic strain energy to accumulate in the specimens.

Keywords Cyclic loading, Pre-peak and post-peak behaviour, Damage, Crack damage threshold stress, Strength hardening

6.1. Introduction

Surface and underground structures are usually exposed to environmental and human-induced cyclic loadings such as earthquakes, wind, volcanism, drilling and blasting, mechanical

excavation and mining seismicity, which threaten their long-term stability (Taheri et al. 2016; Munoz et al. 2016a). Therefore, it is necessary to evaluate the time-dependent behaviour of rocks under cyclic loading. In rock engineering, understanding the fatigue response of rocks is of particular interest since rock stability conditions vary significantly under cyclic loading. A great majority of rock fatigue studies have reported on the reduction in rock strength due to cyclic loading (Bagde and Petroš 2005). However, there are very few studies that have illustrated strength hardening when the cyclic stress level is low enough to prevent failure during cyclic loading (Burdine 1963; Singh 1989; Ma et al. 2013; Taheri et al. 2017). Unlike the static and quasi-static loadings, which the applied load/deformation increases/decreases continuously, cyclic loading is described by a time-dependent displacement/load signal with a repetitive pattern. The loading rate in cyclic experiments is relatively high and propagates waves, and their superposition causes a stress distribution different from that induced by quasi-static loading (Cho et al. 2003). In recent decades, many studies have investigated the mechanical behaviour of rocks under different cyclic loading histories and loading conditions. Most of these studies have reported the results of tests performed under uniaxial compression (Attewell and Sandford 1974; Eberhardt et al. 1999), which can replicate the stress state in mining pillars and around galleries. Other studies have focused on triaxial compression conditions with different confining pressures (Munoz et al. 2016a; Zhou et al. 2019) and indirect tensile tests (Ghamgosar and Erarslan 2016), which are useful to calibrate the advanced constitutive laws and to estimate the tensile strength of a material, respectively. In addition, few cyclic studies of flexural tests (three-point and four-point) (Cardani and Meda 2004) and freeze-thaw tests (Zhang et al. 2019a) can be found in the literature. In prior studies, the fatigue properties of rocks were found to be dependent on the loading stress level, amplitude, frequency, waveform and loading and unloading rate.

Rock behaviour in the post-peak region under uniaxial compression is characterised by either class I or class II behaviour (Fig. 6.1). The former is defined by a negative post-peak modulus describing a stable fracture propagation and the need to do more work on the specimen to degrade its load-bearing capacity, while the latter represents a positive post-peak modulus (i.e., snap-back behaviour) describing a self-sustaining (brittle) failure (Wawersik and Fairhurst 1970; Munoz et al. 2016b). The proper measurement of the post-peak behaviour of rocks can be a useful tool for quantifying the post-peak fracture energy and rock brittleness that can be employed to optimise the designation of surface and underground structures and to mitigate possible hazards (Akinbinu 2016). For instance, to evaluate the proneness and intensity of the

rockburst phenomenon near underground excavation in deep underground conditions, post-peak analysis of the rocks in terms of strain energy evolution is required. In other words, the rockburst hazard in deep underground openings is associated with not only internal strain energy accumulation but also seismic disturbances induced by external sources (Xuefeng et al. 2010). Therefore, the post-peak response of rocks subjected to cyclic loading can unveil the mechanism of geotechnical hazards such as rockburst and provide practical tools for their assessment. As shown in Fig. 6.2, the cyclic loading of rock can be undertaken following two main loading methods:

1. Systematic cyclic loading: These tests have a constant loading amplitude, $Amp.(\sigma_a)$, and can be conducted as single-level (Fig. 6.3a) or multi-level (Fig. 6.3b) testes under load-controlled or displacement-controlled (i.e., axial and lateral displacement-controlled) loading conditions. In both load-controlled and displacement-controlled conditions, the post-peak behaviour cannot be obtained, as the axial load level is the only criterion to define the amount of the load that a specimen should be subjected to during cyclic loading, until failure or even after failure. As a result, the specimen fails during cyclic loading in an uncontrolled manner, and the post-peak response cannot be obtained. Figs. 6.4a-d demonstrate the single-level and multi-level systematic cyclic tests conducted by different researchers under load-controlled and displacement-controlled conditions. As shown in these figures, in all the tests, failure occurred in an uncontrolled manner, and post-peak behaviour was not obtained. Prior systematic cyclic loading studies found that failure occurs at a stress level lower than the determined monotonic strength owing to the strength weakening process. As such, the accumulation of irreversible deformation (plastic strains) is not constant during the experiment, while the hysteresis loops follow a loose-dense-loose law (Xiao et al. 2009).
2. Damage-controlled cyclic loading: These tests involving incremental loading amplitude can be conducted in a load-based mode (Fig. 6.3c) or displacement-based mode (Fig. 6.3d). The former can be conducted either in load-controlled or displacement-controlled loading conditions (i.e., axial and lateral displacement-controlled). However, the post-peak response cannot be obtained, as the specimen might experience an uncontrolled failure when it is forced to reach a pre-defined stress level. Figs. 6.4e and f show representative results. A displacement-based test can be undertaken in either axial or lateral displacement-controlled conditions. In this type of damage-controlled test, axial

stress is reversed when a certain amount of axial or lateral displacement is achieved in a loading cycle. Munoz et al. (2016b) showed that under uniaxial loading conditions, soft, medium-strong and strong rocks demonstrate either class II or a combination of class I and class II post-peak behaviours. As a result, the post-peak response cannot be adequately measured when the test is controlled by axial displacement (Fig. 6.4g). However, by using lateral strain to control the amount of damage in a damage-controlled test, the post-peak behaviour of a brittle rock can be achieved successfully (Fig. 6.4h). From prior damage-controlled cyclic loading studies, it is reported that failure occurs at a stress level close to or lower than the determined monotonic strength. Moreover, the rate of strain accumulation under this type of loading is lower than that during systematic cyclic tests (Cerfontaine and Collin 2018).

It should be noted that previous studies have mostly focused on the influence of cyclic loadings on the mechanical rock properties and damage evolution in the pre-peak region. There are, however, a few studies investigating failure behaviour and deformation localisation during post-peak cyclic loading (e.g., Munoz and Taheri 2017a, 2019). Given the above, to the best of our knowledge, no study has investigated the post-peak response of rocks subjected to pre-peak systematic cyclic loading. This is because failure cannot be controlled when a constant axial load is achieved in every cycle in a systematic cyclic loading. In addition, in a damage-controlled test in which the lateral displacement is used to control the damage, an axial load is reversed when a certain amount of lateral strain occurs. Therefore, systematic cyclic loading cannot be applied in such a way that the load is always reversed at a constant stress level in the pre-peak region. However, rock material in engineering applications (e.g., mining pillars in deep underground conditions) may be subjected to systematic pre-peak cyclic loading and then post-failure cyclic loading. Thus, it is significant to investigate the behaviour of rock subjected to this loading condition. In this study, for the first time, a new cyclic test method considering two cyclic loading control criteria is proposed to capture the complete response of rocks, especially the post-peak behaviour, under cyclic loading. The proposed test method is a combination of multi-level systematic cyclic loading and lateral displacement-based damage-controlled cyclic loading to control both the damage and the rate of cyclic loading (see Fig. 6.2). A critical analysis is carried out to investigate damage evolution in both the pre-peak and post-peak regions, and the influences of pre-peak cyclic loading on the peak strength, crack damage threshold stress and rock stiffness are evaluated in more detail.

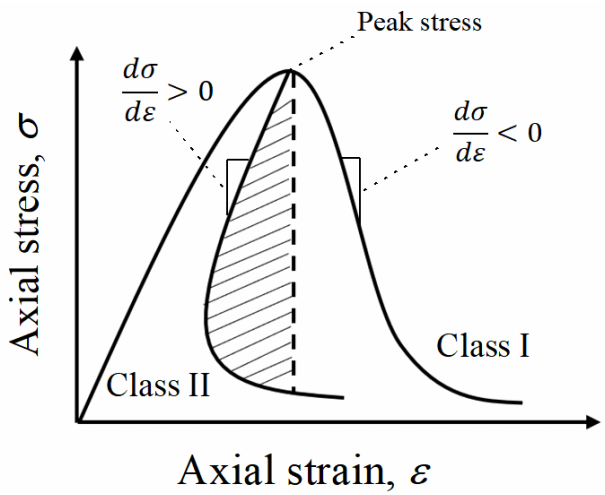

Figure 6.1 Classification of post-peak behaviour of rock in uniaxial compression (modified from Hudson et al. 1971)

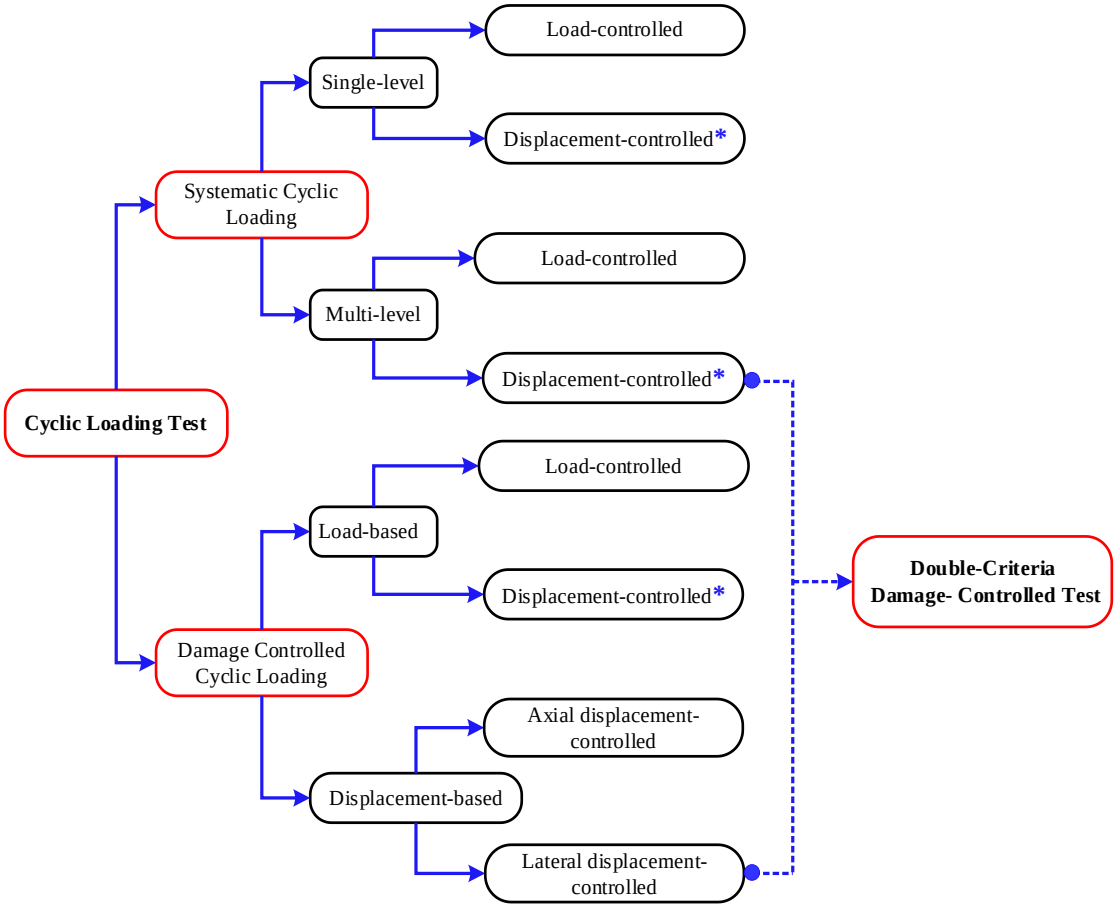

Figure 6.2 Classification of cyclic loading tests, * can be conducted in either axial or lateral displacement-controlled mode

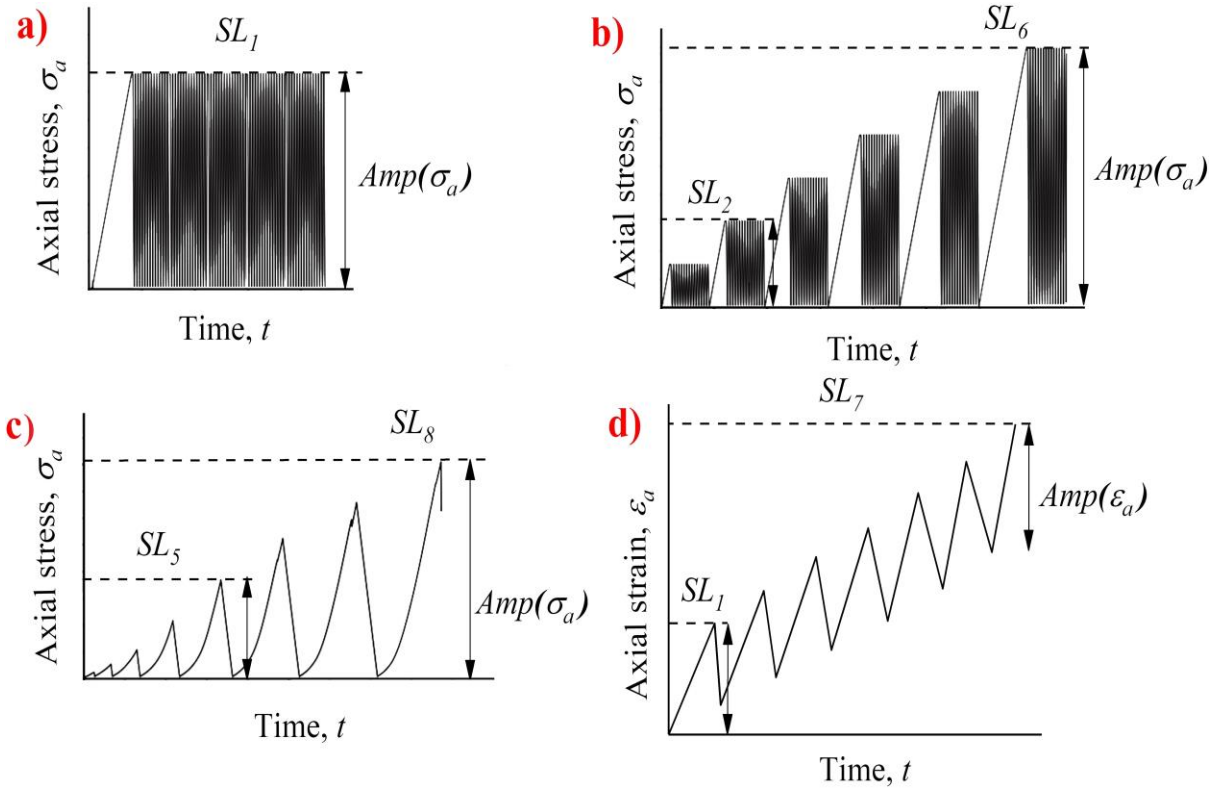

Figure 6.3 Different cyclic loading paths, **a** single-level systematic cyclic loading, **b** multi-level systematic cyclic loading, **c** load-based damage controlled cyclic loading (modified from Li et al. 2019) and **d** displacement-based damage controlled cyclic loading, $Amp(\sigma_a)$ refers to loading amplitude, $Amp(\varepsilon_a)$ refers to axial strain amplitude and SL refers to the stress level

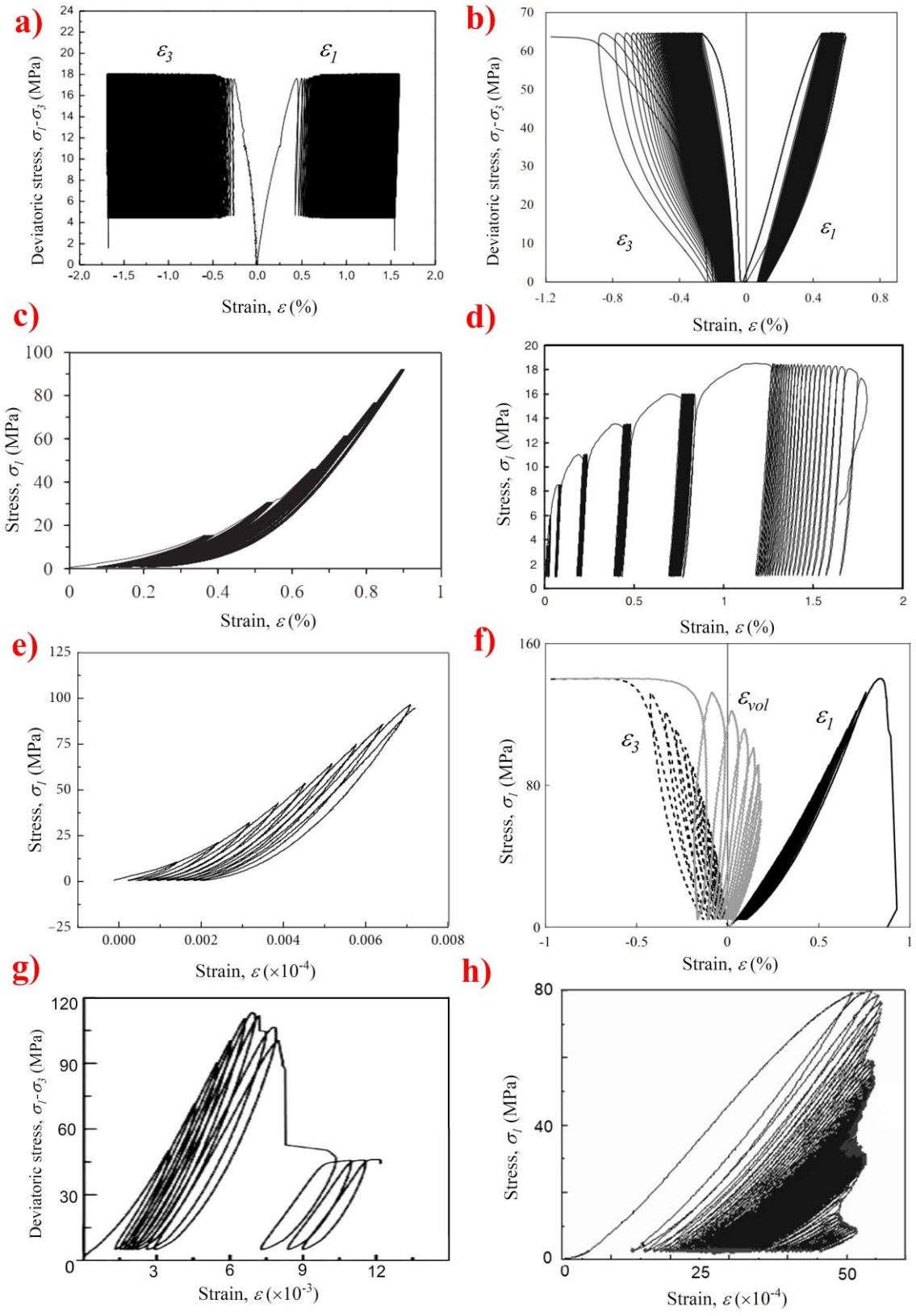

Figure 6.4 Stress-strain relation during cyclic loading in different studies, **a** single-level systematic cyclic loading load-controlled test (Ma et al. 2013), **b** single-level systematic cyclic loading axial displacement-controlled test (Taheri et al. 2016), **c** multi-level systematic

cyclic loading load-controlled test (Li et al. 2019), **d** multi-level systematic cyclic loading axial displacement-controlled test (Liu et al. 2014), **e** load-based damage controlled cyclic loading load-controlled test (Guo et al. 2018), **f** load-based damage controlled cyclic loading axial displacement-controlled test (Heap et al. 2010), **g** displacement-based damage controlled cyclic loading axial displacement-controlled test and (Wang et al. 2019) **h** displacement-based damage controlled cyclic loading lateral displacement-controlled test (Munoz and Taheri 2019)

6.2. Experimental Methodology

6.2.1. Tuffeau Limestone Specimens

Tuffeau limestone is used in this study to undertake double-criteria damage-controlled cyclic loading tests (Fig. 6.5a). The name of this rock comes from the Latin word tofus, meaning spongy rock. This yellowish-white sedimentary rock is a local limestone of the Loire Valley in France and was deposited in the middle Turonian of the Upper Cretaceous, approximately 90 million years ago. This rock type is usually extracted from surface and underground quarries and is used mostly in the building industry (Beck and Al-Mukhtar 2014). X-ray diffraction (XRD) (Fig. 6.5b) and scanning electronic microscopy (SEM) analyses (Fig. 6.5c) were carried out on collected limestone specimens to identify their mineralogical components and microstructural characteristics. Two main crystalline phases, calcite ($CaCO_3$) (≅50%) and silica (SiO_2) (≅30%), which has the two forms of quartz and opal cristobalite-tridymite (opal-CT), were identified. Other phases, such as mica and clayey minerals (e.g., muscovite, biotite, smectite, and glauconite) (≅20%), are disseminated in this limestone. Tuffeau limestone has an average density of 1.43 g/cm^3 and is a lightweight and fine-grained limestone with a complex porous network (total porosity of 45±5%). The arrangement of grains with different sizes contributes to the creation of micropores and macropores within the rock texture (Al-Mukhtar and Beck 2006). The rock specimen in Fig. 6.5c has a heterogeneous porous structure, and the microcracks, microcavities, and quartz are the main components controlling the macrofailure of the specimen under loading conditions. The cylindrical rock specimens with diameters and lengths of 42 mm and 100 mm, respectively (i.e., an aspect ratio of 2.4), were cored from a single rock block and prepared to be smooth and straight according to the ISRM standards (Fairhurst and Hudson 1999) to minimise the end friction effects and to ensure a uniform stress state within the specimen during loading. Additionally, the diameter of the

specimens is more than 20 times larger than the grain size, satisfying the ISRM recommendations (Fairhurst and Hudson 1999).

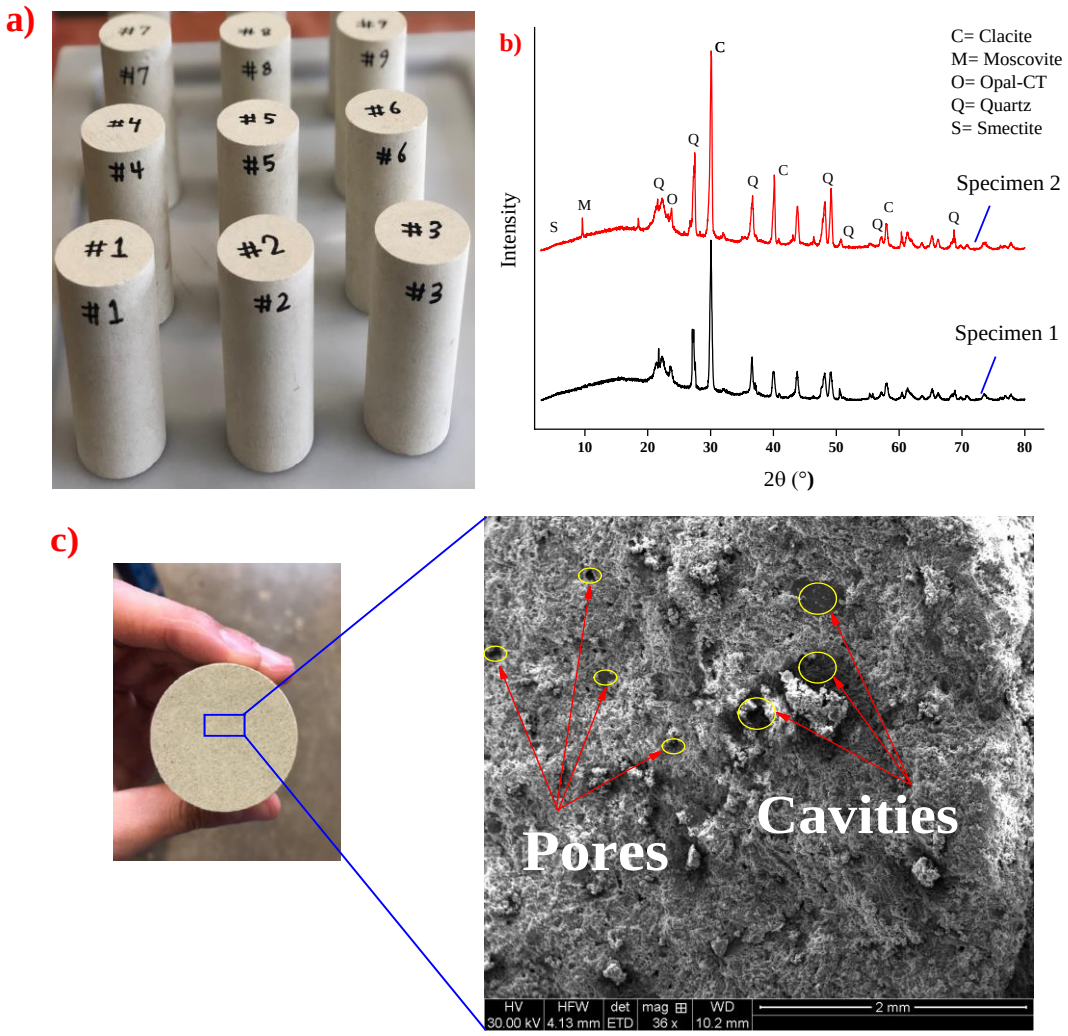

Figure 6.5 Tuffeau limestone specimens, b XRD analysis conducted for two specimens and c SEM photograph showing the diversity of porosities in a Tuffeau limestone specimen

6.2.2. Test Set-Up and Uniaxial Compression Tests

In this study, a closed-loop servo-controlled MTS hydraulic compressive machine (Fig. 6.6a) with a maximum loading capacity of 300 kN was employed to conduct compressive monotonic and cyclic tests. This fully digital servo-controlled system is capable of operating under load- or displacement-control feedback signals using a built-in computer system. In this study, the lateral strain (ε_l) feedback signal measured by a chain extensometer circumferentially mounted at the mid-length of the specimen was used as the control variable for monotonic and cyclic

tests to capture the rock behaviour before and after peak stress. The axial load (acquired by a load cell), axial strain (acquired by a pair of LVDTs), and lateral strain (acquired by a chain extensometer) were recorded simultaneously during the tests by a data acquisition system at a rate of 10 data points per second (see Fig. 6.6a). Five uniaxial monotonic tests were conducted under the lateral strain rate of 0.02×10^{-4}/s to satisfy the static to quasi-static loading conditions (Munoz and Taheri 2017b). These monotonic tests provide a reference for defining the stress levels of cyclic uniaxial compression tests. The time history of the loading (σ_a), axial strain (ε_a), and lateral strain (ε_l) for a typical monotonic loading test is shown in Fig. 6.6b. As seen in this figure, in the pre-peak and the post-peak regions, the lateral strain (ε_l) increases monotonically with time, maintaining a constant lateral strain rate throughout the test, and the complete post-peak response is obtained in a straightforward manner using the lateral strain-controlled technique. Fig. 6.6c shows the normalised stress-strain curves obtained from the five uniaxial monotonic tests. The specimens have an average monotonic compressive strength and Young's modulus of 7.39 MPa and 1.67 GPa. As seen from Fig. 6.6c, in the post-peak region, the axial stress and axial strain fluctuate successively due to the coupled mechanism of strength degradation induced by the coalescence of the macrocracks and strength recovery induced by interlocking the sides of the macrocracks. However, the total behaviour of all the conducted monotonic tests in the post-peak region is a combination of class I and class II behaviours, which is consistent with the results reported by Munoz et al. (2016a). Additionally, the conducted monotonic tests exhibit similar behaviour both in the pre-peak and the post-peak regions, which shows the low discrepancy among the tested specimens.

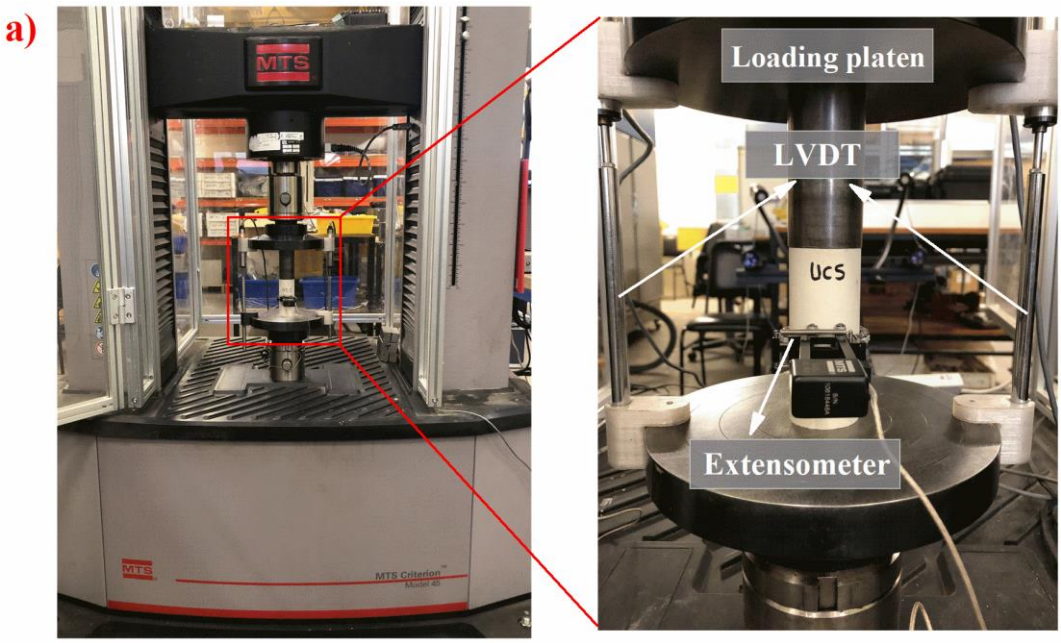

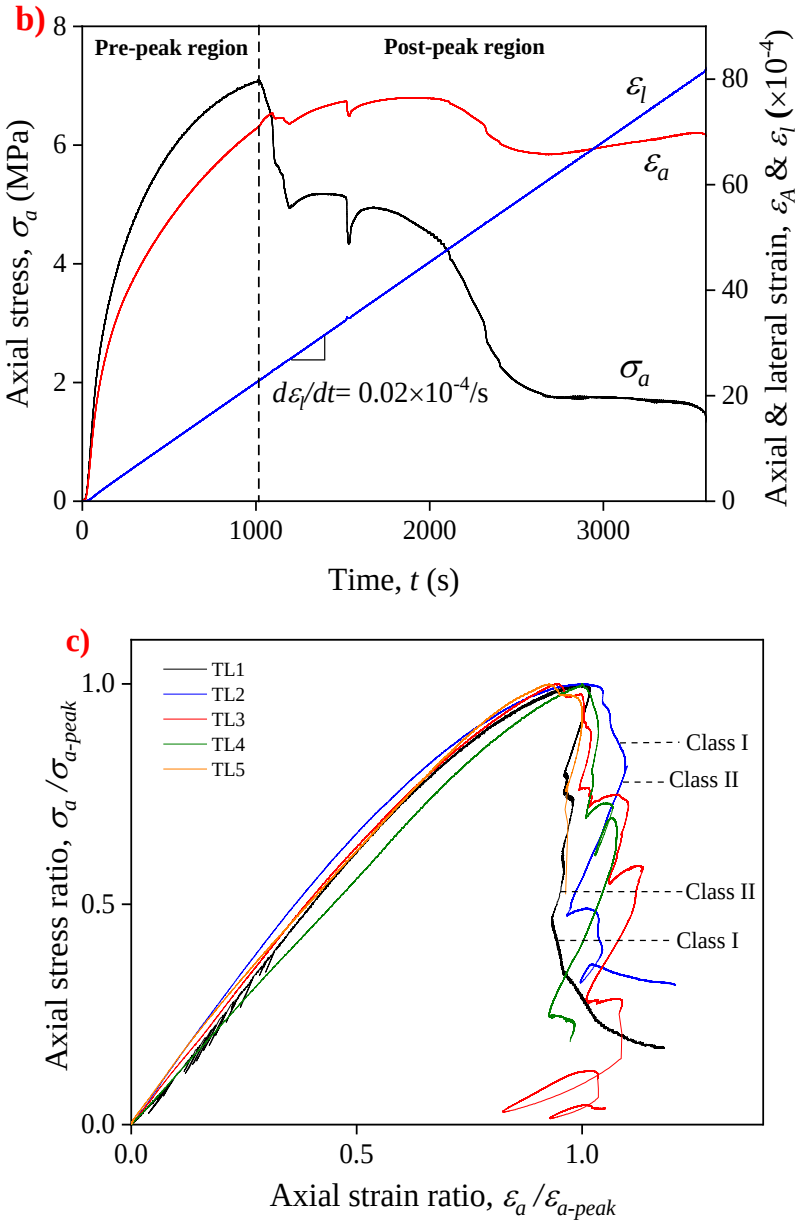

Figure 6.6 a Testing set-up for the uniaxial compression and cyclic loading tests. **b** Typical time history of the loading and strains in lateral strain–controlled uniaxial compression tests. **c** Normalised stress–strain curves of monotonic loading tests. TL tuffeau limestone

6.2.3. Double-criteria damage-controlled cyclic loading test

In this section, an innovative damage-controlled testing method is proposed to capture the post-peak behaviour of Tuffeau limestone in a multi-level systematic cyclic loading test. Fig. 6.7 schematically represents the proposed testing methodology during a closed-loop procedure. However, the test procedure can be summarised as follows:

a) The specimen is subjected to a monotonic loading under a constant lateral strain rate of 0.02×10^{-4}/s, satisfying quasi-static loading conditions, until a prescribed stress level

(here, 6 MPa) is reached. In this stage, the axial stress and lateral strain feedback signals received from the load cell and the chain extensometer, respectively, are continuously compared with the program signals (i.e., the user-defined values) and the errors, if any, are adjusted by the servo-controller. By doing so, it is guaranteed that the axial load is always applied under a constant lateral strain rate and that the axial load does not exceed the initial stress level defined for cyclic loading. Thereafter, the specimen is unloaded until the axial stress is equal to 0.07 MPa, ensuring that the specimen is always in complete contact with the loading platens.

b) Afterwards, cyclic loading is applied under a constant lateral strain rate for a specific number of cycles (i.e., 400 cycles). Two criteria are adopted to control the failure: a maximum axial stress level that can be achieved and a maximum lateral strain amplitude that a Tuffeau limestone specimen is allowed to experience in a cycle during loading, $Amp.(\varepsilon_l)$. In this study, the initial maximum stress level (i.e., the first criterion) is adopted to be equal to 6.0 MPa. The optimum values for $Amp.(\varepsilon_l)$ and the loading rate ($d\varepsilon_l/dt$) were determined based on a previous study conducted by Munoz and Taheri (2017a) on Tuffeau limestone and the results obtained from the trial tests to avoid the sudden failure of a specimen in an uncontrolled manner. Therefore, different loading rates and $Amp.(\varepsilon_l)$ values were evaluated by performing four trial cyclic loading tests, and finally, $Amp.(\varepsilon_l) = 17 \times 10^{-4}$ and $d\varepsilon_l/dt = 2 \times 10^{-4}/s$ were obtained by balancing the capability of the methodology in capturing the post-peak behaviour of the rock and completing the test in the shortest possible time. The axial load is reversed when at least one criterion is met. By following the closed-loop procedure shown in Fig. 6.7, the test is continued until the specimen fails or until 400 cycles are completed.

c) If the specimen does not fail after 400 cycles, the specimen is monotonically loaded under a constant lateral strain rate of 0.02×10^{-4}/s until the specimen is under an axial load of 6.5 MPa (i.e., a 0.5 MPa increase in the stress level compared to the previous stress level in this multi-level cycling loading scheme). If the specimen fails during monotonic loading, the complete post-peak behaviour is measured during lateral strain-controlled loading.

d) The procedure explained in b and c is repeated until the specimen fails.

Fig. 6.8 shows typical results for a Tuffeau limestone specimen. As shown in this figure, after initial monotonic loading under the constant loading rate of 0.02×10^{-4}/s, the prescribed axial

stress level (i.e., 6 MPa) is reached. Afterwards, the specimen is unloaded monotonically, and then cyclic loading is applied under a constant lateral strain rate of 2×10^{-4}/s. At the first step of cyclic loading, the amplitude of lateral strain, $Amp.(\varepsilon_l)$, is relatively low (6×10^{-4}/s after 200 cycles), and the first criterion is always met during cyclic loading (i.e., the stress level remaining below 6 MPa). As the specimen does not fail after 400 cycles, the axial load is increased monotonically to the second stress level (i.e., 6.5 MPa), and the cyclic loading procedure is repeated. As shown in Fig. 8, in the second series of cyclic loading at the onset of the failure, the lateral strain amplitude, $Amp.(\varepsilon_l)$, is equal to 17×10^{-4}. After this cycle, the second criterion controls the cyclic loading, and the strength degradation during post-peak cyclic loading is observed until complete failure. By doing so, the complete post-peak behaviour of the Tuffeau limestone under systematic cyclic loading can be successfully observed.

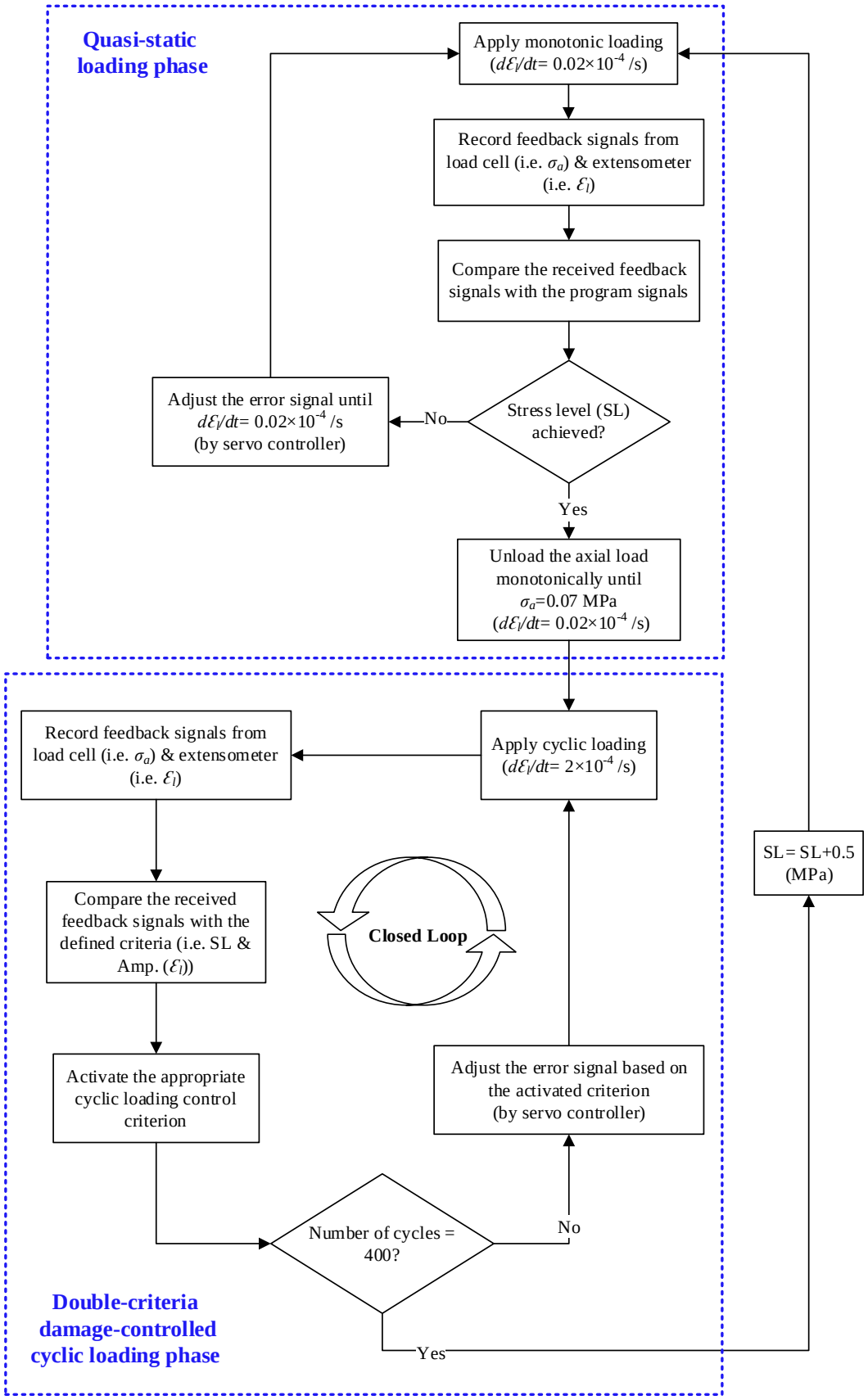

Figure 6.7 Flowchart of the double-criteria damage-controlled test method for the multi-level systematic cyclic loading

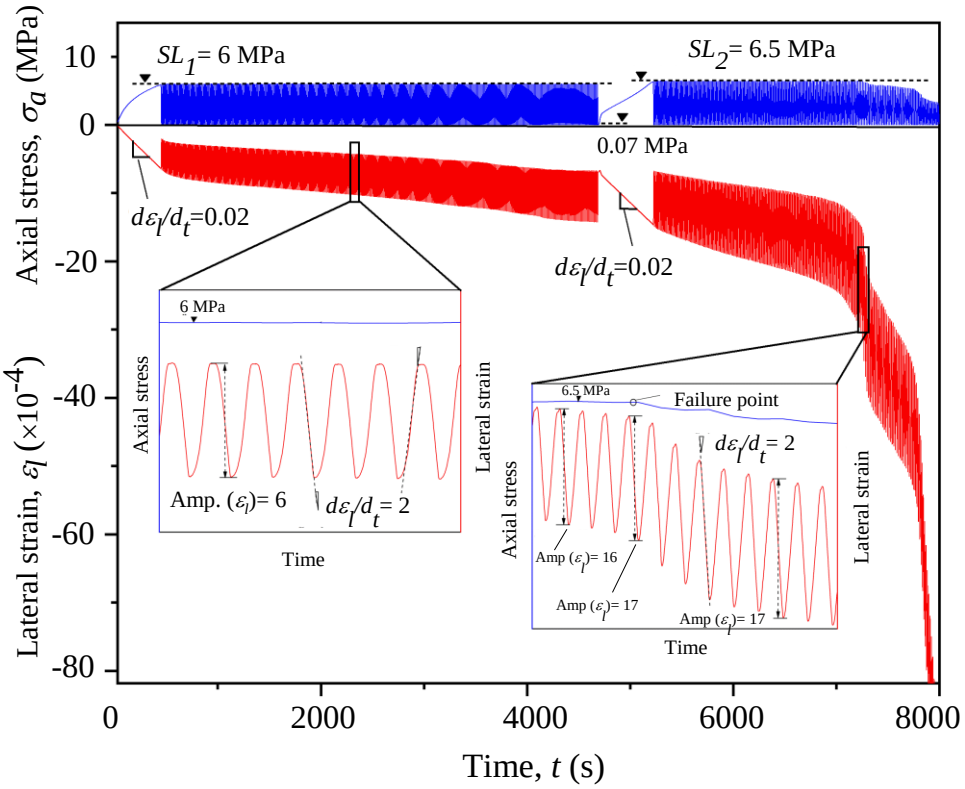

Figure 6.8 Typical time-history of axial stress and lateral strain during a double-criteria cyclic

6.3. Experimental Results

6.3.1. Complete Stress-Strain Response

In this study, three multi-level systematic cyclic loading tests were conducted using the methodology explained above to evaluate the applicability of the proposed testing method in capturing the failure behaviour of the soft and porous Tuffeau limestone. Fig. 6.9 displays the axial stress-strain relations obtained for these tests, in which 6 MPa was defined as the initial stress level, and the specimens were subjected to systematic cyclic loading at different stress levels, taking 0.5 MPa as the stress increment between consecutive cyclic loading steps. The envelope curves showing the overall behaviour of the specimens in the post-peak region were drawn by connecting the loci of the indicator stresses (q_i, the maximum stress of each cycle). As seen from Fig. 6.9, the overall post-peak behaviour of the specimens is characterised by the combination of class I and class II; however, the class I behaviour is more dominant in specimen TL6 (Fig. 6.9a) than in specimens TL7 and TL8 (Figs. 6.9b and c). Table 6.1 summarises the results of the cyclic loading tests. As listed in Table 6.1 and shown in Fig. 6.9, the different cycle numbers and stress levels are recorded for the three specimens before failure; for example, specimen TL8 experienced 2906 cycles before failure, and its failure occurred at

a stress level of 9.5 MPa. On the other hand, specimen TL6 exhibited the lowest fatigue strength (i.e., 6.5 MPa) and underwent the fewest number of cycles (i.e., 564) before the failure point. Similar loading conditions were applied to all the specimens, and the results suggest that with the increase in cycle number and thus the loading level before failure, the fatigue strength of the specimens increased and strength hardening occurred. Strength hardening due to cyclic loading has been reported for porous Hawkesbury sandstone (Taheri et al. 2016), hard greywacke sandstone (Singh 1989), Berea sandstone (Burdine 1963), and rock salt (Ma et al. 2013). This phenomenon is discussed in more detail in section 6.4.

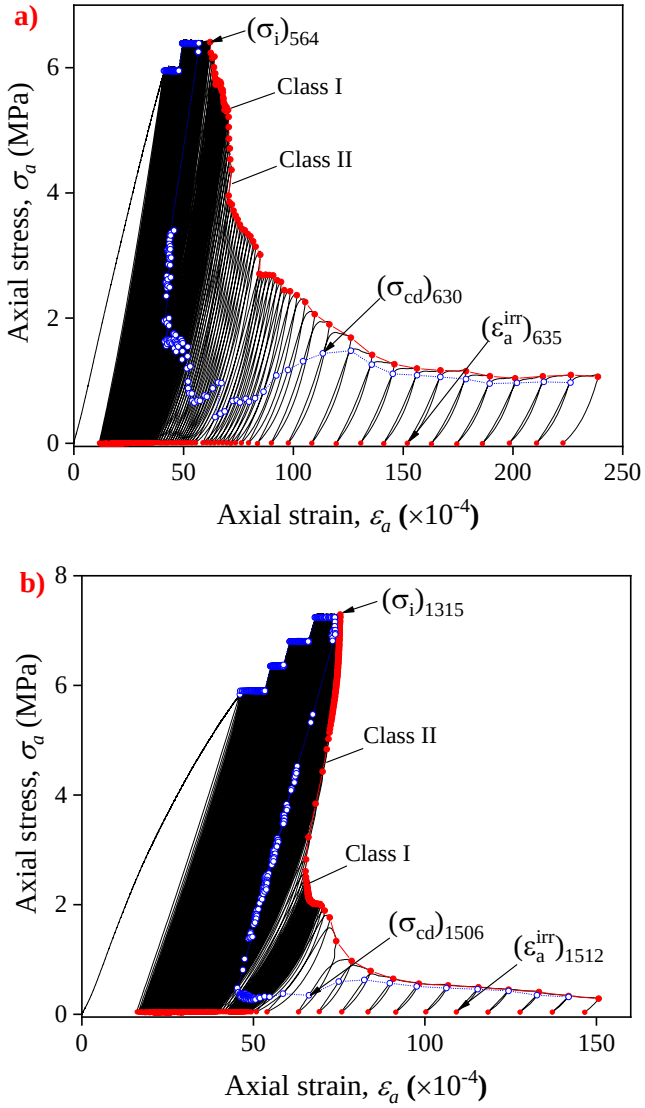

Figure 6.9 Complete axial stress–strain relations for tuffeau limestone specimens obtained from cyclic loading tests. **a** TL6. **b** TL7. **d** TL8

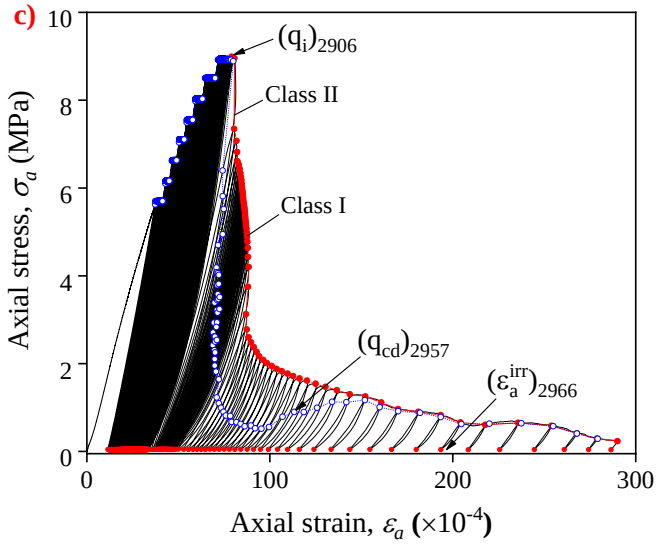

Figure 6.9 (Continued)

Table 6.1 Test scheme for the three Tuffeau limestone specimens under multi-level systematic cyclic loading

Specimen ID	Stress level	Maximum stress (MPa)	N_{before}	Remark
TL6	1	6	400	Not failed
	2	6.5	164	Failed
TL7	1	6	400	Not failed
	2	6.5	400	Not failed
	3	7	400	Not failed
	4	7.5	115	Failed
TL8	1	6	400	Not failed
	2	6.5	400	Not failed
	3	7	400	Not failed
	4	7.5	400	Not failed
	5	8	400	Not failed
	6	8.5	400	Not failed
	7	9	400	Not failed
	8	9.5	106	Failed

TL Tuffeau limestone specimen, N_{before} number of cycles before failure point

6.3.2. Fatigue Damage Evolution

Damage can be characterised by the process of generation, propagation and coalescence of mesoscopic defects and voids through solid materials. Damage can be described by the degradation of some material properties, such as stiffness, residual strength, and P-wave velocity. Additionally, damage during cyclic loading can be investigated by the corresponding irreversible strain, dissipative energy, electrical resistance, and acoustic emission counts (Xiao et al. 2010; Taheri and Tatsuoka 2012). The incremental accumulation of plastic deformation during cyclic loading contributes to the degradation of the cohesive strength and stiffness of the rocks. Therefore, the irreversible strain can be regarded as a suitable indicator for fatigue damage assessment. Hence, a damage variable (D) was defined based on the accumulation of irreversible axial strain (ε_a^{irr}) (see Fig. 6.10) after each loading and unloading cycle as follows:

$$D = \frac{\sum_{i=1}^{m}(\varepsilon_a^{irr})_i}{\sum_{i=1}^{n}(\varepsilon_a^{irr})_i} \tag{6.1}$$

where i is the cycle number, $\sum_{i=1}^{M}(\varepsilon_a^{irr})_i$ is the accumulation of irreversible strain after m cycles, and $\sum_{i=1}^{n}(\varepsilon_a^{irr})_i$ is the total cumulative irreversible strain during the entire multi-level systematic cyclic loading test.

Rock deformability and its failure mechanism are closely related to energy dissipation. Therefore, the energy trends during the rock deformation process can reflect the rock damage mechanism (Zhang et al. 2019b). As shown in Fig. 6.10, a part of the total work done on the unit volume of a specimen (U_t) by the external force during a loading-unloading cycle is stored in the specimen as elastic energy (U_e); the remaining is released as dissipated energy (U_d) due to plastic deformation and rock damage. Because of the complexity in energy conversion during rock deformation and failure, subtle energies (thermal energy, acoustic emission energy, kinetic energy, etc.) are usually ignored to simplify the energy equation as follows (Zhou et al. 2019):

$$U_t = U_e + U_d \tag{6.2}$$

$$\begin{cases} U_t = \int_0^{\varepsilon''} \sigma_a \, d\varepsilon_a \\ U_e = \int_{\varepsilon'}^{\varepsilon''} \sigma_a \, d\varepsilon_a \\ U_d = U_t - U_e \end{cases} \tag{6.3}$$

Fig. 6.11 summarises the evolution of the damage variable (D), elastic modulus (E), and energy dissipation ratio ($K = U_d/U_t$) as damage parameters for specimen TL6. A similar trend was observed for the other tested specimens. As demonstrated in Fig. 6.11, the total behaviour of damage parameters under multi-level systematic cyclic loading conditions can be divided into four stages. In stage I, the damage variable (D) increases slightly and is accompanied by the rapid increase in stiffness (E) from 1.46 GPa to 2.23 GPa, corresponding to the closure of existing defects and expansion of the yield surface (Taheri and Tatsuoka 2015). Furthermore, the energy dissipation ratio (K) decreases suddenly in this stage, which indicates that the elastic energy (U_e) accumulates more rapidly than the dissipated energy (U_d). Stage II, which is the majority of the damage evolution process, shows a nearly unchanging behaviour for all three damage parameters D, E, and K. In this stage, although the specimen has experienced 400 cycles, no notable damage is incurred in the specimen. This stage can be interpreted as a balance between the two mechanisms of dilatant microcracking, which reduces the rock stiffness, and grain crushing and pore collapse, which improves the rock stiffness. This balanced state between two competing inelastic procedures results in a quasi-elastic behaviour of the damage parameters in such a way that the deformation seems elastic, and no more energy is dissipated in this stage. In stage III, during the transition to the second stress level via a monotonic loading, the elastic modulus first increases for several cycles. This increase may be related to the change in the strain rate from 2×10^{-4}/s to 0.02×10^{-4}/s for monotonic loading, which allows the existing microcracks and pores to be more compacted and ultimately results in a small stiffening (Peng et al. 2019). Then, the elastic modulus decreases gradually due to the dilatant cracking that degrades the axial stiffness and simultaneously allows more energy to be dissipated (see the trend of K in Fig. 6.11). In stage IV, the specimen enters the post-peak region due to the coalescence of the microcracks and the generation of macrocracks through the specimen, and the degradation process of the specimen increases dramatically. According to Fig. 6.11, the energy dissipation ratio (K) and damage variable (D) increase rapidly in this stage, while the stiffness of the specimen decreases until the residual state is reached.

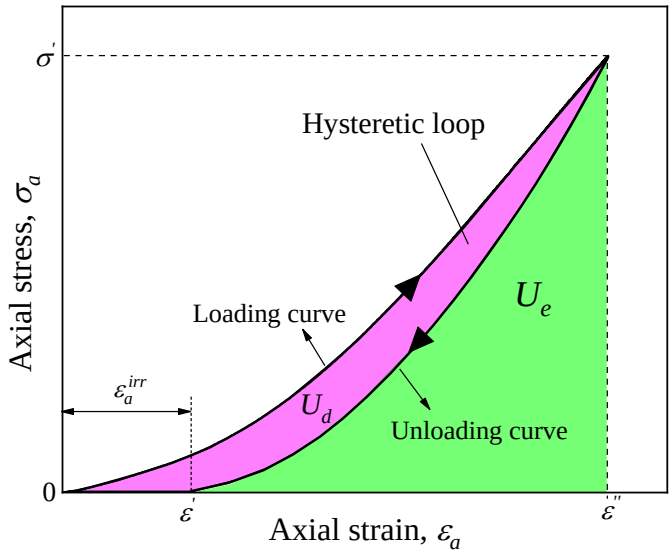

Figure 6.10 Distribution of elastic energy (U_e) and dissipated energy (U_d)

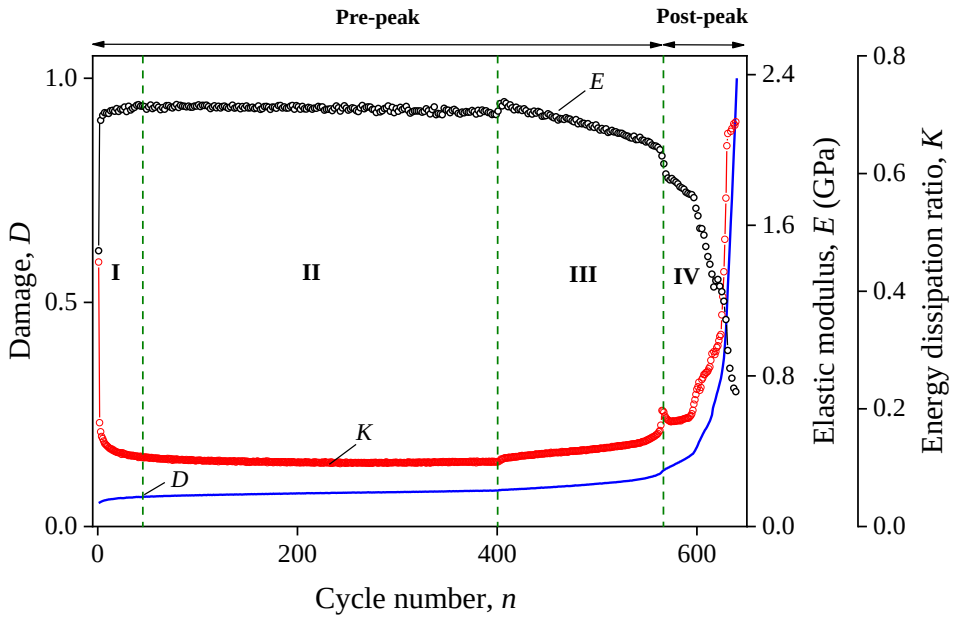

Figure 6.11 Typical evolution of damage and stiffness parameters during multi-level systematic cyclic loading of specimen TL6

6.3.3. Crack Damage Threshold Stress Evolution

The crack damage threshold stress (σ_{cd}), the stress corresponding to the reversal point of volumetric strain at the onset of dilation (Taheri et al. 2020), is an important parameter concerning the unstable damage evolution because it describes the transition of specimen deformation from the compaction-dominated state to the dilatancy-dominated state. As shown in Fig. 6.9, during cyclic loading at each stress level in the pre-peak stage, σ_{cd} is almost

constant and very close to the maximum stress in each cycle. When transitioning to the higher stress levels using a monotonic loading, σ_{cd} increases to reach a stationary state at each stress level. The results presented in Fig. 6.9 show that by applying 400 cycles at each stress level, the closed microvoids and micropores are not re-opened during pre-peak cyclic loading until the cyclic loading damages the rock at the last stress level. Thus, when the cyclic loading stress level is not high enough to cause the specimen to fail, the specimen does not switch from a compaction-dominated state to a dilatancy-dominated state but instead acts as an elastic material. According to Fig. 6.9a, specimen TL6 shows dilatant behaviour in the pre-peak region, in the second cyclic loading stage, by a sudden drop in σ_{cd} due to the re-opening of closed cracks and the generation of new cracks. Degradation of σ_{cd} continues in the post-peak region, followed by strength degradation until the specimen starts to show a residual strength state where σ_{cd} increases to reach a stable condition. For specimens TL7 (Fig. 6.9b) and TL8 (Fig. 6.9c), the drop in σ_{cd} occurs very close to and at the failure point, respectively. This, in turn, causes a sudden release of stored elastic strain energy in a self-sustaining manner.

6.4. Strength Hardening Behaviour

As mentioned earlier, in the cyclic loading tests, an increase in the peak strength of specimens TL7 and TL8 was observed with the increase in fatigue life in the pre-peak region. The discrepancy among specimens may partially contribute to this trend in the results. Considering the previous findings (Burdine 1963; Singh 1989; Ma et al. 2013; Taheri et al. 2017) and the results of cyclic loading tests in this study, the authors believe that the increase in the peak strength of specimens TL7 and TL8 is due to not only this discrepancy but also the cyclic loading. This phenomenon should be investigated in future studies by undertaking more specific cyclic loading tests. The hardening behaviour, however, is discussed briefly below.

As discussed in section 6.3.2 and shown in Fig. 6.11, during pre-peak systematic cyclic loading, when the stress level is not high enough to cause the specimen to fail due to fatigue, a quasi-elastic behaviour dominates the damage evolution process. In this stage, some mesoscopic elements with lower strength and stiffness may reach their maximum load-bearing capacity, and the weak bonding between the grains breaks, producing fine materials. However, as the stress level is not close to the failure point, due to the slippage and dislocation of the produced fine materials, the existing microfissures and pores are filled during cyclic loading. This may result in more compaction of the specimen and, consequently, strength hardening. This behaviour can also be confirmed by the variation in crack damage threshold stress (σ_{cd}) during

cyclic loading (see Fig. 6.9). As explained in section 3.3, specimen TL8, which experienced more loading and unloading cycles in the pre-peak region than the other specimens did, is mostly in the compaction-dominated stage; dilation occurs at the failure point, followed by the sudden decrease in σ_{cd}. This, in turn, resulted in the strength improvement of specimen TL8. However, for specimen TL6 with a shorter fatigue life, dilation occurred earlier in the pre-peak region. The process of rock compaction and porosity reduction in highly porous rock material may be similar to the mechanism explained by Baud et al. (2017). Fig. 6.12 shows the backscattered SEM images of a highly porous limestone in intact and deformed conditions under the same confining pressure of 9 MPa at different axial strain levels. As shown in this figure, when the intact specimen (Fig. 6.12a) deforms to 14% strain, microcracks are created in the calcite grains, and most of the fossil shells are broken and pulverised, while the quartz grains largely remain intact (Fig. 6.12b). With the further deformation of the specimen to 27% strain (Fig. 6.12c), the majority of the calcite grains are broken, and all of the fossil shells are pulverized, resulting in the existing pores being filled and the creation of compacted zones through the specimen. This grain packing is more evident in Fig. 6.12d, at a larger scale. The stress may concentrate more around the compacted areas, which behave elastically during loading and may contribute to the specimens exhibiting more brittle failure.

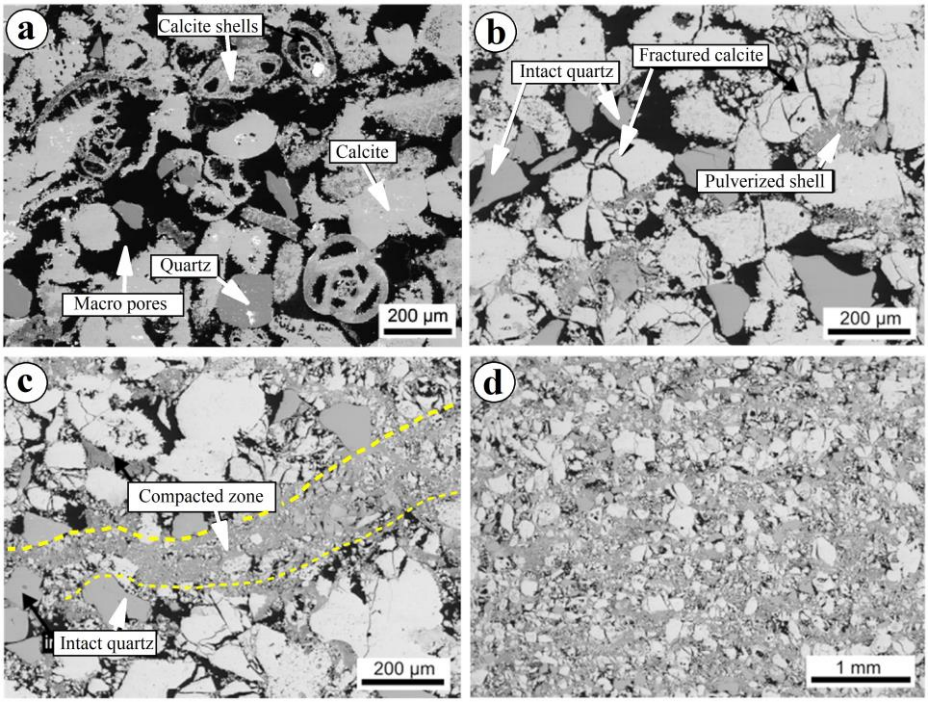

Figure 6.12 Backscattered SEM images of a porous limestone in **a** intact and triaxial compression conditions for **b** 14% and **c, d** 27% axial strain (modified from Baud et al. (2017))

6.5. Conclusions

An innovative testing methodology considering two criteria was proposed in this study to describe the post-peak behaviour of rocks subjected to systematic cyclic loading. Regarding this, the Tuffeau limestone was selected to evaluate the capability of the proposed testing method in capturing the full stress-strain response of soft rocks. After obtaining the optimum values for the loading rate ($d\varepsilon_l/dt$) and $Amp.$ (ε_l) during a trial procedure, three main multi-level systematic cyclic loading tests were conducted on Tuffeau limestone specimens using the proposed damage-controlled test method. The evolution of different parameters, including the peak strength, damage variable, elastic modulus and crack damage threshold stress, was evaluated comprehensively with the results of the conducted cyclic loading tests. The following conclusions were drawn from this study:

1. The proposed double-criteria damage-controlled testing method was successful in capturing the class II post-peak behaviour of Tuffeau limestone subjected to multi-level systematic cyclic loading. This testing method can provide new insights regarding the damage evolution of rocks in the post-peak region under systematic cyclic loading conditions, which was not previously achievable. The test method was successfully performed on Tuffeau limestone, which is a soft rock. The application of the method still needs to be examined on stronger rock types.
2. The whole process of cyclic loading tests conducted in this study can be summarised into several stages: a) The rock specimen initially stiffens and shows elastic behaviour due to the initial compaction, which is accompanied by the reduction in the energy dissipation. b) Due to a balance between the grain-crushing and pore collapse processes during compaction, a quasi-elastic behaviour dominates the whole test. c) The stiffness of the specimen decreases gradually due to dilatant microcracking, which dissipates more energy. d) With the generation and coalescence of microcracks, the rocks transition from a dilatant state, characterised by the rapid increase in damage and energy dissipation, and stiffness reduction.
3. The evolution of the crack damage threshold stress (σ_{cd}) during cyclic loading showed that the specimens do not switch from a compaction-dominated to a dilatancy-dominated state when the cyclic loading stress level is not high enough to cause the specimen to fail. This results in a constant σ_{cd} that is very close to the unloading stress in each cycle.

4. An increase in strength with an increase in fatigue life was observed for the highly porous Tuffeau limestone. According to the variation in the damage parameters, stiffness and crack damage threshold stress during the systematic cyclic loading tests, this hardening behaviour can be due to the further compaction of a rock specimen with increasing number of cycles in the pre-peak region. Indeed, the weak bonding between the grains may break down during cycling loading, and the fine materials produced in this process may fill the existing micropores and microfissures, which can result in a porosity reduction and hardening behaviour.

Acknowledgments

The authors would like to thank the laboratory staff, in particular, Simon Golding and Dale Hodson, for their aids in conducting the tests.

Funding

The first author acknowledges the University of Adelaide for providing the research fund (Beacon of Enlightenment PhD Scholarship) to conduct this study.

References

Akinbinu VA (2016) Class I and Class II rocks: implication of self-sustaining fracturing in brittle compression. *Geotechnical and Geological Engineering* 34(3):877–887

Al-Mukhtar M, Beck K (2006) Physical-mechanical characterisation of hydraulic and non-hydraulic lime based mortars for a French porous limestone. *arXiv Prepr physics*/0609108

Attewell PB, Sandford MR (1974) Intrinsic shear strength of a brittle, anisotropic rock—I: experimental and mechanical interpretation. In: *International Journal of Rock Mechanics and Mining Sciences & Geomechanics Abstracts*. Elsevier, 11(11):423–430

Bagde MN, Petroš V (2005) Fatigue properties of intact sandstone samples subjected to dynamic uniaxial cyclical loading. *International Journal of Rock Mechanics and Mining Sciences* 42(2):237–250

Baud P, Schubnel A, Heap M, Rolland A (2017) Inelastic compaction in high-porosity limestone monitored using acoustic emissions. *Journal of Geophysical Research: Solid Earth* 122:9910–9989

Beck K, Al-Mukhtar M (2014) Cyclic wetting–drying ageing test and patina formation on tuffeau limestone. *Environmental Earth Sciences* 71(5):2361–2372

Burdine NT (1963) Rock Failure Under Dynamic Loading Conditions. *Society of Petroleum Engineers Journal* 3(1):1–8

Cardani G, Meda A (2004) Marble behaviour under monotonic and cyclic loading in tension. *Construction and Building materials* 18(6):419–424

Cerfontaine B, Collin F (2018) Cyclic and fatigue behaviour of rock materials: review, interpretation and research perspectives. *Rock Mechanics and Rock Engineering* 51(2):391–414

Cho SH, Ogata Y, Kaneko K (2003) Strain-rate dependency of the dynamic tensile strength of rock. *International Journal of Rock Mechanics and Mining Sciences* 40(5):763–777

Eberhardt E, Stead D, Stimpson B (1999) Quantifying progressive pre-peak brittle fracture damage in rock during uniaxial compression. *International Journal of Rock Mechanics and Mining Sciences* 36(3):361–380

Fairhurst CE, Hudson JA (1999) Draft ISRM suggested method for the complete stress-strain curve for intact rock in uniaxial compression. *International Journal of Rock Mechanics and Mining Sciences* 36(3):279–289

Ghamgosar M, Erarslan N (2016) Experimental and numerical studies on development of fracture process zone (FPZ) in rocks under cyclic and static loadings. *Rock Mechanics and Rock Engineering* 49(3):893–908

Guo H, Ji M, Zhang Y, Zhang M (2018) Study of mechanical property of rock under uniaxial cyclic loading and unloading. *Advances in Civil Engineering*

Heap MJ, Faulkner DR, Meredith PG, Vinciguerra S (2010) Elastic moduli evolution and accompanying stress changes with increasing crack damage: implications for stress changes around fault zones and volcanoes during deformation. *Geophysical Journal International* 183(1):225–236

Hudson JA, Brown ET, Fairhurst C (1971) Optimising the control of rock failure in servo-controlled laboratory tests. *Rock Mechanics* 3:217–224

Li T, Pei X, Wang D, Huang R, Tang H (2019) Nonlinear behavior and damage model for

fractured rock under cyclic loading based on energy dissipation principle. *Engineering Fracture Mechanics* 206:330–341

Liu J, Xie H, Hou Z, Hou Z, Yang C, Chen L (2014) Damage evolution of rock salt under cyclic loading in unixial tests. *Acta Geotechnica* 9(1):153–160

Ma L, Liu X, Wang M, Xu H, Hua R, Fan P, Jiang S, Wang G, Yi Q (2013) Experimental investigation of the mechanical properties of rock salt under triaxial cyclic loading. *International Journal of Rock Mechanics and Mining Sciences* 34–41

Munoz H, Taheri A (2017a) Local damage and progressive localisation in porous sandstone during cyclic loading. *Rock Mechanics and Rock Engineering* 50(12):3253–3259

Munoz H, Taheri A (2017b) Specimen aspect ratio and progressive field strain development of sandstone under uniaxial compression by three-dimensional digital image correlation. *Journal of Rock Mechanics and Geotechnical Engineering* 9(4):599–610

Munoz H, Taheri A (2019) Postpeak deformability parameters of localised and nonlocalised damage zones of rocks under cyclic loading. *Geotechnical Testing Journal* 42(6):1663–1684

Munoz H, Taheri A, Chanda EK (2016a) Rock Drilling Performance Evaluation by an Energy Dissipation Based Rock Brittleness Index. *Rock Mechanics and Rock Engineering* 49(8):3343–3355

Munoz H, Taheri A, Chanda EK (2016b) Pre-peak and post-peak rock strain characteristics during uniaxial compression by 3D digital image correlation. *Rock Mechanics and Rock Engineering* 49(7):2541–2554

Munoz H, Taheri A, Chanda EK (2016c) Fracture Energy-Based Brittleness Index Development and Brittleness Quantification by Pre-peak Strength Parameters in Rock Uniaxial Compression. *Rock Mechanics and Rock Engineering* 49(12):4587–4606

Peng K, Zhou J, Zou Q, Yan F (2019) Deformation characteristics of sandstones during cyclic loading and unloading with varying lower limits of stress under different confining pressures. *International Journal of Fatigue* 127:82–100

Singh SK (1989) Fatigue and strain hardening behaviour of graywacke from the flagstaff formation, New South Wales. *Engineering Geology* 26(2):171–179

Taheri A, Tatsuoka F (2012) Stress–strain relations of cement-mixed gravelly soil from multiple-step triaxial compression test results. *Soils and Foundations* 52(4):748–766

Taheri A, Tatsuoka F (2015) Small- and large-strain behaviour of a cement-treated soil during various loading histories and testing conditions. *Acta Geotechnica* 10(1):131–155

Taheri A, Royle A, Yang Z, Zhao Y (2016) Study on variations of peak strength of a sandstone during cyclic loading. *Geomechanics and Geophysics for Geo-Energy and Geo-Resources* 2(1):1–10

Taheri A, Hamzah N, Dai Q (2017) Degradation and improvement of mechanical properties of rock under triaxial compressive cyclic loading. *Japanese Geotechnical Society Special Publication* 5:71–78

Taheri A, Zhang Y, Munoz H (2020) Performance of rock crack stress thresholds determination criteria and investigating strength and confining pressure effects. *Construction and Building Materials* 243:118263

Wang S, Xu W, Sun M, Wang W (2019) Experimental investigation of the mechanical properties of fine-grained sandstone in the triaxial cyclic loading test. *Environmental Earth Sciences* 78(14):416

Wawersik WR, Fairhurst CH (1970) A study of brittle rock fracture in laboratory compression experiments. In: *International Journal of Rock Mechanics and Mining Sciences & Geomechanics Abstracts*. Elsevier, 7(5):561–575

Xiao J-Q, Ding D-X, Jiang F-L, Xu G (2010) Fatigue damage variable and evolution of rock subjected to cyclic loading. *International Journal of Rock Mechanics and Mining Sciences* 47:461–468

Xiao J-Q, Ding D-X, Xu G, Jiang F-L (2009) Inverted S-shaped model for nonlinear fatigue damage of rock. *International Journal of Rock Mechanics and Mining Sciences* 46(3):643–648

Xuefeng X, Linming D, Caiping L, Zhang Y (2010) Frequency spectrum analysis on micro-seismic signal of rock bursts induced by dynamic disturbance. *Mining Science and Technology (China)* 20(5):682–685

Zhang J, Deng H, Taheri A, Ke B, Liu C (2019a) Deterioration and strain energy development of sandstones under quasi-static and dynamic loading after freeze-thaw cycles. *Cold*

Regions Science and Technology 160:252–264

Zhang Y, Zhao T, Taheri A, Tan Y, Fang K (2019b) Damage characteristics of sandstone subjected to pre-peak and post-peak cyclic loading. *Acta Geodynamica et Geromaterialia* 16(2):143–151

Zhou HW, Wang ZH, Wang CS, Liu JF (2019) On Acoustic Emission and Post-peak Energy Evolution in Beishan Granite Under Cyclic Loading. *Rock Mechanics and Rock Engineering* 52(1):283–288

Statement of Authorship

Title of Paper	Failure behaviour of a sandstone subjected to the systematic cyclic loading: Insights from the double-criteria damage-controlled test method
Publication Status	☑ Published ☐ Accepted for Publication ☐ Submitted for Publication ☐ Unpublished and Unsubmitted work written in manuscript style
Publication Details	**Shirani Faradonbeh R**, Taheri A, Karakus M (2021) Failure behaviour of a sandstone subjected to the systematic cyclic loading: Insights from the double-criteria damage-controlled test method. *Rock Mechanics and Rock Engineering* x(x):x–x, https://doi.org/10.1007/s00603-021-02553-5

Principal Author

Name of Principal Author (Candidate)	Roohollah Shirani Faradonbeh		
Contribution to the Paper	Conducting laboratory tests, analysis of the results, and preparation of the manuscript		
Overall percentage (%)	80%		
Certification:	This paper reports on original research I conducted during the period of my Higher Degree by Research candidature and is not subject to any obligations or contractual agreements with a third party that would constrain its inclusion in this thesis. I am the primary author of this paper.		
Signature		Date	17 June 2021

Co-Author Contributions

By signing the Statement of Authorship, each author certifies that:

i. the candidate's stated contribution to the publication is accurate (as detailed above);
ii. permission is granted for the candidate in include the publication in the thesis; and
iii. the sum of all co-author contributions is equal to 100% less the candidate's stated contribution.

Name of Co-Author	Abbas Taheri		
Contribution to the Paper	Research supervision, review and revision of the manuscript		
Signature		Date	21 June 2021

Name of Co-Author	Murat Karakus		
Contribution to the Paper	Review and revision of the manuscript		
Signature		Date	21 June 2021

Chapter 7

Failure Behaviour of a Sandstone Subjected to the Systematic Cyclic Loading: Insights from the Double-Criteria Damage-Controlled Test Method

Abstract

The post-peak behaviour of rocks subjected to cyclic loading is very significant to appraise the long-term stability of underground excavations. However, an appropriate testing methodology is required to control the damage induced by the cyclic loading during the failure process. In this study, the post-failure behaviour of Gosford sandstone subjected to the systematic cyclic loading at different stress levels was investigated using the double-criteria damage-controlled testing methodology, and the complete stress-strain relations were captured successfully. The results showed that there exists a fatigue threshold stress in the range of 86-87.5% of the average monotonic strength in which when the cyclic loading stress is below this threshold, no failure occurred for a large number of cycles and in turn, the peak strength improved up to 8%. Also, the variation of the energy dissipation ratio, rock stiffness and acoustic emission hits for hardening tests showed that cyclic loading in the pre-peak regime creates no critical damage in the specimen, and a quasi-elastic behaviour dominates the damage evolution. The post-failure instability of such tests was similar to those obtained for monotonic tests. On the other hand, by exceeding the fatigue threshold stress, the brittleness of the specimens increased with an increase in the applied stress level, and class II behaviour prevailed over total post-peak behaviour. A loose-dense-loose behaviour with different extents was also observed in the post-peak regime of all fatigue cyclic loading tests. This was manifested then as a secondary inverted S-shaped damage behaviour by the variation of the cumulative irreversible axial and cumulative irreversible lateral strains with the post-peak cycle number. Furthermore, it was confirmed that the damage per cycle in the post-peak regime decreases exponentially with an increase in the applied stress level.

Keywords: Pre-peak and post-peak behaviour, Systematic cyclic loading, Brittleness, Hardening, Fatigue, Damage evolution

List of Symbols

E_{tan}	Tangent Young's modulus	ε_a^{irr}	Irreversible axial strain
ν	Poisson's ratio	ε_l^{irr}	Irreversible lateral strain
σ_1	Major principal stress	$\Sigma\varepsilon_a^{irr}$	Cumulative irreversible axial strain
σ_a	Axial stress	$\Sigma\varepsilon_l^{irr}$	Cumulative irreversible lateral strain
σ_i	Indicator stress	U_e	Elastic energy at peak stress
σ_{a-peak}	Axial peak stress	U_e^i	Elastic energy of cycle i
σ_m	Average monotonic strength	U_d^i	Dissipated energy of cycle i
σ_a/σ_m	Applied stress level	U_{pre}	Pre-peak dissipated energy
σ_h/σ_m	Strength hardening ratio	U_{post}	Post-peak dissipated energy
$\sigma_{ci}/\sigma_{a-peak}$	Crack initiation stress ratio	U_t	Total fracture energy
$\sigma_{cd}/\sigma_{a-peak}$	Crack damage stress ratio	$Amp.(\sigma_a)$	Loading amplitude
ε_a	Axial strain	$Amp.(\varepsilon_l)$	Lateral strain amplitude
ε_l	Lateral strain	n	Cycle number
$d\varepsilon_l/dt$	Lateral strain rate	N_{total}	Total number of cycles
ε_{a-peak}	Axial strain at peak stress	N_{after}	Number of cycles after failure point
ε_{l-peak}	Lateral strain at peak stress	BI	Brittleness index
ε_{v-peak}	Volumetric strain at peak stress	D	Damage variable
ε_{a-f}	Axial strain at the final cycle	M	Post-peak modulus

7.1. Introduction

A high-complex stress state usually is created around deep-buried tunnels and caverns due to disturbances induced by different sources as displayed in Fig. 7.1. This stress state may affect mechanical rock properties and in turn, cause some specific failure phenomena such as slabbing/spalling, strainburst and zonal disintegration significantly different from those in shallow conditions (Gong et al. 2012; Shirani Faradonbeh and Taheri 2019). According to Martin and Chandler (1994) and Martin (1997), the surrounding rocks in underground excavations may experience load-and-deformation response to a different extent during operation, and rock may be exposed to cyclic loading. In particular, they argued that in remote to nearby excavation regions, rock may experience failure (i.e. the applied stress level exceeds the peak strength), damage (i.e. the applied stress is below the peak strength) or disturbance (i.e. different stress is applied due to the redistribution of the in-situ stresses) or the rock may remain undisturbed. From this viewpoint, the rock cyclic load-deformation response may take

place in the pre-peak or post-peak regime (Munoz and Taheri 2019). For instance, as depicted in Fig. 7.1, a pillar may experience cyclic loading due to blasting operation or other seismic activities beyond the limit in uniaxial conditions. Under such loading conditions, rock materials may still keep some loadings even in the post-failure regime. Therefore, the investigation of the pre-peak and post-peak behaviour of rocks is of paramount significance to understand more about the fracturing mechanism, resilient design and long-term stability assessment of the various rock engineering structures subjected to seismic disturbances. Experimental research on the influence of cyclic loading parameters on the damage evolution and rock strength and deformation parameters has a long tradition. These studies have been conducted under different loading histories and loading conditions such as uniaxial and triaxial compression tests (Heap and Faulkner 2008; Heap et al. 2009; Liu et al. 2018), indirect tensile tests (Erarslan et al. 2014; Wang et al. 2016), flexural tests (Cattaneo and Labuz 2001; Cardani and Meda 2004) and freeze-thaw tests (Liu et al. 2015; Zhang et al. 2019). A comprehensive review of the rock fatigue studies can be found in Cerfontaine and Collin (2018). The majority of prior rock fatigue studies have emphasised strength weakening of rocks due to incurring permanent deformations during cyclic loading (Haimson 1978; Fuenkajorn and Phueakphum 2010). However, very few studies have reported the strength improvement when the stress level that cyclic loading is applied is low enough to prevent failure (Singh 1989; Ma et al. 2013; Taheri et al. 2017). In prior studies, the process of damage evolution and the failure mechanism of rocks subjected to different cyclic loading histories have been investigated based on the measured stress-strain relations (Cerfontaine and Collin 2018). Indeed, the complete stress-strain relation of rocks (i.e. the pre-peak and the post-peak regimes) is considered as a prominent tool in rock engineering to describe strain energy evolution as well as for rock brittleness determination (Munoz et al. 2016a; Shirani Faradonbeh et al. 2020). According to Wawersik and Fairhurst (1970), the post-peak behaviour of rocks under quasi-static compression can be distinguished into two classes: a) class I which is characterised by the negative post-peak modulus (i.e. $M = d\sigma/d\varepsilon < 0$) representing the gradual strength degradation of rock specimen and the need for extra energy and b) class II having a positive post-peak modulus represents the self-sustaining failure with strain recovery and release of excess elastic strain energy. The proper measurement of the complete stress-strain response of rocks significantly depends on the stiffness of the loading system, the applied load controlling technique throughout the test as well as rock brittleness (Wawersik and Fairhurst 1970; Munoz and Taheri 2019).

Shirani Faradonbeh et al. (2020) categorised the cyclic loading methods based on the loading histories and load control variables into two main groups of systematic cyclic loading (single-level or multi-level) (Figs. 7.2a and b) and damage-controlled cyclic loading (load-based or displacement-based) (Figs. 7.2c and d). Systematic cyclic loading can be conducted under load-controlled or displacement-controlled loading conditions. In both loading conditions, a sudden failure occurs during cyclic loading as a constant axial load amplitude, $Amp.(\sigma_a)$, should be achieved during each loading cycle (e.g. Ma et al. 2013; Li et al. 2019). Similarly, in the load-based damage-controlled cyclic loading tests, as the specimen is forced to reach a prescribed stress level, it may experience an unexpected failure, and the post-peak behaviour cannot be captured (e.g. Heap et al. 2010; Guo et al. 2018). Regarding the displacement-based damage-controlled cyclic loading tests, as the post-peak behaviour of rocks in uniaxial compression is either class II or a combination of class I and class II (Munoz et al. 2016a), the post-peak response cannot be adequately captured by the axial displacement feedback signal (e.g. Wang et al. 2019). The lateral displacement, on the other hand, has been identified as an appropriate variable to control the amount of damage in the post-peak regime (Munoz and Taheri 2019).

To our knowledge, no prior studies have examined the influence of systematic cyclic loading at different stress levels on the post-peak behaviour of rocks. This is due to the difficulties in controlling the axial load when a constant load amplitude should be achieved in every cycle in a systematic cyclic loading test. Also, if a prescribed lateral strain is considered to control the damage in a damage-controlled test, the axial load is reversed when a certain amount of lateral strain occurs, and therefore, the systematic cyclic loading cannot be conducted anymore in the pre-peak regime. However, as mentioned earlier, some mining and civil structures (e.g. mining pillars and bridge columns) may experience systematic cyclic loading at different fractions of their average peak strength. Under such loading conditions, the rocks may exhibit different behaviours in the post-peak regime. An appropriate experimental methodology is, therefore, required for measuring the post-peak behaviour of rocks subjected to systematic cyclic loading histories properly. As demonstrated in Fig. 7.2, a novel cyclic test method by combining the single-level systematic cyclic loading and lateral displacement-based damage-controlled cyclic loading is proposed in this study to control both the damage and the cyclic loading rate. Then, several systematic cyclic tests were conducted in uniaxial compression at different stress levels using the proposed test method. Based on the obtained complete stress-strain relations, the influence of systematic cyclic loading on both the pre-peak and the post-peak behaviours was evaluated comprehensively, and the results were discussed in detail.

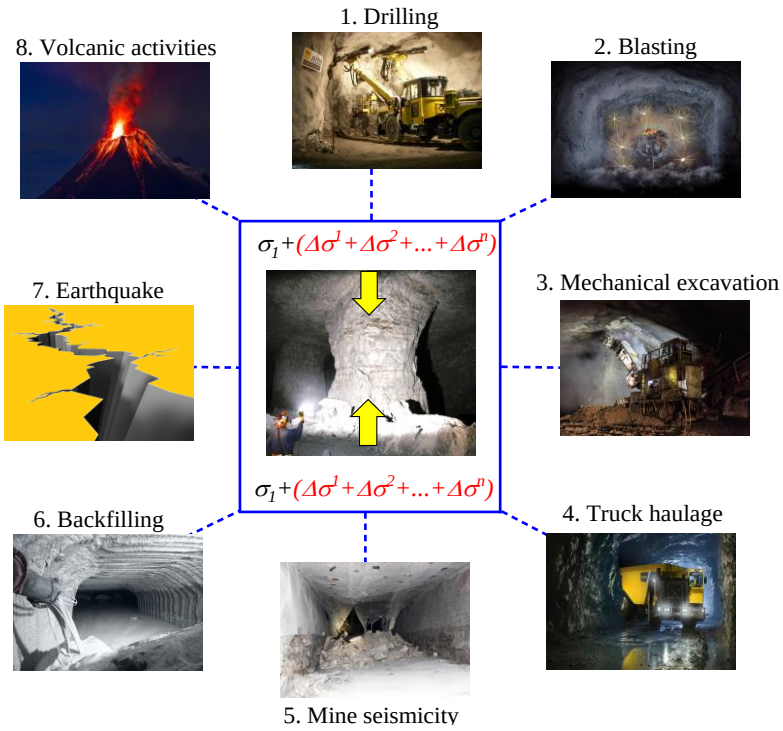

Figure 7.1 Different sources of seismic disturbances imposing on an underground mining pillar, σ_1 corresponds to the major in-situ stress and $\Delta\sigma^i$ refers to the cyclic loadings originated from different sources

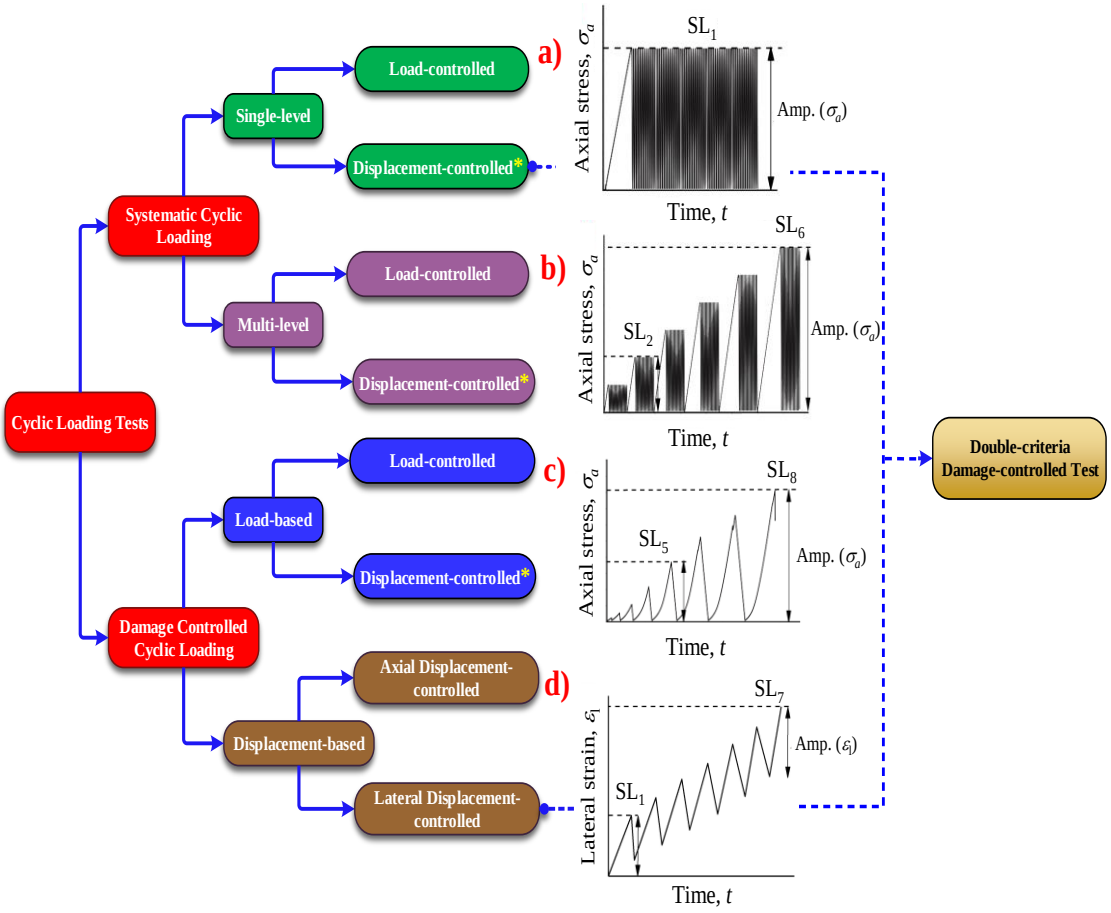

Figure 7.2 Classification of cyclic loading tests, **a** single-level systematic cyclic loading path, **b** multilevel systematic cyclic loading path, **c** load-based damage controlled cyclic loading path and **d** displacement-based damage controlled cyclic loading path, Amp. (σ_a) refers to loading amplitude, Amp. (ε_L) refers to lateral strain amplitude, and ***** can be conducted either in axial or lateral displacement-controlled mode, modified from Shirani Faradonbeh et al. (2020)

7.2. Specimen Preparation and Experimental Set-Up

The Gosford sandstone as a medium-grained (0.2-0.3 mm), poorly cemented, immature quartz sandstone containing 20-30% feldspar and clay minerals with the serrate connection between quartz grains (Sufian and Russell 2013) was used in this study for conducting the experimental tests. According to the X-ray computed tomography scans conducted by Sufian and Russell (2013), the total porosity of this sandstone is about 18%. A total of 23 cylindrical specimens having a constant aspect ratio of 2.4 (i.e. 42 mm diameter and 100 mm length) were all cored from the same rectangular block and in the same direction and prepared according to the ISRM suggested method (Fairhurst and Hudson 1999). In this study, all the experiments were performed in dry condition. To do so, the rock specimens were dried in the room temperature before conducting the tests. The average dry density of the specimens was approximately 2204.26 kg/m^3. Rock monotonic strength should be determined before undertaking systematic cyclic loading tests at different stress levels (σ_a/σ_m). To do so, six uniaxial compression tests were performed following the lateral strain-controlled loading method. An MTS close-looped servo-controlled hydraulic compressive system having the maximum loading capacity of 300 kN (see Fig. 7.3) was used to undertake the monotonic and cyclic loading tests. As stated earlier, the axial load-controlled and axial strain-controlled loading techniques cannot capture the post-peak behaviour of rocks, as rocks usually show a combination of class I and class II behaviour in the post-peak regime (Munoz et al. 2016b). Therefore, as depicted in Fig. 7.4a, a constant lateral strain rate ($d\varepsilon_l/d_t$) of 0.02×10^{-4}/s was utilised during the uniaxial compression tests to control the axial load both in the pre-peak and the post-peak regimes. This strain rate provides a static to quasi-static loading conditions (Wawersik and Fairhurst 1970; Munoz et al. 2016b).

Axial load and axial and lateral displacements were recorded in real-time, respectively using the load cell, a pair of LVDTs externally mounted between the loading platens and a direct-contact chain extensometer wrapped around the specimens (see Fig. 7.3). Due to the large-

strain behaviour of rocks in the post-peak regime, the local strain measurement tools such as strain gauges are not effective. To characterise the post-peak instability of rocks in terms of brittleness, the complete stress-strain curves of rocks are required, and therefore, external LVDTs were used to measure the large-strain properties. LVDTs measure the deformation between loading platens; therefore, the deformation of the loading system is not included in the measurement. Still, the strain data may not be precise due to well-known bedding error (Taheri and Tani 2008). The bedding error refers to the additional deformations measured by LVDTs due to crushing the irregularities/asperities at the end faces of the specimens before the specimen deforms as well as the poor fitting of the specimen to the loading platens. This error is minimised in this study by carefully and smoothly grinding the ends of the specimen following the ISRM standard (Fairhurst and Hudson 1999). Besides, since the focus of this study is complete stress-strain behaviour, this error is deemed negligible in large strain stress-strain properties.

The acoustic emission (AE) technique, as a passive non-destructive monitoring technology, was also employed in this study to measure the real-time formation and growth of local micro-cracks throughout the specimen (internal damage) during cyclic loading (Lockner 1993; Bruning et al. 2018). For this aim, as depicted in Fig. 7.3, two miniature PICO sensors were attached to the specimens, and the recorded acoustic signals by these sensors were amplified using a pre-amplifier (type 2/4/6) set to 60 dB of gain. The AE recordings were carried out using the Express-8 data acquisition card with the sampling rate of 2 MSPS (million samples per second). To ensure that mechanical noises induced by the loading system are not recorded during the tests, the AE threshold amplitude was changed from 20 dB to 60 dB, and it was found that after 45 dB amplitude, no additional noises are recorded. Therefore, this value was set as the AE threshold.

The stress-strain curves obtained from the conducted uniaxial compressive tests and their relevant mechanical properties can be found in Fig. 4b, and Table 7.1, respectively. In Table 7.1, the tangent Young's modulus (E_{tan}) and Poisson's ratio (ν) values were determined at 50% of the axial peak stress (σ_{a-peak}) for each monotonic test. The crack initiation stress (σ_{ci}) and crack damage stress (σ_{cd}) thresholds were also determined using the methods explained in Taheri et al. (2020). According to Fig. 7.4b, the stress-strain curves for all compression tests show almost a similar behavioural trend both in the pre-peak and the post-peak regimes. In the pre-peak regime, as listed in Table 7.1, the deformation parameters of axial (ε_{a-peak}), lateral (ε_{l-peak}) and volumetric strains (ε_{v-peak}) at peak stress points, E_{tan}, ν, crack initiation stress

ratio ($\sigma_{ci}/\sigma_{a-peak}$) and crack damage stress ratio ($\sigma_{cd}/\sigma_{a-peak}$) are approximately similar, which indicates a small discreteness of the tested specimens. As such, in the post-failure regime, the sudden drops and recoveries of the load-bearing capacity can be observed for all specimens which can be associated with the shear strain localisation, grain interlocking in between the sides of the generated macrocracks (Jansen and Shah 1997; Vasconcelos et al. 2009) as well as the automatic adjustment of applied load by the testing machine upon damage extension. The post-peak regime of rocks under uniaxial compressive loading demonstrates a combined class I-II behaviour, which is consistent with the prior study conducted by Munoz et al. (2016b). As listed in Table 7.1, the monotonic compressive strength (σ_{a-peak}) of the tested Gosford sandstone specimens varied between 45.76 MPa and 49.89 MPa with an average value of 48.15 MPa. This average monotonic strength was utilised in the following to define the stress levels where the systematic cyclic loading tests should be commenced.

Table 7.1 The results of uniaxial compressive tests for Gosford sandstone specimens

Test No.	σ_{a-peak} (MPa)	E_{tan} (GPa)	ν	Strains at the peak stress point			$\sigma_{ci}/\sigma_{a-peak}$ (%)	$\sigma_{cd}/\sigma_{a-peak}$ (%)
				ε_{a-peak} (×10^{-4})	ε_{l-peak} (×10^{-4})	ε_{v-peak} (×10^{-4})		
GS-1	48.05	13.30	0.15	54.17	-38.35	-22.54	29.65	58.27
GS-2	49.54	13.43	0.12	52.18	-36.84	-21.51	30.60	58.67
GS-3	47.35	13.42	0.13	52.66	-39.10	-25.55	27.00	55.57
GS-4	45.76	12.97	0.15	51.39	-38.56	-25.73	25.80	55.96
GS-5	49.89	13.15	0.14	53.00	-36.97	-20.95	27.71	57.92
GS-6	48.29	14.14	0.15	50.17	-34.11	-18.05	26.94	52.70
Average	48.15	13.40	0.14	52.26	-37.32	-22.39	27.95	56.51
SD	1.51	0.40	0.01	1.38	1.81	2.93	1.82	2.25

SD standard deviation

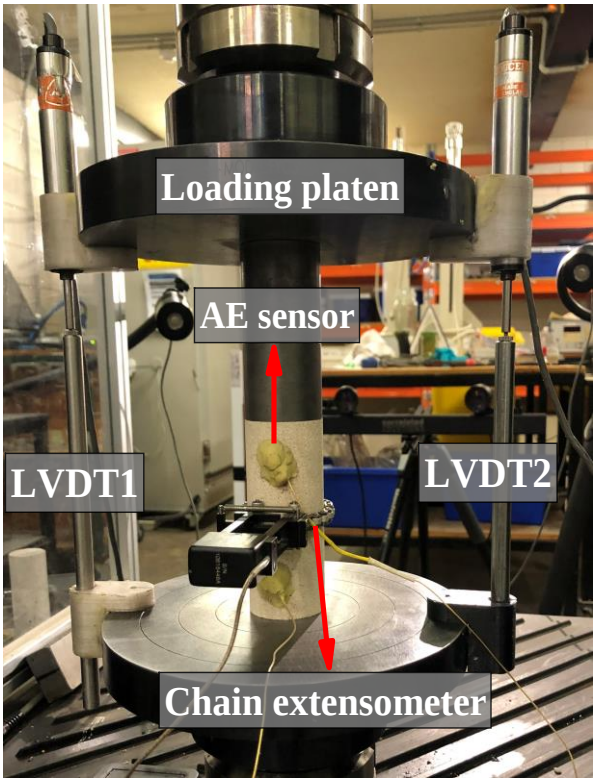

Figure 7.3 Testing set-up for the uniaxial compression and cyclic loading tests

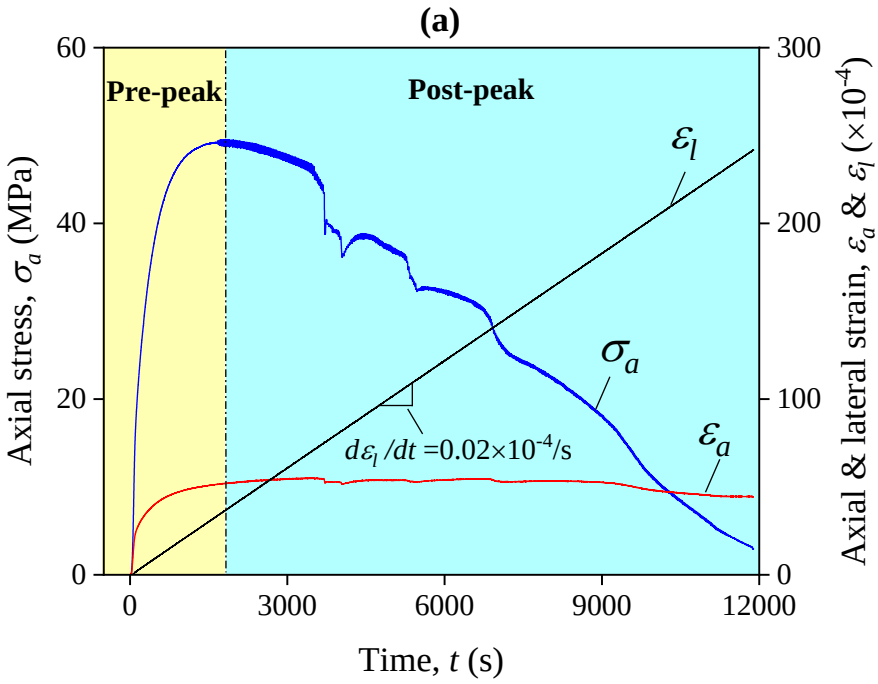

Figure 7.4 a Typical time-history of the loading and strains during compressive tests and **b** axial stress-strain relations obtained from the monotonic loading tests

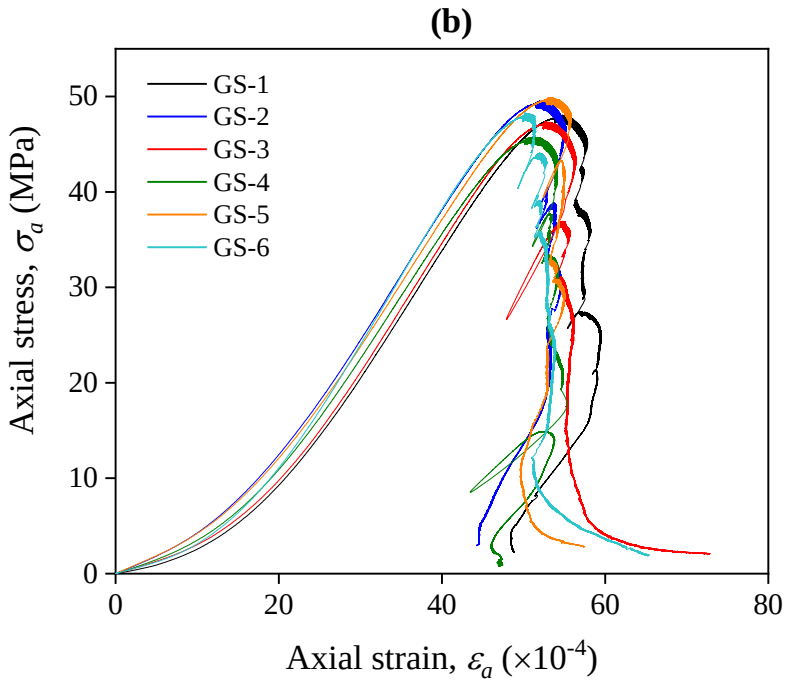

Figure 7.4 (Continued)

7.3. Systematic Cyclic Loading Tests

As discussed earlier, the single-criterion load-based and displacement-based loading methods are not sufficient to control the axial load in the post-failure stage during the systematic cyclic loading tests, especially when rocks demonstrate self-sustained failure behaviour. In this study, to address this issue, a new testing method called "double-criteria damage-controlled test method" (Shirani Faradonbeh et al. 2020) was employed. As demonstrated in Fig. 7.2, this test method is a combination of single-level systematic cyclic loading and damage-controlled cyclic loading lateral displacement-controlled loading method. In this regard, the MTS servo-controlled testing machine was programmed so that the hydraulic system was allowed to be adjusted continuously, automatically and rapidly according to the received feedback signals from both chain extensometer and load cell during a closed-loop procedure. The testing procedure can be summarised into the following four stages:

1. Load the specimen monotonically ($d\varepsilon_l/dt = 0.02\times10^{-4}$) until the pre-defined stress level (σ_a/σ_m), and then, unload it at the same loading rate until σ_a= 0.07 MPa, ensuring the specimen is always in complete contact with the loading platens.
2. Reload the specimen under a constant lateral strain rate of 3×10^{-4}/s until one of the two following criteria is met during loading:

a) the pre-defined maximum axial stress level (σ_a/σ_m) is reached;

b) the pre-defined maximum lateral strain amplitude, $Amp.(\varepsilon_l)$= 32×10^{-4} is reached;

3. Reverse the axial load to σ_a= 0.07 MPa, and repeat steps 1 and 2 until 1500 loading and unloading cycles are completed.
4. If the specimen did no fail during 1500 cycles, apply a monotonic loading ($d\varepsilon_l/dt$ = 0.02×10^{-4}) until complete failure occurs.

In this study, $Amp.(\varepsilon_l)$= 32×10^{-4} was determined based on the conducted monotonic tests and the measured lateral strain of the rocks at the failure point, ε_{l-peak} (see Table 7.1). As seen in Table 7.1, the average value of ε_{l-peak} for the tested specimens is -37.32×10^{-4}. Based on the conducted several trial tests, it was found that 32×10^{-4} is an appropriate value for Gosford sandstone. By adopting this value, it was possible to avoid failing the sample in a single cycle while allowing the axial stress level to reach the pre-defined value to apply a systematic cyclic loading. Figs. 7.5a and b show two representative time histories of axial stress and lateral strain for Gosford sandstone specimens experiencing failure during cyclic loading and final monotonic loading. In Fig. 7.5a, the specimen was loaded monotonically ($d\varepsilon_l/dt$= 0.02×10^{-4}/s) up to 85% of the average monotonic strength (σ_a/σ_m= 85%). Afterwards, the specimen was unloaded with the same rate, and then the systematic cyclic loading was initiated under the lateral strain rate of 3×10^{-4}/s. As shown in the inset figure, the cycles always met the first criterion (i.e. the maximum stress applied during a cycle remained constant) during the systematic cyclic loading and the $Amp.(\varepsilon_l)$ was considerably lower than the pre-defined maximum amplitude for lateral strain (i.e. 32×10^{-4}) in each cycle.

As during 1500 loading/unloading cycles, the $Amp.(\varepsilon_l)$ did not exceed 32×10^{-4}, a monotonic loading was applied automatically to the specimen under the lateral strain rate of 0.02×10^{-4}/s until the specimen is completely failed. By doing so, the post-peak behaviour was captured successfully for further analyses. In Fig. 7.5b, the same cyclic loading procedure was applied to another specimen at a higher axial stress level (i.e. σ_a/σ_m= 87.25%). In the pre-peak stage, the $Amp.(\varepsilon_l)$ increased gradually by increasing the cycle number, while the stress level was kept constant, satisfying the first criterion. However, at the onset of the failure (where the axial stress begins to reduce), the $Amp.(\varepsilon_l)$ reached the pre-defined value of 32×10^{-4} (see the inset figure), and the second criterion was activated to control the cyclic loading. By transferring to the post-peak stage, and strength degradation, the subsequent cycles were carried out so that

the $Amp.(\varepsilon_l)$ was always constant until the complete failure of the specimen occurred. Following this test method, the rock specimen failed in a controlled way, and the post-peak behaviour was captured successfully.

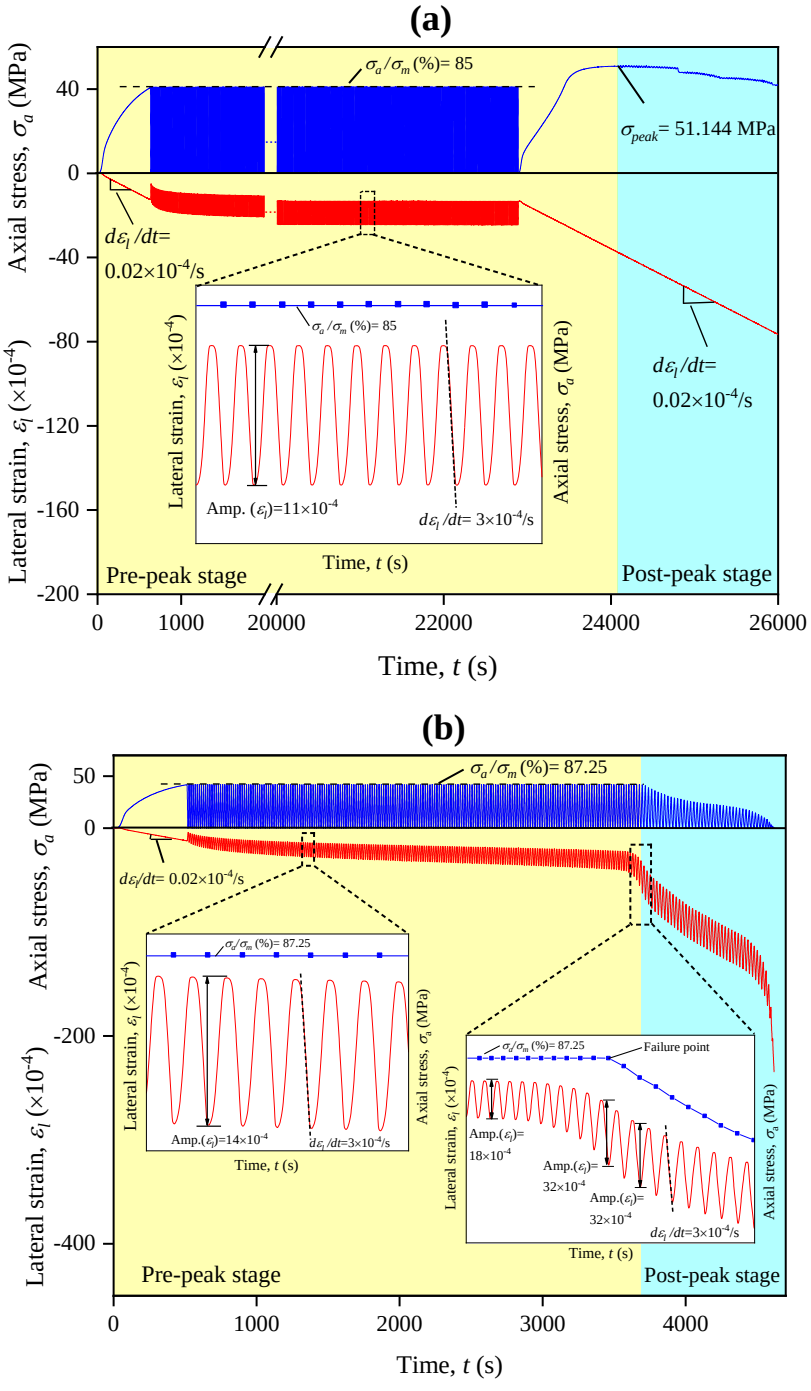

Figure 7.5 Representative axial stress and lateral strain time-histories for the proposed damage-controlled tests for the specimens failed during a final monotonic loading and b systematic cyclic loading

7.4. Stress-Strain Relations

In total, 17 single-level systematic cyclic loading tests (see Table 7.2) were carried out at different stress levels (σ_a/σ_m) ranging from 80% to 96% of the average monotonic strength following the proposed double-criteria damage-controlled testing method. As listed in Table 7.1, the stable and unstable crack growths of rocks on average initiate at $\sigma_{ci}/\sigma_{a-peak}$= 27.95% and $\sigma_{cd}/\sigma_{a-peak}$= 56.51%, respectively. This, in other words, shows that the cyclic loading tests have been conducted in the unstable crack propagation stage, beyond the elastic stress-strain behaviour. To evaluate the influence of cycle number on mechanical properties and post-peak behaviour, the specimens GS-8 and GS-9 were subjected to 5000 and 10000 cycles at σ_a/σ_m=80% and GS-11 experienced 5000 cycles at the stress level of σ_a/σ_m=85% before a monotonic loading. Otherwise, the samples experienced a maximum of 1500 cycles and then a post-monotonic loading should they did not fail during the cyclic loading. According to Beniawski (1967), to ensure fatigue failure of a rock specimen in a timely manner, the cyclic loading test should be conducted just before the onset of the unstable crack propagation stage within the range of 70-85% of the peak strength. A recent review conducted by Cerfontaine and Collin (2018) on rock fatigue studies reported that the rock fatigue threshold ranges from 0.75 to 0.9 of the average monotonic strength for one million loading and unloading cycles depending on rock type and loading conditions. However, in this study, due to test limitations, further cycles did not apply, and the results are valid in the range of 1500-10000 cycles. Based on the results presented in Table 7.2, it is hypothesised that there exists a threshold of σ_a/σ_m which lies between 86% and 87.5 % that indicates the critical boundary of rock strength hardening and fatigue under cyclic loading. In this study, the cyclic loading tests which experienced the monotonic loading at the failure stage were named as hardening cyclic loading tests, while those which failed during cyclic loading at higher stress levels were named as fatigue cyclic loading tests.

Figs. 7.6 and 7.7 show the typical stress-strain results for hardening and fatigue cyclic loading tests, respectively. In these figures, the total post-peak behaviour was highlighted by connecting the indicator stresses (σ_i, the maximum stress of each cycle). The ε_a^{irr} and ε_l^{irr} respectively, represent the irreversible axial strain and the irreversible lateral strain. The areas of interest (AOIs) shown in Figs. 7.6c and 7.7c illustrate the specific parts of the volumetric strain (ε_{vol}) evolution which were enlarged in Figs. 7.6d and 7.7d, respectively. Figs. 7.6a and 7.7a show that the testing methodology was successful in capturing the complete stress-strain

curves of Gosford sandstone specimens subjected to the systematic cyclic loading. Furthermore, like the monotonic tests, a combined class I-II behaviour at different extents can be seen in the post-peak regime for both hardening and fatigue cyclic loading tests. Generally, the variation of hysteretic loops along with the axial strain (Figs. 7.6a and 7.7a), lateral strain (Figs. 7.6b and 7.7b) and volumetric strain (Figs. 7.6c and d and Figs. 7.7c and d) show that the rock specimens which fail during the cyclic loading significantly experience more irreversible strains in the pre-peak regime compared with hardening cyclic loading tests. Also, as shown in Fig. 7.7d, after a few cycles, the hysteretic loops for the fatigue cyclic loading tests switch rapidly from the compaction to dilation, and dilation continues until complete failure.

Table 7.2 The results of the conducted systematic cyclic tests

Test No.	$\sigma_a/\sigma_m(\%)$	N_{total}	N_{after}	Hardening (H) or fatigue (F) test?	ε_{a-f} ($\times 10^{-4}$)	ε_{a-peak} ($\times 10^{-4}$)	Peak strength increase (%)
GS-7	80	1500	-	H	45.80	53.56	0.53
GS-8	80	5000	-	H	43.03	52.36	7.31
GS-9	80	10000	-	H	48.94	55.98	0.05
GS-10	85	1500	-	H	46.38	53.70	6.22
GS-11	85	5000	-	H	48.93	54.29	2.17
GS-12	86	1500	-	H	45.52	50.92	1.93
GS-13	87.50	1500	-	H	47.72	55.04	7.82
GS-14	86.81	636	49	F	-	56.15	-
GS-15	87.23	49	26	F	-	56.06	-
GS-16	87.25	240	42	F	-	54.78	-
GS-17	89.65	40	28	F	-	54.75	-
GS-18	89.82	103	45	F	-	53.12	-
GS-19	91.76	145	97	F	-	52.75	-
GS-20	93	49	36	F	-	54.37	-
GS-21	93.65	280	260	F	-	54.98	-
GS-22	95	752	730	F	-	54.46	-
GS-23	96	474	318	F	-	37.84	-

N_{total} total number of cycles, N_{after} number of cycles after failure point, ε_{a-f} axial strain at the peak of the final cycle, ε_{a-peak} axial strain at the failure point

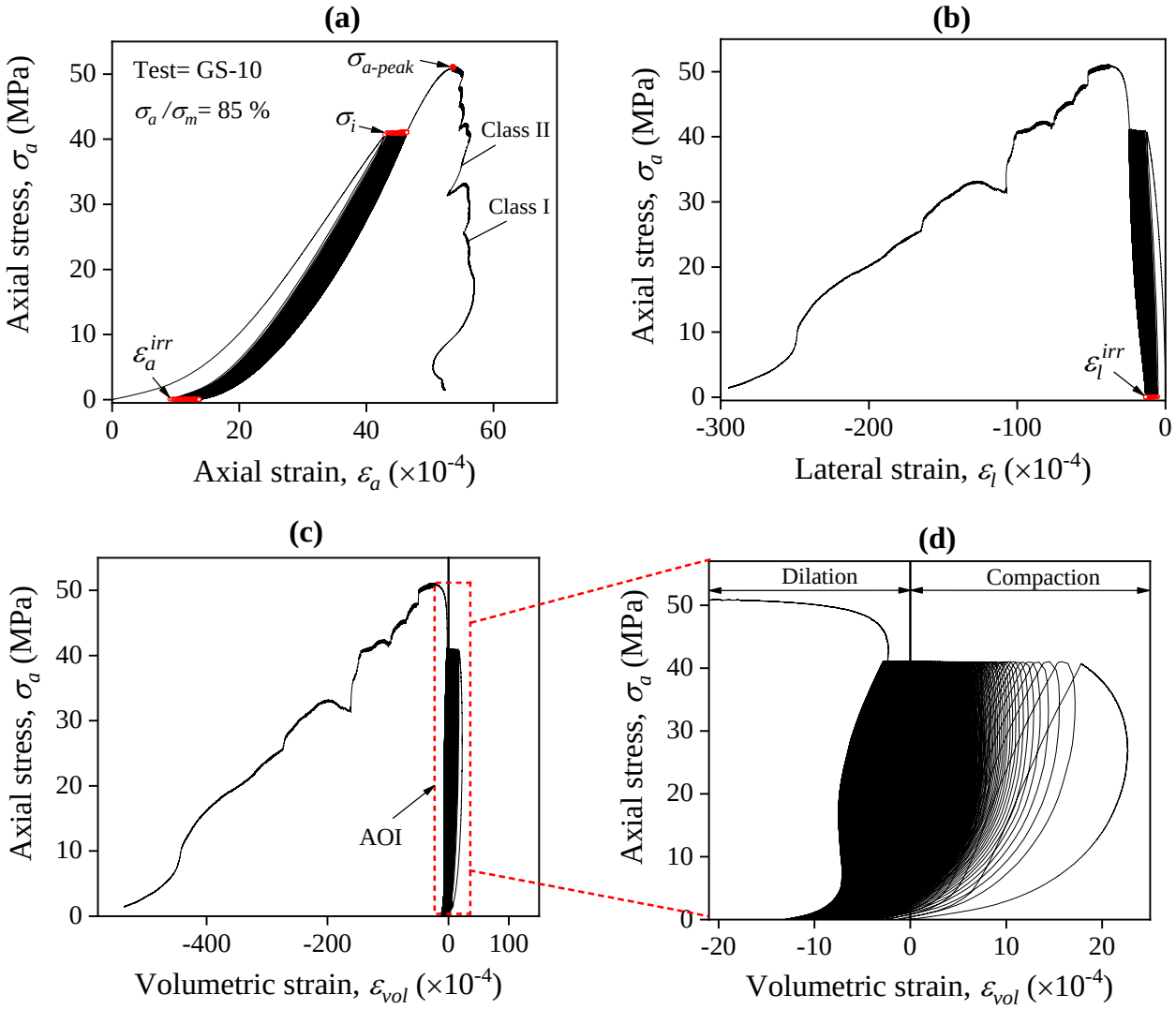

Figure 7.1 Typical stress-strain results for the hardening cyclic loading tests (test GS-10)

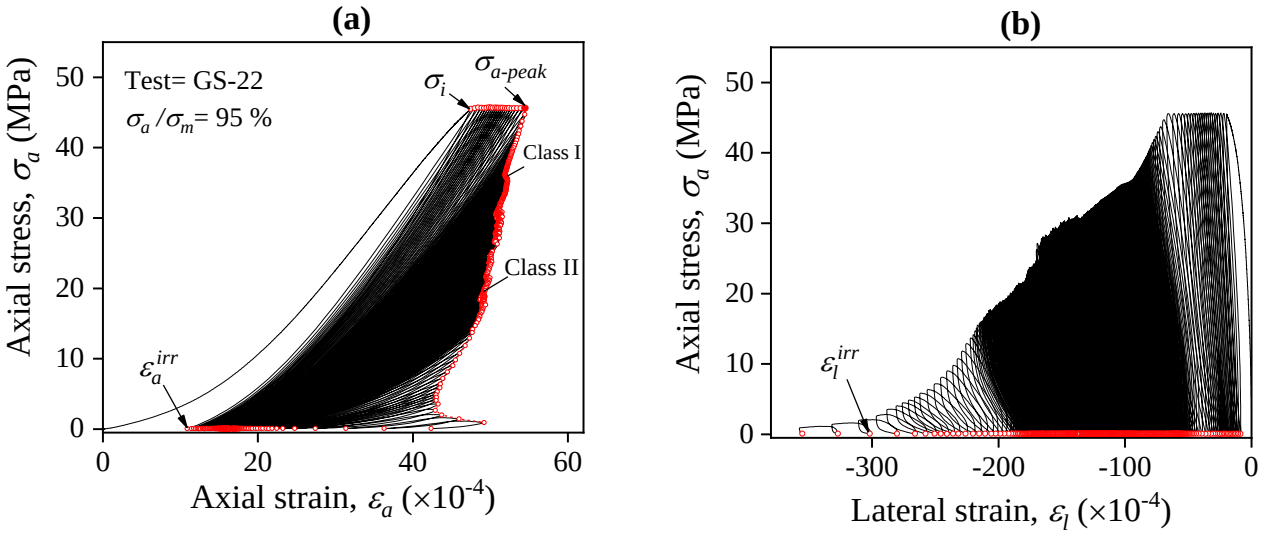

Figure 7.7 Typical stress-strain results for the fatigue cyclic loading tests (test GS-22)

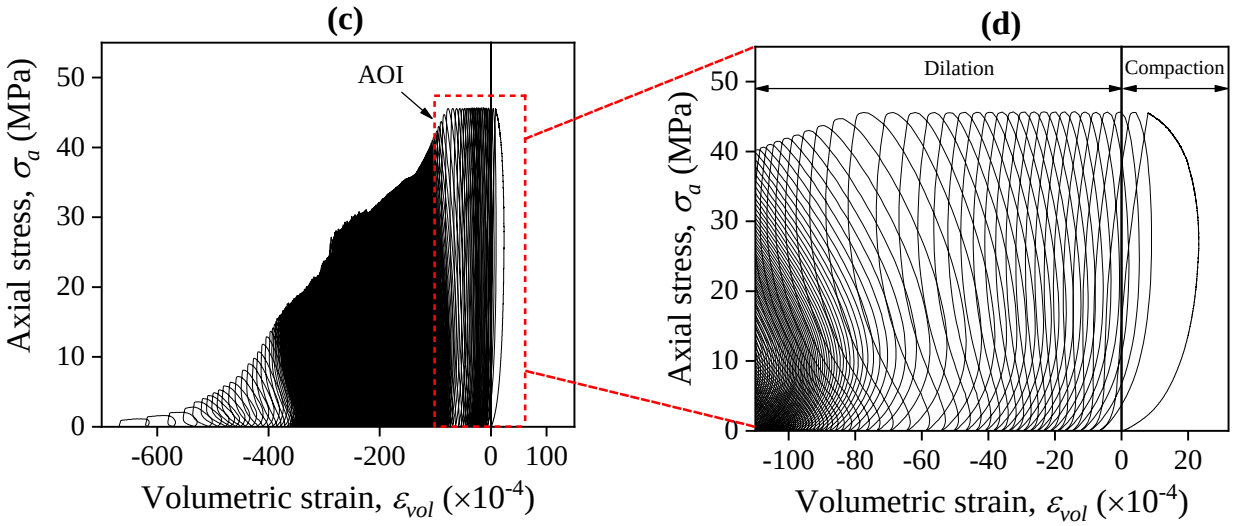

Figure 7.7 (Continued)

7.5. Rock Behaviour During Hardening Cyclic Loading Tests

7.5.1. Damage Evolution in the Pre-Peak Regime

In rock engineering applications, the rock deformation and failure processes are associated with the strain energy evolution (Li et al. 2019). The total inputted mechanical energy during a loading and unloading cycle is transformed into the stored elastic energy (U_e^i) and the dissipated energy (U_d^i) as shown schematically in Fig. 7.8a. The dissipated energy due to the irreversible deformations causes stiffness degradation and rock damage. In this study, the energy dissipation ratio (i.e. $K = U_d/U_e$) and tangent Young's modulus (E_{tan}) were utilised to investigate progressive damage evolution in the pre-peak regime for hardening cyclic loading tests. Fig. 7.8b shows the representative results for specimen GS-10 at σ_a/σ_m=85%. The other hardening cyclic loading tests conducted at different stress levels and with a different number of cycles also showed a similar trend. According to Fig. 7.8b, a two-stage damage evolution procedure can be identified for the hardening cyclic loading tests. In stage A, the E_{tan} increased dramatically during initial cycles (approximately 21.94% compared with the average E_{tan} for monotonic tests in Table 7.1), which can cause to specimen become stiffer. This behaviour can be relevant to the closure of existing defects . An increase of stiffness during initial loading cycle also has been reported by other researchers (Trippetta et al. 2013; Momeni et al. 2015; Taheri and Tatsuoka 2015; Taheri et al. 2016b). On the other hand, the energy dissipation ratio (K) decreased suddenly in stage A, which contributes to the accumulation of elastic strain energy in rock specimen. In stage B, while it was expected to see stiffness degradation due to

incurring irreversible deformations in the specimen by doing more cycles, E_{tan} and K remained fairly constant, and no considerable energy was dissipated until 1500 cycles were completed (i.e. a quasi-elastic behaviour).

This quasi-elastic behaviour can be further investigated using AE results. Fig. 7.8c shows the typical time-history of AE hits recorded for the specimen GS-10. As shown in this figure, few AE hits are observed at the initial monotonic loading stage, which corresponds to seating, loading adjustment by the testing apparatus and the crack closure stage. However, in the second stage, almost no macrocrack (macro-damage) is generated throughout the specimen as a constant trend was observed for the cumulative AE hits during the 1500 cycles. In other words, at this stage, only small amounts of low amplitude AE hits (micro-damages) are generated (see Fig. 7.8c). During the final monotonic loading stage, new microcracks are generated and propagated throughout the specimen, and the cumulative AE hits increase gradually until the peak strength point. This is followed by the rapid rise of cumulative AE hits in the post-peak regime, where the microcracks coalesce, and the cohesive strength of the rock specimen degrades. On the other hand, according to Fig. 7.6, during hardening cyclic loading tests, the specimens do not experience large axial, lateral and volumetric irreversible deformations after 1500 cycles and the hysteretic loops for such tests are very dense. This clearly can be seen from the variation of volumetric strains in the area of interest (AOI) (see Fig. 7.6d). In Fig. 7.6d, it is observed that the slope of the hysteretic loops between the lowest points and the peak points is positive, implying that the current volume of the specimen is mostly at the compaction stage with slight dilation at the end of pre-peak cyclic loading. According to the evolution of damage parameters (i.e. E_{tan} and K), AE hits and the irreversible strains discussed above, the following potential mechanism can be inferred for the observed quasi-elastic behaviour in this study:

During cyclic loading below the fatigue threshold stress, but in the unstable crack propagation stage, some microcracks might be created within the specimens, which may result in grain size reduction and the creation of some pore spaces. The grain size reduction induced by cyclic loading also has been reported by Trippetta et al. (2013) based on the conducted microscopic analysis, although they used different loading history (i.e. damage-controlled cyclic loading tests). On the other hand, by performing additional loading and unloading cycles, the existing or newly generated defects which have been oriented horizontally are closed, and the rock specimen is compacted progressively. This is while the defects which have been oriented vertically are opened progressively. Therefore, it can be hypothesised that the observed quasi-elastic behaviour in this study can be due to the competition between two mechanisms of

dilatant microcracking, which degrades rock stiffness, and rock compaction, which increases stiffness. The damage evolution seems to be independent of the applied stress level as the same trends of K and E_{tan} and AE hits were observed for all hardening cyclic loading tests at different stress levels. This also can be proved by investigating the variation of axial strains at the final loading cycle (ε_{a-f}) and failure point (ε_{a-peak}) for hardening cyclic loading tests (see Table 7.2). As depicted in Fig. 8d, the variation of ε_{a-f} and ε_{a-peak} with stress level is almost similar and constant for all hardening tests, which demonstrates the analogous damage evolution process.

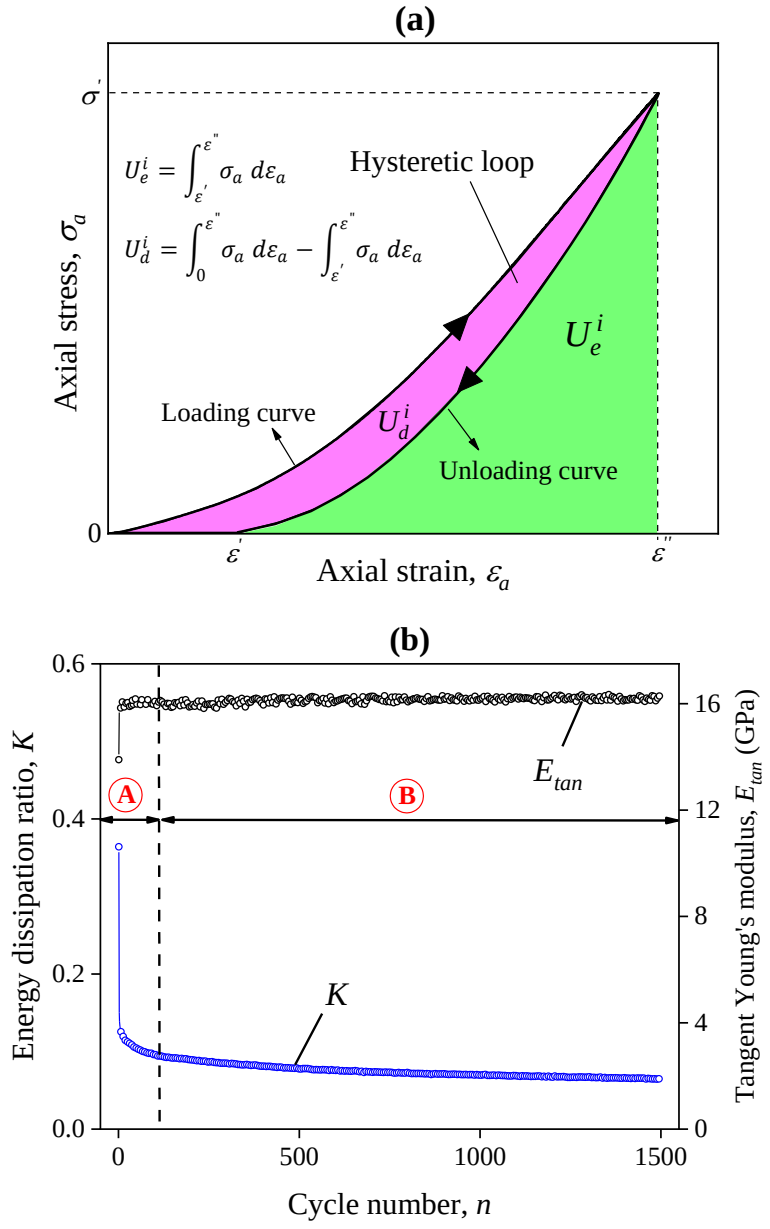

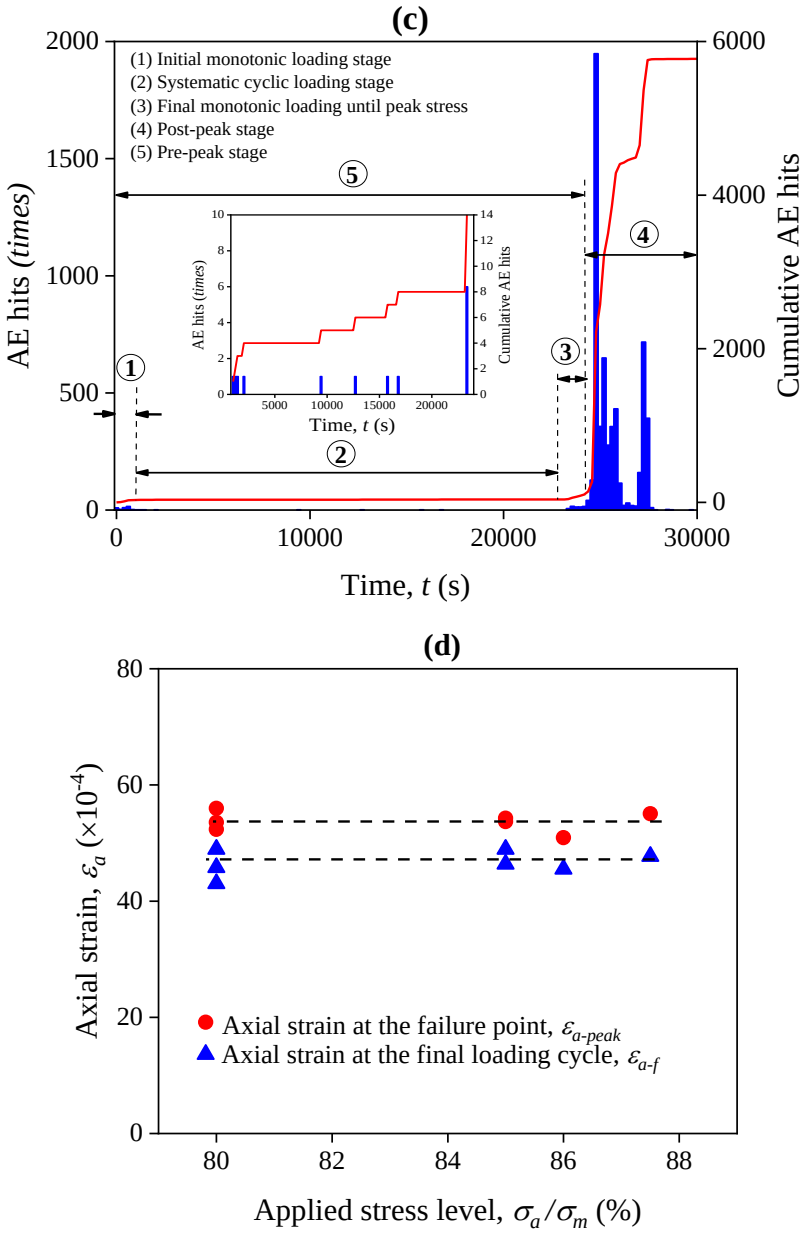

Figure 7.8 a Energy components for a loading and unloading cycle, **b** typical evolution of the energy dissipation ratio and stiffness parameters for the specimen GS-10, **c** typical time-history of AE hits for the specimen GS-10, **d** the variation of axial strain at the final loading cycle and the failure point with stress level for hardening cyclic loading tests

7.5.2. Effect of Pre-Peak Cyclic Loading on the Post-Peak Monotonic Behaviour

In Fig. 7.9, the results of hardening cyclic loading tests are compared with monotonic test results, as normalised axial stress-strain curves. As it may be seen in this figure, the overall post-peak behaviour of monotonic and hardening cyclic loading tests are almost similar. Also, the increase in cycle number at stress levels σ_a/σ_m=80% (from 1500 to 10000 cycles) and σ_a/σ_m=85% (from 1500 to 5000 cycles), has no significant influence on the general post-peak

behaviour. In other words, when the stress level that cyclic loading is applied is not high enough to fail the specimen during cyclic loading, the cyclic loading has a negligible effect on the post-failure behaviour. This can be further investigated based on the variation of rock brittleness. Although there is no consensus regarding the rock brittleness definition and its criterion, it is well-known that brittle rocks show small irreversible deformation before peak strength which is followed by a self-sustaining failure in the post-peak regime (Tarasov and Potvin 2013). From 1956 to date, many rock brittleness indices have been developed by different researchers; however, the strain energy-based indices perform relatively better than others (Zhang et al. 2016). The brittle vs. ductile behaviour of rock materials can be revealed in stress-strain curves during loading and failure. Thus, the rock brittleness indices, which consider the complete stress-strain behaviour of rocks may be more reliable. Munoz et al. (2016a) proposed three fracture energy-based brittleness indices considering both pre-peak and post-peak regimes of stress-strain curves for different rocks under uniaxial compressive tests. They reported that the proposed indices properly describe an unambiguous and monotonic scale of brittleness with increasing pre-peak strength parameters (i.e. σ_{cd}, E_{tan} and σ_{a-peak}). Therefore, in this study, the following equations were used to measure the overall brittleness (BI) of the tested specimens under systematic cyclic loading.

$$BI = \frac{U_e}{U_t} = \frac{U_e}{U_{pre}+U_{post}} \tag{7.1}$$

$$U_e = \frac{\sigma_{a-peak}^2}{2E_{tan}} \tag{7.2}$$

where U_t, U_e, U_{pre} and U_{post} are total fracture energy in the pre-peak and post-peak stages, elastic energy at peak stress, the pre-peak dissipated energy and the post-peak dissipated energy, respectively.

Figure 7.10a shows the different strain energy components defined above for rock brittleness determination under monotonic loading. For hardening cyclic loading tests (i.e. GS-7 to GS-13), the final monotonic loading stress-strain curves were extracted from the stress-strain relations shown in Fig. 7.9. The strain energy components were calculated for all monotonic and hardening cyclic loading tests, and the corresponding BI values were determined. The results are listed in Table 7.3. Fig. 7.10b shows the variation of BI values for these tests. As may be seen in this figure, the BI values of the specimens tested under hardening cyclic loading are almost similar to those obtained under the monotonic loading conditions. Therefore, it can

be stated that the pre-peak systematic cyclic loading, doesn't have a notable influence on the post-peak instability of rocks if it does not lead to failure.

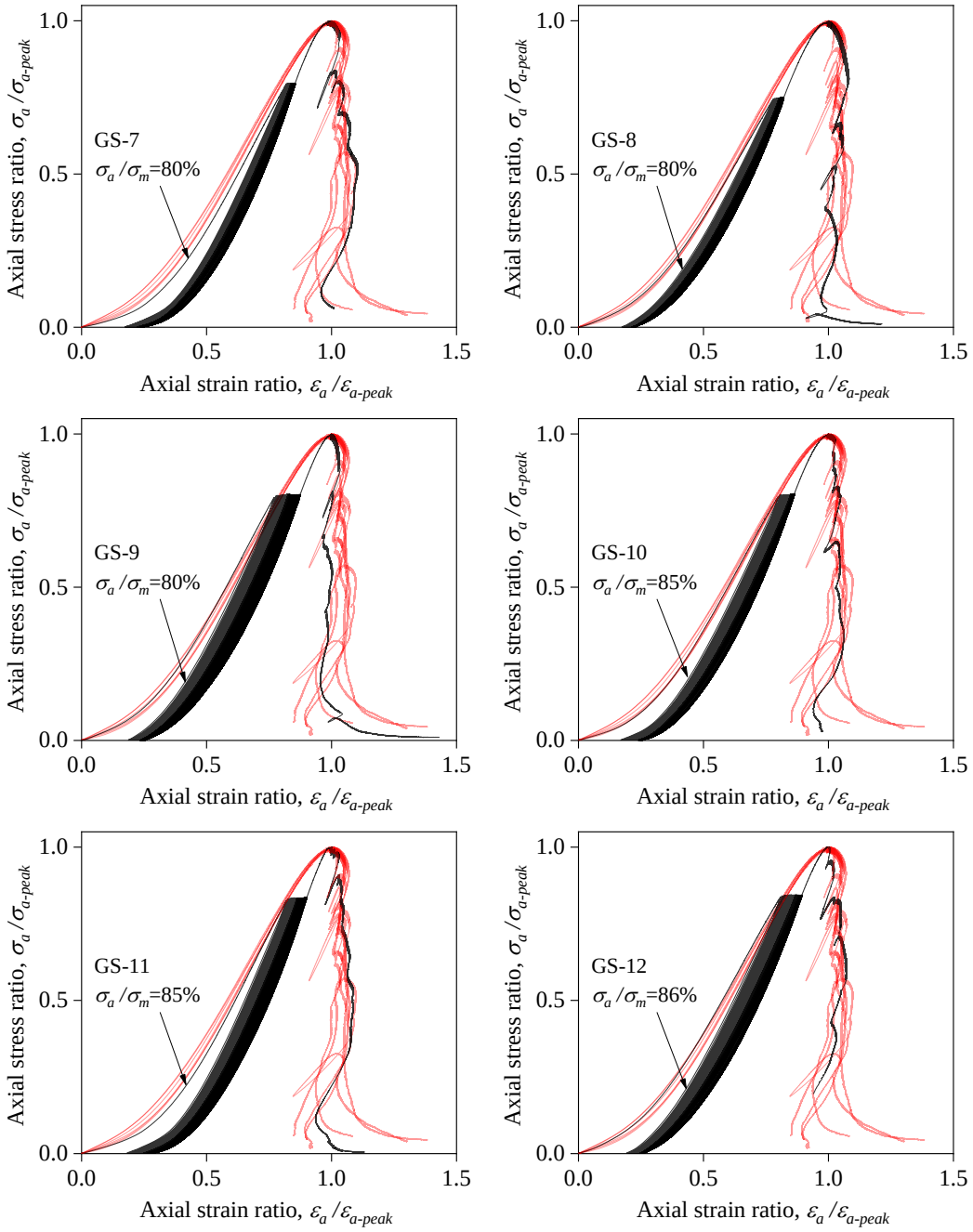

Figure 7.9 Normalised axial stress-strain relations of hardening cyclic loading and monotonic tests

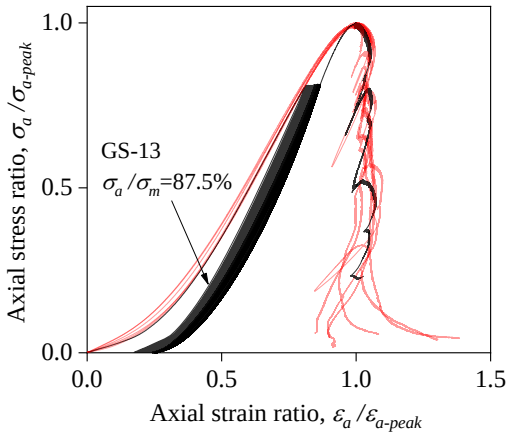

Figure 7.9 (Continued)

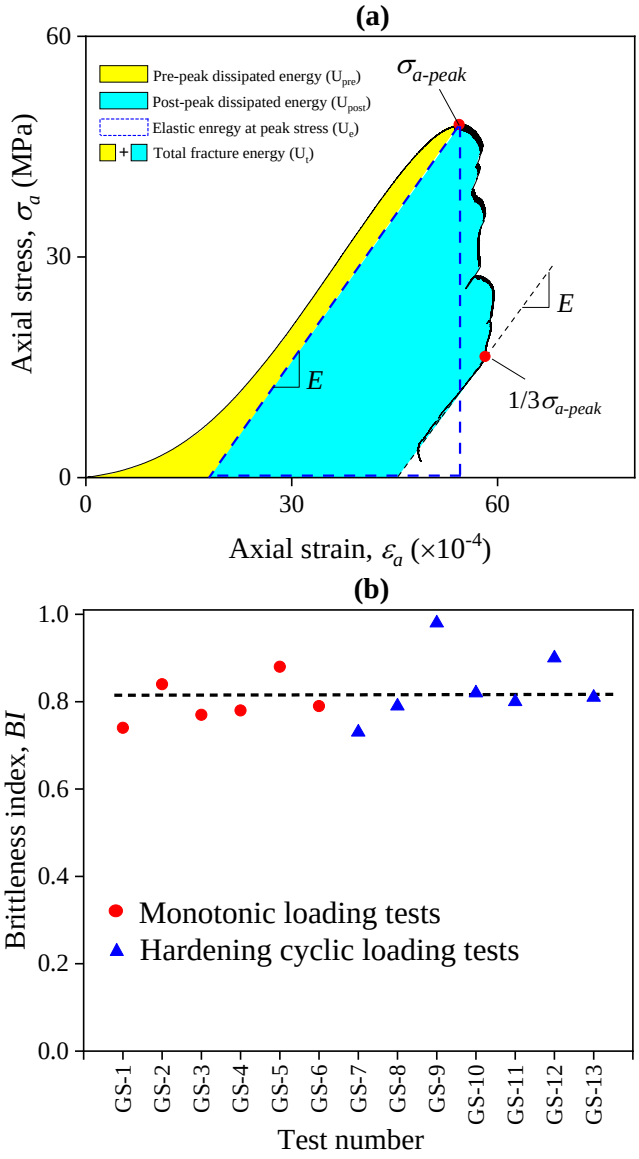

Figure 7.10 a Strain energy components for monotonic loading and **b** brittleness index (*BI*) variation for monotonic loading and hardening cyclic loading tests

Table 7.3 The values of strain energy components and BI for different tests

Test type	Test No.	U_{pre} (MPa)	U_e (MPa)	U_{post} (MPa)	U_{total} (MPa)	BI
Monotonic	GS-1	0.021	0.087	0.096	0.117	0.74
	GS-2	0.023	0.091	0.086	0.109	0.84
	GS-3	0.020	0.084	0.088	0.108	0.77
	GS-4	0.021	0.081	0.082	0.103	0.78
	GS-5	0.021	0.095	0.086	0.107	0.88
	GS-6	0.019	0.082	0.086	0.105	0.78
Hardening	GS-7	0.015	0.067	0.078	0.092	0.73
	GS-8	0.017	0.074	0.078	0.094	0.79
	GS-9	0.010	0.073	0.064	0.074	0.98
	GS-10	0.013	0.075	0.079	0.091	0.82
	GS-11	0.008	0.069	0.078	0.085	0.80
	GS-12	0.008	0.071	0.071	0.079	0.90
	GS-13	0.013	0.077	0.082	0.096	0.81
Fatigue	GS-14	0.042	0.064	0.058	0.100	0.64
	GS-15	0.025	0.066	0.067	0.091	0.73
	GS-16	0.029	0.065	0.064	0.094	0.70
	GS-17	0.023	0.068	0.067	0.090	0.76
	GS-18	0.026	0.067	0.081	0.107	0.62
	GS-19	0.042	0.068	0.058	0.099	0.69
	GS-20	0.038	0.076	0.049	0.087	0.87
	GS-21	0.041	0.073	0.055	0.096	0.76
	GS-22	0.040	0.076	0.049	0.089	0.85
	GS-23	0.021	0.061	0.051	0.072	0.85

7.5.3. Rock Strength Improvement

In this study, as listed in Table 7.2, the strength hardening percentage varied between 0.05% to 7.82% for the tested Gosford sandstone specimens. Figure 7.11a shows the variation of axial peak stress (σ_{a-peak}) for all monotonic and hardening cyclic loading tests. As demonstrated in this figure, in general, higher σ_{a-peak} values are recorded for the specimens which experienced a cyclic loading history (i.e. hardening tests), and about half of the hardening cyclic loading tests have σ_{a-peak} values greater than the upper limit of the monotonic tests. Fig. 7.11b shows the variation of the strength hardening ratio (σ_h/σ_m) against the applied stress level. According to this figure, the strength hardening seems to be independent of the applied stress level (σ_a/σ_m). As discussed in section 5.1, after an initial stiffness improvement of the specimens

for several cycles, a quasi-elastic behaviour dominated the damage evolution during the pre-peak cyclic loading. This behaviour was accompanied by the progressive rock compaction (see Fig. 7.6) and strength improvement up to 8%. It should be noted that rock strength improvement induced by cyclic loading also has been reported in several studies for porous Hawkesbury sandstone (up to 11%) (Taheri et al. 2016a, 2017), hard graywacke sandstone (up to 29%) (Singh 1989) and rock salt (up to 171%) (Ma et al. 2013). This shows that rocks depending on their intrinsic characteristics and the applied loading history and loading conditions, may show strength hardening behaviour at different extents. Taheri et al. (2017) argue that when the rock specimen is subjected to cyclic loading at a stress level lower than a threshold value, the weak bonding between the mesoscopic elements may be broken down, and the created fine materials, may fill up the internal voids, causing rock compaction and strength improvement. It should be mentioned that other potential mechanisms such as microcrack tip blunting and the interlocking of grains/asperities may involve in strength hardening. For instance, by considering the initial porosity of Gosford sandstone (i.e. 18%), due to the grain size reduction induced by cyclic loading during the quasi-elastic stage, some additional pore spaces might be generated within the specimens. When the cyclic loading-induced microcracks meet these pores, their tips may become blunt, resulting in a decrease in stress concentration at the crack tips and an increase in fracture toughness. This, on the other hand, may cause to stopping the microcrack propagation. This behaviour can also be accompanied by grain interlocking, closure of cracks, and finally, compaction of the specimens during cyclic loading. Further microscopic investigations will shed more light on cyclic loading induced hardening mechanism.

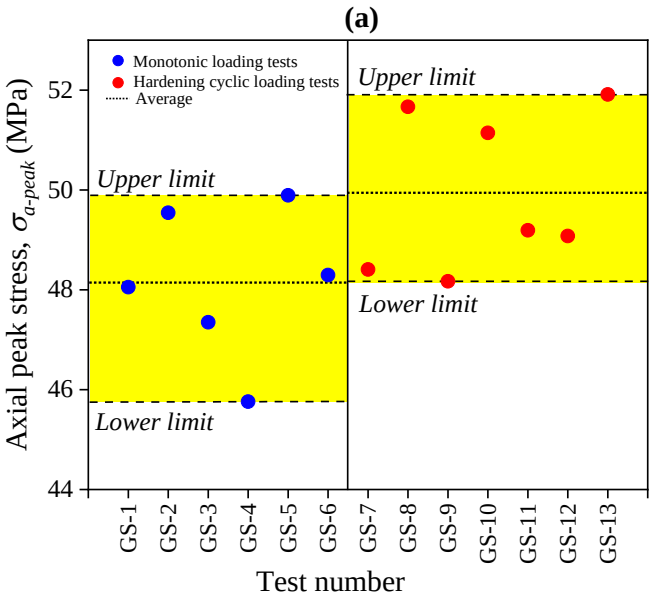

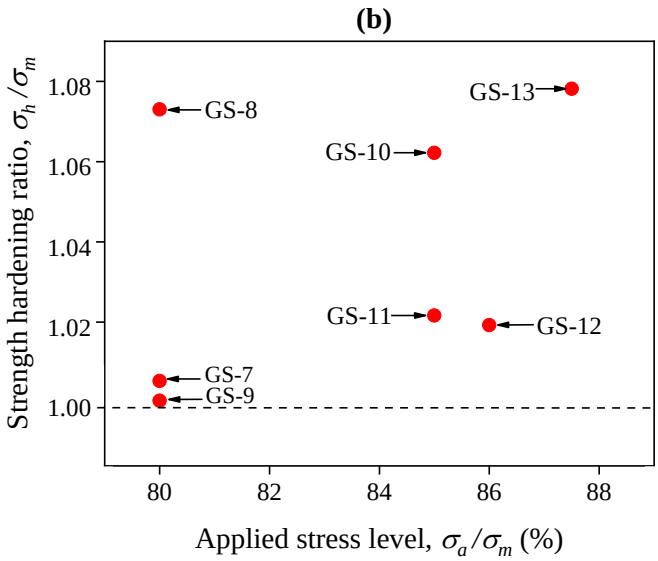

Figure 7.11 a The variation of axial peak stress for all monotonic and hardening cyclic loading tests and **b** strength hardening ratio vs. applied stress level for hardening cyclic loading tests

7.6. Rock Behaviour During Fatigue Cyclic Loading Tests

6.1. Evaluation of Post-Peak Behaviour

As discussed in section 7.5.2, the systematic cyclic loading has no notable effect on the post-peak behaviour of Gosford sandstone specimens if the cyclic stress level is below fatigue threshold stress. In this section, the influence of systematic cyclic loading beyond the fatigue threshold stress on the post-peak behaviour of Gosford sandstone specimens was evaluated. Figure 7.12 shows the normalised axial stress-strain curves for both monotonic tests and fatigue cyclic loading tests. The effect of cyclic loading history on the post-failure behaviour can be evaluated using the variation of rock brittleness index (BI) with the applied stress level. To do so, the envelope curve connecting the loci of the indicator stresses (σ_i) both in the pre-peak and the post-peak regimes were drawn, and the same procedure explained in section 7.5.2 was utilised to measure the overall brittleness index. Fig. 7.13a shows the extracted envelope curve for the typical test of GS-16. The strain energy components along with the BI values were determined for all fatigue cyclic loading tests, and the obtained values were tabulated in Table 7.3. Figure 7.13b displays the variation of BI values with the applied stress level. From this figure, it can be observed that the overall rock brittleness increases with an increase in the applied stress level. This means that rock may fail in a more brittle manner when it experiences cyclic loading at the stress levels close to its monotonic strength. In other words, in deep

underground excavations, a cyclic loading history induced by seismic events that exceed the fatigue threshold stress may result in more violent failure causing casualties and financial loss. On the other hand, the weak seismic events which are applied at stress levels much lower than the rock monotonic strength do not seem critical to damage the structures. These seismic events may even, slightly improve long-term stability.

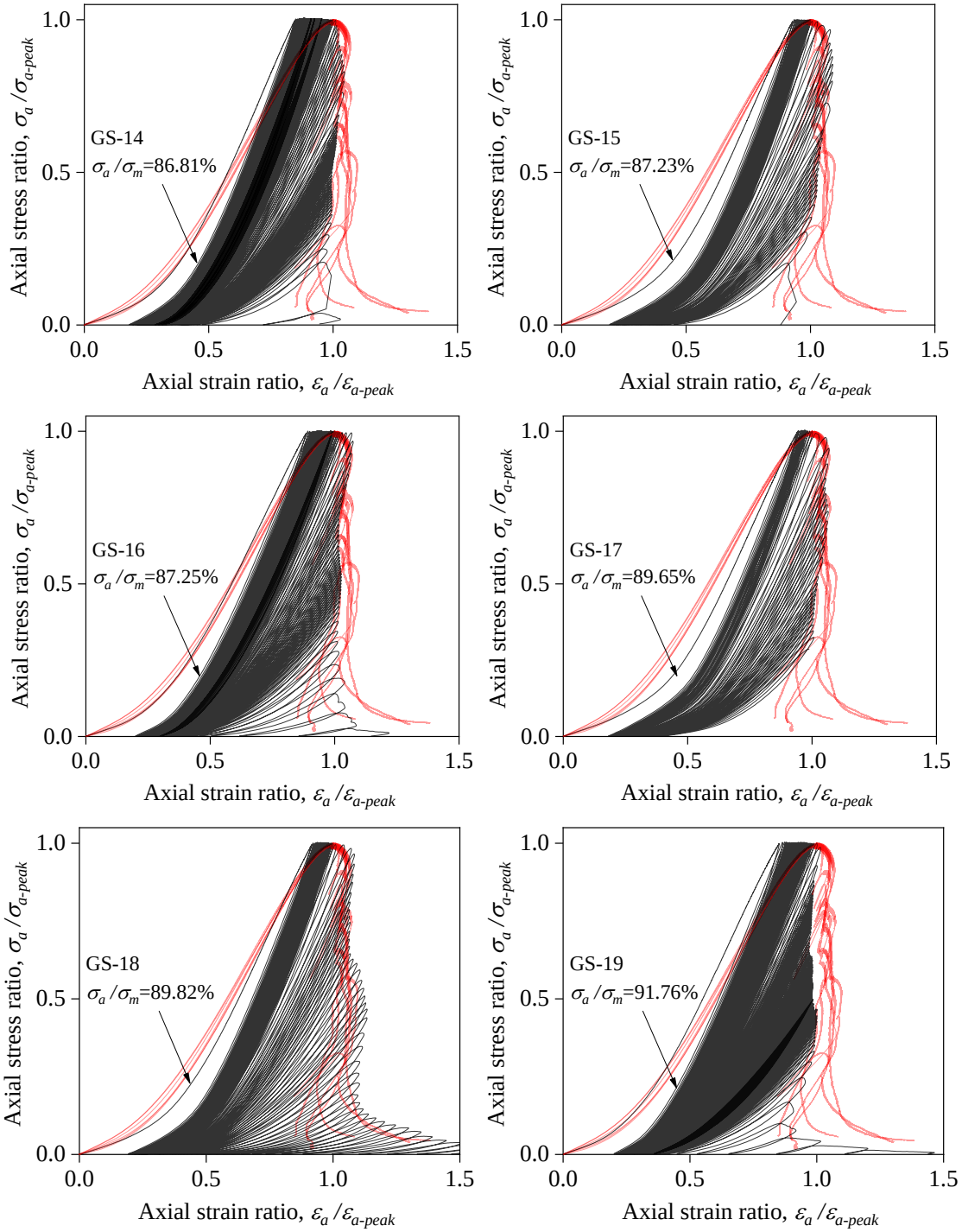

Figure 7.12 Normalised axial stress-strain relations of fatigue cyclic loading and monotonic tests

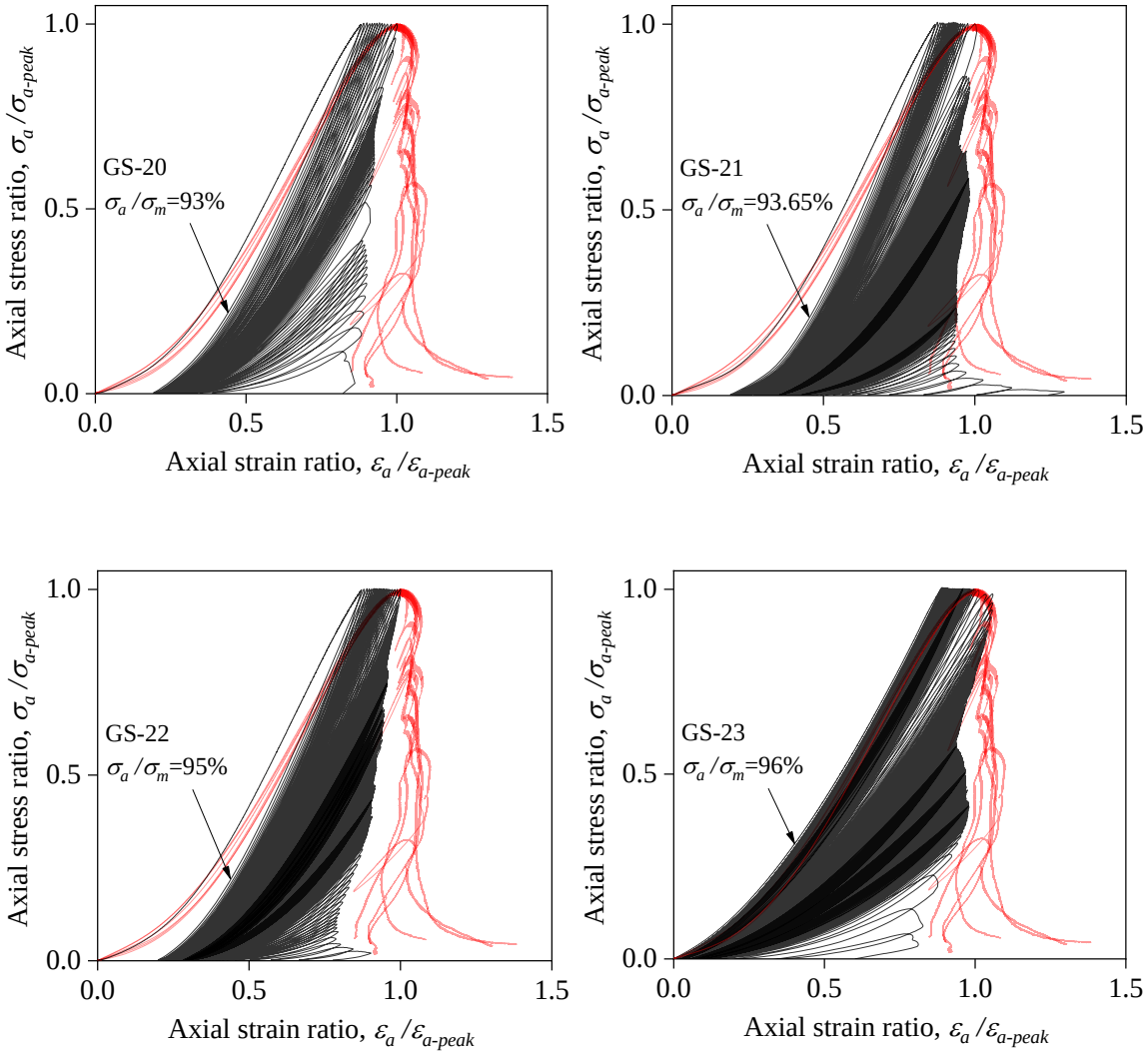

Figure 7.12 (Continued)

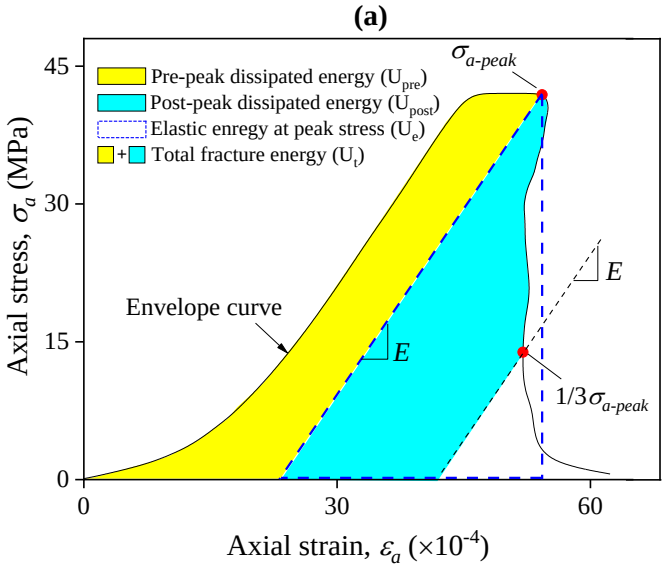

Figure 7.13 a Strain energy components for the fatigue cyclic loading tests and **b** variation of brittleness index with the applied stress level for the fatigue cyclic loading tests

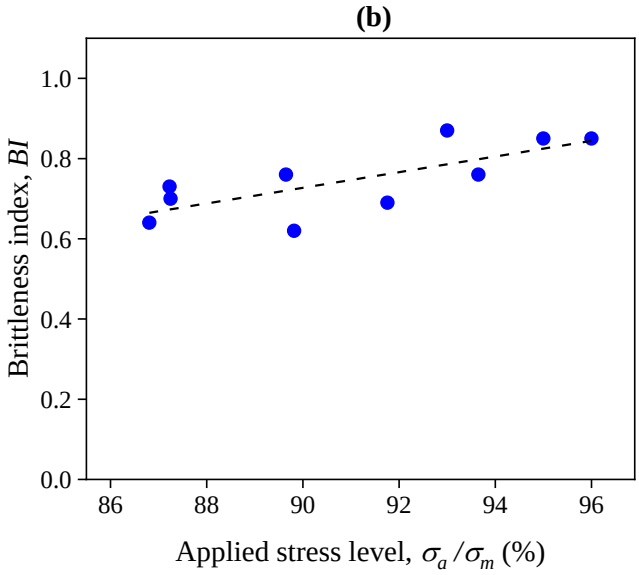

Figure 7.13 (Continued)

7.6.2. Damage Evolution in the Post-Peak Regime

The irreversible deformations are not accumulated at a constant rate in the rock specimen during the pre-peak cyclic loading but follow an inverted S-shaped behaviour comprising three main phases of transient, steady and acceleration (Fig. 7.14a) (Royer-Carfagni and Salvatore 2000; Xiao et al. 2009; Fuenkajorn and Phueakphum 2010). These three phases are manifested as loose-dense-loose behaviour in the stress-strain curves of systematic cyclic loading based on the variation of hysteretic loops (Fig. 7.14b). According to Zoback and Byerlee (1975), the initial loose cycles correspond to the energy consumption for crack growth, that stabilises after several cycles. In the second phase that hysteric loops are closed and dense, the frictional work is more dominant, and the micro-cracks are opened and closed constantly without any significant extension. However, when the rock specimen is close to the failure point (i.e. the acceleration phase), the crack growth dominates, and hysteresis of the cycles increases. At higher stress levels, due to rapid accumulation of damage, the steady phase will not be visible. On the other hand, at lower stress levels (as discussed in section 7.5.1), after the initial phase, a steady-state dominates the whole test for a long time (Xiao et al. 2009).

According to the stress-strain curves obtained for the fatigue cyclic loading tests in this study (Fig. 7.11), the loose-dense-loose behaviour with different extents can be identified for hysteretic loops not only in the pre-peak regime but also in the post-peak regime. For instance, Fig. 7.14c and d shows the typical results for specimen GS-23 in which the loose-dense-loose behaviours are evident. As shown in the inset figure of the axial stress-strain curve, in the pre-peak regime, the hysteretic loops follow a loose-dense-loose behaviour according to the

mechanism explained above. The loose behaviour at the end of the pre-peak systematic cyclic loading extends to the post-peak regime and then accelerates. In Fig. 7.14e and f the cumulative irreversible axial ($\sum \varepsilon_a^{irr}$) and cumulative irreversible lateral strains ($\sum \varepsilon_l^{irr}$) measured after full unloading of each loading cycle in the post-peak regime of specimen GS-23 are plotted against the axial stress ratio (σ_a/σ_{a-peak}). According to these figures, when the specimen loses its load-bearing capacity until σ_a/σ_{a-peak}= 0.69, due to quick dissipation of strain energy, the cumulative irreversible strains increases rapidly, which provided the loose hysteretic loops. Then, interestingly, the hysteretic loops are closed and experience a dense behaviour for a large number of cycles in the post-peak regime until σ_a/σ_{a-peak}= 0.38. Finally, by the creation of large axial and lateral deformations within the specimen, the cumulative irreversible strains increased dramatically until complete failure occurred. This, in turn, provided the final loose hysteretic loops. The observed loose-dense-loose behaviour in the post-peak regime for this specimen can be summarised as a secondary inverted S-shaped damage behaviour, as shown in Fig. 7.14g. Depending on the number of cycles that the specimens have experienced after failure point, similar damage evolution trends with different extents also were observed for other fatigue cyclic loading tests. According to Table 7.2 and as shown in Fig. 7.14h, it can be observed that with the increase of applied stress level (σ_a/σ_m), the number of cycles after failure point increases exponentially, which is consistent with the formation of the secondary three-stage inverted S-shaped behaviour in the post-peak regime. In other words, it can be found out that the damage per loading/unloading cycle in the post-peak regime of the fatigue cyclic loading tests decreases with the increase of the applied stress level.

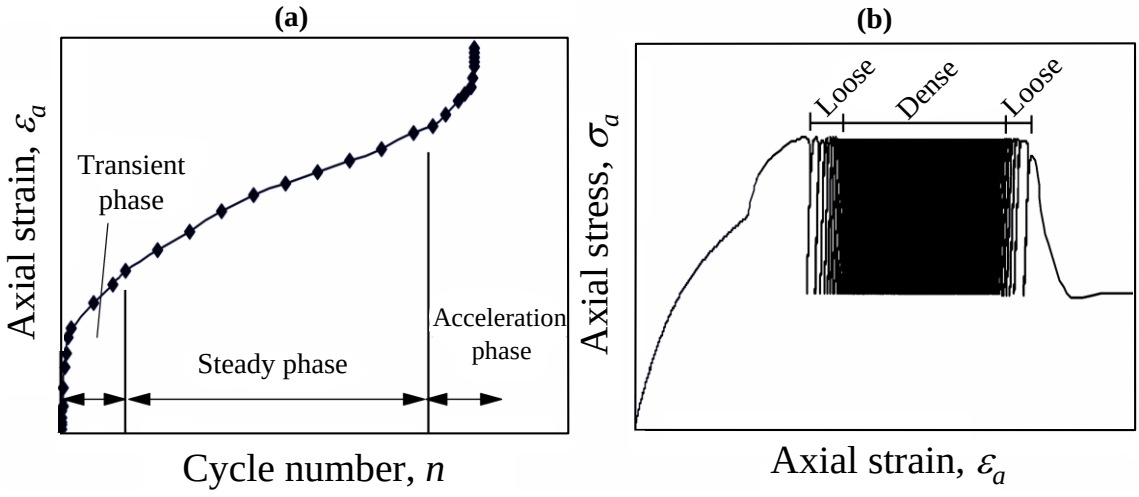

Figure 7.14 a, b Typical inverted S-shaped damage behaviours in the pre-peak regime (Modified from Guo et al. 2012), **c, d** the loose-dense-loose behaviour in the post-peak

regime of specimen GS-23, **e, f** the evolution of cumulative irreversible strains in the post-peak regime for specimen GS-23, **g** the secondary inverted S-shaped damage behaviour in the post-peak regime for specimen GS-23 and **h** the number of cycles after failure point versus the applied stress level for the fatigue cyclic loading tests

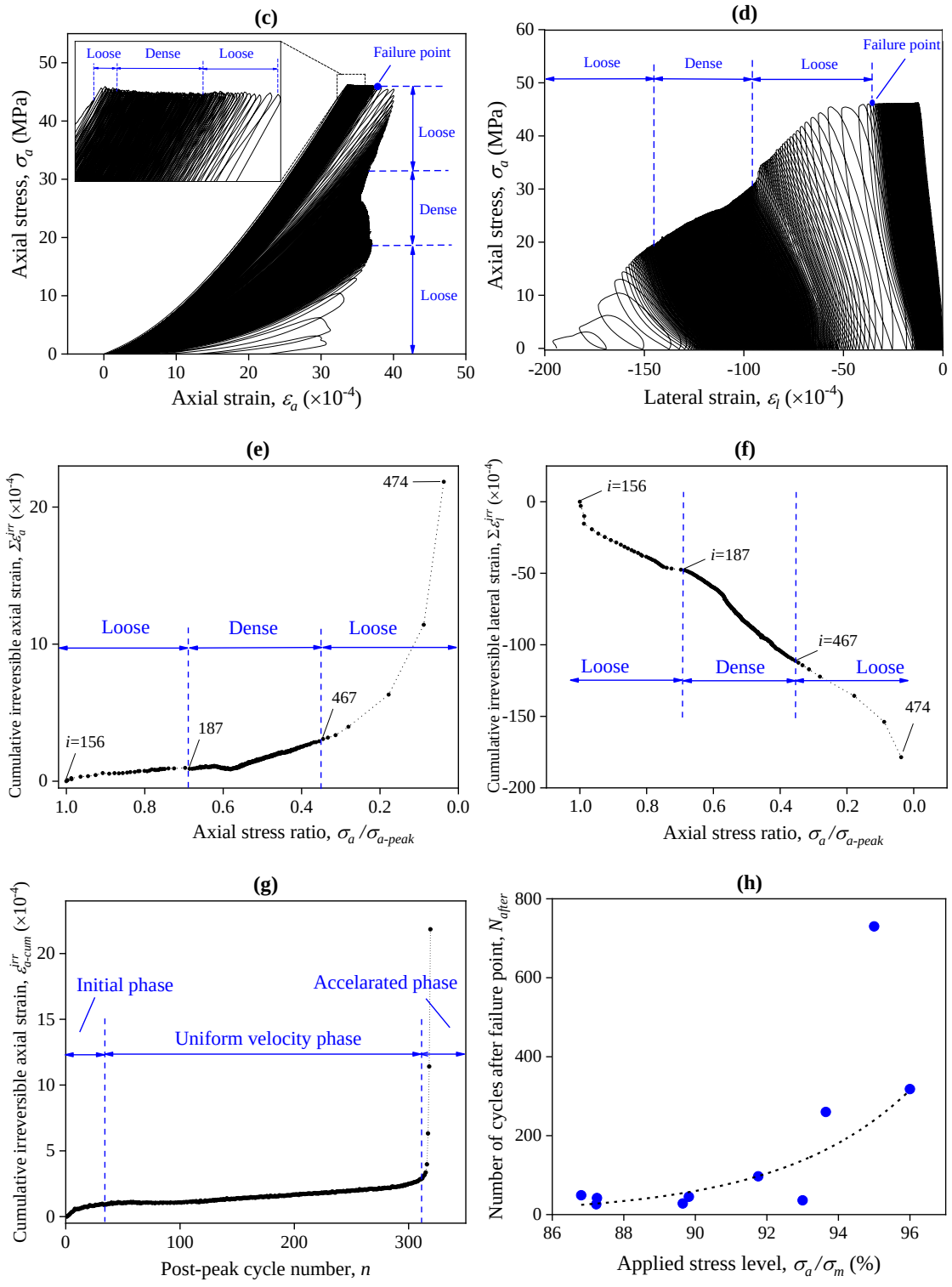

Figure 7.14 (Continued)

7.7. Conclusions

In this study, a series of systematic cyclic loading tests were conducted on Gosford sandstone specimens using an innovative double-criteria damage-controlled testing method. A comprehensive evaluation was carried out on the experimental results in terms of damage evolution, post-peak instability and strength hardening behaviour. The following conclusions can be drawn:

1. It was found that there exists a threshold of σ_a/σ_m, which lies between 86-87.5%. For σ_a/σ_m lower than this range, the specimens did not fail after experiencing a large number of cycles. The evaluation of the energy dissipation ratio, tangent Young's modulus and AE hits for hardening cyclic loading tests showed that the rock specimens follow a two-stage damage evolution law dominated by a quasi-elastic behaviour in the pre-peak regime. This quasi-elastic behaviour can be attributed to a balance between two mechanisms of dilatant microcracking and rock compaction during cyclic loading below the fatigue threshold stress. Moreover, the damage evolution in the pre-peak regime of the hardening cyclic loading tests was found to be independent of the number of cycles, as no significant influence on damage and/or hardening behaviour was observed by increasing the cycle number from 1500 to 10000 cycles.
2. A similar pre-peak and post-peak behaviour was observed for monotonic tests and hardening cyclic loading tests when they were compared as the normalised axial stress-strain relations. Also, according to the variation of an energy-based brittleness index (BI), it was found that the pre-peak systematic cyclic loading has negligible influence on the post-failure instability, when the applied stress level is not high enough to fail the specimen during cyclic loading.
3. For the specimens subjected to the systematic cyclic loading below the fatigue threshold stress, the peak strength increased up to 8% after applying the monotonic loading. This strength enhancement might be due to rock compaction and porosity reduction mechanism induced by cyclic loading. On the other hand, the fatigue failure was observed for the specimens cyclically loaded beyond the fatigue threshold stress. For such tests, a rapid accumulation of lateral and volumetric strains was observed in the pre-peak regime.
4. For the systematic cyclic loading tests conducted beyond the fatigue threshold stress, it was observed that with the increase of the applied stress level, the rock specimens tend to behave as self-sustained in the post-failure stage. This was confirmed by the increase

of brittleness index (BI) with σ_a/σ_m for the fatigue cyclic loading tests. Therefore, rocks may behave in a more brittle/violent manner when the cyclic loading is applied at stress levels close to their monotonic strength.

5. The evolution of hysteretic loops for fatigue cyclic loading tests showed that the rock specimens follow a loose-dense-loose behaviour in the pre-peak regime. However, the loose behaviour before the failure point is extended to the post-peak stage for several cycles. These loose hysteretic loops are followed by a dense behaviour for a large number of cycles until the complete failure of the specimen occurs, demonstrating another loose behaviour. This generally can be manifested as a secondary inverted non-linear S-shaped damage behaviour when the cumulative axial and cumulative lateral irreversible strains are plotted against the post-peak cycle number. It was observed that damage per cycle decreases exponentially with the increase of the applied stress level, and the three phases of the inverted S-shaped damage behaviour become more visible in the post-peak regime.

Acknowledgements

The first author acknowledges the University of Adelaide for providing the research fund (Beacon of Enlightenment PhD Scholarship) to conduct this study. The authors would like to thank the laboratory staff, in particular, Simon Golding and Dale Hodson, for their aids in conducting the tests.

References

Beniawski ZT (1967) Mechanism of brittle fracture of rock. *International Journal of Rock Mechanics and Mining Sciences* 4(4):395-406

Bruning T, Karakus M, Nguyen GD, Goodchild D (2018) Experimental Study on the Damage Evolution of Brittle Rock Under Triaxial Confinement with Full Circumferential Strain Control. *Rock Mechanics and Rock Engineering* 51(11):3321–3341

Cardani G, Meda A (2004) Marble behaviour under monotonic and cyclic loading in tension. *Construction and Building materials* 18(6):419–424

Cattaneo S, Labuz JF (2001) Damage of marble from cyclic loading. *Journal of materials in civil engineering* 13(6):459–465

Cerfontaine B, Collin F (2018) Cyclic and fatigue behaviour of rock materials: review,

interpretation and research perspectives. *Rock Mechanics and Rock Engineering* 51(2):391–414

Erarslan N, Alehossein H, Williams DJ (2014) Tensile Fracture Strength of Brisbane Tuff by Static and Cyclic Loading Tests. *Rock Mechanics and Rock Engineering* 47(4):1135–1151

Fairhurst CE, Hudson JA (1999) Draft ISRM suggested method for the complete stress-strain curve for intact rock in uniaxial compression. *International Journal of Rock Mechanics and Mining Sciences* 36(3):279–289

Fuenkajorn K, Phueakphum D (2010) Effects of cyclic loading on mechanical properties of Maha Sarakham salt. *Engineering Geology* 112(1-4):43–52

Gong QM, Yin LJ, Wu SY, et al (2012) Rock burst and slabbing failure and its influence on TBM excavation at headrace tunnels in Jinping II hydropower station. *Engineering Geology* 124:98–108

Guo H, Ji M, Zhang Y, Zhang M (2018) Study of mechanical property of rock under uniaxial cyclic loading and unloading. *Advances in Civil Engineering* 2018, pp 1-6

Haimson BC (1978) Effect of Cyclic Loading on Rock. In: Silver ML, Tiedemann D (eds) Dynamic Geotechnical Testing. *ASTM International, West Conshohocken, PA*, pp 228–245

Heap MJ, Faulkner DR (2008) Quantifying the evolution of static elastic properties as crystalline rock approaches failure. *International Journal of Rock Mechanics and Mining Sciences* 45(4):564–573

Heap MJ, Faulkner DR, Meredith PG, Vinciguerra S (2010) Elastic moduli evolution and accompanying stress changes with increasing crack damage: implications for stress changes around fault zones and volcanoes during deformation. *Geophysical Journal International* 183(1):225–236

Heap MJ, Vinciguerra S, Meredith PG (2009) The evolution of elastic moduli with increasing crack damage during cyclic stressing of a basalt from Mt. Etna volcano. *Tectonophysics* 471(1):153–160

Jansen D, Shah S (1997) Effect of Length on Compressive Strain Softening of Concrete. *Journal of Engineering Mechanics* 123(1):25–35

Li T, Pei X, Wang D, et al (2019) Nonlinear behavior and damage model for fractured rock under cyclic loading based on energy dissipation principle. *Engineering Fracture Mechanics* 206:330–341

Liu J, Xie H, Hou Z, et al (2014) Damage evolution of rock salt under cyclic loading in unixial tests. *Acta Geotechnica* 9(1):153–160

Liu Q, Huang S, Kang Y, Liu X (2015) A prediction model for uniaxial compressive strength of deteriorated rocks due to freeze-thaw. *Cold Regions Science and Technology* 120:96–107

Liu X, Liang Z, Zhang Y, et al (2018) Experimental study on the monitoring of rockburst in tunnels under dry and saturated conditions using AE and infrared monitoring. *Tunnelling and Underground Space Technology* 82:517–528

Lockner D (1993) The role of acoustic emission in the study of rock fracture. *International Journal of Rock Mechanics and Mining Sciences & Geomechanics Abstracts* 30(7):883–899

Ma L, Liu X, Wang M, et al (2013) Experimental investigation of the mechanical properties of rock salt under triaxial cyclic loading. *International Journal of Rock Mechanics and Mining Sciences* 34–41

Martin CD, Chandler N (1994) The Progressive Fracture of Lac du Bonnet Granite. *International Journal of Rock Mechanics and Mining Sciences and Geomechanics Abstracts* 31(6):643–659

Martin CD (1997) Seventeenth Canadian Geotechnical Colloquium: The Effect of Cohesion Loss and Stress Path on Brittle Rock Strength. *Canadian Geotechnical Journal* 34(5):698–725

Momeni A, Karakus M, Khanlari G, Heidari M (2015) Effects of cyclic loading on the mechanical properties of a granite. *International Journal of Rock Mechanics and Mining Sciences* 100(77):89-96

Munoz H, Taheri A (2019) Postpeak deformability parameters of localized and nonlocalized damage zones of rocks under cyclic loading. *Geotechnical Testing Journal* 42(6):1663–1684

Munoz H, Taheri A, Chanda EK (2016a) Fracture Energy-Based Brittleness Index

Development and Brittleness Quantification by Pre-peak Strength Parameters in Rock Uniaxial Compression. *Rock Mechanics and Rock Engineering* 49(12):4587–4606

Munoz H, Taheri A, Chanda EK (2016b) Pre-peak and post-peak rock strain characteristics during uniaxial compression by 3D digital image correlation. *Rock Mechanics and Rock Engineering* 49(7):2541–2554

Royer-Carfagni G, Salvatore W (2000) The characterization of marble by cyclic compression loading: experimental results. *Mechanics of Cohesive-frictional Materials* 5(7):535–563

Shirani Faradonbeh R, Taheri A (2019) Long-term prediction of rockburst hazard in deep underground openings using three robust data mining techniques. *Engineering with Computers* 35(2):659–675

Shirani Faradonbeh R, Taheri A, Karakus M (2021) Post-peak behaviour of rocks under cyclic loading using a double-criteria damage-controlled test method. *Bulletin of Engineering Geology and the Environment* 80(2):1713–1727

Singh SK (1989) Fatigue and strain hardening behaviour of graywacke from the flagstaff formation. *New South Wales. Engineering Geology* 26(2):171–179

Sufian A, Russell AR (2013) Microstructural pore changes and energy dissipation in Gosford sandstone during pre-failure loading using X-ray CT. *International Journal of Rock Mechanics and Mining Sciences* 57:119–131

Taheri A, Hamzah N, Dai Q (2017) Degradation and improvement of mechanical properties of rock under triaxial compressive cyclic loading. *Japanese Geotechnical Society Special Publication* 5(2):71–78

Taheri A, Tatsuoka F (2015) Small- and large-strain behaviour of a cement-treated soil during various loading histories and testing conditions. *Acta Geotechnica* 10(1):131–155

Taheri A, Royle A, Yang Z, Zhao Y (2016a) Study on variations of peak strength of a sandstone during cyclic loading. *Geomechanics and Geophysics for Geo-Energy and Geo-Resources* 2(1):1–10

Taheri A, Yfantidis N, L. Olivares C, et al (2016b) Experimental Study on Degradation of Mechanical Properties of Sandstone Under Different Cyclic Loadings. *Geotechnical Testing Journal* 39(4):673-687

Taheri A, Zhang Y, Munoz H (2020) Performance of rock crack stress thresholds determination criteria and investigating strength and confining pressure effects. *Construction and Building Materials* 243:118263

Tarasov B, Potvin Y (2013) Universal criteria for rock brittleness estimation under triaxial compression. *International Journal of Rock Mechanics and Mining Sciences* 59:57–69

Trippetta F, Collettini C, Meredith PG, Vinciguerra S (2013) Evolution of the elastic moduli of seismogenic Triassic Evaporites subjected to cyclic stressing. *Tectonophysics* 592:67–79

Vasconcelos G, Lourenço P, Alves C, Pamplona J (2009) Compressive Behavior of Granite: Experimental Approach. *Journal of Materials in Civil Engineering* 21(9):502–511

Wang S, Xu W, Sun M, Wang W (2019) Experimental investigation of the mechanical properties of fine-grained sandstone in the triaxial cyclic loading test. *Environmental earth sciences* 78(14):416

Wang W, Wang M, Liu X (2016) Study on Mechanical Features of Brazilian Splitting Fatigue Tests of Salt Rock. *Advances in Civil Engineering*

Wawersik WR, Fairhurst CH (1970) A study of brittle rock fracture in laboratory compression experiments. In: *International Journal of Rock Mechanics and Mining Sciences & Geomechanics Abstracts*. Elsevier, pp 561–575

Xiao J-Q, Ding D-X, Jiang F-L, Xu G (2010) Fatigue damage variable and evolution of rock subjected to cyclic loading. *International Journal of Rock Mechanics and Mining Sciences* 47(3):461–468

Zhang D, Ranjith PG, Perera MSA (2016) The brittleness indices used in rock mechanics and their application in shale hydraulic fracturing: A review. *Journal of Petroleum Science and Engineering* 143:158–170

Zhang J, Deng H, Taheri A, et al (2019) Deterioration and strain energy development of sandstones under quasi-static and dynamic loading after freeze-thaw cycles. *Cold Regions Science and Technology* 160:252–264

Zoback MD, Byerlee JD (1975) The effect of cyclic differential stress on dilatancy in westerly granite under uniaxial and triaxial conditions. *Journal of Geophysical Research (1896-1977)* 80(11):1526–1530

Statement of Authorship

Title of Paper	Fatigue Failure Characteristics of Sandstone Under Different Confining Pressures
Publication Status	☐ Published ☐ Accepted for Publication ☑ Submitted for Publication ☐ Unpublished and Unsubmitted work written in manuscript style
Publication Details	**Shirani Faradonbeh R**, Taheri A, Karakus M (2021) Fatigue Failure Characteristics of Sandstone Under Different Confining Pressures. *Rock Mechanics and Rock Engineering* x(x):x–x Note: Under review [the paper submitted on 22/05/2021]

Principal Author

Name of Principal Author (Candidate)	Roohollah Shirani Faradonbeh		
Contribution to the Paper	Conducting laboratory tests, analysis of the results, and preparation of the manuscript		
Overall percentage (%)	80%		
Certification:	This paper reports on original research I conducted during the period of my Higher Degree by Research candidature and is not subject to any obligations or contractual agreements with a third party that would constrain its inclusion in this thesis. I am the primary author of this paper.		
Signature		Date	17 June 2021

Co-Author Contributions

By signing the Statement of Authorship, each author certifies that:

i. the candidate's stated contribution to the publication is accurate (as detailed above);
ii. permission is granted for the candidate in include the publication in the thesis; and
iii. the sum of all co-author contributions is equal to 100% less the candidate's stated contribution.

Name of Co-Author	Abbas Taheri		
Contribution to the Paper	Research supervision, review and revision of the manuscript		
Signature		Date	21 June 2021

Name of Co-Author	Murat Karakus		
Contribution to the Paper	Review and revision of the manuscript		
Signature		Date	21 June 2021

Chapter 8

Fatigue Failure Characteristics of Sandstone Under Different Confining Pressures

Abstract

Rock fatigue behaviour including the fatigue threshold stress (FTS), post-peak instability and strength weakening/hardening during cyclic loading, is of paramount significance in terms of safety and stability assessment of underground openings. In this study, the evolution of the foregoing parameters for Gosford sandstone subjected to systematic cyclic loading, in the pre-peak and the post-peak regimes at different stress levels and under seven confinement levels (σ_3/UCS_{avg}) was evaluated comprehensively. The results showed that the FTS of rocks decreases exponentially from 97% to 80%, when σ_3/UCS_{avg} increases from 10% to 100%. The brittleness of rocks under monotonic and cyclic loading conditions increases with an increase in σ_3/UCS_{avg} when σ_3/UCS_{avg} ranging between 10-65% (known as the transition point). For higher confinements, however, the brittleness of rock transits from self-sustaining behaviour into ductile behaviour. The evolution of fatigue damage parameters for hardening tests showed that no critical damage happens within the specimens during cyclic loading; rather, they experience more compaction. This is while for weakening cyclic loading tests, continuous damage along with stiffness degradation was dominant. Furthermore, the variation of axial strain at failure point (ε_{af}) shows that for lower confinement levels, the applied stress level does not affect the pre-peak irreversible deformation; its effect, however, becomes significant when confining pressure is high. For the specimens that did not fail in cycles, cyclic loading resulted in peak strength weakening or hardening depending on the applied stress level. Weakening effect was observed in higher confining pressures, which was mainly due to a higher amount of irreversible deformation accumulation in rocks in the pre-peak cyclic loading. An empirical model was proposed using classification and regression tree (CART) algorithm to estimate the peak strength variation of Gosford sandstone based on σ_3/UCS_{avg} and the applied stress level.

Keywords: Triaxial loading, Systematic cyclic loading, Confinement level, Brittleness, Fatigue threshold stress, Strength hardening/weakening

List of Symbols

M	Post-peak modulus	q_m	Peak deviator stress
E	Pre-peak modulus	q_{res}	Residual deviator stress
N	Number of cycles before failure	q_{un}/q_{m-avg}	Deviator stress level
R	Strain gauge resistance	q_f/q_{m-avg}	Fatigue threshold stress
q	Deviator stress	σ_3/UCS_{avg}	Confinement level
BI	Brittleness index	ε_{af}	Axial strain at failure
GF	Strain gauge factor	ε_{lf}	Lateral strain at failure
ΔR	Change in resistance	ε_a^{irr}	Irreversible axial strain
AE	Acoustic emission	$d\varepsilon_l/dt$	Lateral strain rate
FTS	Fatigue threshold stress	$d\varepsilon_a/dt$	Axial strain rate
$CART$	Classification and regression tree	dU_r	Shear rupture energy
V_o	Output voltage	dU_e	Withdrawn elastic energy
V_{ex}	Excitation voltage	dU_{er}	Residual elastic energy
ε	Mechanical strain	dU_a	Additional energy
E_{tan}	Tangent Young's modulus	ω_a^{irr}	Cumulative irreversible axial strain
UCS	Uniaxial compressive strength	$\Delta\varepsilon_a^{irr}$	Differential irreversible axial strain
U_e	Total elastic energy	σ_1	Major principal stress
$Amp.(\varepsilon_l)$	Lateral strain amplitude	σ_3	Confining pressure

8.1. Introduction

Depending on the depth, the geometry of the structures and the human- and/or environmental-induced seismic activities, rock masses in underground mining and geotechnical projects are usually subjected to a complex stress state, which may result in continuous damage and failure at different extents (Yang et al. 2017; Wang et al. 2021). Systematic cyclic loading induced by the rock breakage operation, mechanical excavation, and truck haulage vibrations is a common dynamic disturbance in underground openings that complicate the deformation and failure characteristics of rocks. Rock materials under such loading conditions are more prone to severe failure phenomena such as strain bursting and large-scale collapses (Bagde and Petroš 2005; Munoz and Taheri 2019, Shirani Faradonbeh et al. 2021a; Meng et al. 2021). Therefore, there is a remarkable theoretical significance and engineering value to deeply understand the cyclic loading effect on the damage mechanism and, more importantly, the post-failure behaviour of rocks in terms of safety and long-term stability of the excavations. During the last decades,

different researchers have made many attempts to unveil the rock fatigue mechanism under different loading conditions using laboratory experiments (Cerfontaine and Collin 2018). In other words, the damage evolution mechanism in rocks can be characterised more efficiently using cyclic loading tests as it is straightforward to distinguish the elastic and plastic strains during each loading and unloading cycle (Zhou et al. 2019; Tian et al. 2021). According to the holistic classification proposed by Shirani Faradonbeh et al. (2021a), rock fatigue studies can be classified into two main groups of systematic cyclic loading tests and damage-controlled cyclic loading tests. Each of these groups can be performed either under load-controlled or displacement-controlled loading conditions. These loading techniques and their limitations have been discussed in more detail by Shirani Faradonbeh et al. (2021a).

Generally, the rock fatigue studies can be discussed from two viewpoints: the pre-peak and post-peak domain analysis. From the viewpoint of the pre-peak-domain analysis, the literature review shows that cyclic loading depending on loading methods, loading conditions and intrinsic rock properties (e.g. porosity and mineral compositions) can either degrade (Wang et al. 2013; Erarslan et al. 2014; Yang et al. 2015; Taheri et al. 2016a) or improve (Burdine 1963; Singh 1989; Ma et al. 2013; Shirani Faradonbeh et al. 2021b) the peak strength of rocks. For instance, Ma et al. (2013) reported a 171.1% increase in triaxial compressive strength of rock salt subjected to systematic cyclic loading. Similarly, Taheri et al. (2016b) observed an 11% peak strength improvement for the porous Hawkesbury sandstone, and they also pointed out that rock strength increases respectively with applied stress level and the number of cycles before failure following linear and exponential functions. On the other hand, most of the fatigue cyclic loading studies have reported peak strength and stiffness degradation due to the accumulation of permanent deformations within the rock specimens following a non-linear S-shaped damage model (e.g. Xiao et al. 2009). Fatigue threshold stress (FTS $= q_f/q_{m-avg}$), the maximum stress level at which rock specimen does not fail during cyclic loading under a constant amplitude, is a significant parameter for long-term stability assessment of underground openings subjected to seismic disturbances. In other words, rock materials never fail (after a few thousand cycles) if the cyclic loading is applied equal or below this threshold. According to Cerfontaine and Collin (2018), different values of FTS can be obtained depending on the tested material. However, FTS is also dependent on other factors, such as loading conditions and confining pressure (Burdine 1963). Therefore, more investigations are needed to unveil the effect of confining pressure on fatigue threshold stress.

From the viewpoint of the post-peak domain, due to difficulties in capturing the complete stress-strain relations of rocks under cyclic loading, especially for brittle rocks which show a class II post-peak behaviour (Wawersik and Fairhurst 1970), very few studies have investigated the influence of the pre-peak cyclic loading on post-failure behaviour. In most prior studies, the damage-controlled cyclic loading tests (with the incremental loading amplitude) have been used under axial displacement-controlled loading conditions to evaluate the post-peak behaviour (e.g. Yang et al. 2015, 2017; Zhou et al. 2019; Meng et al. 2021). These studies, however, were not sufficient to adequately measure the post-peak response of rocks. This is because, during each loading cycle, the axial load is reversed when a certain amount of displacement is achieved, and after the failure point, since most of the rocks show class II or a combination of class I and class II behaviours, rock failure occurs in an uncontrolled manner. However, Munoz and Taheri (2017) showed that lateral displacement control throughout the test is a promising technique in studying the failure behaviour of rocks subjected to the post-peak cyclic loading. Recently, Shirani Faradonbeh et al. (2021a and b) developed a novel testing methodology based on the lateral strain feedback signal to measure the complete pre-peak and post-peak behaviour of rocks under uniaxial systematic cyclic loading.

Although many studies have been undertaken by different researchers on the evolution of rock fatigue damage and deformability parameters under different loading histories and loading conditions, no significant progress has been made regarding the effect of systematic cyclic loading on the cyclic loading-induced strength hardening, fatigue threshold stress and the post-peak instability of rocks under different confining pressures. This is while in underground rock engineering projects, rock materials are usually subjected to triaxial loading conditions with different levels of confinement accompanied by the systematic cyclic loading induced by different dynamic sources. Therefore, having in-depth knowledge concerning the foregoing parameters plays a critical role in stability assessment and reinforcement design. This study, for the first time, investigates the effect of systematic cyclic loading history on pre-peak and post-peak characteristics of rocks under different confinement levels. Some empirical equations are then proposed to manifest the evolution of peak strength, fatigue threshold stress and rock brittleness parameters. The obtained results are expected to provide a better understanding of the mechanical response of rocks to systematic cyclic loading under various confining pressures.

8.2. Experimental Profile

8.2.1. Gosford Sandstone

In this study, Gosford sandstone (Fig. 8.1a) extracted from the massive Triassic Hawkesbury sandstone of the Sydney Basin, New South Wales, Australia, was chosen as the testing material (Ord et al. 1991; Masoumi et al. 2017). X-ray powder diffraction (XRD) analysis of this medium-grained (0.2-0.3 mm) sandstone revealed that quartz (86%) is the dominant mineral and illite (7%), kaolinite (6%) and anatase (1%) are other forming mineral composition. Fig. 8.1b displays the SEM analysis result of this sandstone. Sufian and Russell (2013) reported that Gosford sandstone has a total porosity of about 18%, and the density distribution of the pre-existing micro-cracks within its matrix is homogenous. This type of sandstone is usually known as a uniform or very uniform sandstone (Hoskins 1969; Vaneghi et al. 2018). Cylindrical specimens (Fig. 8.1a) having 42 mm diameter and 100 mm length were extracted from a single rock block and prepared following the ISRM recommended standards (Fairhurst and Hudson 1999). The specimens were air-dried before conducting the static and cyclic loading tests, and the average dry density of this rock type was approximately about 2.215 g/cm^3.

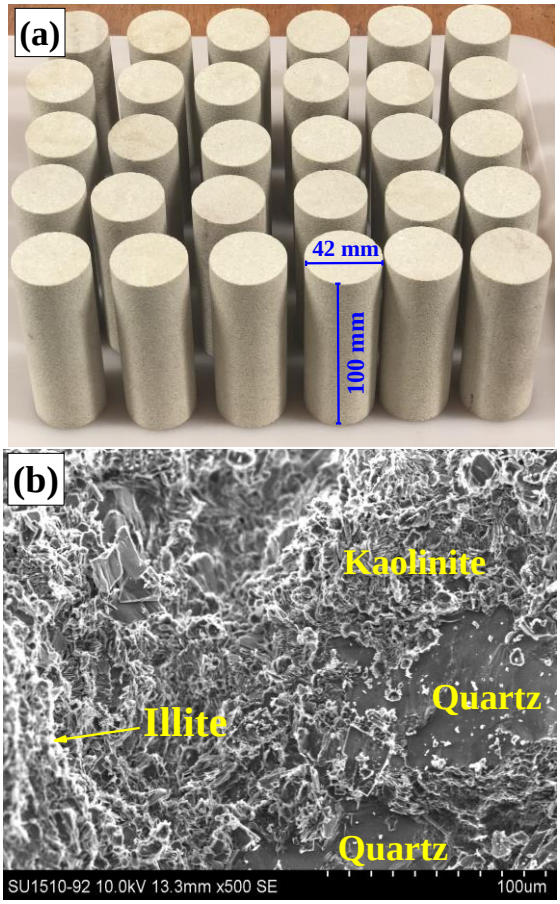

Figure 8.1 Gosford sandstone used in this study: **a** prepared specimens and **b** SEM photograph

8.2.2. Testing Equipment

A fully digital closed-loop servo-controlled hydraulic compressive machine, i.e. Instron-1282 with the maximum loading capacity of 1000 kN, was employed to conduct the triaxial monotonic and cyclic loading tests. The testing machine can be programmed and equipped to perform different loading schemes using either the load-controlled or displacement-controlled loading techniques. As shown in Fig. 8.2a, a Hoek cell with a maximum capacity of 65 MPa was used to apply confining pressure. Also, a pair of LVDTs were installed between the loading platens to measure the axial displacement of the specimens during loading. Strain gauges are commonly used to measure the axial and/or lateral deformations of rocks in triaxial conditions. However, the strain gauges are only effective for local small-strain measurement, and they usually break after the peak stress when the specimen experiences large deformations (Munoz et al. 2016a; Bruning et al. 2018). A modified test arrangement is made to overcome this problem; four strain gauges were attached immediately alongside one another around the centre line of the Hoek cell membrane, as displayed in Fig. 8.2b. Then, the strain gauges were connected to form a Wheatstone bridge (half-bridge circuit). Any deformation in specimen changes the resistance and, therefore, facilitates a unique output voltage (V_o) as a lateral strain feedback signal. In the Wheatstone bridge shown in Fig. 8.2b, R_1 and R_3 represent the total resistance values provided by the pairs of strain gauges (each gauge has 120Ω resistance) which are connected in series. To balance the bridge and achieve zero voltage when the specimen is unstrained, two 240 Ω precision resistors (i.e. R_2 and R_4) were used in this circuit. The feedback signal, indeed, is the average of the lateral strain (ε_l) values measured by the strain gauges, which is calculated as follows:

$$V_o = \frac{V_{ex}}{4}\left(\frac{\Delta R_1}{R_1} + \frac{\Delta R_3}{R_3}\right) = \frac{V_{ex}}{4}.GF.(\varepsilon_1 + \varepsilon_3) \tag{8.1}$$

$$\mathrm{GF} = \frac{\Delta R/R}{\varepsilon} \tag{8.2}$$

where R is the resistance of the undeformed strain gauge, ΔR is the change in resistance caused by strain, ε is the mechanical strain, GF is the strain gauge factor and V_{ex} is the bridge excitation voltage.

Through a high-pressure wire and a feed-through connector fitted to the Hoek cell, the feedback signal is sent to the control unit of the testing machine to adjust the loading rate. By doing so, the membrane gauges are protected from damage during loading, and finally, the complete lateral deformation of rocks can be recorded in both pre-peak and post-peak regimes. Moreover, two miniature AE sensors (type PICO, from the American Physical Acoustics Corp.) were attached to the spherical seats, which have a direct connection to the specimen in the Hoek cell, to record the microcracking process during loading. The pre-amplifier was set to 60 dB of gain (Type 2/4/6) to amplify the acoustic emission (AE) signals during loading. To ensure that mechanical noises induced by the loading system are not recorded during the tests, the AE threshold amplitude was changed from 20 dB to 60 dB, and it was found that after 40 dB amplitude, no additional noises are recorded. Therefore, this value was set as the AE threshold. The axial load, axial and lateral displacements, and the AE outputs were recorded simultaneously by running the tests.

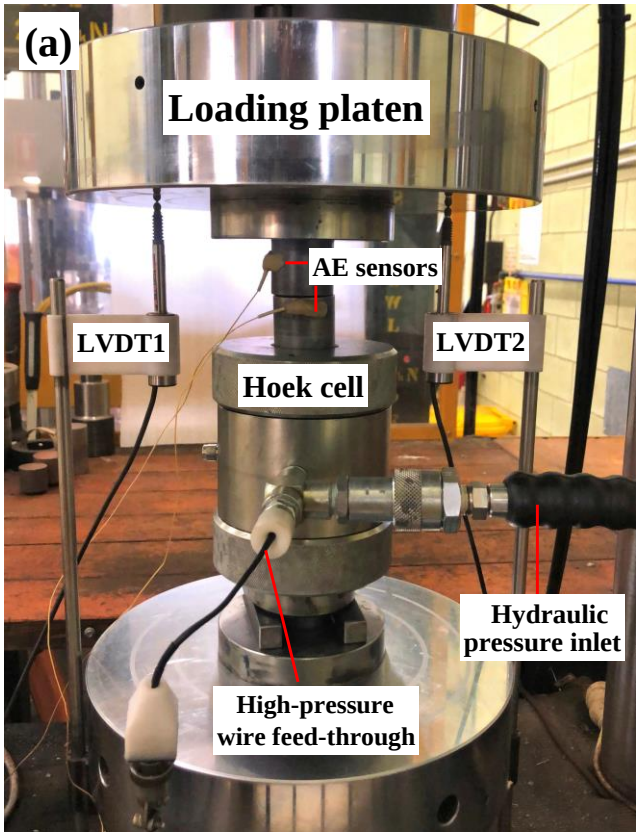

Figure 8.2 Experimental set-up, **a** overview of the experiment and **b** strain gauged membrane

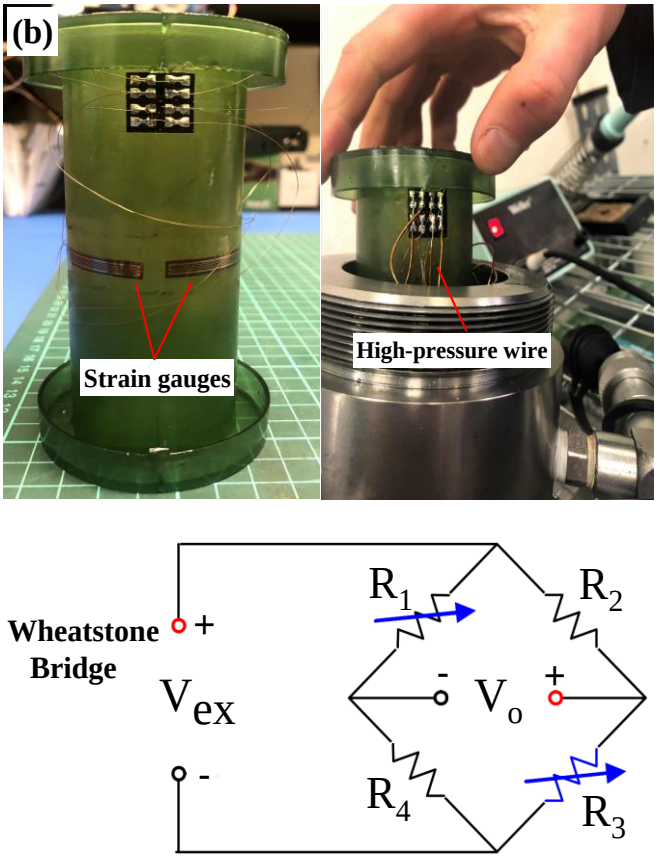

Figure 8.2 (Continued)

8.3. Test Scheme and Conditions

8.3.1. Uniaxial and Triaxial Monotonic Loading Tests

Before conducting the triaxial monotonic and cyclic loading tests at different confining pressures, the uniaxial compressive strength (UCS) of Gosford sandstone should be determined. Shirani Faradonbeh et al. (2021b) performed a series of uniaxial monotonic tests on this rock type under a constant lateral strain rate ($d\varepsilon_l/dt$) of 2×10^{-6}/s. In their study, the axial strain was measured using a pair of external LVDTs, and the lateral strain feedback signal was measured using a direct-contact chain extensometer. Fig. 8.3a shows the normalised stress-strain relations of the performed uniaxial monotonic tests. As it is shown in this figure, the rock specimens are quite uniform and demonstrate almost similar pre-peak and post-peak stress-strain relations. Gosford sandstone has an average uniaxial peak strength (UCS_{avg}) and tangent Young's modulus ($E_{tan-avg}$) values of 48.15 MPa and 13.4 GPa, respectively.

Based on the determined UCS_{avg}, seven different confinement levels, i.e. σ_3/UCS_{avg}= 10%, 20%, 35%, 50%, 65%, 80% and 100%, were adopted for triaxial monotonic and cyclic compression tests. For each confinement level, three triaxial monotonic tests were carried out.

The tests were conducted in a way that the axial load and confining pressure were applied simultaneously to the rock specimen under a constant axial strain rate of $d\varepsilon_a/dt$= 0.03 mm/min until the desired confining pressure level is achieved. Thereafter, the confining pressure and axial load were kept constant for five minutes to ensure the stress was distributed uniformly (pre-consolidation stage). Then, while the confining pressure was maintained constant, the deviator stress (i.e. $q = \sigma_1 - \sigma_3$) was applied under a constant lateral strain rate ($d\varepsilon_l/dt$) of 2×10^{-6}/s until the complete failure occurs. The lateral strain rate was adjusted during the test based on the feedback signal received from the four strain gauges mounted on the Hoek cell membrane. Fig. 8.3b shows a typical time history of stress and strains during a triaxial compression test at σ_3/UCS_{avg}=10%. Table 8.1 presents a summary of results for all conducted triaxial monotonic tests. Fig 3c, shows the representative stress-strain relations for the triaxial monotonic tests. According to Table 8.1 and Fig. 8.3c, the increase in σ_3/UCS_{avg}, affected both the pre-peak and the post-peak characteristics of rocks. Generally, with an increase in confining pressure, the axial strain at the failure point (ε_{af}) increases. Also, as shown in Fig. 8.3d, the average peak deviator stress (q_{m-avg}) of Gosford sandstone increased by confining pressure following a quadratic trend. Section 5 discusses the triaxial compression test results in more detail.

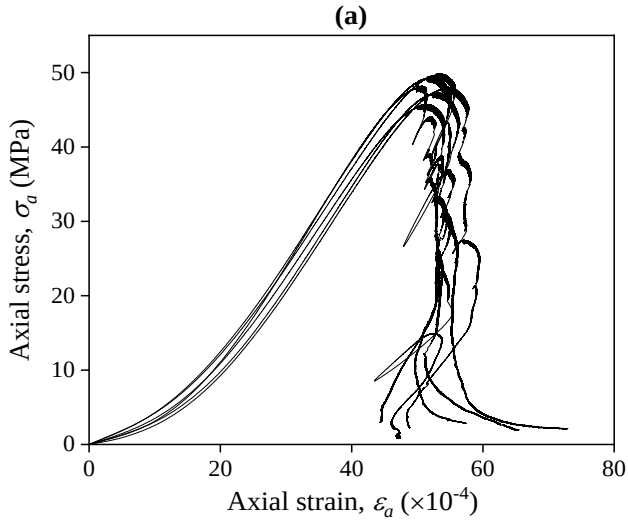

Figure 8.3 a Normalised stress-strain relations for uniaxial monotonic tests, modified from Shirani Faradonbeh et al. (2021b), **b** typical time-history of stress and strains for a triaxial monotonic test at 10% confinement level, **c** representative stress-strain relations for triaxial monotonic tests at different confinement levels and **d** the variation of peak deviator stress with confinement level

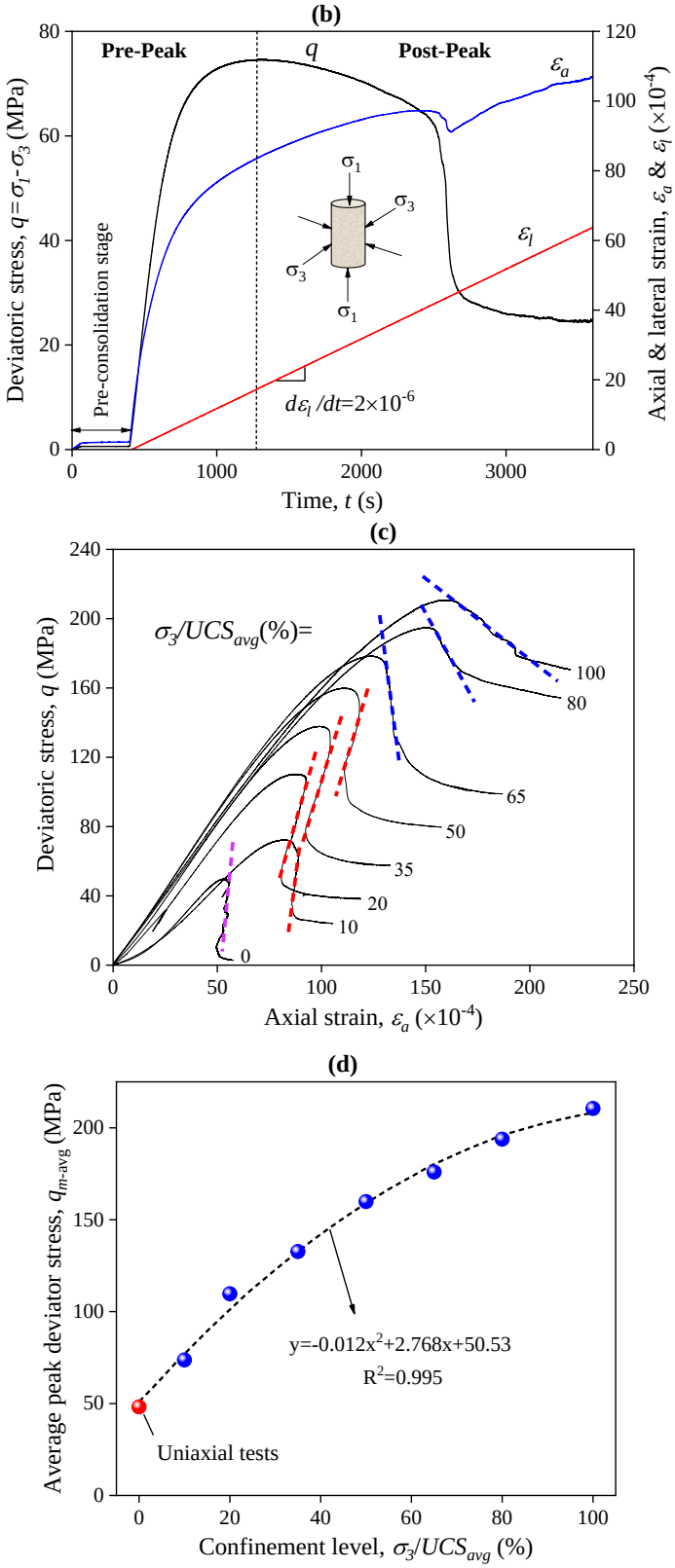

Figure 8.3 (Continued)

Table 8.1 Summary results of triaxial monotonic loading tests

Test ID	σ_3 (MPa)	σ_3/UCS_{avg} (%)	q_m (MPa)	q_{res} (MPa)	Strains at the failure point		E_{tan} (GPa)
					ε_{af} ($\times 10^{-4}$)	ε_{lf} ($\times 10^{-4}$)	
GS-M-1	4.82	10	74.36	27.17	82.04	-18.39	13.00
GS-M-2	4.82	10	74.60	24.53	84.32	-18.03	12.50
GS-M-3	4.82	10	72.21	24.25	82.17	-14.59	12.50
Average	4.82	10	73.72	25.32	82.84	-17.00	12.67
GS-M-4	9.63	20	110.32	38.85	86.35	-12.05	16.31
GS-M-5	9.63	20	109.94	40.20	89.80	-17.27	16.04
GS-M-6	9.63	20	108.80	42.46	86.62	-22.63	16.50
Average	9.63	20	109.69	40.50	87.59	-17.32	16.28
GS-M-7	16.85	35	137.83	57.70	99.09	-21.47	17.64
GS-M-8	16.85	35	129.91	60.42	91.77	-14.81	17.33
GS-M-9	16.85	35	130.35	60.45	90.30	-14.65	17.32
Average	16.85	35	132.69	59.52	93.72	-16.97	17.43
GS-M-10	24.08	50	159.89	79.74	110.94	-21.55	18.17
GS-M-11	24.08	50	161.47	87.64	112.21	-23.95	18.38
GS-M-12	24.08	50	158.19	89.62	111.71	-23.74	18.12
Average	24.08	50	159.85	85.66	111.62	-23.08	18.22
GS-M-13	31.30	65	175.34	103.49	119.97	-21.90	18.54
GS-M-14	31.30	65	175.89	103.66	1119.92	-19.95	18.68
GS-M-15	31.30	65	176.48	97.20	120.45	-21.59	18.68
Average	31.30	65	175.90	101.45	120.11	-21.15	18.64
GS-M-16	38.52	80	194.86	154.25	151.33	-29.06	16.66
GS-M-17	38.52	80	195.18	156.92	152.66	-28.52	16.41
GS-M-18	38.52	80	191.43	154.25	145.43	-27.13	16.37
Average	38.52	80	193.82	155.14	149.81	-28.24	16.48
GS-M-19	48.15	100	210.95	173.48	159.04	-24.36	16.69
GS-M-20	48.15	100	210.63	170.77	161.17	-26.19	16.83
GS-M-21	48.15	100	209.99	164.18	158.52	-23.82	16.76
Average	48.15	100	210.52	169.48	159.58	-24.79	16.76

q_m: peak deviator stress, q_{res}: residual deviator stress, ε_{af}: axial strain at failure, ε_{lf}: lateral strain at failure and E_{tan}: tangent Young's modulus.

8.3.2. Triaxial Cyclic Loading Tests

To evaluate the influence of confining pressure and systematic cyclic loading history on the mechanical rock behaviour, including the fatigue threshold stress, post-peak behaviour, and peak strength, a series of systematic cyclic loading tests were performed at different deviator stress levels (q_{un}/q_{m-avg}). For this aim, the testing machine was programmed to perform the cyclic tests automatically and continuously. Fig. 8.4, schematically, shows the testing procedure for a triaxial cyclic loading test with a final monotonic loading. Similar to monotonic loading tests, the axial load and confining pressure were initially applied to the specimen under

a constant axial strain rate of 0.03 mm/min until the pre-defined confinement level was reached. Then, the axial load and confining pressure were kept constant for five minutes to pre-consolidate the specimen. Afterwards, the deviator stress was increased under a constant lateral strain rate of 2×10^{-6}/s to reach a specific deviator stress level while σ_3 remained constant. The deviator stress was then reversed completely, and systematic cyclic loading was commenced under a higher lateral strain rate of $d\varepsilon_l/dt = 150\times10^{-6}$/s. During the cyclic loading, the axial load did not exceed the prescribed stress level, and confining pressure was always constant. The rock specimens were let to experience a maximum of 1000 loading and unloading cycles. Should the specimen did not fail during 1000 cycles, it was then subjected to a final monotonic loading at a constant rate of $d\varepsilon_l/dt = 2\times10^{-6}$/s until complete failure occurred. By doing so, the post-peak stress-strain behaviour of rocks was obtained in a controlled manner. Table 8.2 summarises all the loading scenarios and the obtained results for the performed triaxial cyclic loading tests in this study. Figs. 8.5 and 8.6 show the representative stress-strain results of the specimens that experienced final monotonic loading and failure during cyclic loading, respectively. The stress-strain relations of other cyclic loading tests can be found in "Appendix A".

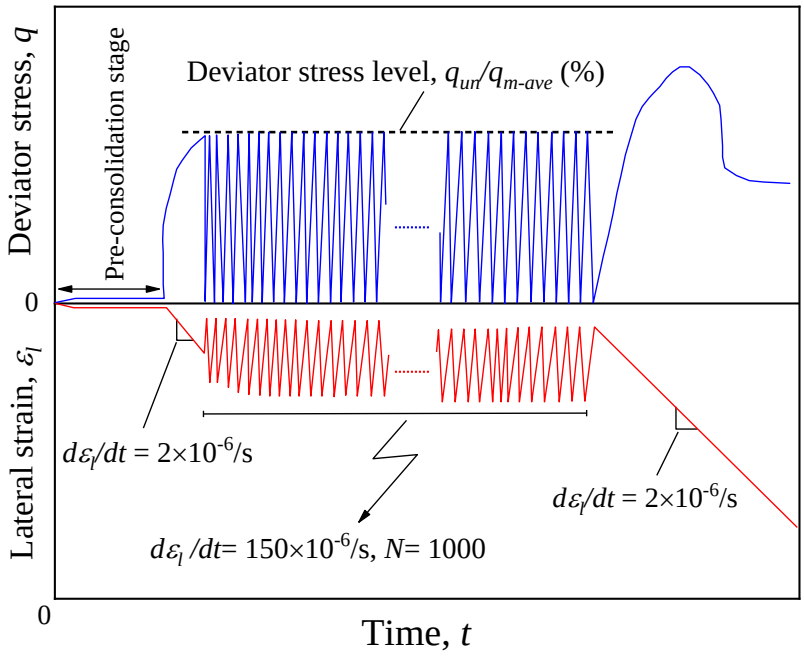

Figure 8.4 Schematic time-history of deviator stress and lateral strain for triaxial cyclic loading tests

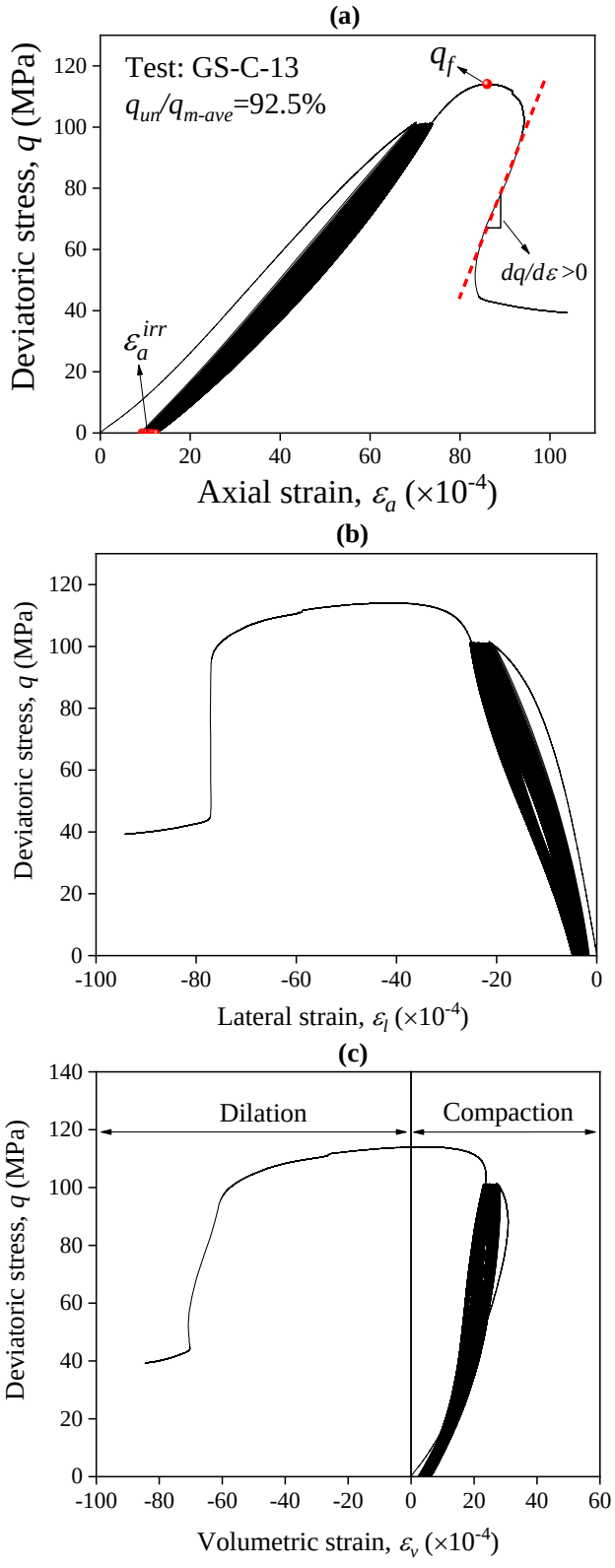

Figure 8.5 Typical stress-strain results for the tests which did not fail during cyclic loading (test GS-C-13)

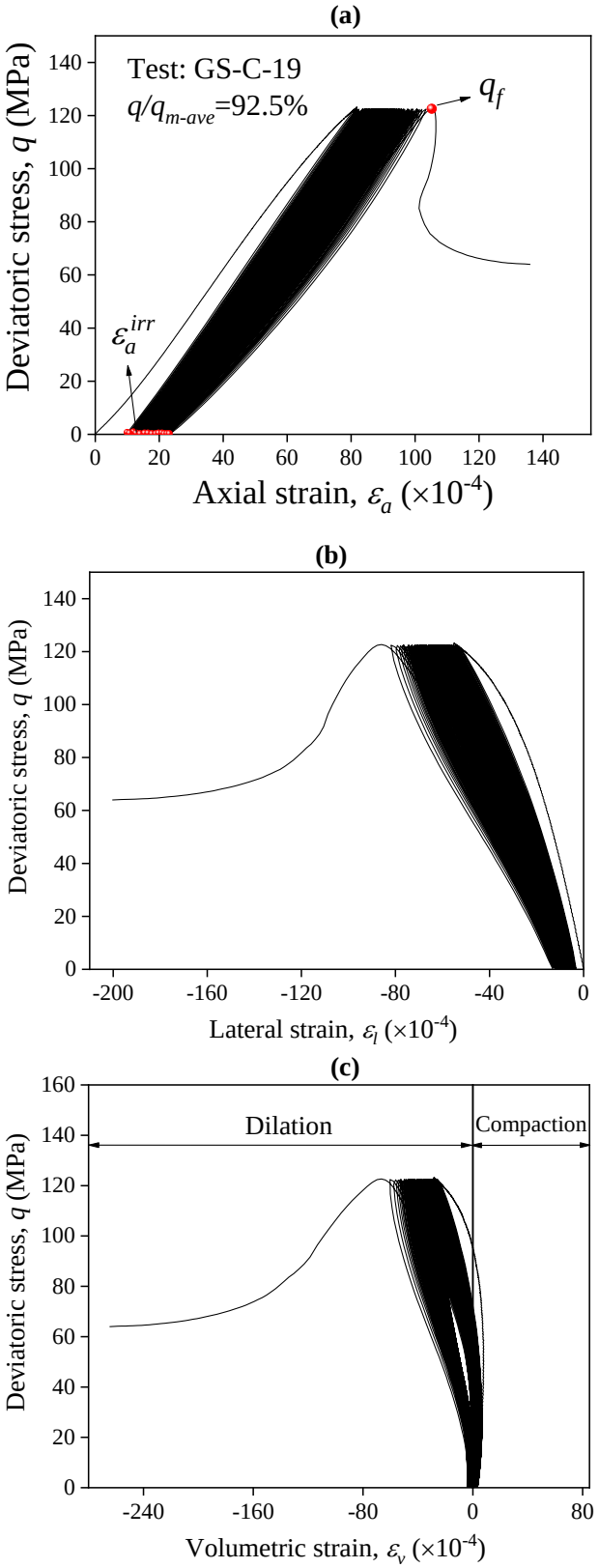

Figure 8.6 Typical stress-strain results for the tests which failed during cyclic loading (test GS-C-19)

Table 8.2 Summary results of triaxial cyclic loading tests

Test ID	σ_3 (MPa)	σ_3/UCS_{avg} (%)	q_{un}/q_{m-avg} (%)	N	Failed in cycle? (Yes/No)	ε_{af} ($\times 10^{-4}$)	q_{res}/q_{m-avg} (%)	Peak strength variation (%)
GS-C-1	4.82	10	80	1000	N	80.60	37	1.47
GS-C-2	4.82	10	85	1000	N	78.86	40	3.66
GS-C-3	4.82	10	87.50	1000	N	82.52	36	3.61
GS-C-4	4.82	10	90	1000	N	84.74	36	3.89
GS-C-5	4.82	10	92.50	1000	N	86.95	44	2.21
GS-C-6	4.82	10	95	1000	N	84.60	52	5.38
GS-C-7	4.82	10	97	1000	N	87.29	47	3.62
GS-C-8	4.82	10	97.5	48	Y	88.77	38	-
Average	4.82	10	-	-	-	84.29	41	3.40
GS-C-9	9.63	20	80	1000	N	82.18	41	2.33
GS-C-10	9.63	20	85	1000	N	85.51	36	3.94
GS-C-11	9.63	20	87.50	1000	N	85.92	39	1.66
GS-C-12	9.63	20	90	1000	N	86.50	35	3.03
GS-C-13	9.63	20	92.5	1000	N	86.67	36	4.06
GS-C-14	9.63	20	95	671	Y	90.30	40	-
Average	9.63	20	-	-	-	86.19	38	3.00
GS-C-15	16.85	35	80	1000	N	99.71	54	4.38
GS-C-16	16.85	35	85	1000	N	103.30	55	7.19
GS-C-17	16.85	35	87.50	1000	N	104.21	51	3.65
GS-C-18	16.85	35	90	1000	N	100.83	47	6.66
GS-C-19	16.85	35	92.50	428	Y	105.29	48	-
Average	16.85	35	-	-	-	102.67	51	5.47
GS-C-20	24.08	50	80	1000	N	110.55	53	0.00
GS-C-21	24.08	50	85	1000	N	114.20	51	0.75
GS-C-22	24.08	50	86.25	262	Y	127.86	63	-
GS-C-23	24.08	50	87.5	346	Y	130.10	53	-
Average	24.08	50	-	-	-	120.68	55	0.38
GS-C-24	31.30	65	80	1000	N	119.99	63	1.86
GS-C-25	31.30	65	82.5	1000	N	120.59	60	1.11
GS-C-26	31.30	65	83.75	1000	N	123.57	63	1.64
GS-C-27	31.30	65	85	526	Y	141.05	59	-
Average	31.30	65	-	-	-	126.30	61	1.54
GS-C-28	38.52	80	80	1000	N	158.48	79	1.21
GS-C-29	38.52	80	82.50	1000	N	379.83	79	-13.18
GS-C-30	38.52	80	85	405	Y	217.693	78	-
Average	38.52	80	-	-	-	252.00	79	-5.99
GS-C-31	48.15	100	77.5	1000	N	187.97	84	-6.67
GS-C-32	48.15	100	80	1000	N	168.59	81	-3.96
GS-C-33	48.15	100	82.5	103	Y	580.75	82	-
GS-C-34	48.15	100	85	196	Y	431.43	82	-
Average	48.15	100	-	-	-	342.19	82	-5.32

N: number of cycles before failure.

8.4. Confining Pressure Effect on Fatigue Threshold Stress

As mentioned earlier, fatigue threshold stress (FTS) is a critical parameter, that can be used as an effective compressive strength of the intact rock subjected to static, dynamic and cyclic loads. Depending on the rock type, testing method and loading history, various range of values for FTS were reported by different researchers. Table 8.3 reviews these studies and lists the used materials and testing methods along with the determined FTSs. Table 8.3 shows that most of the existing studies have been conducted in uniaxial loading condition. Taheri et al. (2016b) performed the systematic cyclic loading tests on Hawkesbury sandstone under a single confining pressure of σ_3= 4 MPa. In an earlier study, Burdine (1963) performed a series of triaxial dynamic loading tests under three confining pressures (i.e. σ_3= 0.21 MPa, 1.38 MPa and 5.17 MPa) on Berea sandstone. The study showed that with an increase in confining pressure from 0 to 5.17 MPa, the fatigue threshold stress increases from 74% to 93% of the monotonic strength.

In the current study, a more comprehensive range of confining pressure was considered to evaluate the variation of FTS under systematic cyclic loading for Gosford sandstone. According to Table 8.2, for each confinement level, a fatigue threshold stress (q_f/q_{m-avg}) can be derived. Fig. 8.7 plots the variation of the determined FTS values against the confinement level. As can be seen in this figure, with an increase in σ_3/UCS_{avg} from 10% to 100%, q_f/q_{m-avg} decreases constantly, which shows the weakening/negative influence of confining pressure on the fatigue life of the rock under cyclic loading. These results, show that in underground projects, with the increase of depth, rock materials may fail at a stress level lower than the determined monotonic strength. The behavioural trend observed for FTS in this study is in contrast to that reported by Burdine (1963). According to Fig. 8.7, the FTS can be predicted using the following logarithmic function with high accuracy:

$$FTS = \frac{q_f}{q_{m-avg}} = -0.074Ln\left(\frac{\sigma_3}{UCS_{avg}}\right) + 0.806 \quad ; \quad R^2 = 0.982 \tag{8.3}$$

Also, based on the proposed Eq. 3, a binary condition can be defined to classify the failure status of the rock specimens, i.e. occurrence (1) or non-occurrence (0), under a specific stress level and confining pressure as follows:

$$\text{Failure status} = \begin{cases} 1 & q_{un}/q_{m-avg} > FTS \\ 0 & q_{un}/q_{m-avg} \leq FTS \end{cases} \tag{8.4}$$

Table 8.3 Summary of studies reporting the fatigue threshold stress values

Reference	Testing material	Test type	Confining pressure, σ_3 (MPa)	Fatigue threshold stress, q_f/q_{m-avg} (%)
Grover et al. (1950)	Limestone	Uniaxial	-	65
Burdine (1963)	Sandstone	Uniaxial		74
		Triaxial	0.21	76
			1.38	87
			5.17	93
Haimson and Kim (1971)	Marble	Uniaxial	-	75
Rajaram (1981)	Granite	Uniaxial	-	70
Singh (1989)	Sandstone	Uniaxial	-	87
Yamashita et al. (1999)	Tuff	Uniaxial	-	60
	Sandstone			75
	Marble			80
	Granite			80
Åkesson et al. (2004)	Granite	Uniaxial	-	60
Guo et al. (2012)	Salt	Uniaxial	-	75
Erarslan and Williams (2012)	Tuff	Brazilian	-	70
Erarslan et al. (2014b)	Tuff	Brazilian	-	68
Nejati and Ghazvinian (2014)	Marble	Brazilian	-	60
	Sandstone			70
	Limestone			80
Taheri et al. (2016b)	Sandstone	Triaxial	4	93.7
Jamali Zavareh et al. (2017)	Gabbro	Bending	-	53
	Onyx			60
	Limestone			46
Shirani Faradonbeh et al. (2021b)	Sandstone	Uniaxial	-	87.5

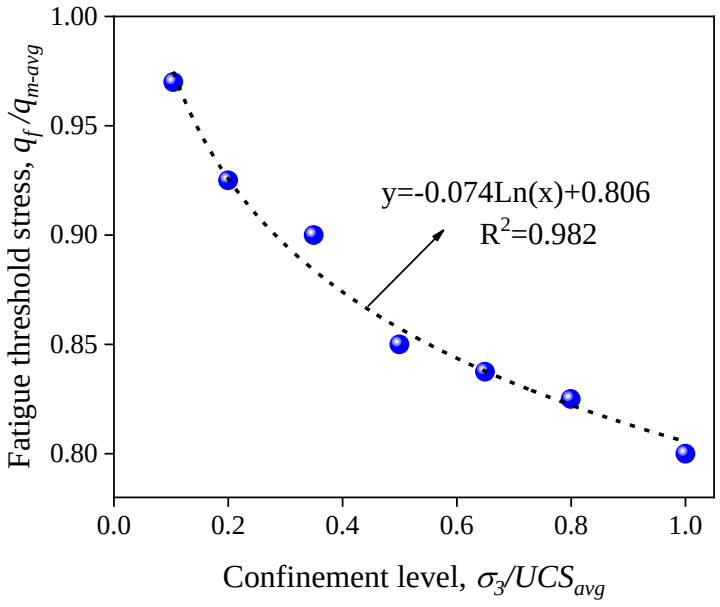

Figure 8.7 Variation of fatigue threshold stress with confinement level

8.5. Confining Pressure Effect on Post-Peak Instability

As mentioned earlier, the post-peak instability of rocks can be characterised as class I and class II, representing the stable and unstable rock fracturing process under a specific loading history, respectively. Brittleness is an appropriate intact rock property that can be employed to quantify the post-peak instability. Many rock brittleness indices can be found in the literature (Meng et al. 2020). However, as the evolution of strain energy accompanies the process of rock deformation and failure, the energy balance-based indices can better reflect the post-peak instability and the potential of severe failures (Li et al. 2019). Therefore, in this study, the following strain energy-based brittleness indices (BIs) proposed by Tarasov and Potvin (2013) were used to evaluate the post-peak instability of rocks:

$$BI_1 = \frac{dU_r}{dU_e} = \frac{M-E}{M} \tag{8.5}$$

$$BI_2 = \frac{dU_a}{dU_e} = \frac{E}{M} \tag{8.6}$$

$$\begin{cases} dU_e = \frac{q_B^2 - q_A^2}{2E} \\ dU_a = \frac{q_B^2 - q_A^2}{2M} \\ dU_r = dU_e - dU_a \end{cases} \tag{8.7}$$

where dU_e, dU_a and dU_r are, respectively, the withdrawn elastic energy, the additional/excess energy and the shear rupture energy in the post-peak regime (see Fig. 8.8). The q_A and q_B are the deviator stresses corresponding to points A and B, respectively, and E and M are, respectively, the pre-peak and the post-peak modulus.

To evaluate the effect of both confining pressure and loading history on rock brittleness, BI_1 and BI_2 were calculated for all monotonic and the cyclic loading tests (the tests that experienced the final monotonic loading). The evolution of the average BI values was plotted against σ_3/UCS_{avg} in Fig. 8.9. Shirani Faradonbeh et al. (2021b) performed a series of uniaxial systematic cyclic loading tests on Gosford sandstone at different stress levels and found that below the fatigue threshold stress, the rock brittleness values are similar to those obtained in monotonic loading conditions. In this study, the BI values were calculated again for all uniaxial monotonic and cyclic loading tests using Eqs. 8.5 and 8.6. According to Fig. 8.9, similar BI values were obtained for these two types of tests in uniaxial conditions. Also, as can be seen in Fig. 8.9, with an increase in σ_3/UCS_{avg} from 0% to 65%, the rock brittleness for both monotonic and cyclic loading tests changed similarly from an almost transitional state (i.e.

$BI_1 \approx 1$ and $BI_2 \approx 0$) to more class II/brittle behaviour. By increasing the confining pressure to a certain amount (i.e. σ_3/UCS_{avg}=50%), the maximum rock brittleness was achieved, and then, the BI values showed a decremental trend. A drastic drop in BI was observed for $\sigma_3/UCS_{avg} > 65\%$, specifically for cyclic loading tests, where the rock specimens transferred from the class II region (green area) to the class I region (yellow area). Indeed, there is more opposition against the self-sustaining failure at high confinement levels, and more energy should be added axially by the loading system to yield the specimen completely. Therefore, a transition point at 65% confinement level can be estimated for Gosford sandstone, as the rock specimens transfer from a brittle to ductile failure behaviour. The evolutionary trend observed in Fig. 8.9 is also consistent with the stress-strain curves of rocks shown in Fig. 8.3c.

Similar unconventional trends for BI also have been reported in a few studies, (i.e. Tarasov and Potvin 2013 and Ai et al. 2016), for stronger rocks such as quartzite and black shale. According to these studies, the increase in brittleness of rocks with confining pressure can be attributed to the energy-efficient fan-head mode shear failure. Indeed, during Class II failure behaviour, a domino structure of blocks is created by tensile cracks along the future failure plane. Due to the fracture propagation, these blocks are rotated without collapse behaving as hinges and create a fan-shaped structure in the fracture tip. This, in turn, provides an active force (negative shear resistance) that is beneficial for maintaining the crack propagation and is responsible for the self-sustaining failure behaviour of rocks. Therefore, the increase in confining pressure for these rock types seems to provide a higher amount of active forces and consequently increases rock brittleness. By considering the decremental trend of fatigue threshold stress with confinement level, discussed in the previous section, as well as the incremental trend of rock brittleness with confinement for a specific extent, it can be inferred that with an increase in depth in rock engineering projects, the propensity of rock structures to violent/brittle failures such as strain bursting at stress levels lower than the determined average peak strength can be aggravated. The brittleness reduction at high confinement levels can be attributed to the more plastic deformation accumulation induced by the loading and unloading cycles within the specimens, which result in more energy dissipation in the pre-peak regime. This, in turn, provides less amount of elastic strain energy (the source for self-sustaining behaviour) at the failure point, leading to more ductile post-peak behaviour. This behaviour is more evident for cyclic loading tests than monotonic ones due to the more weakening effect of loading and unloading cycles at higher confinement levels. The damage evolution of rocks under different confinement levels is evaluated in more detail in section 8.6.

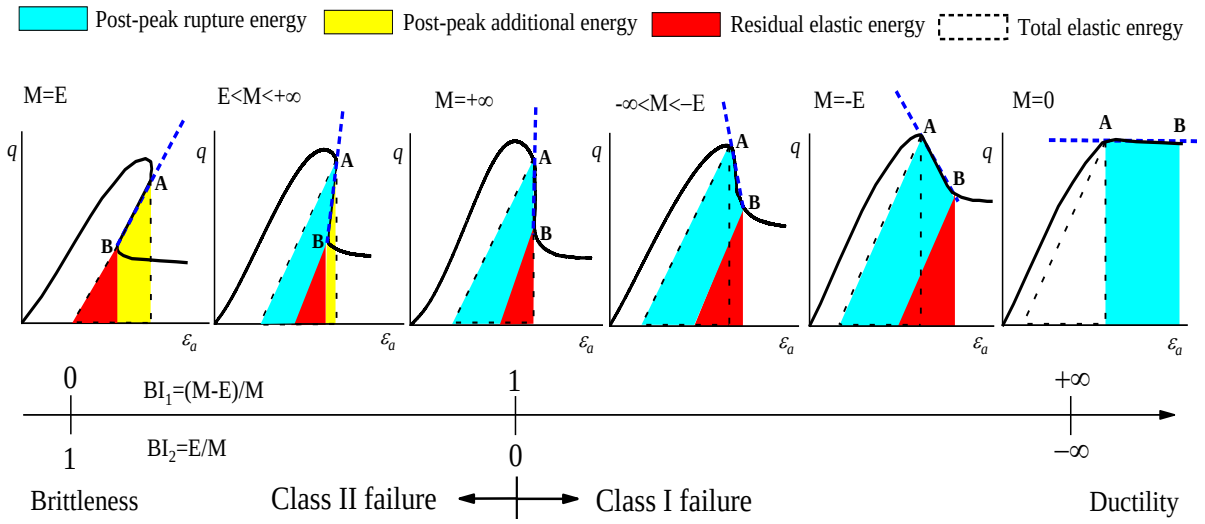

Figure 8.8 Change in brittleness degree of BI_1 and BI_2 with the stress-strain relations and energy evolution, modified from Tarasov and Potvin (2013)

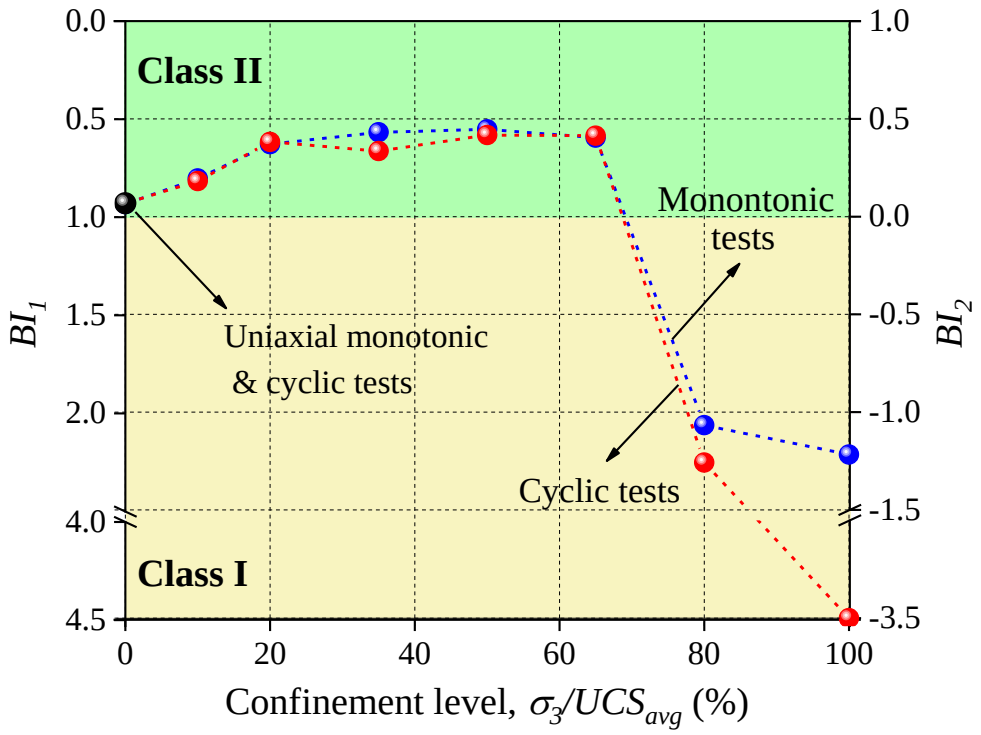

Figure 8.9 Variation of the average BI values with confining pressure for Gosford sandstone

8.6. Confining Pressure Effect on Fatigue Damage Evolution

8.6.1. Hardening and Weakening Cyclic Loading Tests

Rock specimens usually experience deformation under external forces, and a part of this deformation can be recovered by withdrawing the applied force, representing elastic characteristics. However, owing to intrinsic material properties, e.g., porosity and microcracks, and loading-induced damage, the complete deformation recovery after unloading is not possible. Therefore, a certain amount of irreversible/plastic deformation is retained in the specimens (Taheri and Tatsuoka, 2015; Peng et al. 2019). The irreversible strain is accumulated incrementally by applying more cycles, which is accompanied by rock stiffness degradation. Cumulative strain can be utilised to manifest the non-visible damage incurred in the specimen during the systematic cyclic loading tests (Taheri et al. 2016b). According to Table 8.2, for the specimens that did not fail during 1000 loading and unloading cycles, two types of tests can be distinguished based on peak strength variation: strength weakening tests (i.e., final monotonic loading strength is less than UCS_{avg}) and strength hardening tests (i.e., final monotonic loading strength is more than UCS_{avg}). As seen in Table 8.2, the strength weakening is evident for the tests undertaken under $\sigma_3/UCS_{avg} \geq 80\%$. To appraise the rock damage evolution in both conditions, the cumulative irreversible axial strain (ω_a^{irr}) and tangent Young's modulus (E_{tan}) were determined for two representative tests. Fig. 8.10 shows the variation of ω_a^{irr} and E_{tan} for specimens GS-C-15 (with 4.38% strength hardening) and GS-C-31 (with -3.96% strength weakening) at 35% and 100% confinement levels, respectively. The other weakening and hardening cyclic loading tests also showed similar behaviour.

According to Fig. 8.10, for both specimens, the elastic modulus increased notably for initial cycles, making the specimens stiffer and more difficult to deform. This can be related to the closure of pre-existing defects and yield surface expansion during cyclic loading (Taheri and Tatsuoka 2015; Peng et al. 2019). However, for specimen GS-C-15 (i.e., hardening test), by performing further cycles, the stiffness of the specimen decreased slightly and then remained almost constant until 1000 cycles were completed, which is consistent with the trend observed by Ma et al. (2013) triaxial systematic cyclic loading tests. On the other hand, during the initial cycles for specimen GS-C-15, ω_a^{irr} evolved slightly to a certain amount due to the primary loose hysteretic loops, and then like E_{tan}, retained almost constant, which shows that no more damage is cumulated within the specimen. As stated by Shirani Faradonbeh et al. (2021b), this quasi-elastic behaviour can be due to the competition between the mechanisms of grain-size

reduction and rock compaction under consecutive loading and unloading cycles. For specimen GS-C-31 (i.e., weakening test), although no failure was recorded during the cycles, a different trend for variations of ω_a^{irr} was observed (see Fig. 8.10). For the weakening test, ω_a^{irr} increased rapidly, first for several cycles (i.e., initial hysteretic loops), and then by experiencing the dense hysteretic loops, shows a linear increase. At the end of cyclic loading, the increase of ω_a^{irr} becomes more pronounced which may indicate that the specimen could have failed during cyclic loading should the test be continued. These results are consistent with E_{tan} variations for the weakening test, shown in Fig. 8.10. As can be seen in this figure, unlike the hardening test, the damage evolution for weakening test was accompanied by the progressive stiffness degradation of rock during the whole cyclic loading test. Therefore, it can be stated that the strength weakening observed in Table 8.2 for systematic cyclic loading tests can be relevant to the progressive damage evolution/stiffness degradation of rocks in the pre-peak regime, which is aggravated when confining pressure exceeds the transition point (i.e. σ_3/UCS_{avg} >65%). This is while for lower confinement levels, when cyclic stress level is low enough, cyclic loading has no considerable effect on damage evolution; rather, improves peak strength. The above observations are further investigated using AE results.

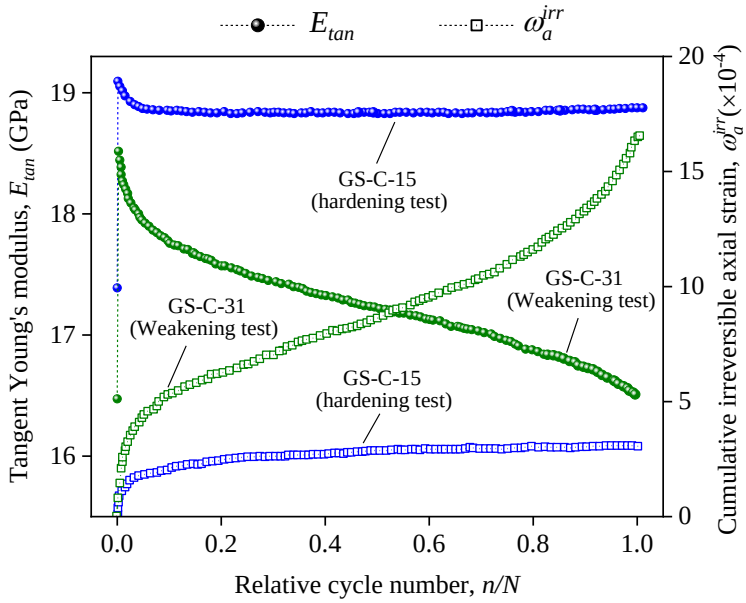

Figure 8.10 Typical evolution of ω_a^{irr} and E_{tan} for hardening and weakening cyclic loading tests

8.6.1.1. Acoustic Emission Characteristics

Acoustic emission (AE) is a well-known non-destructive technique that can monitor the micro and macrocrack evolution in rocks during loading in real-time. Due to the local micro-scale deformations, small fracturing events corresponding to the immediate release of strain energy are created in the form of elastic waves within the specimens. Recording and analysing these elastic waves during the tests can directly measure internal damage (Cox and Meredith 1993; Lockner 1993). Therefore, the AE technique was utilised to elucidate the cracking procedure during the hardening and weakening cyclic loading tests better. In this regard, the evolution of AE hits, representing the number of generated cracks, and its cumulation throughout the representative hardening and weakening tests GS-C-15 and GS-C-31 were respectively depicted in Figs. 8.11a and b. To better unveil the damage mechanism under different confining pressures, the AE results of specimen GS-C-29 (σ_3/UCS_{avg}=80%) which showed the greatest peak strength decrease (i.e. -13.18% strength weakening) were also displayed in Fig. 8.11c. As shown in Fig. 8.11, the evolution of AE hits for the specimens can be investigated throughout three main loading phases: initial monotonic loading (phase A), systematic cyclic loading (phase B) and final monotonic loading (phase C). For all three specimens, during the seating of loading platens on the specimens and the closure of pre-existing defects, few AE hits were recorded in stage A and cumulative AE hits increased slightly. For specimen GS-C-15 (σ_3/UCS_{avg}=35% and q_{un}/q_{m-avg}= 80%), as shown in Fig. 8.11a, the cumulative AE hits then remained almost constant (i.e. quasi-elastic behaviour) during loading and unloading cycles. The zoomed-in figure also shows only small amounts of low-amplitude AE hits during phase B. The cumulated AE hits at the end of stage B is almost 1.77% of the total damage experienced by the specimen during the test. This shows that no considerable cyclic loading induced damage is generated should the specimens be loaded below the fatigue threshold stress and at confinement levels lower than the transition point. This behaviour also is consistent with the variation of ω_a^{irr} discussed in the previous section. The majority of rock damage for specimen GS-C-15 occurred in phase C, where the final monotonic loading was applied to the specimen. In this phase, due to opening the compacted microcracks, the generation of new ones and their coalescence close to and after peak strength point, the cohesive strength of rock is gradually substituted by the frictional resistance, which was accompanied by a higher amount of AE hits.

Unlike specimen GS-C-15 which showed a quasi-elastic behaviour during the systematic cyclic loading, a different AE evolution behaviour was observed for specimen GS-C-31

(σ_3/UCS_{avg}=100% and q_{un}/q_{m-avg}=80%) in phase B. According to Fig. 8.11b, after a slight increase in AE hits during the initial monotonic loading, the microcracking increased with a higher rate by increasing loading and unloading cycles in phase B, which is manifested by a higher number of AE hits. The cumulated AE hits at the end of phase B is almost 27.09% of the total damage incurred in the specimen throughout the test, which is relatively higher than that observed for specimen GS-C-15. As discussed earlier, this microcracking induced by cyclic loading results in stiffness degradation (see Fig. 8.10) and more ductile behaviour in the pre-peak regime. The generated damage was not enough to fail the specimen, however, it resulted in strength weakening of -3.96% during the final monotonic loading. For specimen GS-C-29 which experienced a -13.18% decrease in peak strength at 80% confinement level, as seen in Fig. 8.11c, by applying systematic cyclic loading, the AE hits began to grow first with a lower rate until about 500 cycles were completed. Then by performing further cycles, the rate of AE hits cumulation increased dramatically, representing the continuous generation of macrocracks within the specimen. According to Fig. 8.11c, about 93.90% of the total rock damage happened at the end of phase B, which is far greater than those observed for specimens GS-C-15 and GS-C-31. Based on the above observations for AE outputs, it can be stated that for confinement levels beyond the transition point (σ_3/UCS_{avg}= 65%), although cyclic loading below the fatigue threshold stress does not lead to fatigue failure during 1000 loading cycles, it creates significant damage, which results in a considerable strength weakening during final monotonic loading.

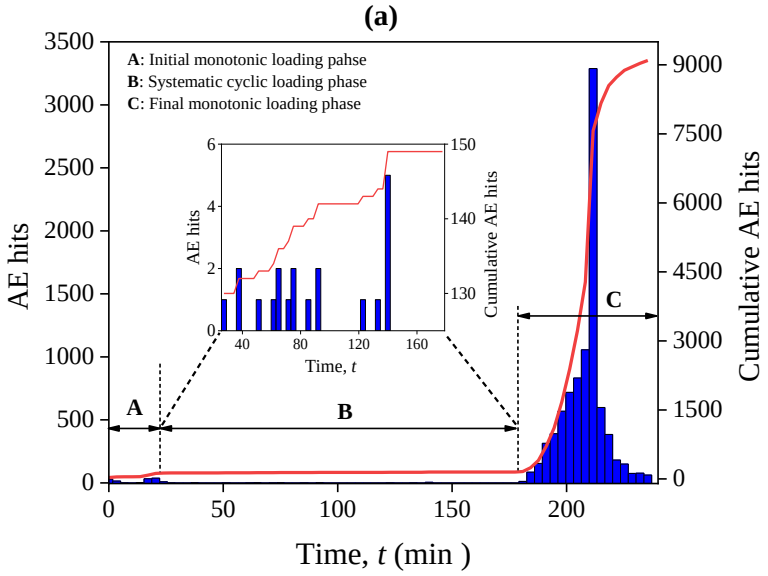

Figure 8.11 Representative AE results for cyclic loading tests: **a** hardening test (GS-C-15), **b** weakening test (GS-C-31) and **c** weakening test (GS-C-29)

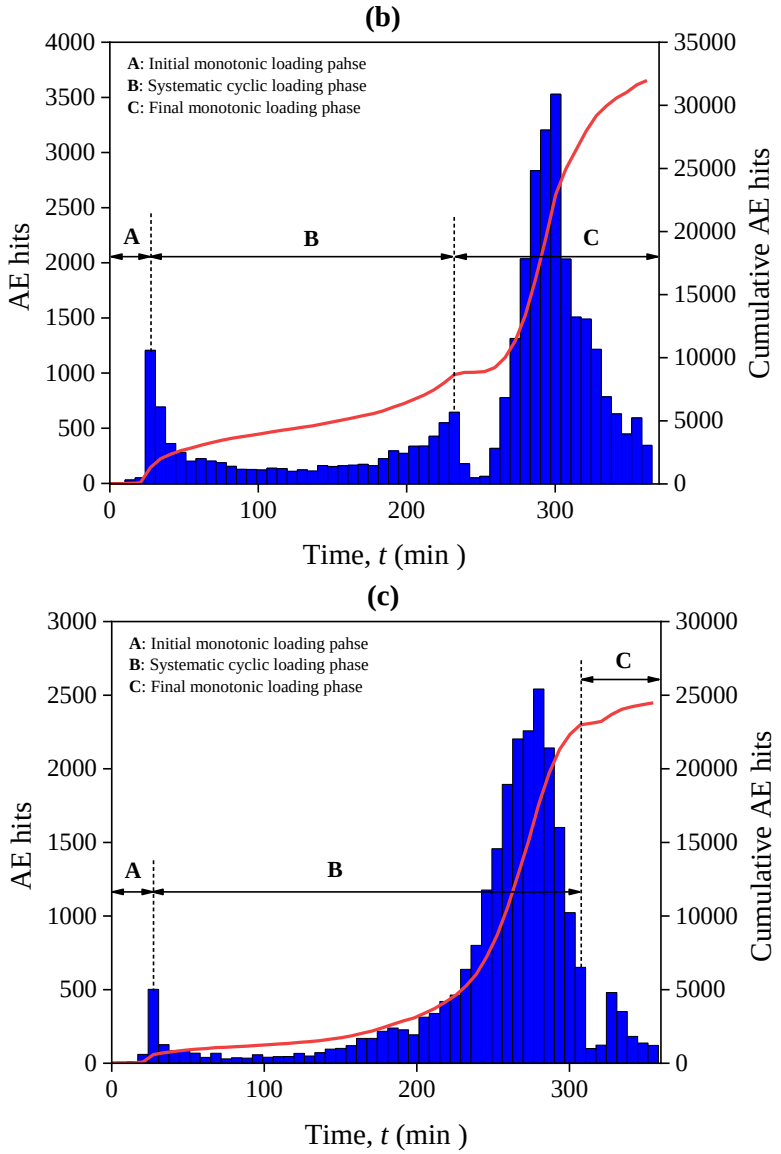

Figure 8.11 (Continued)

8.6.2. Damage Cyclic Loading Tests

In this section, the effect of confining pressure is evaluated on the Gosford sandstone specimens which failed during loading and unloading cycles, i.e., damage cyclic loading tests. Fig. 8.12a displays the variation of ω_a^{irr} for damage cyclic loading tests under different confinement levels. To prevent Fig. 8.12a be crowded, only one damage test was considered for each confinement level. Generally, the irreversible strain increased quickly at the beginning of the tests. Then, a relatively uniform accumulation in strain followed by a rapid strain increase as the rock specimens head toward failure. As is clear from Fig. 8.12a, the damage accumulation rate increased by an increase in σ_3/UCS_{avg} from 10 to 100%. This damage evolution, however, is more significant for the tests undertaken under high confining pressures (i.e. over the transition point) where the irreversible/plastic deformations largely incurred in the pre-peak

regime. The total accumulated plastic deformation values for specimen GS-C-30 (σ_3/UCS_{avg}= 80%) and GS-C-33 (σ_3/UCS_{avg}= 100%) are respectively 77.25×10^{-4} and 381.92×10^{-4}, which are considerably higher than the values obtained for those undertaken under lower confining pressures. The large pre-peak deformation also is evident from the stress-strain relations shown in the Appendix A for these specimens. Also, for lower confinement levels, the specimens follow a three-phase damage evolution law (Xiao et al. 2009) (i.e. transient phase, steady phase and acceleration phase), while it is switched into a two-phase process (i.e. the transient and acceleration phases) for high confinement levels, especially at σ_3/UCS_{avg}=100%. Thus, it can be deduced that confining pressure increases the damage evolution rate in rocks, and this is more evident for confinement levels higher than the transition point.

Fig. 8.12b plots the variation of tangent Young's modulus (E_{tan}) for damage cyclic loading tests at different σ_3/UCS_{avg}. According to this figure, for all damage cyclic loading tests, E_{tan} initially increased in the second loading cycle due to closure of existing micro-cracks, reduction in rock porosity and expansion of yield surface (Taheri and Tatsuoka 2015). Then, a continuous degradation in E_{tan} at different extents can be observed due to accumulation of the cyclic loading induced damage. This damage seems to increase with an increase in confining pressure. Fig. 8.12c illustrates the variation of the stiffness reduction from the second loading cycle (i.e., the maximum value of E_{tan}) until the failure point (i.e., the minimum value of E_{tan}) with respect to the applied confinement level. As seen in this figure, generally, the increase in confinement level resulted in stiffness reduction following an exponential manner. According to Fig. 8.12c, by an increase in confinement level until 80%, the amount of stiffness degradation increases progressively from 2.33 GPa (17.57%) to 3.86 GPa (21.59%), after which a sharp increase in the amount of stiffness reduction, i.e., 5.38GPa (31.67%), can be observed for 100% confinement level. This dramatic degradation in E_{tan} in high confining presures might be due to the excessive damage (irreversible deformation) cumulated in rock in the pre-peak regime, resulting in more ductile failure behaviour.

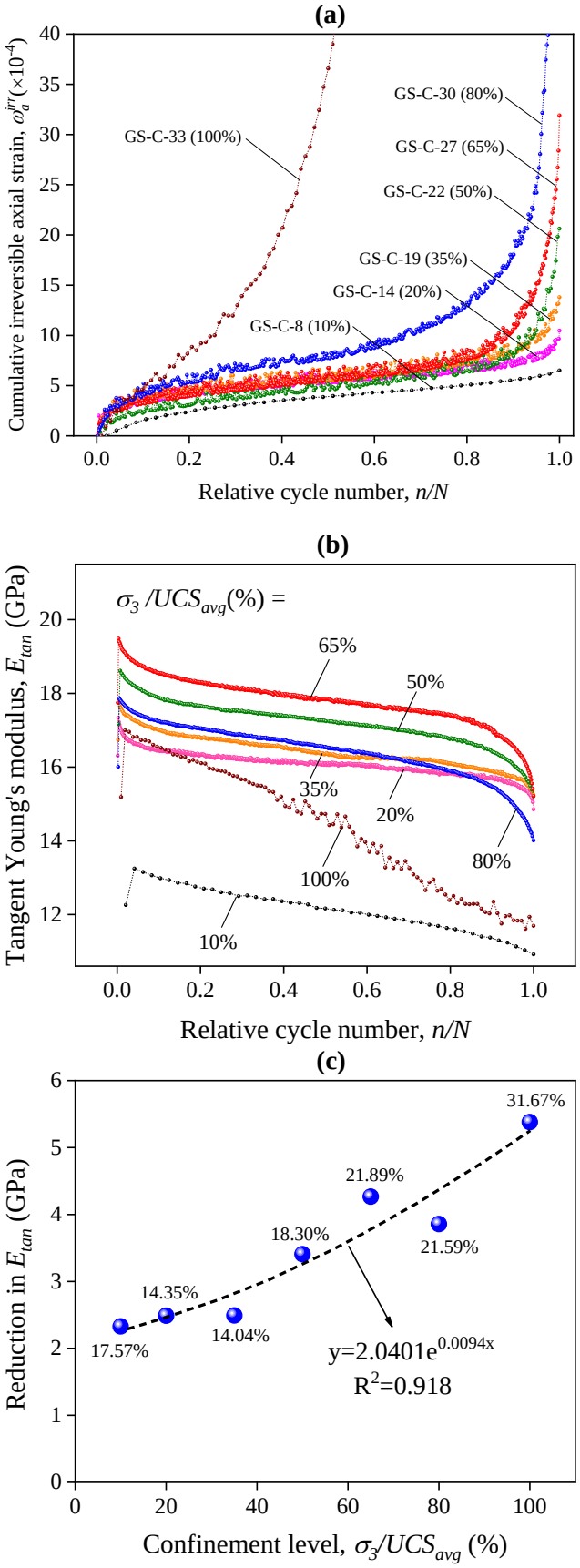

Figure 8.12 Variation of **a** ω_a^{irr} and **b, c** E_{tan} for damage cyclic loading tests under different confinement levels

8.6.2.1. Acoustic Emission Characteristics

To have an insight regarding the AE evolution of rocks that failed during loading and unloading cycles, the typical results of AE hits for specimen GS-C-33 (σ_3/UCS_{avg}= 100% and q_{un}/q_{m-avg}= 82.5%) was shown in Fig. 8.13. As shown in this figure, only two phases of A and B can be distinguished for cyclic damage tests. After an initial increase in AE hits due to closure of pre-existing defects and loading system adjustments, the specimen experienced dense hysteretic loops, and AE hits were accumulated at a constant rate. However, as the applied stress level for this specimen is higher than the estimated fatigue threshold stress for 100% confinement level (i.e., q_f/q_{m-avg}=80%), the rock specimen entered the second loose hysteric loops' region, and large irreversible deformations were incurred in the specimen, which was accompanied by the cumulation of AE hits with a higher rate (phase B). Finally, by coalesce of the generated micro and macrocracks within the specimen and experiencing a large amount of axial strain at the failure point/plastic behaviour, i.e. ε_{af}= 580.75×10^{-4}, the specimen failed in the cycle, demonstrating a class I behaviour. The observed damage evolution for specimen GS-C-33 is also consistent with its measured stress-strain relation shown in the Appendix A.

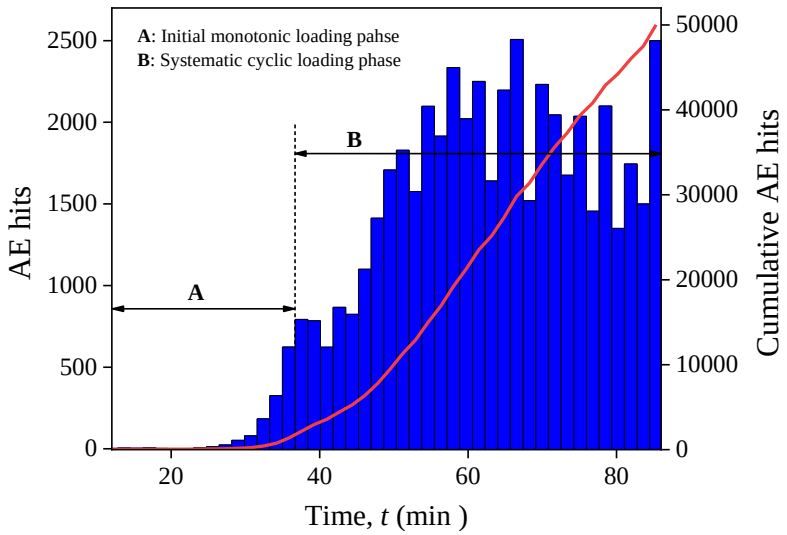

Figure 8.13 Typical AE results for damage cyclic loading tests (σ_3/UCS_{avg}= 100% and q_{un}/q_{m-avg}= 82.5%)

8.6.3. Applied Stress Level Effect on Damage Evolution

As stated earlier, systematic cyclic loading was applied to the specimens at different stress levels (q_{un}/q_{m-avg}). To evaluate the effect of the applied stress level on damage evolution of rocks under different confining pressures, the axial strain at the failure point (ε_{af}) was determined for all monotonic and cyclic loading tests. The results were listed in Tables 8.1 and 8.2. For uniaxial monotonic and cyclic loading conditions, ε_{af} values were adapted from Shirani Faradonbeh et al. (2021b). Fig. 8.14 represents the variation of ε_{af} for monotonic, hardening, weakening and damage cyclic loading tests with q_{un}/q_{m-avg}. It can be seen from Fig. 8.14 that under a specific confinement level (i.e. 35%), cyclic loading at various stress levels has no significant influence on ε_{af} and their values are almost similar to those obtained for monotonic loading tests. However, for higher confinements, larger values of ε_{af} is observed at the stress levels equal to or greater than the fatigue threshold stresses, due to the accumulation of irreversible strain in the sample during the pre-peak regime before the failure. The above behaviour is more evident in Fig. 8.15, where the variation of average axial strain at failure point (ε_{af-avg}) for different stress levels was depicted against σ_3/UCS_{avg}. As seen in this figure, for monotonic loading tests, ε_{af-avg} evolved linearly with the increase of σ_3/UCS_{avg}; this is while, for hardening/weakening and damage cyclic loading tests, this evolution occurred exponentially. According to Fig. 8.15, for σ_3/UCS_{avg} ≤35%, the monotonic and cyclic loading tests have almost similar ε_{af-avg} values, which means that loading and unloading cycles below and beyond the fatigue threshold stress have no striking influence on pre-peak behaviour, and damage evolution under cyclic loading is similar to monotonic loading conditions. However, for higher confinement levels, ε_{af-avg} increased first gradually until σ_3/UCS_{avg}= 65% representing more accumulation of plastic deformations within the specimens in the pre-peak regime compared with the monotonic loading conditions. The evolutionary trend of ε_{af-avg}, then, was aggravated for confinement levels of 80 and 100%, where a sharp increase in ε_{af-avg} was observed for weakening and damage cyclic loading tests.

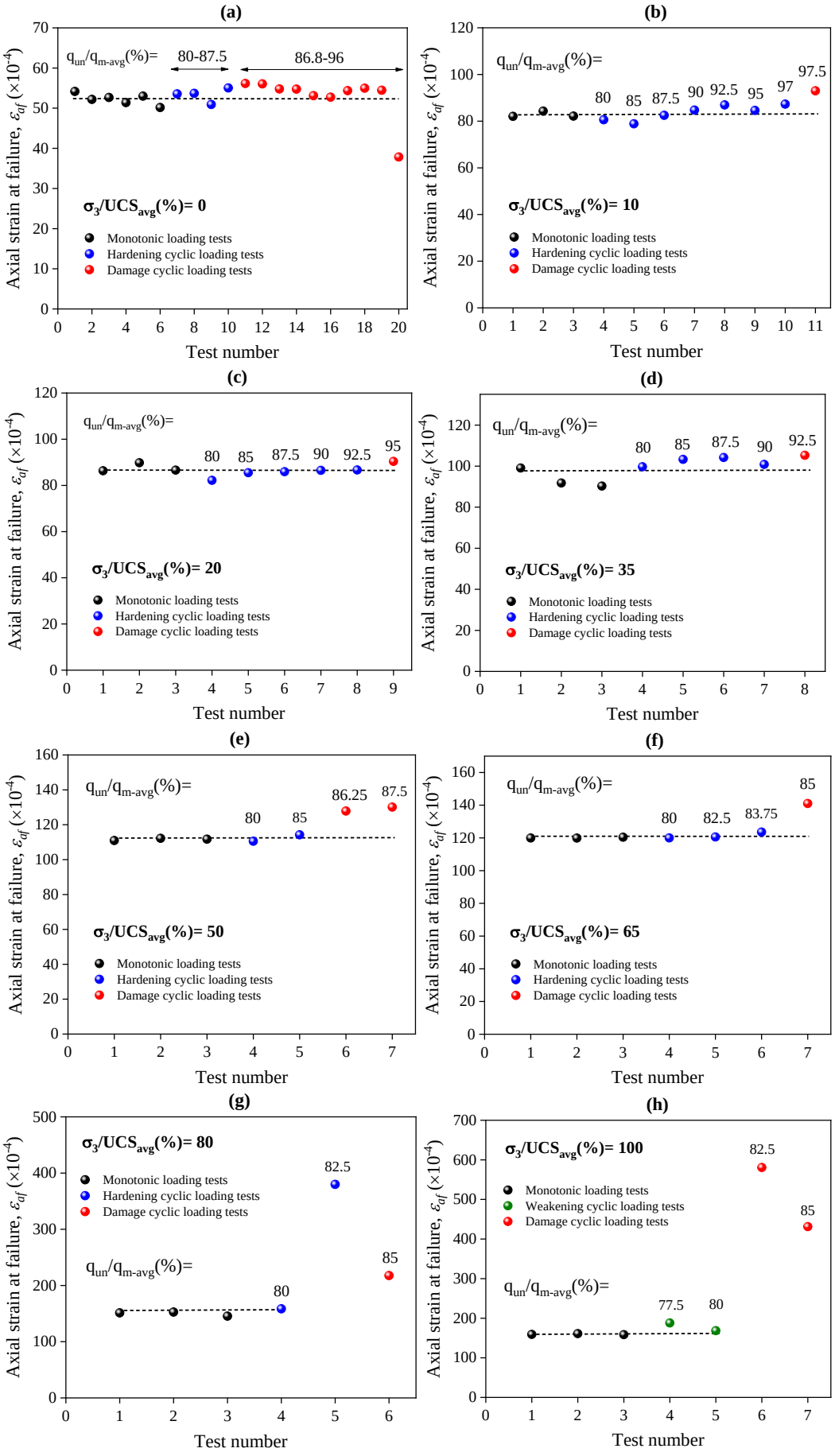
(a)
$q_{un}/q_{m\text{-}avg}$(%)= 80-87.5 86.8-96
σ_3/UCS_{avg}(%)= 0
Monotonic loading tests
Hardening cyclic loading tests
Damage cyclic loading tests
(b)
$q_{un}/q_{m\text{-}avg}$(%)= 80 85 87.5 90 92.5 95 97 97.5
σ_3/UCS_{avg}(%)= 10
(c)
$q_{un}/q_{m\text{-}avg}$(%)= 80 85 87.5 90 92.5 95
σ_3/UCS_{avg}(%)= 20
(d)
$q_{un}/q_{m\text{-}avg}$(%)= 80 85 87.5 90 92.5
σ_3/UCS_{avg}(%)= 35
(e)
$q_{un}/q_{m\text{-}avg}$(%)= 80 85 86.25 87.5
σ_3/UCS_{avg}(%)= 50
(f)
$q_{un}/q_{m\text{-}avg}$(%)= 80 82.5 83.75 85
σ_3/UCS_{avg}(%)= 65
(g)
σ_3/UCS_{avg}(%)= 80
$q_{un}/q_{m\text{-}avg}$(%)= 80 82.5 85
(h)
σ_3/UCS_{avg}(%)= 100
Weakening cyclic loading tests
$q_{un}/q_{m\text{-}avg}$(%)= 77.5 80 82.5 85
Axial strain at failure, ε_{af} ($\times 10^{-4}$)
Test number

Figure 8.14 Variation of axial strain at failure point for monotonic and cyclic loading tests under different confinement levels: **a** 0%, **b** 10%, **c** 20%, **d** 35%, **e** 50%, **f** 65%, **g** 80% and **h** 100%

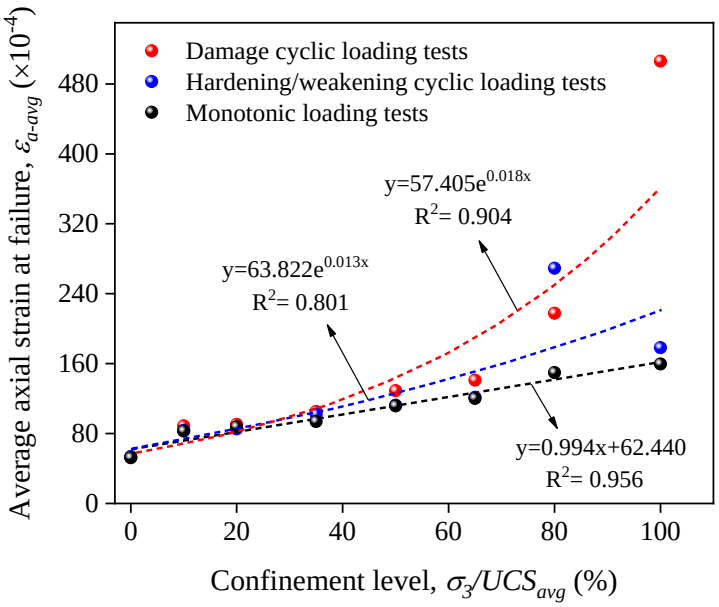

Figure 8.15 Average axial strain at failure for monotonic and cyclic loading tests

8.7. Confining Pressure Effect on Strength Hardening/Weakening

8.7.1. Peak Strength Variation

As seen in Table 8.2, depending on the stress level that cyclic loading is applied as well as the confinement level, rock specimens have experienced different values of increase/decrease in peak strength during final monotonic loadings. As discussed in sections 8.6.1 and 8.6.1.1, when the stress level during cyclic loading is low enough (i.e. lower than the estimated FTS), cyclic loading at lower confinement levels did not create macro-damage in the specimens, and a quasi-elastic behaviour dominated the rock damage evolution. This, in turn, resulted in a hardening behaviour under loading and unloading cycles, and consequently, strength improvement which is observed during final monotonic loading. The rock compaction due to cyclic loading in the hardening region is evident in Fig. 8.5 for the representative test GS-C-13 (with 4.06% hardening), where the specimen did not experience large axial, lateral and volumetric irreversible strains, and the rock volume was entirely in the compaction stage during cyclic loading. This is while for rocks that failed during cycles (see Fig. 8.6), relatively higher strain values were recorded, and rocks were mainly in the dilation-dominated stage. The strength hardening induced by cyclic loading also has been reported by other researchers for different

rock types under various loading conditions, such as Gosford sandstone (up to 7.82% increase) under uniaxial systematic cyclic loading (Shirani Faradonbeh et al. 2021b), Tuffeau limestone under uniaxial multi-level systematic cyclic loading (up to 28.55% increase) (Shirani Faradonbeh et al. 2021a), hard graywacke sandstone under uniaxial systematic cyclic loading (up to 29% increase) (Singh 1989), Hawkesbury sandstone under triaxial systematic cyclic loading (up to 11% increase) (Taheri et al. 2016b) and rock salt under triaxial systematic cyclic loading (up to 171% increase) (Ma et al. 2013).

Fig. 8.16a represents variation in peak strength with confinement level (σ_3/UCS_{ave}). The results of hardening tests under uniaxial condition (σ_3=0) were extracted from Shirani Faradonbeh et al. (2021b). According to Fig. 8.16a and Table 8.2, the peak strength parameter varies between two distinct zones, i.e. hardening zone and damage zone. Also, the maximum increase and decrease in peak strength values of Gosford sandstone specimens are 7.82% and -13.18%, respectively. Generally, with an increase in σ_3/UCS_{avg}, the amount of strength hardening induced by cyclic loading decreased and when σ_3/UCS_{avg}> 65% (i.e. transition point), rock specimens demonstrate strength weakening behaviour (see Fig. 8.16a). To better reflect the mechanism behind the rock moving from hardening into weakening, a parameter is proposed as below:

$$\Delta\varepsilon_a^{irr} = (\varepsilon_a^{irr})_f - (\varepsilon_a^{irr})_i \tag{8.8}$$

where $\Delta\varepsilon_a^{irr}$ is the differential irreversible axial strain (measured between valley points), and $(\varepsilon_a^{irr})_f$ and $(\varepsilon_a^{irr})_i$ are, respectively, the irreversible axial strains measured for final and initial loading cycles.

Fig. 8.16b demonstrates the variation of $\Delta\varepsilon_a^{irr}$ for cyclic loading tests at different stress levels with σ_3/UCS_{avg}. As can be seen in this figure, the range of variation for $\Delta\varepsilon_a^{irr}$ increased continuously with an increase in confining pressure, and this is more significant for σ_3/UCS_{avg}> 65%, where a high amount of irreversible deformation was experienced by the specimens. The incremental trend of $\Delta\varepsilon_a^{irr}$ with confinement results in more plastic behaviour and, therefore, pre-peak damage even when cycles don't result in a failure. This, finally, resulted in a decremental trend of the maximum peak strength variation at each confinement level under cyclic loading, as shown in Fig. 8.16c.

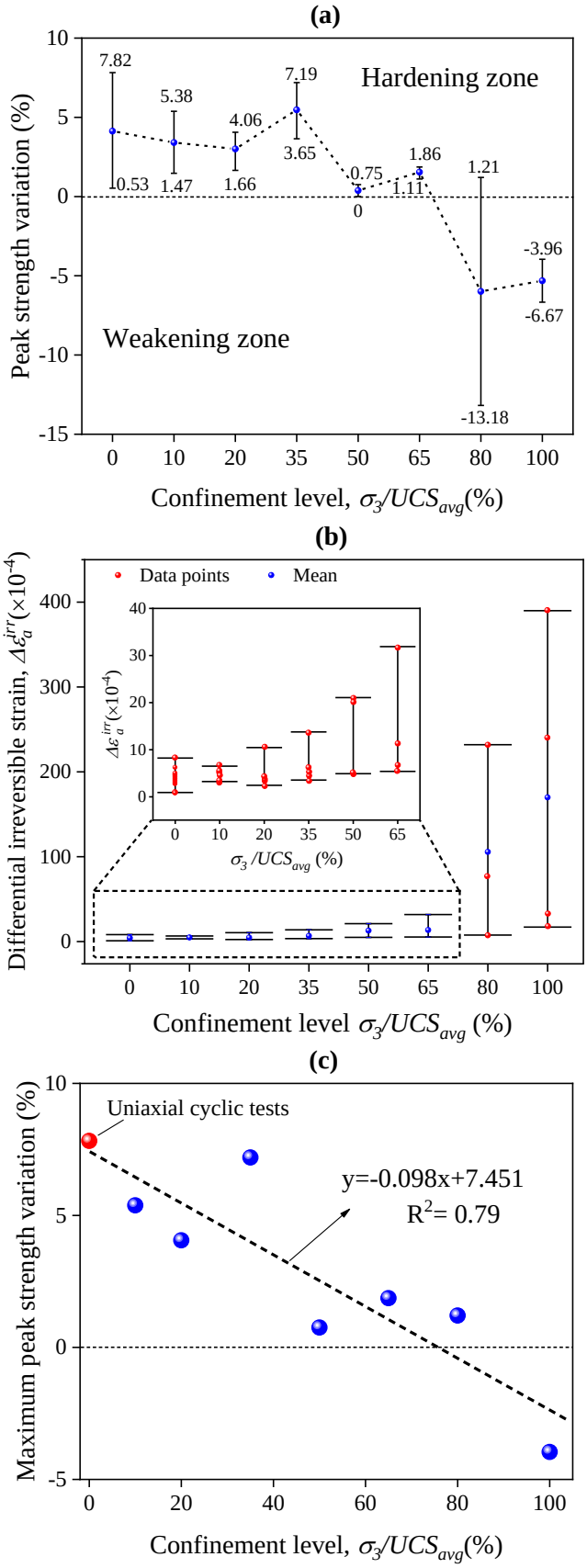

Figure 8.16 a Variation of a peak strength during final monotonic loading at different stress levels, **b** differential irreversible strain and **c** maximum peak strength with confinement level

8.7.2. An Empirical Model for Strength Prediction

As discussed above, the study on strength variation of rocks under the coupled influence of cyclic loading and confining pressure is rare and limited to some specific confining pressures. Therefore, no empirical model can be found in the literature to predict strength variation after loading cycles. The classification and regression tree (CART) algorithm was employed in this study to predict the amount of strength hardening/weakening in Gosford sandstone after cyclic loading history. The CART algorithm, developed by Breiman et al. (1984), is a computational-statistical algorithm that can predict the target variable in the form of a decision tree. The CART tree is created by the binary splitting of the datasets from the root node into two sub-nodes using all predictor variables. The best predictor usually is chosen based on impurity or diversity measures (e.g. Gini, twoing and least squared deviation). The aim is to create subsets of the data which are as homogeneous as possible concerning the output variable. For each split, each input parameter (predictor) is evaluated to find the best groupings of categories (for nominal and ordinal predictors) or cut point (for continuous predictors) according to the improving score or reduction in impurity. Thereafter, the predictors are compared, and the predictor with the greatest improvement is selected for the split. This process is repeated until one of the stopping criteria (e.g. the maximum tree depth) is met (Salimi et al. 2016; Liang et al. 2016; Khandelwal et al. 2017). A detailed description of the CART algorithm can be found in (Breiman et al. 1984).

In this study, the applied stress level (q_{un}/q_{m-avg}) and confinement level (σ_3/UCS_{avg}) were defined as input variables to predict the percentage of strength hardening/weakening as output variable. Based on the results presented in Table 8.2 and the conducted cyclic loading tests in uniaxial conditions by Shirani Faradonbeh et al. (2021b), a database containing 28 tests that experienced a monotonic loading after a cyclic loading history was compiled. The test GS-C-29, which showed -13.18% strength weakening was identified as an outlier (in terms of statistics) and excluded from the modelling procedure. The CART parameters, including the maximum tree depth, impurity index and the minimum size of parent and child nodes (i.e. the minimum number of objects that a node must contain to be split) were changed for different runs to obtain a predictive model with high accuracy and low complexity. Finally, the best model was achieved according to the settings listed in Table 8.4. The modelling procedure was carried out in the MatLab environment. Fig. 8.17 represents the obtained regression tree for the best model. As shown in this figure, the developed regression tree provides a practical tool to estimate the percentage variation of the peak strength straightforwardly. Fig. 8.18 compares

the measured values of the peak strength variation with those predicted by the developed CART model. As seen in this figure, the CART is capable of predicting the peak strength variation of Gosford sandstone with high accuracy (R^2= 90%).

Table 8.4 The settings for the CART model

CART parameter	Value
Predictors (terminal & root nodes)	q_{un}/q_{m-avg}, σ_3/UCS_{avg}
Maximum tree depth	6
Minimum parent size	2
Minimum child size	1
Impurity measure	Gini

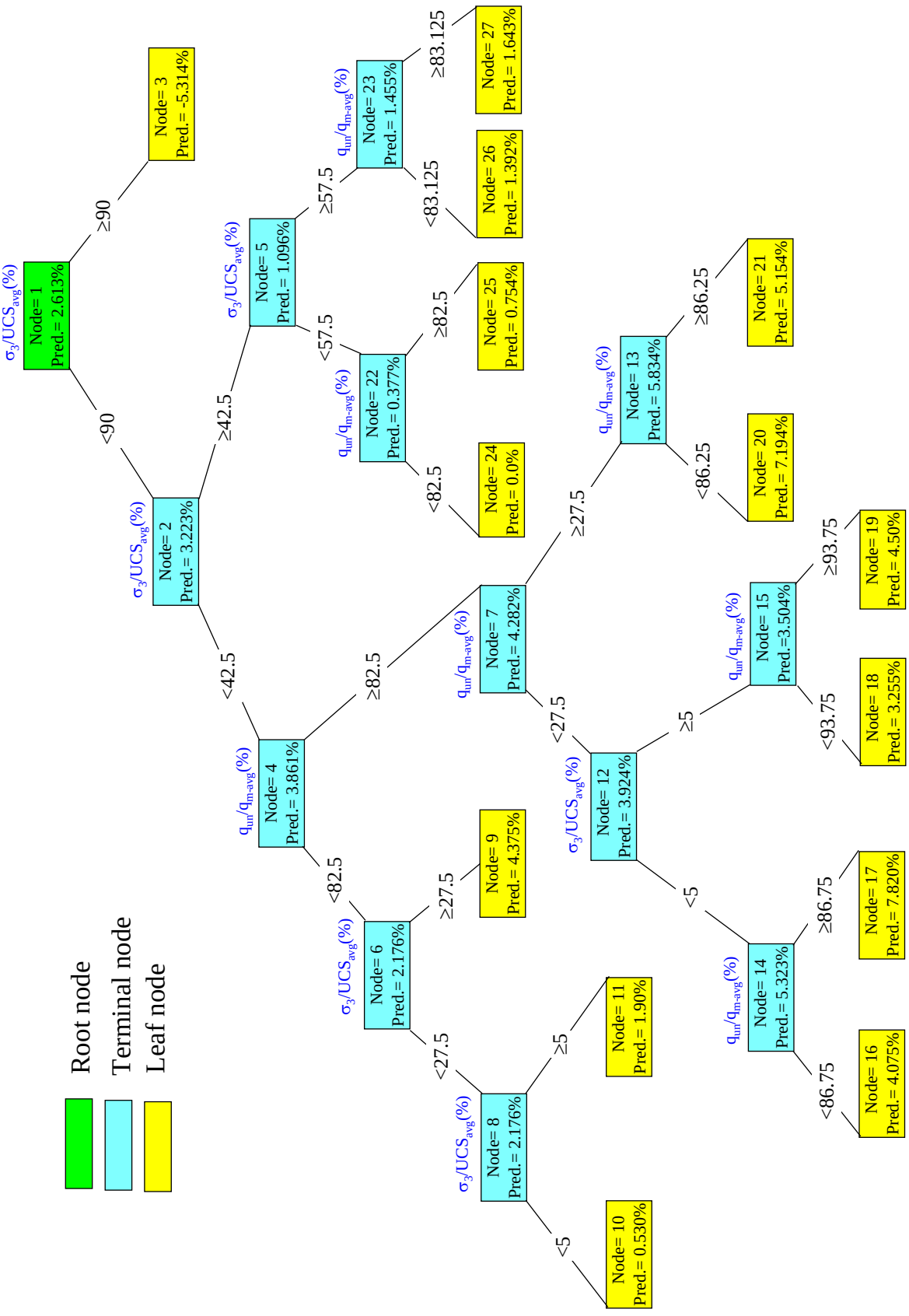

Fig. 8.17 Regression tree developed for the prediction of strength hardening/weakening percentage

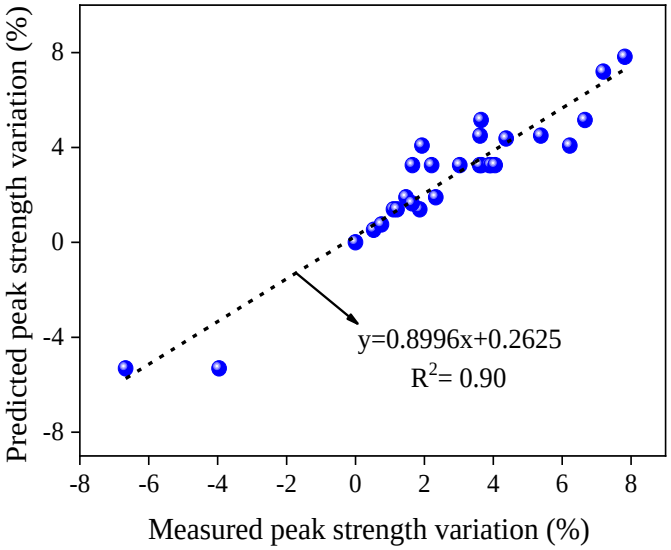

Fig. 8.18 The comparison of the measured and predicted values of peak strength variation

8.8. Conclusions

Triaxial monotonic and cyclic loading tests were undertaken in this study on Gosford sandstone at different confinement levels to scrutinise the effect of both systematic cyclic loading history and confining pressure on the evolution of rock fatigue characteristics. For this aim, a modified triaxial testing procedure was employed to control the axial load during the tests using a constant lateral strain feedback signal. Based on the experimental results, the following conclusions were drawn:

1. The confining pressure displayed a significant effect on fatigue threshold stress (FTS). It was found that with an increase in σ_3/UCS_{avg} from 10% to 100%, FTS decreases from 97% to 80%. This indicates that rocks in great depth experience failure due to cyclic loading at stress levels much lower than the determined monotonic strength.
2. According to the obtained stress-strain relations, the post-peak behaviour of rocks followed an unconventional trend with the increase in confining pressure so that for lower σ_3/UCS_{avg}, rock specimens showed a self-sustaining (brittle) failure behaviour, while for higher σ_3/UCS_{avg}, the ductile behaviour was dominant. The post-peak instability of rocks was quantified using strain energy-based brittleness indices (BIs), and a transition point at σ_3/UCS_{avg}= 65% was identified, where the rocks transited from the brittle failure behaviour to ductile one. The results also showed that cyclic loading at confinement levels lower than the transition point has no notable effect on

rock brittleness, while for σ_3/UCS_{avg}= 80% and 100%, the weakening effect of systematic cyclic loading history on rock brittleness was more significant.

3. Fatigue damage evaluation of rocks using different parameters (i.e. E_{tan}, $\omega_a^{irr}$and AE hits) showed that for hardening cyclic loading tests, no macro-damage is observed within the specimens, and the stiffness of the rocks remain almost constant during a large number of cycles, representing a quasi-elastic behaviour. However, for weakening cyclic loading tests, although no failure was observed during cycles, E_{tan} and ω_a^{irr} increased and decreased, respectively, with cycle loading. Compared to the hardening cyclic loading tests, the AE activities (micro-cracking) was more evident for specimens that showed a higher amount of strength degradation. On the other hand, for damage cyclic loading tests, it was found that damage is accumulated with a higher rate and extent with an increase in confining pressure.
4. Looking at the variation of axial strain at the failure point (ε_{af}) for monotonic, hardening/weakening and damage cyclic loading tests, it was found that under confinement levels below the transition point, the applied stress level has no notable effect on the cumulation of irreversible deformations in the pre-peak regime and the values of ε_{af} are similar to those in monotonic loading conditions. However, for higher confinements, cyclic loading resulted in larger irreversible strain values before the failure point.
5. After a cyclic loading history, the peak deviator stress of Gosford sandstone varied between -13.18% and 7.82%. According to the evolution of damage parameters, the observed quasi-elastic behaviour during cyclic loading and the variation of plastic axial, lateral and volumetric strains for hardening cyclic loading tests, the strength hardening can be related to the rock compaction induced by cyclic loading. It was observed that the increase in confining pressure decreases the amount of strength hardening due to the accumulation of irreversible strains in the rock specimens. An empirical regression tree-based model was proposed to estimate peak strength variation of Gosford sandstone based on the applied stress level and confining pressure. The results showed the high accuracy of the model.

Acknowledgements

The first author acknowledges the University of Adelaide for providing the research fund (Beacon of Enlightenment PhD Scholarship) to conduct this study. The authors would like to thank the laboratory technicians particularly Simon Golding and Dale Hodson, for their aids in

conducting the tests. The first author also acknowledges Arash Mazinani for his help in conducting the microscopic analysis.

Appendix A:

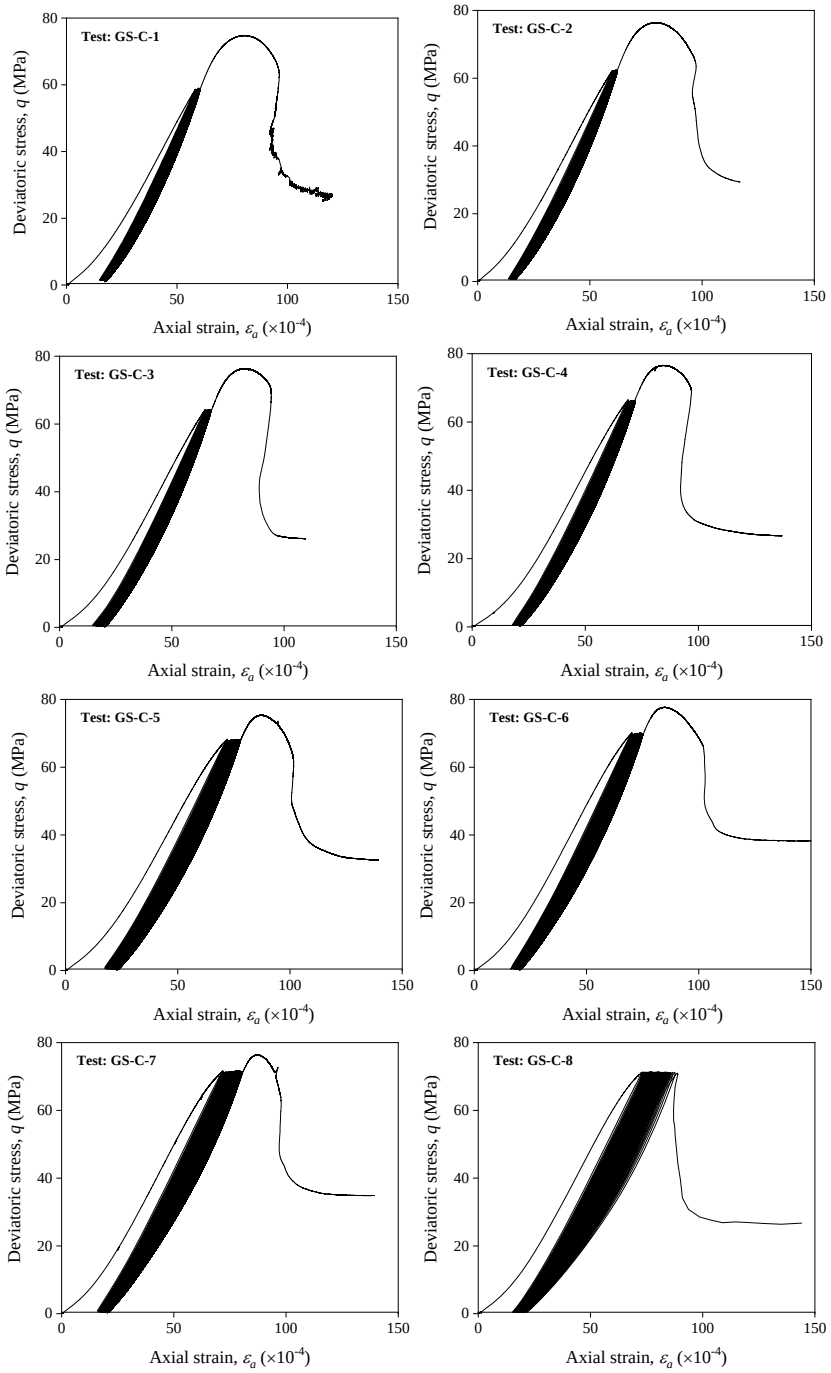

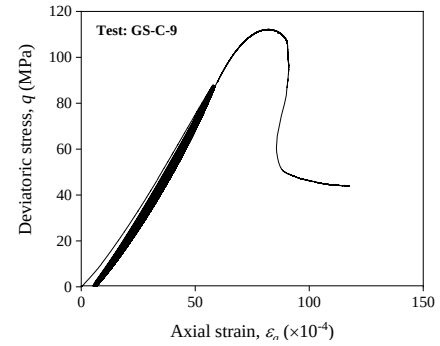
Test: GS-C-9
Deviatoric stress, q (MPa)
Axial strain, ε_a ($\times 10^{-4}$)

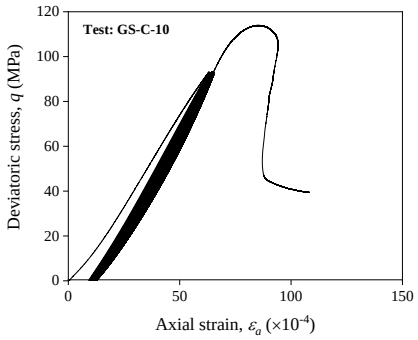
Test: GS-C-10
Deviatoric stress, q (MPa)
Axial strain, ε_a ($\times 10^{-4}$)

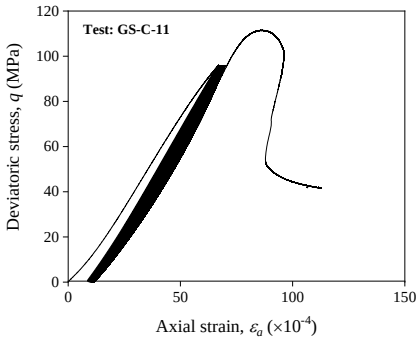
Test: GS-C-11
Deviatoric stress, q (MPa)
Axial strain, ε_a ($\times 10^{-4}$)

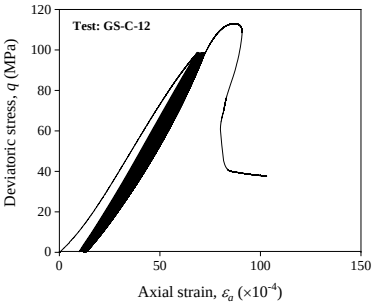
Test: GS-C-12
Deviatoric stress, q (MPa)
Axial strain, ε_a ($\times 10^{-4}$)

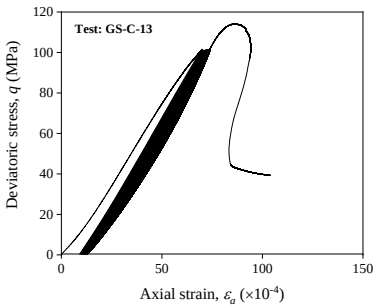
Test: GS-C-13
Deviatoric stress, q (MPa)
Axial strain, ε_a ($\times 10^{-4}$)

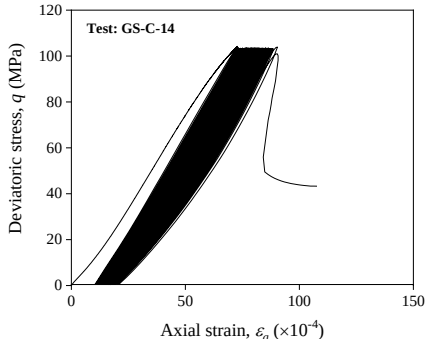
Test: GS-C-14
Deviatoric stress, q (MPa)
Axial strain, ε_a ($\times 10^{-4}$)

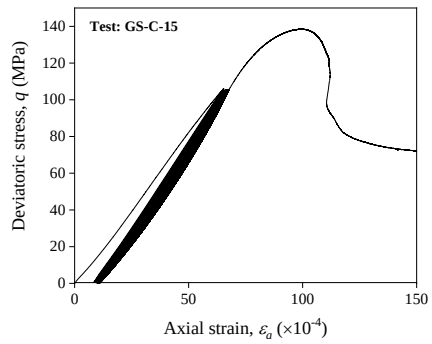
Test: GS-C-15
Deviatoric stress, q (MPa)
Axial strain, ε_a ($\times 10^{-4}$)

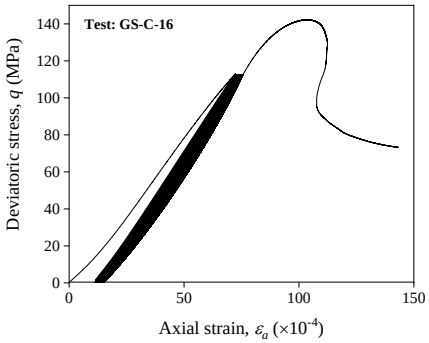
Test: GS-C-16
Deviatoric stress, q (MPa)
Axial strain, ε_a ($\times 10^{-4}$)

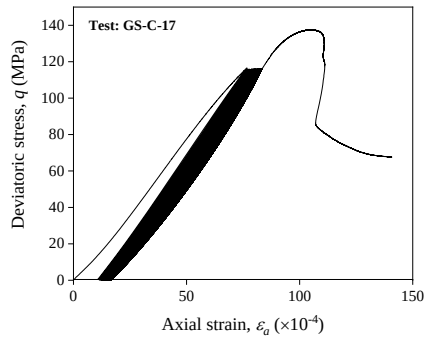
Test: GS-C-17
Deviatoric stress, q (MPa)
Axial strain, ε_a ($\times 10^{-4}$)

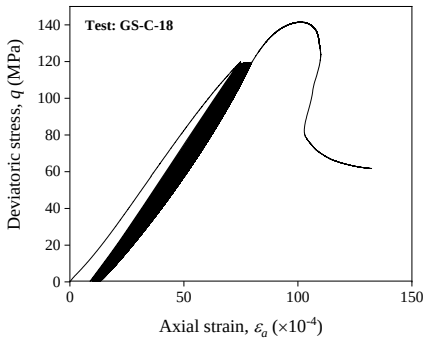
Test: GS-C-18
Deviatoric stress, q (MPa)
Axial strain, ε_a ($\times 10^{-4}$)

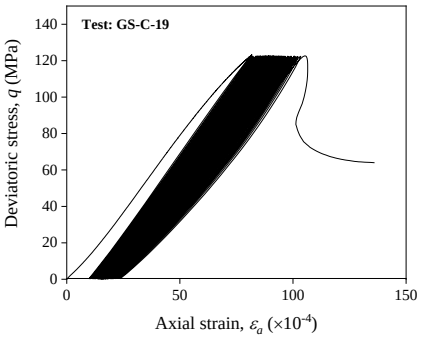
Test: GS-C-19
Deviatoric stress, q (MPa)
Axial strain, ε_a (×10^{-4})

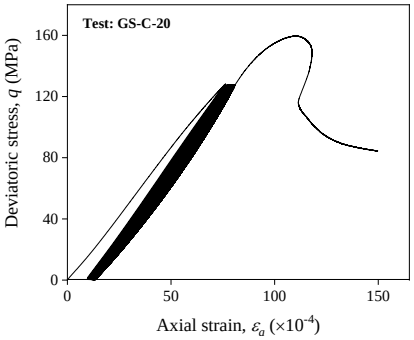
Test: GS-C-20
Deviatoric stress, q (MPa)
Axial strain, ε_a (×10^{-4})

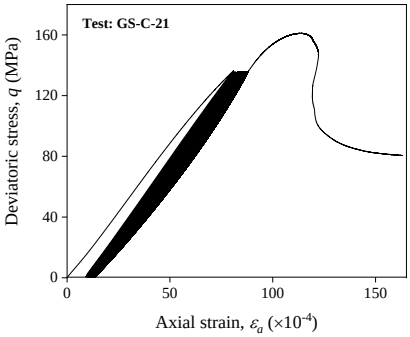
Test: GS-C-21
Deviatoric stress, q (MPa)
Axial strain, ε_a (×10^{-4})

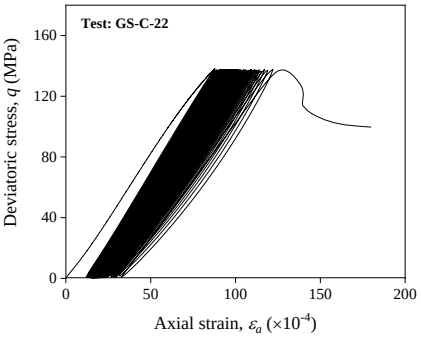
Test: GS-C-22
Deviatoric stress, q (MPa)
Axial strain, ε_a (×10^{-4})

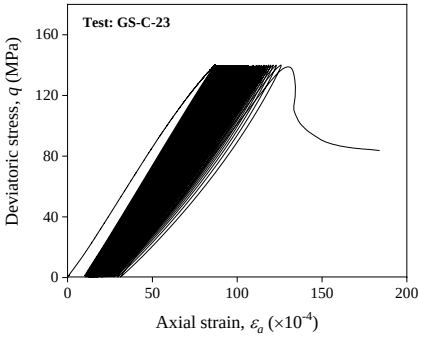
Test: GS-C-23
Deviatoric stress, q (MPa)
Axial strain, ε_a (×10^{-4})

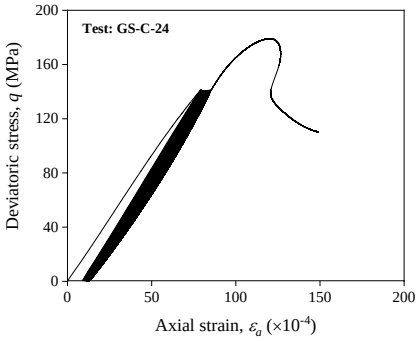
Test: GS-C-24
Deviatoric stress, q (MPa)
Axial strain, ε_a (×10^{-4})

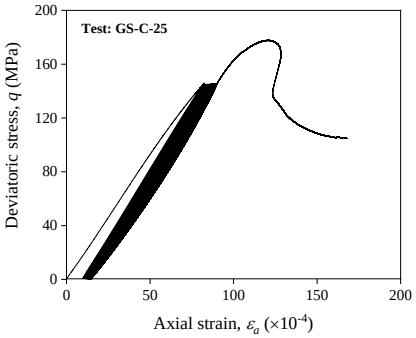
Test: GS-C-25
Deviatoric stress, q (MPa)
Axial strain, ε_a (×10^{-4})

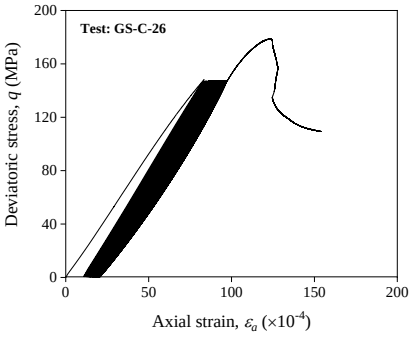
Test: GS-C-26
Deviatoric stress, q (MPa)
Axial strain, ε_a (×10^{-4})

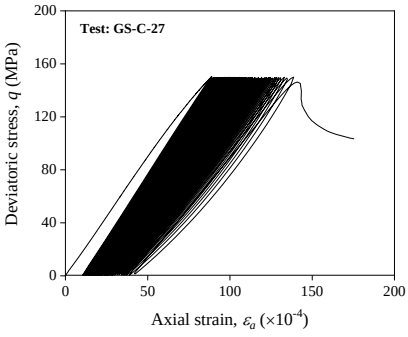
Test: GS-C-27
Deviatoric stress, q (MPa)
Axial strain, ε_a (×10^{-4})

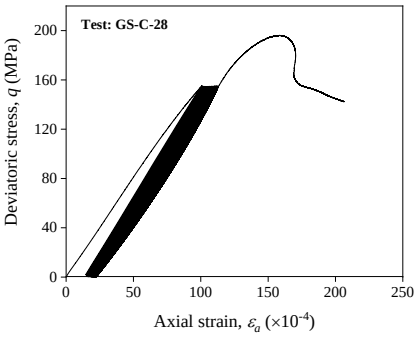
Test: GS-C-28
Deviatoric stress, q (MPa)
Axial strain, ε_a (×10^{-4})

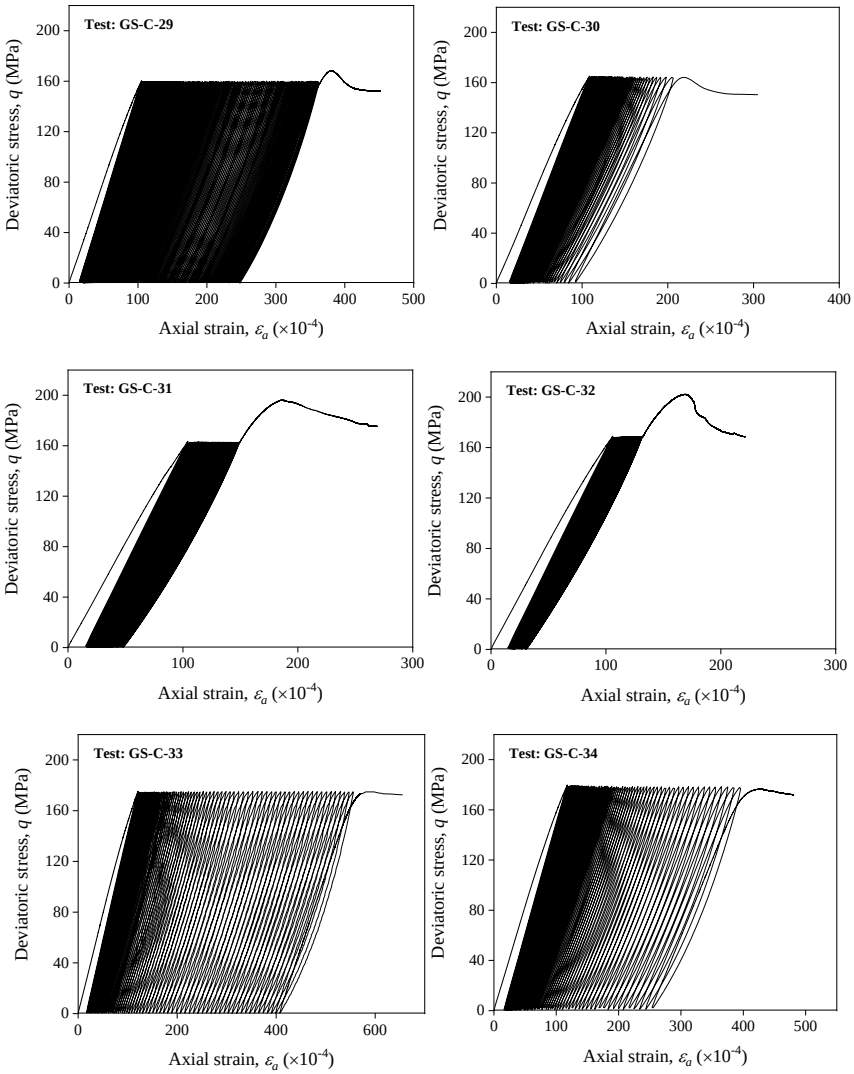

Figure A.1 Stress-Strain Results of Triaxial Cyclic Loading Tests

References

Ai C, Zhang J, Li Y, et al (2016) Estimation criteria for rock brittleness based on energy analysis during the rupturing process. *Rock Mechanics and Rock Engineering* 49(12):4681–4698

Åkesson U, Hansson J, Stigh J (2004) Characterisation of microcracks in the Bohus granite, western Sweden, caused by uniaxial cyclic loading. *Engineering Geology* 72(1-2):131–142

Bagde MN, Petroš V (2005) Fatigue properties of intact sandstone samples subjected to dynamic uniaxial cyclical loading. *International Journal of Rock Mechanics and Mining*

Sciences 42(2):237–250

Breiman L, Friedman J, Stone CJ, Olshen RA (1984) Classification and Regression Trees. *CRC press*

Bruning T, Karakus M, Nguyen GD, Goodchild D (2018) Experimental Study on the Damage Evolution of Brittle Rock Under Triaxial Confinement with Full Circumferential Strain Control. *Rock Mechanics and Rock Engineering* 51(11):3321–3341

Burdine NT (1963) Rock Failure Under Dynamic Loading Conditions. *Society of Petroleum Engineers Journal* 3(1):1–8

Cerfontaine B, Collin F (2018) Cyclic and fatigue behaviour of rock materials: review, interpretation and research perspectives. *Rock Mechanics and Rock Engineering* 51(2):391–414

Cox SJD, Meredith PG (1993) Microcrack formation and material softening in rock measured by monitoring acoustic emissions. In: *International journal of rock mechanics and mining sciences & geomechanics abstracts*. Elsevier 30(1):11–24

Erarslan N, Alehossein H, Williams DJ (2014) Tensile Fracture Strength of Brisbane Tuff by Static and Cyclic Loading Tests. *Rock Mechanics and Rock Engineering* 47(4):1135–1151

Erarslan N, Williams DJ (2012) Investigating the effect of cyclic loading on the indirect tensile strength of rocks. *Rock Mechanics and Rock Engineering* 45(3):327–340

Grover HJ, Dehlinger P, McClure GM (1950) Investigation of fatigue characteristics of rocks. *Rep Battelle Mem Inst Drill Res Inc*

Guo Y, Yang C, Mao H (2012) Mechanical properties of Jintan mine rock salt under complex stress paths. *International Journal of Rock Mechanics and Mining Sciences* 56:54–61

Haimson BC, Kim C (1971) Mechanical behaviour of rock under cyclic fatigue. *Proceedings of the 13th symposium on rock mechanics*. ASCE, New York, pp 845–863

Hoskins ER (1969) The failure of thick-walled hollow cylinders of isotropic rock. In: *International Journal of Rock Mechanics and Mining Sciences & Geomechanics Abstracts*. Elsevier 6(1):99–125

Jamali Zavareh S, Baghbanan A, Hashemolhosseini H, Haghgouei H (2017) Effect of

microstructure on fatigue behavior of intact rocks under completely reversed loading. *Analytical and Numerical Methods in Mining Engineering* 6:55–62

Khandelwal M, Armaghani DJ, Faradonbeh RS, et al (2017) Classification and regression tree technique in estimating peak particle velocity caused by blasting. *Engineering with Computers* 33(1):45–53

Li N, Zou Y, Zhang S, et al (2019) Rock brittleness evaluation based on energy dissipation under triaxial compression. *Journal of Petroleum Science and Engineering* 183:106349

Liang M, Mohamad ET, Faradonbeh RS, et al (2016) Rock strength assessment based on regression tree technique. *Engineering with Computers* 32(2):343–354

Lockner D (1993) The role of acoustic emission in the study of rock fracture. *International Journal of Rock Mechanics and Mining Sciences & Geomechanics Abstracts* 30:883–899

Ma L, Liu X, Wang M, et al (2013) Experimental investigation of the mechanical properties of rock salt under triaxial cyclic loading. *International Journal of Rock Mechanics and Mining Sciences* 34–41

Masoumi H, Horne J, Timms W (2017) Establishing empirical relationships for the effects of water content on the mechanical behavior of Gosford sandstone. *Rock Mechanics and Rock Engineering* 50(8):2235–2242

Meng F, Wong LNY, Zhou H (2020) Rock brittleness indices and their applications to different fields of rock engineering: A review. *Journal of Rock Mechanics and Geotechnical Engineering*

Meng Q, Liu J-F, Ren L, et al (2021) Experimental Study on Rock Strength and Deformation Characteristics Under Triaxial Cyclic Loading and Unloading Conditions. *Rock Mechanics and Rock Engineering* 54(2):777-797

Munoz H, Taheri A (2017) Local damage and progressive localisation in porous sandstone during cyclic loading. *Rock Mechanics and Rock Engineering* 50(12):3253–3259

Munoz H, Taheri A, Chanda EK (2016) Pre-peak and post-peak rock strain characteristics during uniaxial compression by 3D digital image correlation. *Rock Mechanics and Rock Engineering* 49(7):2541–2554

Munoz H, Taheri A (2019) Post-peak deformability parameters of localised and non-localised

damage zones of rocks under cyclic loading. *Geotechnical Testing Journal* 42(6), 1663-1684

Nejati HR, Ghazvinian A (2014) Brittleness effect on rock fatigue damage evolution. *Rock Mechanics and Rock Engineering* 47(5):1839–1848

Ord A, Vardoulakis I, Kajewski R (1991) Shear band formation in Gosford sandstone. In: *International journal of rock mechanics and mining sciences & geomechanics abstracts*. Elsevier 28(5):397–409

Peng K, Zhou J, Zou Q, Yan F (2019) Deformation characteristics of sandstones during cyclic loading and unloading with varying lower limits of stress under different confining pressures. *International Journal of Fatigue* 127:82–100

Salimi A, Faradonbeh RS, Monjezi M, Moormann C (2016) TBM performance estimation using a classification and regression tree (CART) technique. *Bulletin of Engineering Geology and the Environment* 77(1):429-440

Shirani Faradonbeh R, Taheri A, Karakus M (2021a) Post-peak behaviour of rocks under cyclic loading using a double-criteria damage-controlled test method. *Bulletin of Engineering Geology and the Environment* 80(2):1713-1727

Shirani Faradonbeh R, Taheri A, Karakus M (2021b) Failure Behaviour of a Sandstone Subjected to the Systematic Cyclic Loading: Insights from the Double-Criteria Damage-Controlled Test Method. *Rock Mechanics and Rock Engineering* [In Press]

Singh SK (1989) Fatigue and strain hardening behaviour of graywacke from the flagstaff formation, New South Wales. *Engineering Geology* 26(2):171–179

Sufian A, Russell AR (2013) Microstructural pore changes and energy dissipation in Gosford sandstone during pre-failure loading using X-ray CT. *International Journal of Rock Mechanics and Mining Sciences* 57:119–131

Taheri A, Yfantidis N, L. Olivares C, et al. (2016a) Experimental study on degradation of mechanical properties of sandstone under different cyclic loadings. *Geotechnical Testing Journal* 39(4):673-687

Taheri A, Royle A, Yang Z, Zhao Y (2016b) Study on variations of peak strength of a sandstone during cyclic loading. *Geomechanics and Geophysics for Geo-Energy and Geo-Resources* 2(1):1–10

Taheri A, Tatsuoka F (2015) Small- and large-strain behaviour of a cement-treated soil during various loading histories and testing conditions. *Acta Geotechnica* 10(1):131–155

Tarasov B, Potvin Y (2013) Universal criteria for rock brittleness estimation under triaxial compression. *International Journal of Rock Mechanics and Mining Sciences* 59:57–69

Tian W-L, Yang S-Q, Wang J-G, Dong J-P (2021) Failure behavior of the thermal treated granite under triaxial cyclic loading–unloading compression. *Geomechanics and Geophysics for Geo-Energy and Geo-Resources* 7(1):1–21

Vaneghi RG, Ferdosi B, Okoth AD, Kuek B (2018) Strength degradation of sandstone and granodiorite under uniaxial cyclic loading. *Journal of Rock Mechanics and Geotechnical Engineering* 10(1):117–126

Wang Y, Feng WK, Hu RL, Li CH (2021) Fracture evolution and energy characteristics during marble failure under triaxial fatigue cyclic and confining pressure unloading (FC-CPU) conditions. *Rock Mechanics and Rock Engineering* 54(2):799–818

Wang Z, Li S, Qiao L, Zhao J (2013) Fatigue behavior of granite subjected to cyclic loading under triaxial compression condition. *Rock Mechanics and Rock Engineering* 46(6):1603–1615

Wawersik WR, Fairhurst CH (1970) A study of brittle rock fracture in laboratory compression experiments. In: *International Journal of Rock Mechanics and Mining Sciences & Geomechanics Abstracts*. Elsevier, pp 561–575

Xiao J-Q, Ding D-X, Xu G, Jiang F-L (2009) Inverted S-shaped model for nonlinear fatigue damage of rock. *International Journal of Rock Mechanics and Mining Sciences* 3(46):643–648

Yamashita S, Sugimoto F, Imai T, et al (1999) The relationship between the failure process of the creep or fatigue test and of the conventional compression test on rock. In: *9th ISRM Congress. International Society for Rock Mechanics and Rock Engineering*

Yang S-Q, Ranjith PG, Huang Y-H, et al (2015) Experimental investigation on mechanical damage characteristics of sandstone under triaxial cyclic loading. *Geophysical Journal International* 201(2):662–682

Yang SQ, Tian WL, Ranjith PG (2017) Experimental Investigation on Deformation Failure Characteristics of Crystalline Marble Under Triaxial Cyclic Loading. *Rock Mechanics*

and Rock Engineering 50(11):2871–2889

Zhou HW, Wang ZH, Wang CS, Liu JF (2019) On Acoustic Emission and Post-peak Energy Evolution in Beishan Granite Under Cyclic Loading. *Rock Mechanics and Rock Engineering* 52(1):283–288

Chapter 9

Conclusions and Recommendations

9.1. Conclusions

In this thesis, state-of-the-art methodologies comprising machine learning (ML)- and experimental-based approaches were employed to investigate the rockburst phenomenon in detail. The significant findings and major contributions of the conducted research project can be outlined as follows:

- The statistical analysis techniques, including the box-plot, principal component analysis (PCA) and agglomerative hierarchical clustering (AHC) were identified as robust tools to visually represent the distribution of data points, analyse the interrelationship of the parameters, detect the outliers and natural groups in the datasets and finally, prepare a homogeneous database. [see Chapters 2, 4 and 5]
- The three ML algorithms of gene expression programming (GEP), genetic algorithm-based emotional neural network (GA-ENN) and the decision tree-based C4.5 algorithm showed the high performance in predicting the occurrence or non-occurrence of rockburst hazard as a binary classification problem (i.e. the prediction accuracy was higher than 80%). [see Chapter 2]
- The hybrid GA-ENN algorithm overcame the limitations of the prior ANNs (e.g., getting trapped in local minima) and provided a global solution for the problem. The C4.5, as a white-box ML algorithm, provided a visual simple tree structure for determining the rockburst status straightforwardly based on the specific range of values defined by the algorithm for different input parameters. The GEP algorithm, unlike the other ML techniques, through its inherent capability of function finding, successfully detected the latent complex non-linear relationship between the input parameters and the corresponding output. The GEP algorithm can open the black-box nature of the common ML algorithms and by providing the explicit models, facilitates the in-depth investigation of mining and geotechnical hazards. [see Chapter 2]

- The results of the sensitivity analysis conducted on the developed GEP-based binary model for rockburst status prediction revealed that the input parameters of maximum tangential stress (σ_θ), elastic energy index (W_{et}), uniaxial tensile strength (σ_t) and uniaxial compressive strength (σ_c) have the highest influence on rockbursting in deep underground mines, respectively. Due to the significant role of σ_θ in rockburst occurrence, more considerations should be taken into account during the design stage of the underground projects to control this parameter (i.e. by optimisation of the mining layout). [see Chapter 2]
- The comparison of the five conventional rockburst criteria, i.e., Russeness criterion, Hoek criterion, stress coefficient criterion, brittleness index criterion and elastic energy index (EEI) criterion, with the proposed ML-based models, showed that except for EEI criterion, the other conventional criteria have the prediction accuracy lower than 80% and cannot provide reliable estimations in practice. This can be attributed to the case study-based nature of the conventional criteria and considering few input parameters in their equations. [see Chapter 2]
- The complex relationship between different strength/stress- and energy-based parameters with the rockburst risk levels (i.e. the intensities of "none", "light", "moderate" and "strong") was recognised with high accuracy using the unsupervised learning algorithm of self-organising map (SOM). This algorithm, through an intelligent procedure, categorised the rockburst events having similar conditions in distinct clusters. [see Chapter 3]
- The determined weighted distances between the clusters by the SOM algorithm were also consistent with the rockburst intensities defined by the engineers. This demonstrated the high capability of this technique in adapting to mining-related problems, specifically for rockburst risk level investigation as a multi-class problem. [see Chapter 3]
- The evaluation of the weights of input variables in each cluster revealed that the maximum tangential stress of the surrounding rock mass (σ_θ) has the strongest influence on rockbursting, which is consistent with the results of the binary classification of rockburst status reported in Chapter 2. [see Chapter 3]
- The SOM algorithm with the value of 100% for the five performance indices of accuracy rate, precision, recall, F1 score and Kappa, proved its superiority over fuzzy c-mean (FCM) algorithm and the rockburst conventional criteria in clustering the rockburst risk levels. [see Chapter 3]
- The intact rock properties (i.e., uniaxial compressive strength, tensile strength, elastic

modulus, and Poisson's ratio) represented a significant effect on the failure mechanism (i.e., squeezing, slabbing, and strain burst) of the competent overs-stressed rock masses. The initial assessment of the compiled database from different underground mining projects showed that the failure mechanisms cannot be predicted solely by a single indicator. [see Chapter 4]

- Although the GEP algorithm can provide a mathematical equation to estimate the output parameter, it cannot be used solely to solve multi-class classification problems such as failure mechanism detection. It was found that the combination of the GEP algorithm with the logistic regression (LR) is an efficient methodology to overcome this difficulty. The GEP score calculated for each binary model of the failure mechanisms can be fed into the logistic regression as the independent variable to determine the occurrence probability of each failure mechanism. The failure mechanism having the highest probability value is selected as the final prediction. [see Chapter 4]
- According to the results of the confusion matrices and the receiver operating (ROC) curves, the developed GEP-based binary models in this research project were able to predict the status (occurrence or non-occurrence) of each failure mechanism, respectively, with 100% (AUC=1), 100% (AUC=1), and 97.14% (AUC=0.964) accuracy for squeezing, slabbing and strain bursting failure. However, the developed multi-class classifier of GEP-LR predicted the final class of failure based on the given intact rock properties with 100% accuracy. [see Chapter 4]
- The further validation of the GEP-LR model with nine unseen/new datasets also proved the high capability of this model in predicting the failure mechanisms accurately. Therefore, the developed GEP-LR model can be used as a practical tool by engineers and researchers to measure the propensity of the competent over-stressed rock masses to different failure mechanisms at the preliminary stages of the projects. [see Chapter 4]
- It was found that the maximum rockburst stress (σ_{RB}), i.e., the stress level that bursting occurs and the rockburst risk level (I_{RB}) inferred from the conducted comprehensive true-triaxial unloading tests are appropriate and reliable indices to investigate the rockburst phenomenon. [see Chapter 5]
- The correlation analysis and the stepwise selection and elimination (SSE) procedure were identified as efficient tools for dimension reduction (i.e., recognition of the most influential parameters), removing the multicollinearity among the independent parameters, and

reducing the complexity of the problem. According to the results of the foregoing analyses, the parameters of the uniaxial compressive strength (UCS), Young's modulus (E) and horizontal pressure coefficient (K) were identified as the most influential parameters for modelling of σ_{RB}; while, the parameters of Young's modulus (E), Poisson's ratio (υ), horizontal pressure coefficient (K) and σ_{RB} were recognised as the best combination of inputs for modelling of I_{RB}. [see Chapter 5]

- The mathematical functions and the visual patterns provided by the GEP and classification and regression tree (CART) techniques unravelled the latent relationship between the rockburst parameters (i.e. σ_{RB} and I_{RB}) and their corresponding influential parameters. The performance analysis of the developed models showed that the GEP-based models with the values of 0.94, 14.25 and 9.80 for the indices of R^2, $RMSE$ and MAE for σ_{RB} and the values of 0.94, 0.19 and 0.14 for the foregoing performance indices for I_{RB} outperformed the CART-based models. However, the CART algorithm was recognised as the efficient tool for solving the high-complex non-linear problems in mines. [see Chapter 5]
- The performed parametric analysis on the best models showed that by an increase in UCS and σ_v, σ_{RB} increases monotonically. Also, the risk of rockburst occurrence showed a downward non-linear trend with the independent parameters of K, E, υ and σ_{RB}. Furthermore, the parametric analysis showed strong correlations among the rockburst parameters and their input parameters, representing that the selected inputs are potential indicators for assessing and predicting the rockburst phenomenon in deep underground mines. [see Chapter 5]
- The developed "Double-Criteria Damage-Controlled Test Method" in this research project by adapting two controlling criteria, including the maximum axial stress level that can be achieved and the maximum lateral stain amplitude that the rock specimen can experience in a cycle during loading, i.e. $Amp.(\varepsilon_L)$, was successful in capturing the post-peak stress-strain behaviour of Tuffeau limestone subjected to the uniaxial multi-level systematic cyclic loading history. This technique opens new insights into the rock failure mechanism and the long-term stability assessment of the underground structures under seismic disturbances. [see Chapter 6]
- It was found that the overall post-peak behaviour of rocks under multi-level systematic cyclic loading is characterised by the combination of class I and class II; however, the class II behaviour was more dominant for the specimens that experienced more loading and unloading cycles. [see Chapter 6]

- The specimens which experienced more cycles in the pre-peak regime failed at stress levels higher than the determined average UCS for Tuffeau limestone specimens, i.e. the strength hardening occurred. [see Chapter 6]
- The following four main stages were distinguished for the evolution of damage parameters of Tuffeau limestone specimens subjected to the multi-level systematic cyclic loading history: (a) The increase in rock stiffness due to the closure of the pre-existing voids and rock compaction, which was accompanied by the decrease in energy dissipation ; (b) the domination of the quasi-elastic behaviour due to the balance between two mechanisms of grain-crushing and pore collapse over the pre-peak domain; (c) the gradual decrease in rock stiffness due to dilatant microcracking with more energy dissipation; and (d) the generation and coalescence of microcracks which resulted in a rapid increase in damage and energy dissipation and more reduction in stiffness. [see Chapter 6]
- According to the evolution of the crack damage stress (σ_{cd}) during the cyclic loading, the rock specimens did not switch from the compaction-dominated to a dilatancy-dominated state, should the applied stress level is not high enough to create critical damage within the specimens. This resulted in a constant σ_{cd} that is approximately equal to the unloading stress in each cycle. [see Chapter 6]
- The observed strength hardening for the Tuffeau limestone specimens can be attributed to the rock compaction induced by the cyclic loading history. The weak bonding between the grains can be broken during loading and unloading cycles and the produced fine materials may fill up the internal pores, which finally may result in more rock compaction and hardening behaviour. [see Chapter 6]
- The proposed testing methodology was also successful in capturing the complete stress-strain curves (i.e. the pre-peak and the post-peak regimes) of Gosford sandstone specimens subjected to single-level systematic cyclic loading at different stress levels (i.e. σ_a/σ_m=80-96%). [see Chapter 7]
- A threshold of σ_a/σ_m was identified which lies between 86-87.5%. For the stress levels lower than this range (i.e. the hardening cyclic loading tests), failure did not occur for a large number of cycles, and the rock specimens followed a two-stage damage evolution law (dominated by the quasi-elastic behaviour). For these tests, the damage evolution also was found to be independent of the cycle number, as no considerable effect was observed on damage parameters by increasing the cycle number from 1500 to 10000 cycles. [see Chapter 7]

- Below the fatigue threshold stress, the rock behaviour under cyclic loading in the pre-peak and the post-peak regimes was approximately similar to those in monotonic loading conditions. For the specimens subjected to the cyclic loading below the fatigue threshold stress, no considerable damage was incurred within the specimens and the peak strength increased up to 8% after applying the monotonic loading (i.e. the strength hardening occurred). [see Chapter 7]
- For the specimens which experienced cyclic loading beyond the fatigue threshold stress (i.e. the fatigue cyclic loading tests), the failure occurred during loading and unloading cycles. For such tests, the lateral and volumetric irreversible strain were accumulated more rapidly in the specimens. Moreover, beyond the fatigue threshold stress, the increase in σ_a/σ_m resulted in rock failure in a more brittle/self-sustaining manner. [see Chapter 7]
- According to the evolution of the cumulative irreversible axial strain ($\sum \varepsilon_a^{irr}$), a secondary inverted S-shaped damage behaviour was identified in the post-peak regime of the fatigue cyclic loading tests. In other words, the second loose behaviour before the failure point extends to the post-peak stage for several cycles. These loose hysteretic loops are followed by a dense behaviour for a large number of cycles until the complete failure of the specimens occurs, showing another loose behaviour. With the increase of the applied stress level, the damage per cycle decreased exponentially, and the three stages of the secondary inverted S-shaped damage behaviour was more visible in the post-peak regime. [see Chapter 7]
- The modified triaxial testing procedure, i.e. mounting four lateral strain gauges at the mid-length of the rubber membrane and connecting them to a Wheatstone bridge to provide a single lateral strain feedback signal, was successful in controlling the axial load and performing the single-level systematic cyclic loading tests at different stress levels and confining pressures. [see Chapter 8]
- By increasing the confinement level (σ_3/UCS_{avg}) from 10% to 100%, the fatigue threshold stress (FTS) of Gosford sandstone decreased from 97% to 80%, which indicated that rocks in great depth experience the failure due to cyclic loading at stress levels much lower than the determined monotonic strength. [see Chapter 8]
- An unconventional post-peak stress-strain behaviour was observed for rocks by an increase in confinement level (σ_3/UCS_{avg}) so that for lower σ_3/UCS_{avg}, the rock specimens mostly showed a class II/self-sustaining behaviour, while for higher confinements, the ductile behaviour was dominant. [see Chapter 8]

- According to the calculated energy-based brittleness index for the rock specimens which did not fail in cycles, a transition point at σ_3/UCS_{avg}= 65% was identified, where the rock specimens switch from the brittle failure behaviour to ductile one. It was found that the cyclic loading at confinement levels lower than the determined transition point has no considerable effect on the post-peak instability of rocks, while for confinement levels of 80% and 100%, the weakening effect of the systematic cyclic loading history on rock brittleness was significant. [see Chapter 8]
- According to the evolution of the tangent Young's modulus (E_{tan}), cumulative irreversible axial strain (ω_a^{irr}) and acoustic emission (AE) hits for hardening cyclic loading tests, it was observed that cyclic loading creates no macro-damage within the specimens in the pre-peak regime, and the rock stiffness remains almost constant until 1000 loading and unloading cycles are completed. [see Chapter 8]
- For weakening cyclic loading tests (i.e., the tests that did not fail during the cycles and showed negative peak strength variation), the gradual decrease and increase in E_{tan} and ω_a^{irr} were observed, respectively, with cycle loading. Moreover, compared to the hardening cyclic loading tests, the AE activities were more evident for specimens that showed a higher amount of strength degradation. This is while for damage cyclic loading tests (i.e., the tests that failed during cycles), the damage was accumulated with a higher rate and extent in the specimens with an increase in confining pressure. [see Chapter 8]
- According to the variation of the axial strain at the failure point (ε_{af}) for the monotonic, hardening/weakening and damage cyclic loading tests, it was found that under confinement levels below the transition point, the applied stress level (q_{un}/q_{m-avg}) has no significant effect on the cumulation of the plastic deformations in the pre-peak regime and the values of ε_{af} are similar to those in monotonic loading conditions. However, for higher confinement levels, cyclic loading resulted in larger plastic deformations before the failure point. [see Chapter 8]
- For the Gosford sandstone specimens that did not fail in cycles, it was found that the peak strength varies between -13.18% and 7.82%. The strength hardening at lower confinement levels, as observed for uniaxial systematic cyclic loading tests, can be related to the rock compaction induced by cyclic loading. However, the increase in confining pressure resulted in a decrease in strength hardening amount due to the accumulation of plastic deformations in the specimens. [see Chapter 8]
- A CART-based model was proposed in this research project to estimate the peak strength

variation of Gosford sandstone as a function of the applied stress level (q_{un}/q_{m-avg}) and confinement level (σ_3/UCS_{avg}). The coefficient of determination (R^2) for this practical model was 90% which proved the high prediction performance of this model. [see Chapter 8]

9.2. Recommendations

According to the methodologies used in this thesis and the corresponding obtained results, the following recommendations are suggested for future studies to better address the rockburst-related issues in deep underground mining operations:

- By considering the performance of the machine learning (ML) algorithms used in this thesis (i.e., GA-ENN, C4.5, GEP, CART, and GEP-LR techniques) in dealing with high-complex non-linear problems (e.g. rockburst hazard), establishing a more comprehensive and precise rockburst database by including the intact rock properties, rock mass parameters, geostress conditions, hydrogeological conditions and the geometry of the excavations, holistic approaches can be developed to predict the rockburst occurrence and its risk level accurately.
- Taking into account the well-known ML principle of "Garbage in, garbage out", the selection of the appropriate training datasets has a crucial effect on the reliability and accuracy of the models. The ML-based rockburst models available in the literature have been mostly developed based on the limited datasets (maximum 250 datasets, while almost 80% of them are considered for training the models). This is while the small amount of the training samples cannot provide sufficient information for the ML algorithms, and finally, the developed models may not be able to estimate the output parameter correctly by feeding the new compiled datasets from the real projects. On the other hand, the available rockburst databases in the literature are imbalanced, i.e., the number of data cases for each rockburst risk level (i.e. "none", "light", "moderate" and "strong") are not equal. This may create biased models and decrease the applicability of the proposed models. Therefore, in future studies, bigger and balanced databases should be provided to better analyse the rockburst phenomenon. A promising technique to balance the database is over/under-sampling.
- Many studies can be found in the literature regarding the rockburst potential evaluation in the long term; however, no significant progress has been made in the short-term assessment of this hazard using machine learning (ML) techniques. Microseismic signals

are significant precursors of rockburst occurrence. However, the genuine rock microseismic signals usually interfere with the signals/noises induced by other sources, such as mechanical excavations, haulage systems, drilling and blasting operations, etc. The correct distinguishing of the genuine signals from the noise signals can provide some critical features to estimate the rockburst occurrence. As proved in this research project, the developed hybrid GEP-LR model is a powerful technique for multi-class classification tasks and can be utilised in future studies to provide a practical model to discriminate between different microseismic signals in burs-prone areas. By doing so, a proper relationship can be established between the burst signals and rockburst occurrence, and finally, the time of bursting can be predicted.

- The "Double-Criteria Damage-Controlled Test Method" developed in this research project was recognised as an efficient methodology for capturing the post-peak behaviour of rocks subjected to seismic events/cyclic loadings. In future studies, this technique can be adjusted for the triaxial testing system to better analyse the failure mechanism of rocks under different confining pressures.
- More in-depth numerical and experimental investigations should be undertaken concerning the true post-peak behaviour of stable and unstable rock failures under monotonic and cyclic loading conditions. In this regard, the influence of loading system stiffness as well as the applied load control technique should be evaluated on the failure behaviour of rocks. Although the lateral strain-controlled technique was identified as an appropriate technique in capturing the complete stress-strain behaviour of rocks, the capability of other load control techniques such as the linear combination of axial stress (σ) and strain (ε) (i.e., $\varepsilon - \alpha.\sigma/E = C.t$, where α is a constant less than 1.0, C is the loading rate which is usually set at 10^{-5}/s and E is Young's modulus), which has been reported as the potential load control technique in very few studies in the literature, needs to be further investigated. It is also recommended to apply a large number of cycles (e.g., more than 1,000,000 cycles) in future rock fatigue studies to better replicate the seismic events in real mining projects and evaluate its effect on fatigue threshold stress (FTS).